Structural and thermal stability of metal halide perovskite solar cells

Susana Iglesias Porras

School of Engineering

Newcastle University

A thesis submitted for the degree of

Doctor of Philosophy

December 2021

Abstract

Metal halide perovskite solar cells were crowned the top-performing emerging photovoltaic technology with a certified maximum efficiency of 25.2 % in 2021. Their facile low-cost processability and wide optoelectronic properties make them both a powerful contender against traditional crystalline silicon cells and the perfect ally in tandem configurations. However, their rapid degradation upon operational conditions, including long-term exposure to temperature oscillations, represents a major obstacle to their commercialization. Hence, finding perovskite compositions that are structurally stable within the operational temperature range is crucial for the development of market-viable photovoltaic panels.

This thesis firstly explores the validity of the most popular method used in the literature to assess structural stability in perovskites: integral breadth (IB) XRD microstrain analysis. It unveils how IB techniques are unsuitable for the extraction of microstrain in perovskite thin films since the results breach the Wilson-Stokes approximation constraint: parallel *hkl* planes do not report equivalent values of microstrain as expected. This phenomenon persists even when using instrumental error minimized scan conditions, suggesting the presence of a microstrain gradient across the order-of-diffraction.

Additionally, B-site mixing is explored as a delayer of the thermal decomposition of triple cation mixed halide perovskites, creating a symbiosis between high entropy and structural stability. Partially replacing Pb^{2+} with Sb^{3+} in multi-mixed systems improves their heat endurance without compromising their structural stability as proven by XRD and an in-house designed *in-situ* colourimetry test kit. The complex interplay between the defect-prone optoelectronic properties and the improved structural strength of these heterovalent perovskites is also investigated in solar cells using different charge transporting materials.

Overall, this thesis highlights the importance the structural stability has in the thermal endurance of perovskites, suggesting the distribution of microstrain both between crystallographic orientations and within their order-of-diffraction as a playing factor in the pursuit of long-lasting operational devices.

Acknowledgements

First and foremost I would like to thank my supervisors, Prof. Dr Noel Healy, Dr Pablo Docampo and Dr Dumitru Sirbu for their support and guidance during my doctoral studies and for reviewing this thesis.

Noel, I am very thankful for your willingness to take an active part in my supervision team and for becoming my first supervisor in the middle of my PhD. I am grateful for all the interesting points and discussions you raised in the meetings and for always showing a positive attitude. I enjoyed very much doing lab demonstrations in Physics under your supervision and I really appreciate all the numerous times you had to repeat sentences while on my first year because I just could not get them. I must say that, at that time, I could not imagine I would end up being able to have the fluent conversations we have now.

Pablo, I am very much appreciative of your constant advice and expertise in perovskites during all of my PhD journey. Yet, I am the most thankful for often pushing me out of my comfort zone. I am certain I would not have developed the strong equipment setting-up skills I have now without that push. I value very much that you always came to the rescue whenever I was in trouble (e.g. that day that I accidentally stabbed myself with perovskite) and that you managed to keep a supervising role from Glasgow. I am also very thankful for your Geordie-English live-interpretation skills during my first year when all I could do in the workshop was smiling and nodding. I also want to acknowledge the work you have done on most of the Labview codes for the automatic JV scan setups.

Dima, I can not thank you enough for the continuous support you have offered during practically all of my PhD journey. I have enjoyed very much having you both as a 'lab buddy' and a mentor and I am very grateful and proud that you accepted to be part of my supervision team. I want to thank you for teaching me all I know about crystallization, for helping me lose the fear of managing chemicals in the lab and especially for always acknowledging all the effort, hours and work I was putting into my PhD. I really enjoyed discussing both science and life with you in the lab with Red Hot Chilly Peppers somehow playing on repeat in the background (even though it was in shuffle mode). I am also very thankful for all the sound advice you have given me over the years and for becoming a really good friend. Lastly, I want to acknowledge your work synthesizing the EDOT-Amide-TPA.

I would want to thank my collaborators at Newcastle University Dr Fabio Cucinotta for the TRPL measurements, Nathan Hill for the fabrication of the $(PEA)_2PbI_4$ single crystal and Harvey Morrit and Hannes Michaels for helping me acquire the temperature-dependent conductivity measurements.

I would also want to acknowledge the work of the mechanical workshop team, especially that of John Smith and Samuel Burn, who manufactured most of the metal pieces from my equipment designs and thank them for their patience with me and my difficulties understanding Geordie during my first year. Equivalently, I want to acknowledge the work of Jeffrey Warren and the electronic workshop team in the manufacturing and soldering of the PCBs, and highlight the impeccable attention to detail they put in all those tiny connections.

My gratitude also goes to Dr Konstantin Vasilevskiy for teaching me how to operate the equipment in the clean rooms and for always ensuring everything was neat, tidy and operative. I deeply appreciate that you trusted me in using equipment, especially when I had to add my own 'creations' to the XRD diffractometer.

Furthermore, I want to express my sincere thanks to the people from the perovskite group including Nathan Hill, Abigail Seddon, Miriam Fsadni, Ivan Shmarov, Amy Neild, Naseem Alsaif and Eman Alkhudhayr for being able to sustain a nice atmosphere in the lab during both the good and the more challenging times. Nathan, I have enjoyed very much sharing the office with you and I am really appreciative of all the discussions we have had over the years (both scientific and non-scientific). You always offered a helping hand with Labview, listened to my ridiculously bad-English rants ('What is the ****!?') and most importantly, always showed up as a good friend. Likewise, I want to thank Abbi and Miriam for being really good lab mates and friends. Abbi, you truly brought joy into the lab every time you stopped by to say hi ('to the pigeon') and Miriam, I can not thank you enough for the enormous amount of pure kindness you always bring with you to work.

My gratitude also goes to the members of the ETM group with whom I have shared many hours of work in the clean rooms. I want to thank Dr Enrique Escobedo-Cousin for introducing me to the e-beam and especially for showing me the secrets of the AFM. Likewise, I would like to give special thanks to Dr Luke Bradley and Dr Johannes Gausden for their friendship and all the PhD advice, support, chats and beers we have shared during the past four years.

I also want to extend my gratitude to the members of the Gibson and Freitag groups for taking part in many useful scientific discussions and for making work in the labs really welcoming and fun. In this context, I must give a special mention to Dr Joshua Karlsson for the numerous times I had to resort to his magic to open the stuck mineral oil bottles.

I wish to thank the School of Engineering and the Student Progress Service at Newcastle University for the exceptional measures they put in place to safeguard me during the last year of my PhD. My special thanks go to Nicola Hawdon and Rachel Rice at

the Merz Court office, who have shown endless support and help during such challenging times. Likewise, I would like to show my deepest appreciation for the help my colleagues and supervisors have provided me with, especially Dima, Luke, Hannes, Johan, Enrique and Nathan, who have escorted me in and out of the University on numerous occasions. I literally would not have been able to carry out the last pieces of the work contained in this thesis without you.

I would also like to express my deepest gratitude to the members of my progression panel, Dr Jonathan Goss and Dr Rishad Shafik. I am truly thankful for your support and advice during the very uncertain and challenging times I have lived through the past four years. I can not thank you enough for always seeing all the work and effort I was putting into my PhD and for acknowledging and understanding the unusual set of circumstances surrounding my journey. Your support truly kept me going when I thought the system would engulf me.

My special thanks go to my dearest friends Sandra, Alba and Víctor. I appreciate very much that we consistently kept the 'brain wire' connection despite the distance and our many times incompatible working schedules. Our weekly Skype conversations always lifted my spirits independently of the stage of my PhD journey. Needless to say, playing 'the misfortunes competition' has been a magnificent way of keeping ourselves in check through humour ('aunque solo fuera por las risas').

Last but not least, I want to thank my family for being the strongest source of love, support and encouragement in my life. Your contribution to this thesis goes beyond my own because you always held the vision. You were able to see the importance of higher education and science without having had access to it. You have always seen and had faith in my abilities when I could not see them anymore. If I have been resilient enough to somehow endure hardship, it is because I have learned from the masters I had at home. I do not have enough words to thank you for the astonishing work of reconstruction you have done on me during the last months of my PhD. Have no doubt that if I can write these lines on a scientific document it is thanks to you.

Contents

List of Abbreviations

General abbreviations

2D	Two-dimensional
3D	Three-dimensional
ADC	Analog to Digital Converter Reading
CI	Confidence Interval
E_{a}	Activation energy
E_{g}	Bandgap energy
FF	Fill Factor
FWHM	Full Width at Half Maximum
GOF	Goodness of Fit
HI	Hysteresis Index
IV	Current-Voltage
JV	Current density-Voltage
J_{mp}	Current density at maximum power point
J_{SC}	Current density at Short-Circuit
PCE	Power Conversion Efficiency
QFLS	Quasi Fermi Level Splitting
V_{mp}	Voltage at maximum power point
V_{OC}	Open-Circuit Voltage
a-Si	Amorphous silicon
AFM	Atomic Force Microscope

c-Si	Crystalline silicon
c-TiO_2	Compact titanium oxide
CB	Conduction Band
CIGS	Copper Indium Gallium Selenide
DIP	Dual In-line Package
DSSC	Dye Sensitized Solar Cell
ETL	Electron Transporting Layer
FI	Fixed Illumination length (XRD configuration)
FPA	Fundamental Parameters Approach
FS	Fixed Slit (XRD configuration)
GND	Ground
HOMO	Highest Occupied Molecular Orbital
HTL	Hole Transporting Layer
HTM	Hole Transporting Material
IB	Integral Breadth
IDC	Insulation Displacement Contact
ITC	Inverse Temperature Crystallization
JST	Japan Solderless Terminal
LED	Light Emitting Diode
m-TiO_2	Mesoporous titanium oxide
mod-WH	modified Williamson-Hall
MPP	Maximum Power Point
MS	Microstrain
MUX	Multiplexer
NIST	National Institute of Standards and Technology
NREL	National Renewable Energy Laboratory

NTC	Negative Temperature Coefficient
OPV	Organic Photovoltaic
PCB	Printed Circuit Board
PCT	Pixel Colour Tracking
PL	Photoluminescence
PSC	Perovskite Solar Cell
PSD	Position Sensitive Device
PV	Photovoltaic
QD	Quantum Dot
QDSC	Quantum Dots Solar Cell
RH	Relative Humidity
RMS	Root Mean Square
RT	Room Temperature
SC	Single Crystal
SRH	Shockley-Read-Hall
STC	Standard Test Conditions
STS	Scanning Tunnelling Spectroscopy
TCO	Transparent Conductive Oxide
TCSPC	Time-Correlated Single-Photon Counting
TRPL	Time-Resolved Photoluminescence
UDEDM	Uniform Deformation Energy Density Model
UDSM	Uniform Deformation Stress Model
UPS	Ultraviolet Photoelectron Spectroscopy
UV	Ultra-Violet
UV-Vis	Ultra-Violet-Visible
VB	Valence Band

VBM	Valence Band Maximum
VDD	Voltage Drain Drain
VSS	Voltage Source Source
WH	Williamson-Hall
XRD	X-ray Diffraction

Chemical abbreviations

ABS	Acrylonitrile Butadiene Styrene
C_{60}	(C_{60}-Ih) [5,6] fullerene
CB	Chlorobenzene
CuSCN	Cuprous Thiocyanate
DMF	Dimethylformamide
DMSO	Dimethyl Sulfoxide
ETOH	Ethanol
FA	Formamidinium
FTO	Fluorine-doped Tin Oxide
GUA	Guanidinium
HDPE	High-Density Polyethylene
IPA	Isopropanol/2-propanol
ITO	Indium-doped Tin Oxide
Li-TFSI	Lithium bis(trifluoromethanesulfonyl)imide
MA	Methylammonium
MDA	Methylenediammonium
P3HT	Poly(3-Hexylthiophene)
PCBM	Phenyl C_{61} Butyric Acid Methyl Ester
PEA	Phenylethylammonium
PEDOT:PSS	Poly(3,4-ethylenedioxythiophene) Polystyrene Sulfonate

PET	Polyethylene Terephthalat
PMMA	Poly(Methyl Methacrylate)
PTAA	Poly(triaryl amine)
tBP	4-tert-Butyl Pyridine

Perovskite compositions

Cs_5	$Cs_{0.05}FA_{0.789}MA_{0.161}PbI_{2.49}Br_{0.51}$
$Cs_{7.5}$	$Cs_{0.075}FA_{0.768}MA_{0.157}PbI_{2.778}Br_{0.222}$
Sb_5	$Cs_{0.075}FA_{0.768}MA_{0.157}Pb_{0.95}Sb_{0.05}I_{2.825}Br_{0.225}$

List of Figures

List of Tables

Chapter 1. Introduction

1.1 The energy landscape and solar power

Human population is currently growing at an approximate rate of 1.05 % per year as of 2020.[313] Although the number is almost half of the historical maximum (around 2 % in the late 1960s), it still represents 81 million more people in the world annually. Added to the current 7.9 billion people and the increasing efforts to reduce energetic poverty, a significant rise in the global energy demand is expected.[313] The ability to guarantee the energy supply for the world's population while doing so in a sustainable manner is probably the main challenge humanity faces nowadays.

Unfortunately, the pre-COVID energetic scenario stood out for quite the opposite, as highlighted in figure 1.1. In 2018 the global energy consumption grew at a rate of 2.9 %, almost doubling the average rate for the decade while increasing carbon emissions by 2 %: the fastest growth in seven years.[22] The data contradicted the increasing environmental awareness and energy efficiency policies the developed countries had been implementing for the past decade.[148,221,88] The explanation behind these numbers highlighted a worrying reality: global warming is hitting us back. The out-of-trend energy consumption displayed in 2018 was related to extreme weather effects: an unusually large number of hot and cold days was registered in countries like China, the US and Russia which explained the increased demand for cooling and heating services.[22] Although in 2019 the global primary energy consumption and CO_2 emissions growth got reduced to 1.3 % and 0.5 %, respectively, carbon-based energy sources still represented 84.3 % of the global primary energy share.[23]

The unexpected hit of the COVID global pandemic in 2020 significantly reversed the energetic trends producing a 4.5 % decline in the global primary energy consumption and a 6.3 % reduction in carbon emissions.[24] However, these numbers were linked to the unprecedented collapse of oil demand as transport-related restrictions imposed by lockdowns took place.[24] Although more efforts than ever are put into the application of energy efficiency policies, the existence of extreme weather to energy consumption patterns could be throwing humanity into a dangerous vicious cycle: extreme weather that increases consumption, producing more carbon emissions which keep fostering extreme weather.

The links between extreme weather conditions, anthropogenic CO_2 emissions and global warming are undeniable. Although the natural greenhouse effect provided by the

atmosphere helped the development of life on Earth, the excess of the so-called greenhouse gases (CO_2, N_2O, methane, water vapour or chlorofluorocarbons) contributes to the trapping of excess heat, which translates into an increase of the global temperature. Changes in precipitation patterns, more droughts and heat waves, changes in the ocean currents and oceanic acidity levels, melting of the polar caps and increase of the sea levels are among the multiple and dangerous effects associated with global warming.[236,344,97,25] These phenomena not only affect our energy consumption habits but are also a critical threat to ecosystems and life on Earth. Hence, this climate and energy crisis demands a switch towards an efficient consumption of renewably sourced energy.

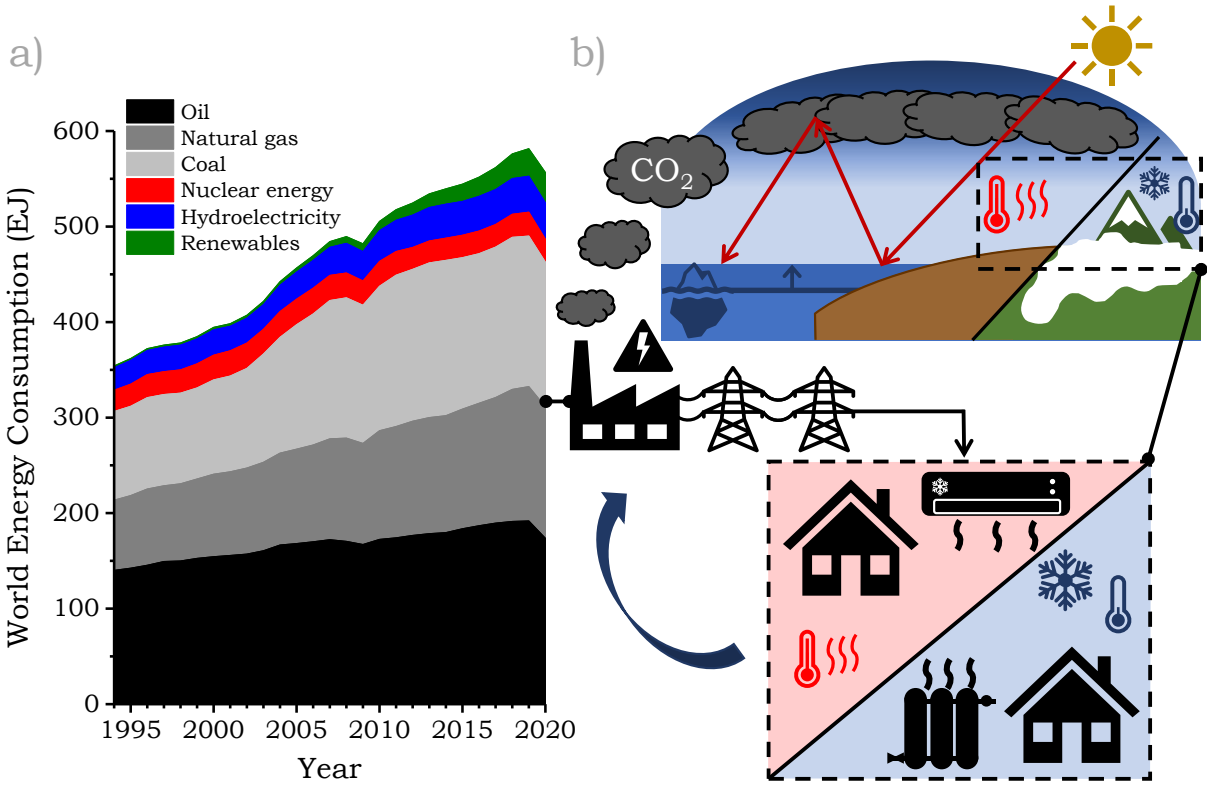

Figure 1.1: a) World energy consumption by energy source from 1994 until 2020. Data extracted from[24]. b) Schematic representation of the extreme-weather-to-energy-consumption pattern.

Nearly four million exajoules (EJ) of solar energy reach the earth annually, of which approximately 50 000 EJ are claimed to be easily harvestable.[128] Yearly global consumption energy levels stood roughly between 550 EJ and 560 EJ in the past five years, less than 1.2 % of the above-mentioned usable solar potential.[24] Hence, provided an adequate development of solar cell technologies, solar power is the obvious answer to the present energy and climate crisis.[128] Despite the potential, currently, only 3.2 % of the total power generation is produced with photovoltaic technologies,[24] which highlights the urgent need for investing in both PV installation and development to reach the climate objectives marked by the Paris Agreement and the Glasgow Climate Pact.[221,88]

The development of PV technology started with the fabrication of the first working solar cell in 1883 by Charles Fritts,[82] 44 years after the discovery of its operational

principle, the photovoltaic effect, observed by Alexandre-Edmond Becquerel.[15] Yet, it was not until 1946 that the first modern solar cell made of silicon was invented by Russel Ohl.[213] Figure 1.2 displays modern top-performing solar cells classified by technology.

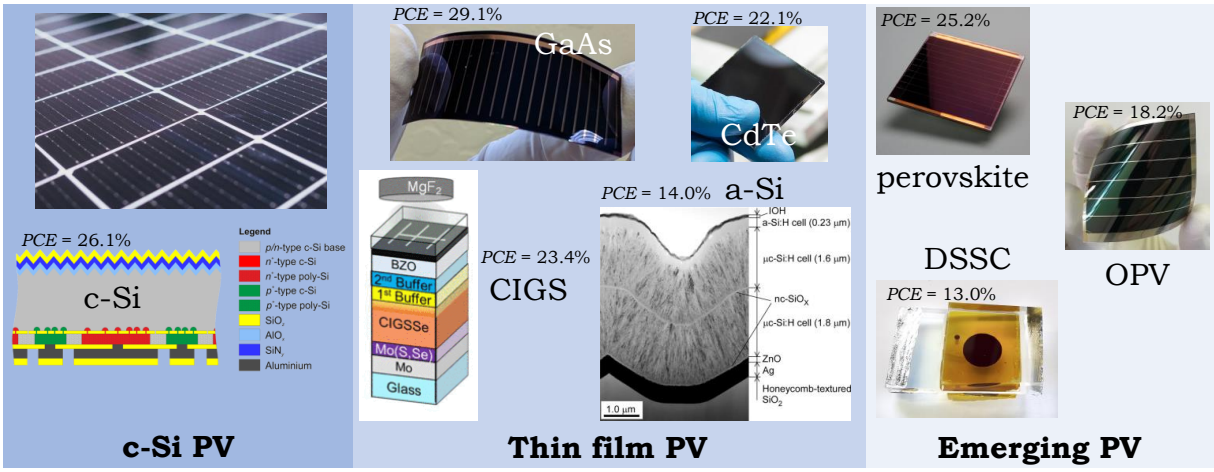

Figure 1.2: High performing solar cells classified by technology. Certified performances are extracted from[210]. Schematic drawing of a top-performing c-Si solar cell with n and p-type poly-Si regions adapted with permission from[96]. Copyright 2019, John Wiley & Sons, Ltd. Image credits for GaAs and CdTe cells: *Alta Devices/Business Wire*,[7] and *First Solar*[81]. Schematics of CIGS solar cell adapted with permission from[199]. Copyright ©2019, IEEE. Cross-sectional TEM image of a-Si cell reproduced with permission from[250]. Copyright 2016 AIP Publishing. Image credits for perovskite, OPV and DSSC cells: *UNIST*,[297] *CEA/Toyobo*,[36] and *EPFL*,[76].

Since the 1950s, silicon wafer-based devices have dominated the photovoltaic energy market, accounting for the 95 % of the global production in 2020.[231] Particularly, crystalline silicon (c-Si) based solar cells have reported substantial performances both at laboratory (∼27 %) and commercial scale (∼20 %) while guaranteeing an operational life of 25 years.[210,231,56] However, the use of silicon requires the fabrication of relatively thick layers (several hundreds of microns) due to its indirect band gap, and the use of a very precise manufacturing process to ensure optimal performance, requiring high purity and low defect concentrations.[214] Although the price of manufacturing processes has observed a significant decrease in the past twenty years, cheapening the generated power from ∼76 USD/W to ∼0.3 USD/W in 2017,[276] the rigidity requirements imposed by thick c-Si layers limit the fabrication of light-weight flexible PV modules.

Second-generation PV technologies are based on the fabrication of thin film devices, thanks to the direct band gap of the absorbers such as copper indium gallium selenide (CIGS), cadmium telluride (CdTe), gallium arsenide (GaAs) or amorphous silicon (a-Si). However, the limited availability of the elements conforming the highest performing devices such as Ga, Te, Se and In (CdTe, 22.1 %; CIGS, 23.4 %; GaAs, 29.1 %) and the low performance of the easily processable a-Si solar cells (14 %) set the use of these technologies far behind c-Si modules.[300,210]

Lastly, third-generation PV overcame the large-scale feasibility handicap of the previous generation thanks to the large availability of raw materials and low fabrication costs.[133] Amongst them stand dye-sensitized solar cells (DSSCs), organic photovoltaics (OPVs) and quantum dot solar cells (QDSCs). While easy and cheap to make, these devices rarely surpass the 18 % in performance.[210] Hence, for the past 10 years, research interest has drifted towards the most recent technology: perovskite solar cells.

1.2 Perovskite photovoltaics: a rising technology

Currently, halide perovskite solar cells stand out as the top-performing emerging photovoltaic technology, which linked to their low-cost facile processability, pose them as the ideal candidate to revolutionize the PV market. In slightly over a decade, the efficiency of single-junction devices has grown from 3.8 % in 2009 up to a certified 25.2 % in 2021, returning comparable results to the record value for crystalline silicon (26.7 %) (figure 1.3).[142,120,210] Their tunable band gaps have also made them a suitable technology to combine with traditional silicon cells in tandem architectures, rendering certified record performances close to 30 %.[210,145,327,139]

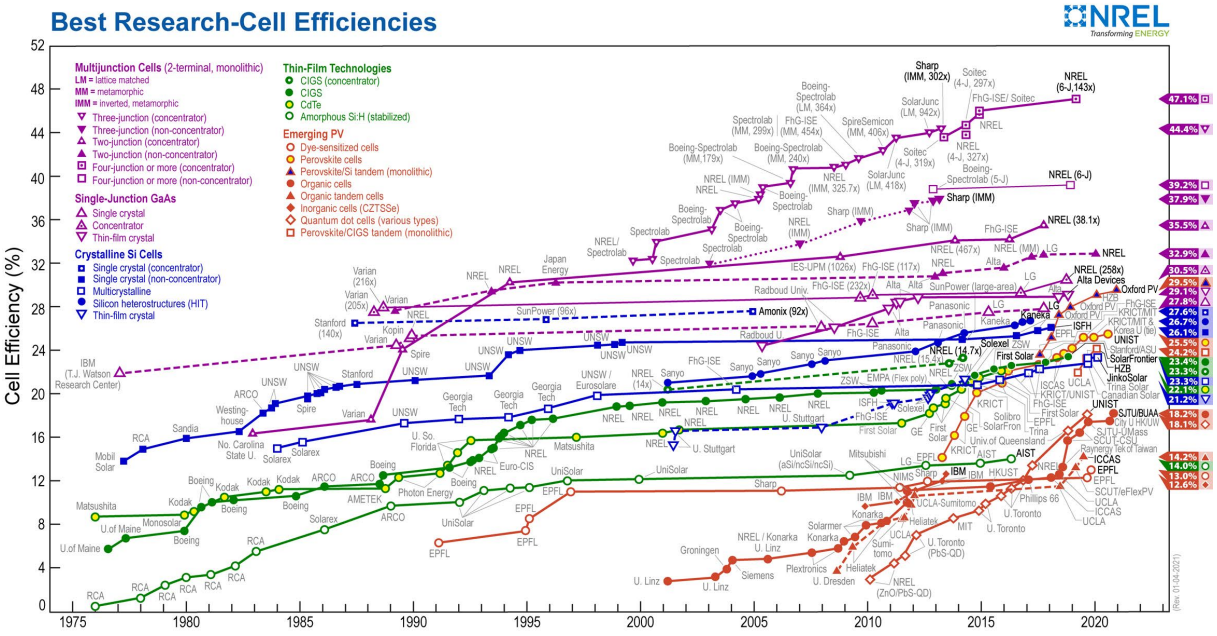

Figure 1.3: Record certified efficiencies of research photovoltaic cells plotted by technology. Published by the National Renewable Energy Laboratory (NREL).[210]

Halide perovskite semiconductors take their name from their oxide counterpart calcium titanate ($CaTiO_3$), named after the Russian mineralogist Lev Perovski since they crystallize in the same ABX_3 structure.[131] Figure 1.4 represents the ideal cubic perovskite structure, with the A cation positioned at the centre of a cube defined by the smaller B cations. These are octahedrally coordinated by 6 X halide anions (I^-, Br^- and/or Cl^-), forming a three-dimensional lattice of corner-sharing BX_6 octahedra.

Methylammonium lead iodide ($MAPbI_3$) is considered the archetypal perovskite used in photovoltaic applications with a mixed organic-inorganic composition where iodide is positioned at the X site, Pb^{2+} at the B site and the organic cation $CH_3NH_3^+$ (commonly abbreviated as MA) at the A-site. However, a variety of perovskites with different A, B and X ions are commonly used in photovoltaic applications, including fully inorganic compositions such as the caesium lead trihalides ($CsPbX_3$; X=I, Br, Cl).[237]

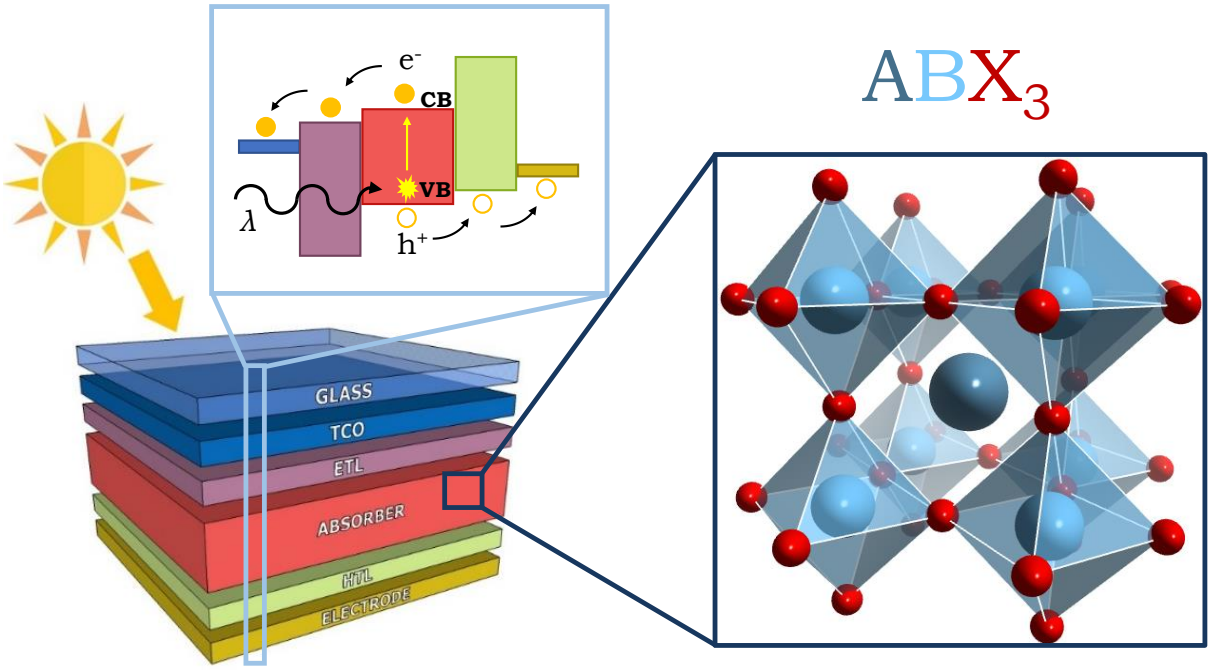

Figure 1.4: Schematic planar-heterojunction perovskite cell device. The right inset represents the crystallographic arrangement of the perovskite ABX_3 structure. The top inset summarizes the process of charge generation and extraction within the device upon light exposure. Perovskite structure image credit: *chemicalstructure.net*.[227]

In a solar cell, perovskite semiconductors function as the absorber material, traditionally in an *n-i-p* junction as schematically depicted in figure 1.4. Sunlight passes through the glass-coated transparent conductive oxide (TCO) and the electron transporting material (ETL) and is absorbed by the perovskite layer. Photons with higher energies than the band gap of the perovskite generate an electron-hole pair, shifting the electron from the valence band (VB) into the conduction band (CB) and leaving a hole in the VB, which can be understood as a positively charged quasi-particle. The charges travel towards the charge selective extraction layers aided by a suitable alignment of the bands.

In the dark and at equilibrium, the Fermi levels of the ETL, HTL and perovskite layers align, generating an electric field inside the perovskite that is often shielded by ionic accumulation at the interfaces.[74] Under illumination, the Fermi level in the perovskite splits into the quasi-Fermi level for electrons ($E_{F,e}$) and the quasi-Fermi level for holes ($E_{F,h}$), representing the density of free photogenerated electrons in the conduction band and of holes in the valence band, respectively, and producing the characteristic band bending observed in figure 1.5 a. This bending allows the electrons to travel from the

CB in the perovskite to the CB of the ETL, to then be injected into the TCO, and the remaining holes to move from the VB of the perovskite towards the VB (or HOMO level in the case of a molecule-based layer) of the HTL, to be later extracted at the metallic electrode. Note that the inverse trajectory of the charges is blocked by the formed Schottky barriers, therefore electrons from the conduction band in the perovskite cannot travel through the HTL nor holes can through the ETL. The incidence of light also reverses the direction of the internal electric field in the perovskite layer, where now cations drift towards the ETL electron-filled reservoir and the anions towards the HTL, often becoming a source of undesired charge recombination.[74]

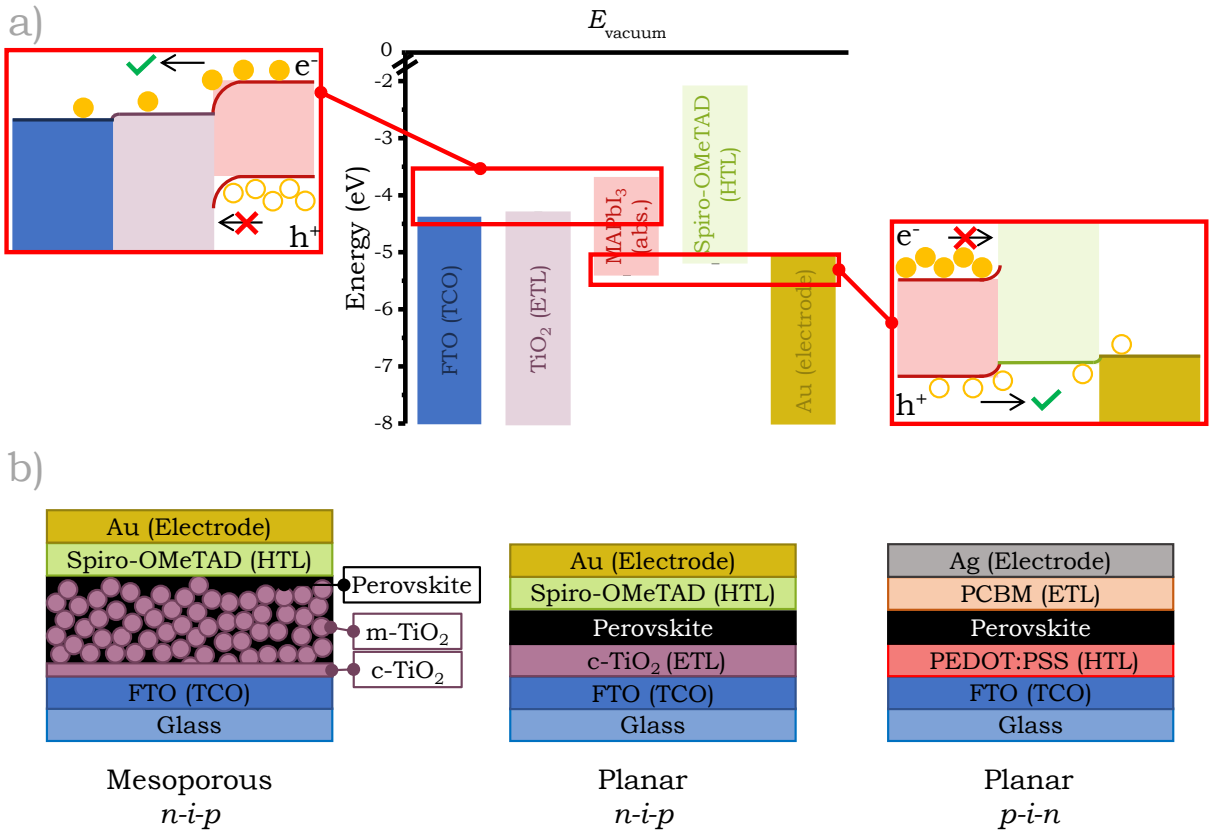

Figure 1.5: a) Schematic representation of band alignment between the perovskite layer and the charge extraction layers. The inset on the left represents the band bending allowing the extraction of electrons through the ETL and blocking the holes. The inset on the right showcases the band bending enabling the movement of holes through the HTL and blocking the electrons. b) Principal perovskite solar cell architectures.

The distance between these quasi-Fermi levels, known as the quasi-Fermi level splitting (*QFLS*), determines the final open-circuit voltage of the perovskite solar cell. In fact, the *QFLS* in the perovskite is proportional to the V_{OC} of the cell when there is no bending of the quasi-Fermi levels and each of them aligns with the respective electrode work function.[34] Thus, attaining a close alignment of the bands between the electrodes, charge extraction and perovskite layers and a low ion mobility is a fundamental goal in the pursuit of high device performances.

A correct band alignment is achieved through the appropriate selection of the charge extraction layers, depending on the band gap of the perovskite absorber and the device architecture. Conventional *n-i-p* configurations evolved from dye-sensitized solar cells, starting with a mesoporous TiO_2 scaffold as the ETL that transformed into a planar heterojunction over time.[142,356] Later on, the inverse *p-i-n* architecture was developed, covering the TCO with the HTL to then incorporate the perovskite and ETL, as shown in figure 1.5 b.[118,197] Commonly used ETLs are TiO_2 and SnO_2 in conventional architectures while PCBM and P3HT are usually the material of choice for the inverse structures.[185] Equivalently, Spiro-OMeTAD is the predominant hole transporting material in direct architectures and PEDOT:PSS in inverted ones. However, other hole transporting materials are also used in *n-i-p* configurations such as PTAA and P3HT or NiO_x, CoO_x, CuO_x and CuSCN in *p-i-n* architectures.[147] The transparent conductive oxide used by default is tin oxide, either doped with fluorine (FTO) or with indium (ITO).

As occurs with other photovoltaic technologies, not all incident photons are transformed into electrons. The performance of an ideal perovskite solar cell is limited by its band gap to the theoretical maximum determined by the Shockley-Queisser limit.[268] This top boundary sets an efficiency maximum at 32.91 % (E_g=1.4 eV) for a solar cell operated at 298.15 K and illuminated with the AM 1.5 G spectral irradiance, assuming the generation of only one exciton per incident photon, the use of non-concentrated sunlight and the thermal relaxation of the exciton energy to be greater than the band gap.[249] However, in a real cell, reflection losses and charge recombination processes lower this maximum value. Of all bulk recombination processes summarized in figure 1.6 a,[109] trap-assisted or Shockley-Read-Hall (SRH) is dominant in perovskite solar cells.[312,265] This type of non-radiative recombination occurs when an electron (or hole) is trapped in a defect with an energy level within the perovskite band gap (E_{trap}) and recombines with a hole (or electron) present in the valence (or conduction) band of the perovskite. This energy is thermally released with a phonon, reducing the PSC device performance.

Perovskite polycrystalline thin films usually accumulate these defects at the grain boundaries (figure 1.6 b) and at the existing interfaces between the absorber and the charge transporting layers (figures 1.6 c and d).[211,241] While the role of grain boundaries in trap-assisted recombination is under debate in the literature,[335,114,232] most reports conclude that their effects are not dominant despite significantly affecting device hysteresis and degradation.[265,35] On the other hand, trap-assisted recombination at interfaces is the dominant loss mechanism, which paired with an unsuitable band alignment critically lowers the open-circuit voltage and performance of PSCs.[265,280,91,341] Therefore, a substantial body of research is dedicated to the reduction of these recombination losses, primarily through interfacial engineering.[315,179,58,106]

The unquestionable success of perovskite solar cells lies in the favourable intrinsic properties of these ionic crystals for PV applications. The generation of charge upon illumination is enhanced in perovskite semiconductors thanks to their high absorption co-

efficient and direct band gaps,[63] which can be tailored to different light wavelengths just by modifying their halide or A cation composition, as pointed out in figure 1.7.[209,145,163,27] The collection of these charges is also enhanced due to their long charge diffusion lengths and excellent carrier mobilities,[354,212] limiting the recombination processes that lower device performance. Additionally, optimized crystallization techniques can render perovskite films and crystals with low defect densities, limiting the formation of carrier traps.[204,5,177] Notwithstanding this, halide perovskite materials are also defect-tolerant, meaning the impact of a significant density of defects is mitigated in the system, allowing the achievement of high performance in devices.[278,130,50]

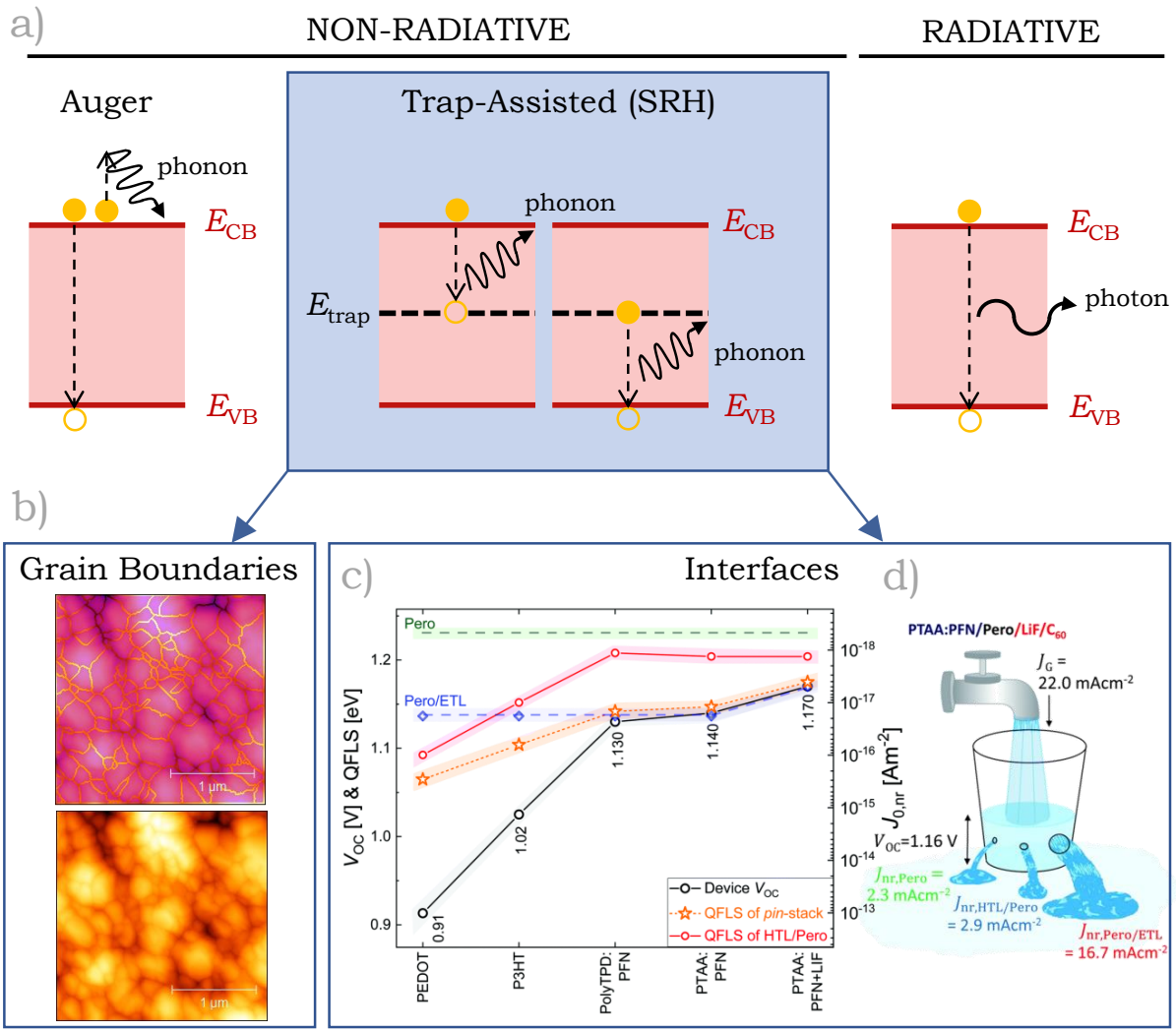

Figure 1.6: a) Main recombination processes on a bulk semiconductor.[109] b) Grain boundaries highlighted on a perovskite film. c) Average open-circuit voltage (V_{OC}) of *p-i-n* cells with different HTLs and a C_{60} ETL, compared to the average quasi-Fermi level ($QFLS$) of the corresponding HTL/perovskite bilayers. The $QFLS$ of the perovskite/C_{60} junction and the neat perovskite on fused silica are shown in dashed blue and green lines, respectively. Adapted with permission from[280]. Copyright (2019) American Chemical Society. d) Illustration of the solar cell V_{OC} losses at the bulk and interfaces. Adapted with permission from[280]. Copyright (2019) American Chemical Society.

However, what makes perovskite solar cells truly revolutionary is the combination of their excellent optoelectronic properties with their facile and cheap fabrication. The use of earth-abundant materials, which can also be extracted from waste sources,[43,46,339] in solution-based low-temperature deposition processes significantly lowers their fabrication price.[303] This makes them a low-cost photovoltaic technology that is also suitable for the development of lightweight flexible modules and tandem devices with other established solar cell technologies.[51,309,327,139,257] Moreover, their applications extend to a variety of electronic devices such as LEDs,[180] lasers,[196] field-effect transistors,[176] memristors,[321] and photodetectors.[307]

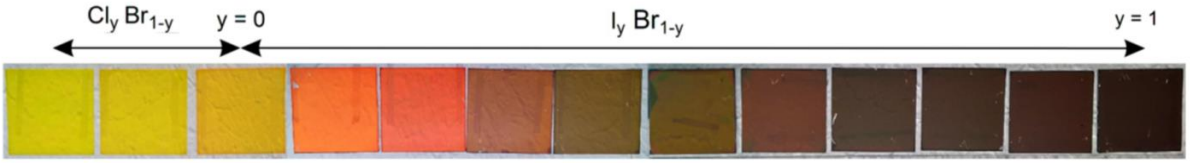

Figure 1.7: Photographs of triple cation perovskites with halide compositions ranging from $Cl_{0.2}Br_{0.8}$ to $I_{1.0}$, depicting composition-dependent colouration and band gap. Reproduced with permission from[27]. 2017 Optica Publishing Group.

1.3 The stability challenges of perovskite solar cells

Notwithstanding the favourable properties reported in the previous section, perovskite solar cells face significant challenges regarding their long-term stability, which severely hampers their commercialization prospects.[246,161]

From a device perspective, sources of instability can be divided into extrinsic, concerning changes within the multi-layer device architecture affecting the solar cell performance, and intrinsic, regarding the degradation of the perovskite material itself. The former involves changes within the charge extraction layers such as the loss of conductivity of the HTL (Spiro-OMeTAD) due to additive evaporation,[195,117] the migration of the metal electrode into the perovskite,[68] or the accumulation of trapped charges at the perovskite/TiO_2 interface upon illumination that interact with other degrading agents, accelerating the device performance loss.[4] These challenges are often addressed from an interfacial engineering approach by selecting more thermally enduring and more conductive charge extraction layers and/or incorporating various interlayers.[171,8,189,173,353] On the other hand, the intrinsic degradation of the perovskite layer is often a complex process, heavily dependent on its crystal structure and elemental composition.

Perovskites have been reported to severely degrade when they are exposed to heat, moisture, light and oxygen.[72] This degradation normally involves the irreversible decomposition of the perovskite into metallic Pb or metallic salts (PbI_2) through the release of I_2 and the evaporation of the organic cations, especially when heat is involved in the process.[164,85,125,55] Moisture often triggers the formation of hydrated phases in

$MAPbI_3$ prior to its irreversible decomposition,[154] while complex mixtures such as the triple cation CsFAMA tend to report the irreversible formation of inorganic side phases such as $CsPb_2I_4Br$.[99] Illumination has been found to trigger ion migration in lead halide perovskite solar cells under voltage bias causing device hysteresis and phase segregating the perovskite into iodide- and bromide-rich regions.[26,44,306] Additionally, light soaking can induce the incorporation of atmospheric oxygen into the crystal lattice, contributing to the degradation of the perovskite through the formation of superoxide species.[259] The detrimental effects of water and oxygen can be successfully addressed by appropriate encapsulation.[153,242,267,182] However, long-term exposure to operational temperatures, which can range up to 85 °C, is unavoidable.

Perovskite thermal endurance is intrinsically linked to its structure and composition. Forming a thermally stable three-dimensional perovskite often involves the compliance with both structural and thermodynamic requirements given by the Goldschmidt tolerance factor and the Gibbs free energy of a crystal, respectively. The Goldschmidt tolerance factor (t) is an empirical index representing a measure of the structural stability of perovskite materials based on the ionic radius r of the A, B and X ions as described by equation 1.1.[89]

$$t = \frac{r_A + r_X}{\sqrt{2}\,(r_B + r_X)} \tag{1.1}$$

A tolerance factor of 1 indicates a perfect fit of the A-site cation within the cavities of the BX_3 framework.[292] Cubic structures lay the tolerance factor between 0.9 and 1, with the upper limit being close to the tetragonal structure (figure 1.8 a). Perovskite structures can form for lower factors (up to 0.8), but they tend to show distortions related to the tilting of the BX_6 octahedra as occurring in the orthorhombic phase. Tolerance factors above 1 present an A-site cation that is too large to fit properly, which encourages the formation of alternative structures.[135,292] Therefore, the combination of elements with suitable ionic sizes that lay the tolerance factor within the cubic structure range is highly desirable to form 3D thermally stable perovskites. Alternative perovskite structures known as layered hybrid perovskites (LPKs) have emerged as a viable solution to address perovskite stability concerns.[273] However, their poor charge transport properties place the device performance below that of the state-of-the-art, multi-cation perovskite materials.[273]

Notwithstanding these general guidelines, lattice strain (also known as microstrain) originated from the ionic size mismatch between the A and the $[PbX_6]^{4-}$ octahedral cages often induces tilting and distortion within the perovskite structure. Structural arrangements and lattice microstrain change with temperature independently of the perovskite tolerance factor, as depicted in figures 1.8 b and c. For instance, $MAPbI_3$ is presented in a tetragonal structure at room temperature, yet it transitions to the predicted cubic arrangement between 54-57 °C (figure 1.8 c).[65] Equivalently, temperature affects the crystal arrangement of $CsPbBr_3$ that displays the orthorhombic γ-phase at room temperature, transitioning to a tetragonal β-phase at 88 °C and finally reaching the cubic

structure (α-phase) above 130 °C (figure 1.8 c).[340] Despite being an orthorhombic structure, $CsPbBr_3$ presents a reasonably good structural stability at room temperature,[166,37] contrary to what has been observed for $FAPbI_3$ and $CsPbI_3$ perovskites, which transform into non-photoactive δ-phases when high temperatures are not maintained.[188,162,225] Often, an anisotropic distribution of microstrain in the perovskite structure provoking a high degree of octahedral distortion is the trigger behind the transition of the α phase into the δ-phase in these materials.[352,282]

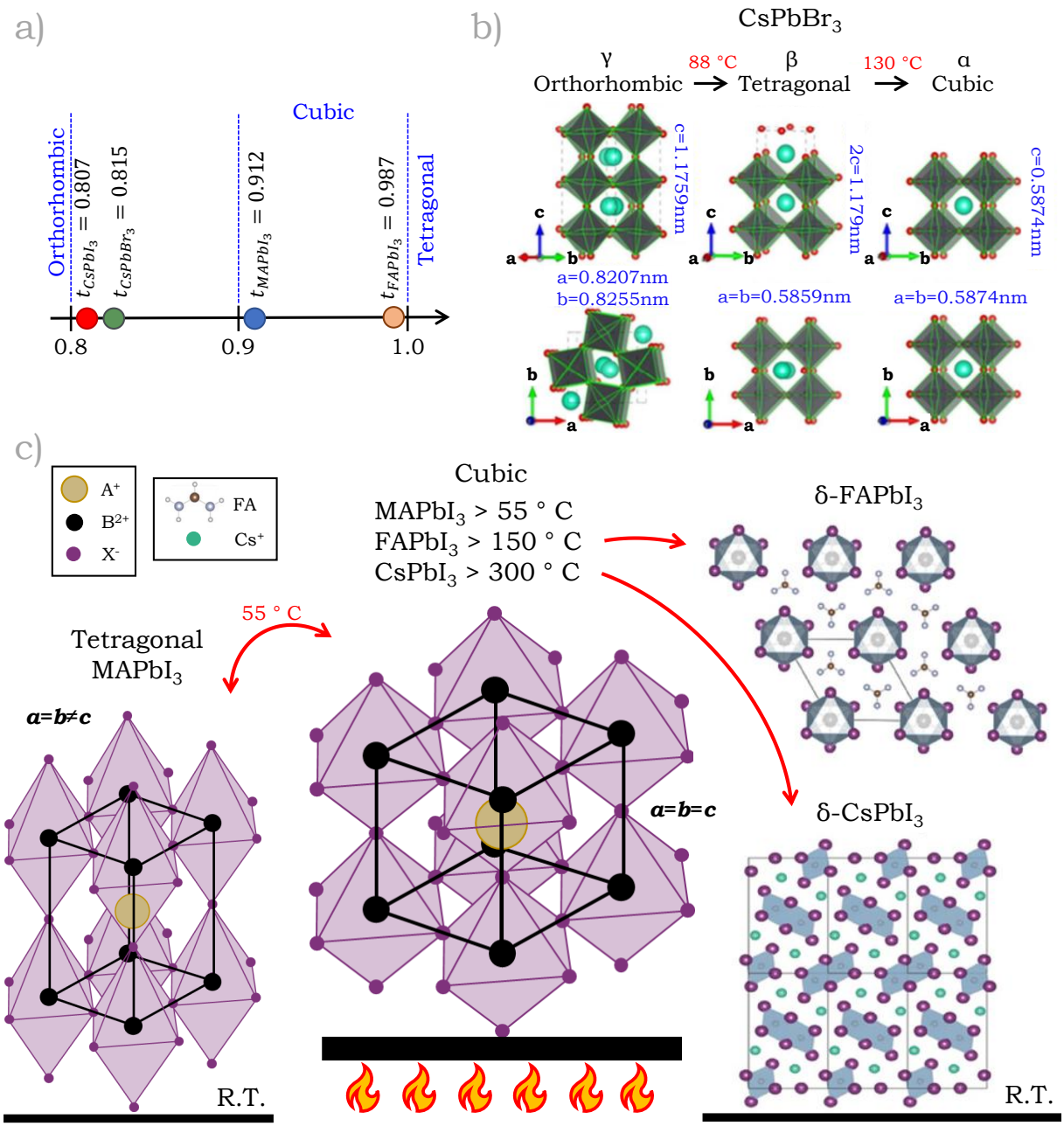

Figure 1.8: a) Tolerance factors of various single cation halide perovskites. b) Phase transitions of $CsPbBr_3$ with temperature. Adapted with permission from[340]. Copyright 2017, Royal Society of Chemistry. c) Phase transitions of $MAPbI_3$, $FAPbI_3$ and $CsPbI_3$. Image of δ-$FAPbI_3$ and δ-$CsPbI_3$ adapted with permission from[225]. Copyright 2017, John Wiley & Sons, Inc.

Structural changes in the perovskite are closely linked to their thermodynamic stability, given by the Gibbs free energy (ΔG). This property, mathematically defined in equation 1.2, corresponds to the difference between the change in enthalpy (ΔH) and the product between the temperature (T) and the change in entropy (ΔS) of the ionic crystal and determines the spontaneity of a reaction.

$$\Delta G = \Delta H - T\Delta S \tag{1.2}$$

The spontaneity of the reaction dictates whether the desired perovskite would form naturally from its precursors ($\Delta G < 0$) or if the addition of energy would be required to complete the process ($\Delta G > 0$). Thus, it is a measure of the stability of a system, since the products reach chemical equilibrium with their environment when ΔG is minimized.

Improving the thermodynamic stability of the perovskite crystal goes in hand with an appropriate selection of elements with high decomposition points to form the structure. For instance, organic cations such as methylammonium have been reported to sublime from $MAPbI_3$ at temperatures above 80 °C.[125,55] Therefore, replacing MA with FA or Cs has reported an improvement in the perovskite thermal stability due to their larger enthalpy and activation energy.[126,75] Yet, as discussed above, unoptimized tolerance factors trigger the decomposition of caesium and formamidinum lead iodide perovskites at room temperature.[188,162] Other substitutions such as the replacement of iodide with bromide have been reported to enhance the B-X and A-X bonds, retrieving a more thermally stable material.[11,284] However, the selection of bromide perovskites entangles an enlargement of the band gap, which translates into a lower photon absorption and a significantly lower device performance.[209,284]

These full ionic replacements are a common strategy to improve the thermal and structural stability of perovskite, held under the umbrella of compositional engineering.[47] Beyond A and X substitutions, ionic replacements on the B-site have also been considered in the literature. The full substitution of Pb has been studied in the fabrication of three-dimensional perovskites, primarily in tin-halide perovskites ($ASnX_3$) and double perovskites ($A_2B(I)B'(III)X_6$). While the latter presents better stability than their ABX_3 counterparts, their performance in devices barely surpasses the 3 %.[331] On the other hand, tin halide perovskites face a significant stability issue through the oxidation of Sn^{2+} to Sn^{4+}.[243,60]

Given the limitations of single element replacement in perovskites, most of the current research is focused on the partial substitution of elements since multi-mixed systems have been found to provide a combined enhancement of both performance and stability.[136,8,189]

1.4 The improved structural and thermal stability of multi-mixed perovskites

A reduced ΔG can be achieved by adjusting the second term of equation 1.2: increasing the entropy of the system. In a crystal, entropy can be seen as a measure of the number of possible microscopic configurations or microstates (Ω) of a system in thermodynamic equilibrium. That is, entropy represents the number of possible arrangements the atoms can take in a crystal structure. Mathematically, Boltzmann introduced the term entropy as the product between the Boltzmann constant (k_B) and the natural logarithm of the number of possible microstates:

$$S = k_B \ln(\Omega) \tag{1.3}$$

Therefore, increasing the entropy of a system involves increasing the number of microstates or possible configurations of its constituents, which can be done by mixing multiple elements in a system. This strategy has been successfully implemented in perovskites, mixing individually on the A, B or X sites or predominantly on both the A and X sites to attain an optimum synergy between stability and performance.

As reported in the literature, mixing multiple A cations in lead iodide perovskites has demonstrated a substantial improvement in both their structural and thermal stability. The incorporation of smaller cations such as Cs or MA successfully addressed the structural instabilities presented by $FAPbI_3$ at room temperature.[343,352,64] (figure 1.9 a1). Additionally, the high volatility of $MAPbI_3$ was reduced with the incorporation of Cs or larger cations such as methylenediammonium (MDA) and guanidinium (GUA).[208,264,143,122] MDA has been found to also improve the structural stability of $MAPbI_3$ at room temperature, crystallizing in a cubic arrangement rather than the expected tetragonal phase.[264] Even the incorporation of a substantially large cation such as GUA has reported an enhanced structural and thermal stability in methylammonium lead iodide thanks to the strengthening of the H-I bonds (figure 1.9 a2).[143,122] On the other hand, the inclusion of GUA alone in $FAPbI_3$ resulted in the formation of a thermodynamically unstable perovskite.[143] Yet, its use in more complex arrangements such as the triple cation system (GUAFACs) retrieved improved thermal stability and reduced hysteresis in devices.[230] Further entropic stabilization with triple cation combinations has proven beneficial for the increase of the thermal and structural stability of devices while providing astonishing efficiencies in the RbCsFA (20.58 % *PCE*) and MDACsFA systems (24.4 % *PCE*).[342,136]

Mixing on the X-site of the perovskite structure with either Cl^- or Br^- has become a common strategy to tune the optoelectronic properties of the material.[237,79,27,163,145] From a stability point of view, halide mixtures commonly address the tendency of I^- anions to oxidize under light illumination producing I_2, which has been found to induce a catalytic

reaction and the corrosion of the perovskite layer.[47] The benefits of the incorporation of chloride in organic-inorganic mixed iodide perovskites have been primarily associated with an enhancement of crystallization and the promotion of carrier transport.[54,160,289]

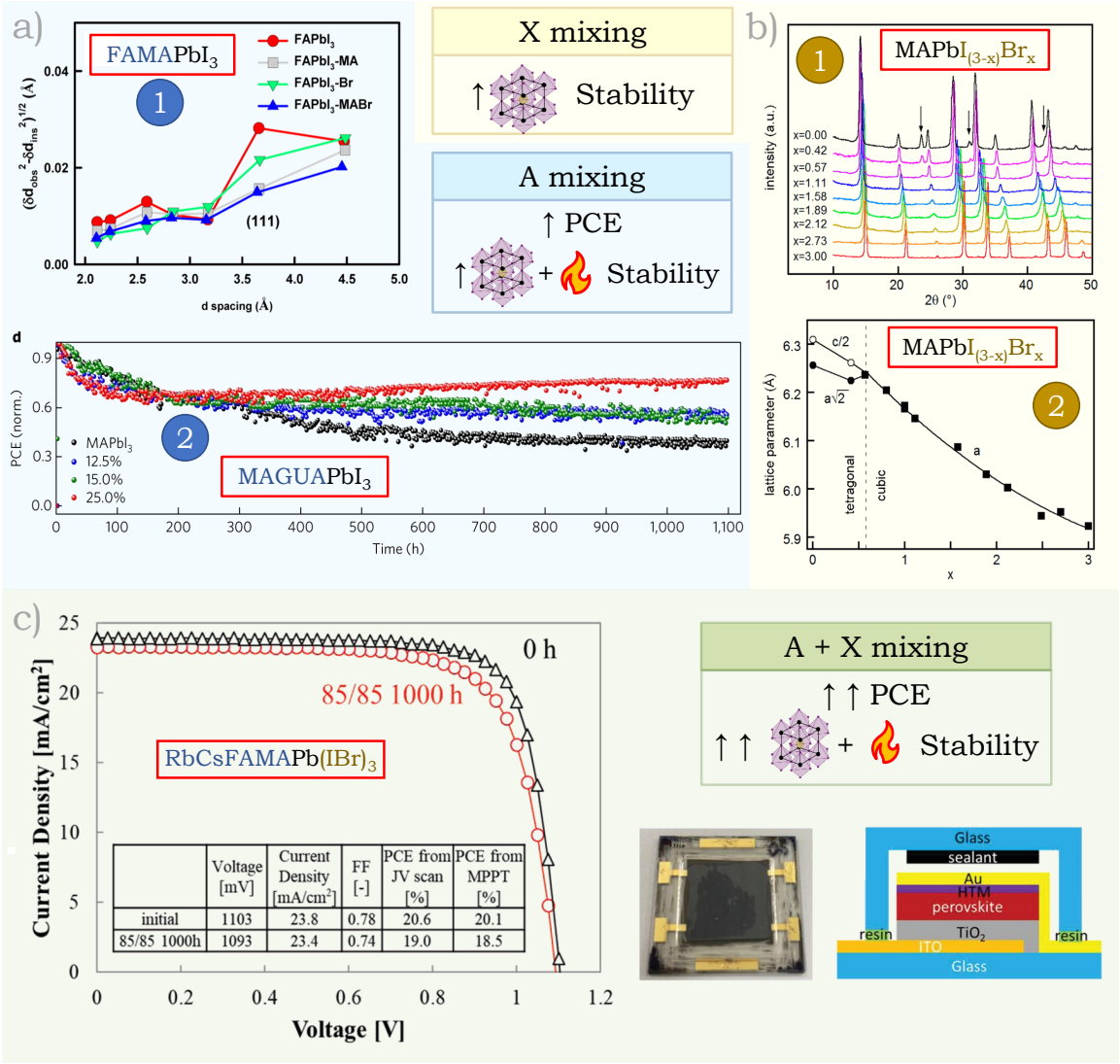

	Voltage [mV]	Current Density [mA/cm²]	FF [-]	PCE from JV scan [%]	PCE from MPPT [%]
initial	1103	23.8	0.78	20.6	20.1
85/85 1000h	1093	23.4	0.74	19.0	18.5

Figure 1.9: Improvement of thermal and structural stability of perovskites with mixing on the A-site (a), X-site (b) or both A and X-sites (c). a1) Reduced microstrain anisotropy in $FAMAPbI_3$. Adapted with permission from[352]. Copyright 2016 American Chemical Society. a2) Improved thermal stability of $MAGUAPbI_3$ solar cells. Adapted with permission from[122]. Copyright 2017 under Creative Commons CC BY license. b1-2) Structural change of $MAPbI_3$ with Br mixtures. Adapted with permission from[79]. Copyright 2015, American Chemical Society. c) High performance and thermal stability of $RbCsFAMAPb(IBr)_3$. Adapted with permission from[189]. Copyright 2019, John Wiley & Sons, Inc.

While its incorporation in the 3D $MAPbI_3$ structure is possible, the mixtures are unstable and end up dissociating.[239] On the other hand, the incorporation of bromide into the iodide site has been found to structurally stabilize the α-phase of $CsPbI_3$ at room temperature,[165] and to shift the $MAPbI_3$ structure from tetragonal to cubic without decomposition (figure 1.9 b).[33,79,155] The bromide-induced lattice contraction of the structure

has been found to increase the stability by suppressing MA^+ migration.[190] However, the incorporation of large amounts of Br is linked to halide segregation of the perovskite, particularly under illumination.[26,44,306] Less common anions such as the superhalogen BH^{4-} have been found to substantially increase the thermal stability of $MAPbI_3$ by bonding with the proton hydrogen in MA, reducing the volatility of the perovskite.[324]

Ultimately, boosting the entropy of the system by combining the mixing in both the A and X sites has reported a more effective improvement of the stability and performance of perovskite solar cells. A clear example of this success is represented by the state-of-the-art triple cation mixed halide $CsFAMAPb(IBr)_3$ perovskite. The combination of high performance (PCE>21 %) and stability reported in the literature commonly establishes it as a reference material in perovskite photovoltaics.[255,48,98] Its enhanced thermal stability in working devices, provided the appropriate selection of HTL (CuSCN), was highlighted by Arora et al., who fabricated cells able to preserve 95 % of their efficiency after 1000 h under illumination in an N_2 atmosphere at 60 °C.[8]

Methylammonium-free combinations are often selected for the fabrication of highly thermally stable devices, yet to the expense of reducing the maximum performance. For instance, $CsFAPb(IBr)_3$ cells fabricated by Yuqian et al. were able to maintain 88 % of the original PCE of 19.6 % at 85 °C in the dark after 500 h.[107] In a triple cation combination, the incorporation of guanidimium into the system has shown improved phase stability of the wide band gap $CsFAGUAPb(IBr)_3$ perovskites thanks to an increased structural microstrain, yet their maximum efficiency was limited to 14.6 %.[279]

Further exploitation of entropic stabilization has rendered highly stable and highly performing combinations including MA in quadruple and even quintuple cation mixed iodide-bromide systems. KCsFAMA perovskites have achieved a hysteresis-free maximum efficiency device of 20.56 % that reported no decrease in PCE over 1000 h of storage under ambient air (10±5 % RH) without encapsulation.[29] Moreover, RbCsFAMA devices have been reported to maintain 92 % of their initial PCE (20.6 %) after 1000 h of exposure to 85 °C heat in an 85 % RH nitrogen atmosphere (figure 1.9 c).[189] Provided optimal encapsulation, this system has proven to retain approximately 90 % of its initial efficiency after being heated at 65 °C in humid air (40–60 % RH) for over 1000 h.[184] The combination of both potassium and rubidium ions has also proven successful for the fabrication of quintuple cation KRbCsFAMA perovskite solar cells with a maximum PCE of 20.10 %, although further studies are required to assess their device stability.[351]

The addition of guanidinium to the CsFAMA perovskite has also been the focus of several studies. Wu et al reported the role of this large cation as a defect passivator, achieving large open-circuit voltages (1.19 V) with good PCEs (>21 %). Although no stability tests were performed, the addition of GUA decreased the XRD peak intensity of PbI_2, which is considered the main degradation product.[314] A study conducted by Zhang et al. confirmed the improved operational device stability of the high-performing

GUA containing quadruple cation perovskite, yet large proportions of guanidimium were reported to induce the phase segregation of the 3D phase into 2D $FAGAPbI_4$ and 1D δ-$FAPbI_3$.[345]

1.4.1. B site mixing

Although less common than the A or X site ion partial replacements, B site mixing has been reported to increase stability in perovskites by modifying the octahedral cage. An improvement in the phase stability has also enhanced their endurance upon air, high temperature and humidity exposure.

In inorganic perovskites suffering from the transition to a non-photoactive phase, such as the case of $CsPbI_3$, the partial substitution of lead by Bi^{3+}, Ca^{2+}, Sb^{3+} or Eu^{3+} reported a substantial increase in the phase and ambient stability of the material. It is thought that the small microstrain induced in the orthorhombic δ phase when 4 % Bi was introduced in the system, triggered the phase transition into a distorted cubic phase that helped keep the α-$CsPb_{0.96}Bi_{0.04}I_3$ solar cells stable for more than 6 days, maintaining 68 % of the initial *PCE* for 168 h under ambient conditions without encapsulation (figure 1.10 a).[100] The partial substitution of 5 % of Ca in a $CsPbI_3$ encapsulated device also showed an outstanding stability, maintaining 85 % of the initial *PCE* for over two months, in contrast with the 65 % *PCE* kept by the reference device.[150] Unencapsulated $CsPb_{0.96}Sb_{0.04}I_3$ carbon-based cells retained 96 % of the initial *PCE* after 37 days of storage in air (figure 1.10 a).[317] The introduction of europium in either its 3^+ or 2^+ oxidation states also reported increased phase stability for the α-$CsPbI_3$ when annealing at low temperatures (85 °C).[116] Compared with the europium-free sample, which transformed into the delta phase during the annealing process, the 10 % Eu^{3+} sample was kept in the alpha phase even after 30 days of storage.[116] The introduction of Eu^{2+} into the more stable system $CsPbI_2Br$ also resulted favourably in the stability of both films and solar cells. Europium-containing thin films in ambient air at a relative humidity of 40 % remained black over six months while the $CsPbI_2Br$ became yellow-white in less than 50 h.[318] $CsPb_{0.95}Eu_{0.05}I_2Br$ devices retained 93 % of initial *PCE* after 370 h under 100 mW cm^{-2} continuous white light illumination under MPP in N_2, while the reference device dropped to half of its initial efficiency in less than 30 h (figure 1.10 a).[318]

Beyond phase stability, the partial substitution of Pb with Sr^{2+}, Ba^{2+}, Mn^{2+} or Cu^{2+} also improved the thermal stability of inorganic caesium-based perovskites. Encapsulated $CsPb_{0.98}Sr_{0.02}I_2Br$ devices showed no difference in performance after 1 h of heat at 100 °C in ambient conditions, while the $CsPbI_2Br$ reference experienced V_{OC} and *FF* drops (figure 1.10 a).[151] The introduction of BaI_2 in $CsPbIBr_2$ devices helped retain 70 % of the *PCE* after 4 h at 85 °C, whereas the reference kept only 20 %.[283] In $CsPbX_3$ systems, the Mn^{2+} substitution was able to stabilize quantum dots even at temperatures up to 200 °C under ambient conditions, while the partial substitution with Cu^{2+} in QD films maintained stable luminescence performance even when annealed above 250 °C.[355,17]

The partial replacement of Pb has also improved the thermal stability of mixed organic-inorganic perovskites like $MAPbI_3$. The partial substitution of lead with Sr in $MAPbI_{3-x}Cl_x$ modified the onset temperature for thermal degradation from 166 °C in the reference to 181 °C, 216 °C and 197 °C in the samples containing 5 %, 10 % and 20 % of Sr, respectively (figure 1.10 b).[262]

In a different work, $MAPbI_3$ devices partially substituted with 10 % of Sr from $SrCl_2$ presented an almost invariant *PCE* of 15 % at 85 °C after 18 thermal cycles heating for 2 h and let cool down at RT for 1 h, while the reference sample dropped its initial *PCE* below the 90 % threshold after the same test (figure 1.10 b).[337]

Additionally, B-site mixing with other ions such as Sn^{2+} or In^{3+} has also reported improvements in the photo and ambient stability of $MAPbI_3$, with a $MAPb_{0.9}Sn_{0.1}I_3$ cell retaining 90 % of *PCE* after operation at MPP under 1 sun for 500 h and the $MAPb_{0.85}In_{0.15}(ICl)_3$ reaching half efficiency after 350 h of air exposure. Here, the reference dropped the *PCE* to a tenth of its original value.[334,308]

Even the addition of lower amounts of B elements in a doping fashion have reported beneficial for the thermal and environmental stability of $MAPbI_3$. The incorporation of Zn^{2+} in very low amounts $(MA(1Zn{:}100Pb)I_{(3-x)}Cl_x)$ has been correlated with an improvement of the phase and the environmental stability of $MAPbI_3$ through the release of lattice strain within the BX_6 octahedron, which was thermodynamically reflected as an increase in the energy cost of the degradation process.[261]

Similarly, doping with Al^{3+} has reported a decrease in the lattice microstrain of $MAPbI_3$, although no stability tests were performed in this study.[302] The introduction of CaI_2 as an additive in exchange for excess PbI_2 produced devices which retained 93 % of its initial *PCE* after 300 h of light soaking in an N_2 environment, evidencing a lower release of iodide from the perovskite after ageing for 3 days at 85 °C.[40] Likewise, the incorporation of 1 % of MgI_2 helped maintain a 90 % *PCE* after storage in a 30-40 % RH environment for 60 hours compared to the pristine sample, whose *PCE* decreased to 60 % of its original value.[328]

While some advances have been done on B-site partial substitutions as a way of improving structural and thermal stability, most of the research is focused on single cation perovskites rather than complex mixtures. Exploring B-site substitutions in mixed cation mixed halide perovskites could open the door to further improvements in the stability of the already top-performing solar cells, both from an entropic and structural perspective.

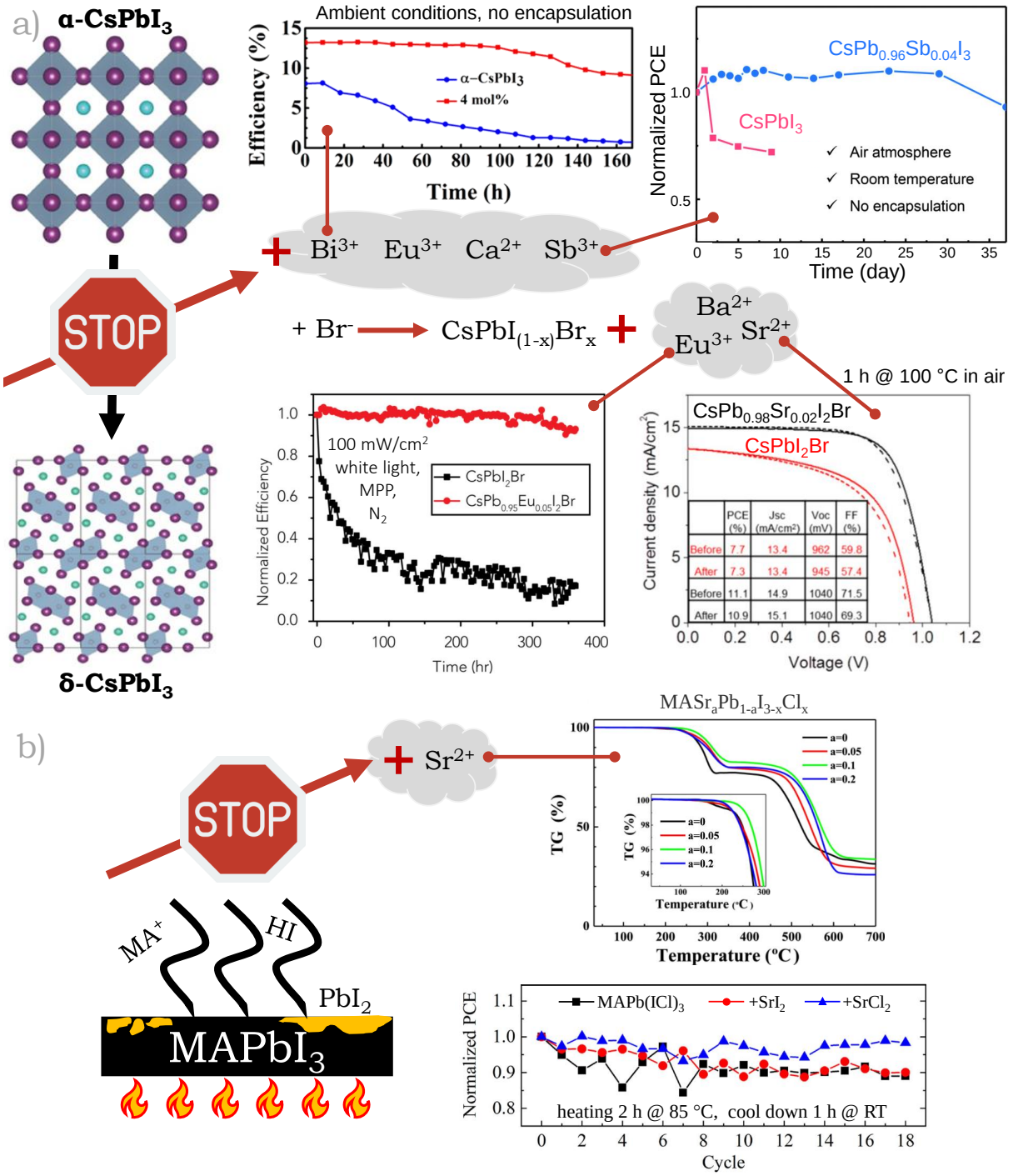

Figure 1.10: Structural and thermal stability improvements induced by B-site mixing on $CsPbI_3$ (a) and $MAPbI_3$ (b). Image of α-$CsPbI_3$ and δ-$CsPbI_3$ adapted with permission from [225]. Copyright 2017, John Wiley & Sons, Inc. Device performance plots over time of bismuth, antimony, europium and strontium partial substitutions in (a) adapted with permission from [100,317,318,151]. Copyright 2017, American Chemical Society. Copyright 2018, Royal Society of Chemistry. Copyright 2018, Elsevier, Inc. Copyright 2017, American Chemical Society. TGA and device performance over temperature cycles plots of $MAPb(ICl)_3$ partially mixed with Sr^{2+} adapted with permission from [262] and [337]. Copyright 2017, Elsevier Ltd. Copyright Elsevier Ltd and Techna Group S.r.l. Stop sign icon image credit: *Flaticon.com*. [281]

1.5 Outline of the thesis

The work presented in this thesis is aimed at reducing the structural instability presented by metal halide perovskite solar cells when exposed to heat through tailored compositional engineering of the B-site both in simple and multi-mixed systems. Additionally, efforts are put into understanding the validity of state-of-the-art X-ray diffraction methods for the analysis of microstrain in halide perovskites.

Chapter 3 contains information on the design, fabrication and operational principles of three original in-house-built instruments used for the characterization and analysis of perovskite materials studied in the following chapters: an automated JV measuring equipment, a hydration chamber for X-ray diffraction and a colourimetry-based instrument for thermal degradation assessment named pixel colour tracking (PCT).

Chapter 4 explores the validity of integral breadth (IB) methods in the XRD microstrain analysis of perovskite films. It unveils the unsuitability of the technique, highlighting the breach of the Wilson-Stokes approximation constraint observed in both literature and experimental results: parallel *hkl* planes do not return equivalent values of microstrain as expected. Here, the persistence of this aberration is reported even after the use of instrumental error minimized scan conditions, which suggests the presence of a microstrain gradient across the order-of-diffraction.

Chapter 5 introduces the concept of B-site mixing in triple cation mixed halide perovskites (CsFAMA) as a thermal decomposition delayer by partially replacing Pb^{2+} with Sb^{3+}. Here, the thermal and structural stability improvement of mixed Pb-Sb films is evidenced using XRD and an in-house designed *in-situ* colourimetry test kit, demonstrating a successful symbiosis between high entropy and a more isotropic microstrain distribution. Additionally, the morphological and optical properties of these novel antimony mixed perovskites are characterized, and their interaction with moisture is explored.

Chapter 6 unveils the principal characteristics of the more stable B-site mixed triple cation mixed halide planar heterojunction solar cells containing 5 % of Sb and their behaviour over time when aged under degrading conditions. Here, the performance and ionic conductivity of antimony mixed devices are studied in combination with different extraction layers and interlayers, revealing a hysteretic behaviour dominated by interfacial photogenerated charge accumulation powered by the trap-inducing nature of Sb.

Chapter 2. Experimental methods

In this chapter the experimental methods used for perovskite synthesis, solar cell fabrication and material characterization are described. The content is divided into two main blocks. The first contains the general synthesis methods for perovskite films, crystals and devices. The second block includes information on the characterization equipment employed to quantify sample properties, as well as the main analytical techniques used for data interpretation.

2.1 Perovskite synthesis

2.1.1. Perovskite crystals

Two methods were followed for the synthesis of perovskite crystals: cooling crystallization in a reflux setup and inverse temperature crystallization. The former was used for lead-free perovskites and performed in an acidic environment inside a fume hood while the latter required the use of a nitrogen-filled glovebox.

$Cs_3Sb_2Br_9$ was crystallized using the reflux setup described in figure 2.1 a. In it, 72 mL of an 8.9 M HBr solution (Honeywell Fluka) were added to 6 mmol of CsBr (Alfa Aesar, 99 %) and 4 mmol of $SbBr_3$ (Alfa Aesar, 99.5 %) and dissolved under heavy stirring at boiling point. After an overnight crystallization in the dark, the crystals were filtered and washed with isopropanol and diethyl ether. The remaining powder was dried under vacuum overnight, resulting in the crystals depicted in figure 2.1 b.

Single crystals of methylammonium lead bromide perovskites (**$MAPbBr_3$**) were synthesized using the inverse temperature crystallization (ITC) method. In this process, the crystallization was based on the retrograde solubility of perovskite, which enabled the precipitation of crystals in solution with increasing temperature. $MAPbBr_3$ single crystals (SC) were fabricated following the procedure described by Saidaminov et al.,[251] as showcased in figure 2.1 c. One molar solution of $PbBr_2$ (TCI chemicals, >98 %) and MABr (Greatcell solar) were dissolved in N,N-Dimethylformamide (DMF, Acros Organics, 99.8 %) in a 1:1 ratio at room temperature under heavy stirring for 30 min. Before triggering the crystallization, the solutions were filtered through a 0.45 µm hydrophilic syringe filter at room temperature. The vials of the filtrate were placed in an oil bath at 80 °C and kept undisturbed until relatively large crystals were formed (>2 mm) over a time-lapse of 72 h. The SCs were then removed from the solution by extracting the hot

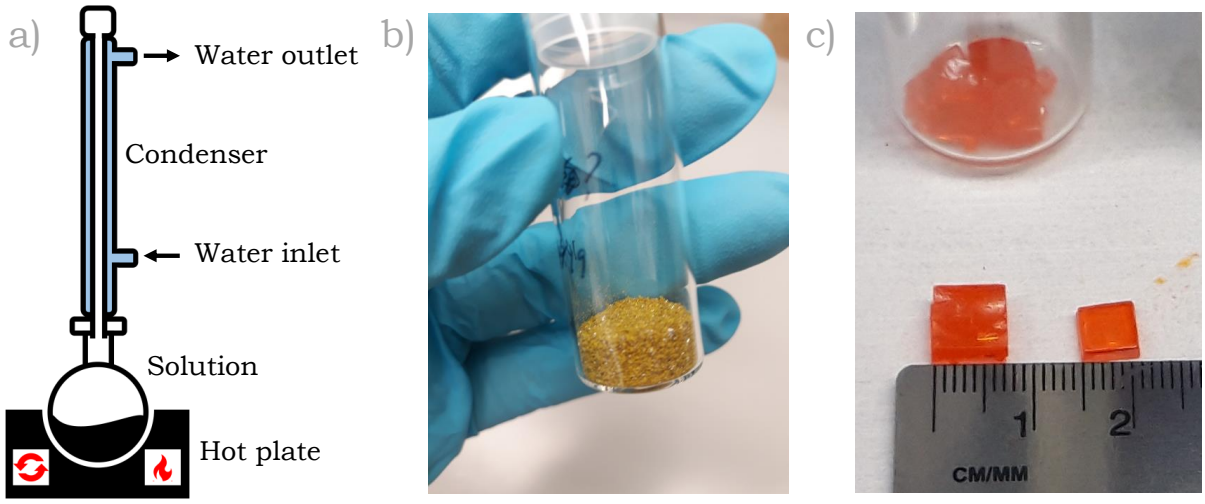

Figure 2.1: a) Reflux setup. b) $Cs_3Sb_2Br_9$ crystals. c) $MAPbBr_3$ single crystals.

solvent with a syringe. The remaining solids were removed from the vial, washed with IPA and diethyl ether and dried under vacuum. To achieve larger crystal sizes, SCs were re-introduced into a fresh solution and the process was repeated.

2.1.2. Perovskite films

Perovskite films were deposited on glass or FTO substrates via dynamic spin coating following the steps detailed in the sections below.

Substrate cleaning

Both FTO on glass (20×20×3 mm) and white soda-lime glass (25×25×1 mm) substrates were used. Before the perovskite deposition, the substrates were thoroughly brushed on both sides with a 2 % Hellmanex (Sigma Aldrich) in a deionized water solution. They were subsequently rinsed with deionized water, sonicated for 15 min in the 2 % Hellmanex solution and rinsed with deionized water again. Then, they were sonicated first in 2-propanol (Acros Organics, 99.6 %) and later in acetone (Acros Organics, 99.6 %) for 5 min each, rinsed and dried with a nitrogen gun. Previous to the spin coating, substrates were plasma or ozone cleaned for 10 min. To streamline the process, clean glass was stored in acetone if not used immediately.

Precursors

For the perovskite solution preparation two main solvents were used: N,N- Dimethylformamide (DMF, Acros Organics, 99.8 %) and methyl sulfoxide (DMSO, Acros Organics, 99.7+ %, extra dry). The organic cation salts methylammonium iodide (MAI), methylammonium bromide (MABr) and formamidinium iodide (FAI) were purchased from Greatcell solar. The lead precursors, PbI_2 (99.99 %) and $PbBr_2$ were acquired from TCI chemicals as well as the inorganic cation salt CsI (>99.0 %). CsBr (99 %) and SbI_3 (99.999 %) were purchased from Alfa Aesar. All chemicals were used without further purification.

$MAPb_{(1-x)}Sb_xI_{(3+x)}$ solution preparation

Both $MAPbI_3$ and $MAPb_{(1-x)}Sb_xI_{(3+x)}$ perovskite solutions were prepared inside a nitrogen-filled glovebox by dissolving the solid precursors in a 4:1 (v/v) ratio of DMF:DMSO. To do so, four 1.5 M stock solutions were prepared: MAI in DMF, MAI in DMSO, PbI_2 in DMF and SbI_3 in DMF. Both the cation and the antimony solutions were dissolved at 100 °C while the PbI_2 stock solution was heated up until 130 °C to ensure the complete dissolution of the powders. Stock solutions were kept at those temperatures while mixing in the proportions highlighted in table 2.1. The final solutions were cooled down naturally at room temperature and filtered through a 0.45 µm hydrophilic syringe filter.

Precursors per mL of solution					**Final solution molar ratio**			
Sb	**MAI**		**PbI_2**	**SbI_3**	**$MAPb_{(1-x)}Sb_xI_{(3+x)}$**			
(%)	**DMF** (µm)	**DMSO** (µm)	**DMF** (µm)	**DMF** (µm)	**MA**	**Pb**	**Sb**	**I**
0	300	200	500	0	1	1	0	3
1			495	5		0.99	0.01	3.01
2			490	10		0.98	0.02	3.02
5			475	25		0.95	0.05	3.05
10			450	50		0.9	0.1	3.1
15			425	75		0.85	0.15	3.15
30			350	150		0.7	0.3	3.3
50			250	250		0.5	0.5	3.5
75			125	375		0.25	0.75	3.75

Table 2.1: $MAPb_{(1-x)}Sb_xI_{(3+x)}$ solution stoichiometry.

$CsFAMAPb(IBr)_3$ solution preparation

Two combinations of the triple cation mixed halide perovskite $CsFAMAPb(IBr)_3$ were fabricated as references, mixing the precursors in a 4:1 (v/v) DMF:DMSO at 100 °C in the proportions described by table 2.2. Note that the caesium content was added from a 1.5 M stock solution of CsI in DMSO. After cooling down, the solution was filtered through a 0.45 µm hydrophilic syringe filter.

In devices, the $Cs_{0.05}[(FA)_{0.83}(MA)_{0.17}]_{0.95}Pb(I_{0.83}Br_{0.17})_3$ (abbreviated as Cs_5) perovskite was prepared with excess PbI_2 and spin-coated following a similar procedure to the one employed by Saliba et al.[255] A mixture of 172 mg of FAI (1 mmol), 22.4 mg of MABr(0.2 mmol), 507 mg of PbI_2 (1.1 mmol) and 80.7 mg of $PbBr_2$ (0.22 mmol) was dissolved in 1 mL of 4:1 (v/v) DMF:DMSO at 100 °C. The 5 % caesium content was added with 42 µL from a 1.5 M stock solution of CsI in DMSO. After cooling down, the solution was filtered through a 0.45 µm hydrophilic syringe filter.

$\mathbf{Cs_x[(FA)_{0.83}(MA)_{0.17}]_{(1-x)}Pb(I_{(1-y)}Br_y)_3}$					
(x,y) (%)	CsI (µL)	FAI (mg)	MABr (mg)	PbI_2 (mg)	$PbBr_2$ (mg)
(5,17)	33.3	135.6	18.1	380.7	64.0
(7.5,7.4)	50	132.0	17.6	446.1	11.9

Table 2.2: Proportions of CsFAMA precursors per mL of solution.

$Cs_3Sb_2Br_9$:FAMAPbI$_3$ solution preparation

One molar triple-A-cation double-B-cation and double-halide perovskite solutions were prepared by the combination of the in-house synthesized $Cs_3Sb_2Br_9$ and commercial FAI, MAI and PbI_2. Because of the choice of the antimony source, both the final caesium and bromide content were determined by the stoichiometry of $Cs_3Sb_2Br_9$. Restrictions were applied to the addition of the other precursors so that the molar sum of the A cations and the molar sum of the B metals did not exceed unity, respectively. The relative proportion of the organic cations was set to 83 % FA and 17 % MA. Equation 2.1 shows the correlation between the moles of antimony added (x) and the proportions of each anion and/or cation in the final compound. Cations were added into the mix via two 2 M solutions of FAI and MAI in DMF. The metal halides and the remaining solvents were incorporated following the numbers highlighted in table 2.3, keeping a solvent ratio of 4:1 (v/v) DMF:DMSO. For the fabrication of 5 % Sb-CsFAMA devices (Sb_5), the molarity of the solution was increased to 1.25 M, equivalently to the molarity of the Cs_5 solution used in solar cells.

$$\frac{x}{2}Cs_3Sb_2Br_9 + (1-x)PbI_2 + 0.83(1-1.5x)FAI + 0.17(1-1.5x)MAI \rightarrow$$
$$\rightarrow Cs_{\mathbf{1.5x}}FA_{\mathbf{0.83(1-1.5x)}}MA_{\mathbf{0.17(1-1.5x)}}Pb_{\mathbf{(1-x)}}Sb_{\mathbf{x}}I_{\mathbf{(3-3.5x)}}Br_{\mathbf{4.5x}} \quad (2.1)$$

Precursors per mL **of solution**						
Sb (%)	**FAI** (µL)	**MAI** (µL)	$\mathbf{PbI_2}$ **(mg)**	$\mathbf{Cs_3Sb_2Br_9}$ **(mg)**	**DMF** (µL)	**DMSO** (µL)
5	384	78	438	34	338	200
10	352	72	415	68	376	200
15	322	66	391.8	102.2	412	200
20	290	60	368.8	136.2	450	200
30	228	46	322.8	204.2	526	200

Table 2.3: $Cs_3Sb_2Br_9$:FAMAPbI$_3$ precursor ratios.

Perovskite deposition

Perovskite films were fabricated via dynamic spin coating in a one-step method inside a nitrogen-filled glovebox.[86] An anti-solvent step was included to enhance the crystallization.[319,220] Before the deposition, clean substrates were subject to a plasma or ozone treatment for 10-15 min. Immediately after this, perovskite solutions were spin-coated on the substrates followed by the addition of the anti-solvent, as depicted in figure 2.2. Finally, solvents were evaporated on a hot plate resulting in glossy-looking perovskite films. Note that annealing times and temperatures were optimized for each type of perovskite and application. Therefore, specific details will be addressed in the correspondent technical chapters.

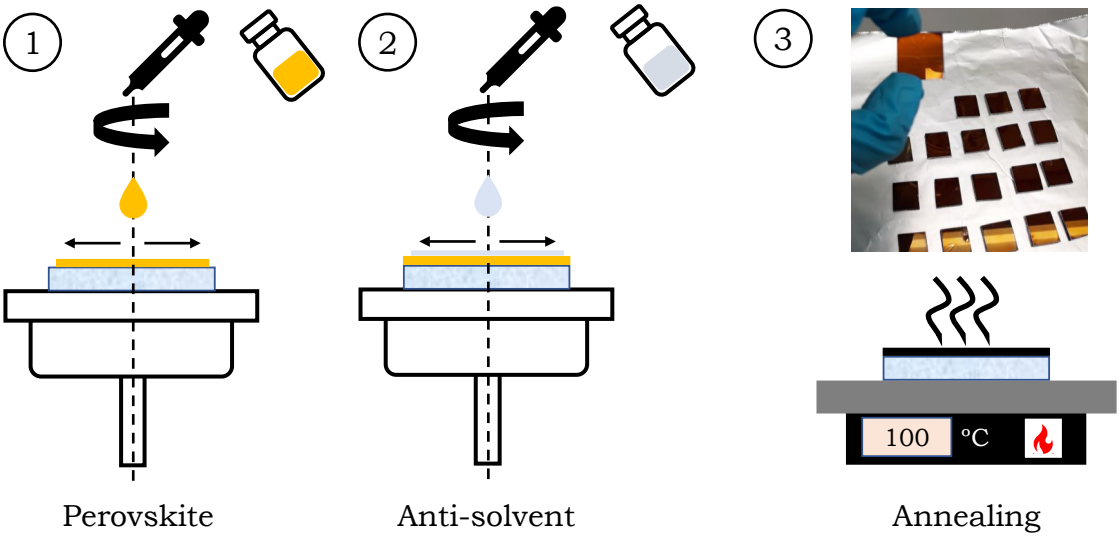

Figure 2.2: Perovskite deposition process.

For the standard spin coating of Cs_5 solar cells, 50 µL of perovskite solution was spin-coated at 1000 rpm for 10 s. Chlorobenzene (CB, Acros Organics, 99.5 %, extra dry) was selected as the antisolvent and 335 µL were added to the substrate 15 s after the start of the second spin coating step, rotating at 5000 rpm for 30 s. Finally, samples were annealed at 100 °C for 1 h.

Sb_5 devices were deposited with the same speed conditions as Cs_5, adding the CB 20 s after the start of the second spin coating step. The annealing was performed for 1 h at 140 °C. Likewise, $MAPb_{(1-x)}Sb_xI_{(3+x)}$ perovskite films were spin-coated in equivalent speed conditions, adding the CB drop at 23 s. Annealing times and temperatures are detailed in chapter 5.

To prevent moisture ingress during the characterization of perovskite films, a thin layer of poly(methyl methacrylate) (PMMA, Sigma Aldrich) dissolved in chlorobenzene was spin-coated on top of the perovskite at 2000 rpm for 40 s.

2.2 Device fabrication

2.2.1. Solar cells

Perovskite solar cells were fabricated in a planar heterojunction architecture via sequential deposition of the following layers: transparent electrode (glass/FTO), electron transporting layer (ETL), perovskite absorber, hole transporting layer (HTL) and counter electrode.

FTO glass layer

Fluorine-doped tin oxide (FTO) coated glass sheets (7/sq, Pilkington, USA) were patterned by etching 12 by 12 cm slides with zinc powder (Sigma Aldrich, purum) and a 3 M HCl (Honeywell Fluka, 37 %) solution. To do so, stripes of 12 mm wide scotch tape were glued to the FTO surface in either a vertical or a cross pattern as depicted in figure 2.3, depending on the selected solar cell electrode architecture. The transparent electrode was removed by rubbing a cotton bud on the exposed areas after covering them in zinc powder and adding the acid. In the next step, the slides were rinsed with water while removing the tape to prevent any further reaction of the acid and dried with a nitrogen gun. Once etched, they were aligned against the initial pattern with the glass side facing upwards and scribed with a diamond cutter in 36 pieces of 20 by 20 mm. Thereafter, cuts in fourths (3×3 samples) were done for easiness of the cleaning process, which was performed following the steps reported in section 2.1.2. Finally, as an immediate step to the deposition of the ETL, remaining organic residues were removed by either an oxygen plasma treatment for 10 min or ozone treatment for 15 min.

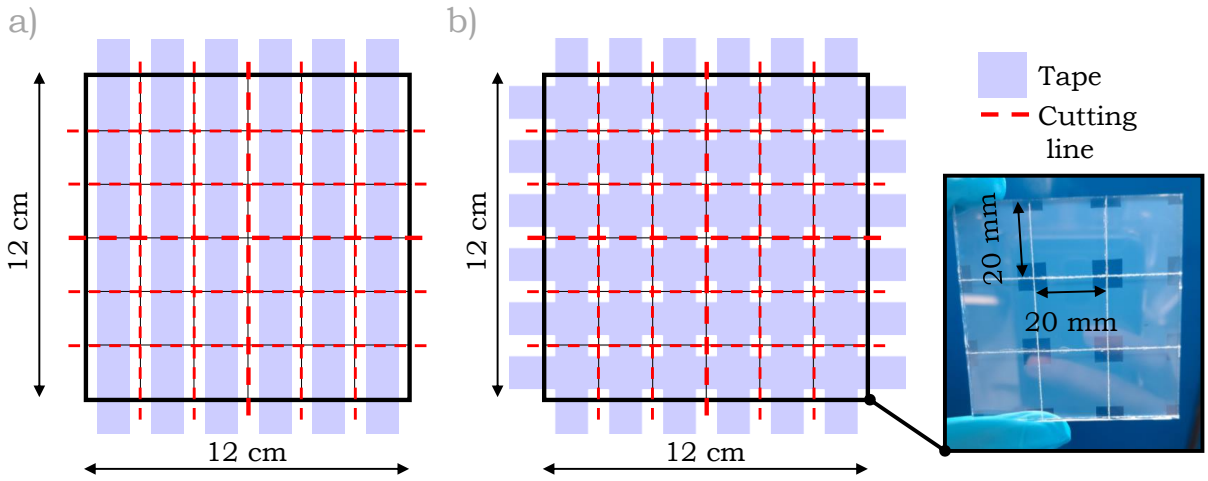

Figure 2.3: Vertical (a) and crossed (b) FTO etching patterns. Inset of a crossed etched and scribed 3×3 sample block.

Electron transporting layer (ETL)

For the electron transporting layer (ETL), three different metal oxide recipes were used to fabricate compact layers using: a sol-gel TiO_2 solution, a sol-gel SnO_2 solution and a colloidal SnO_2 dispersion, following the steps reported in figure 2.4.

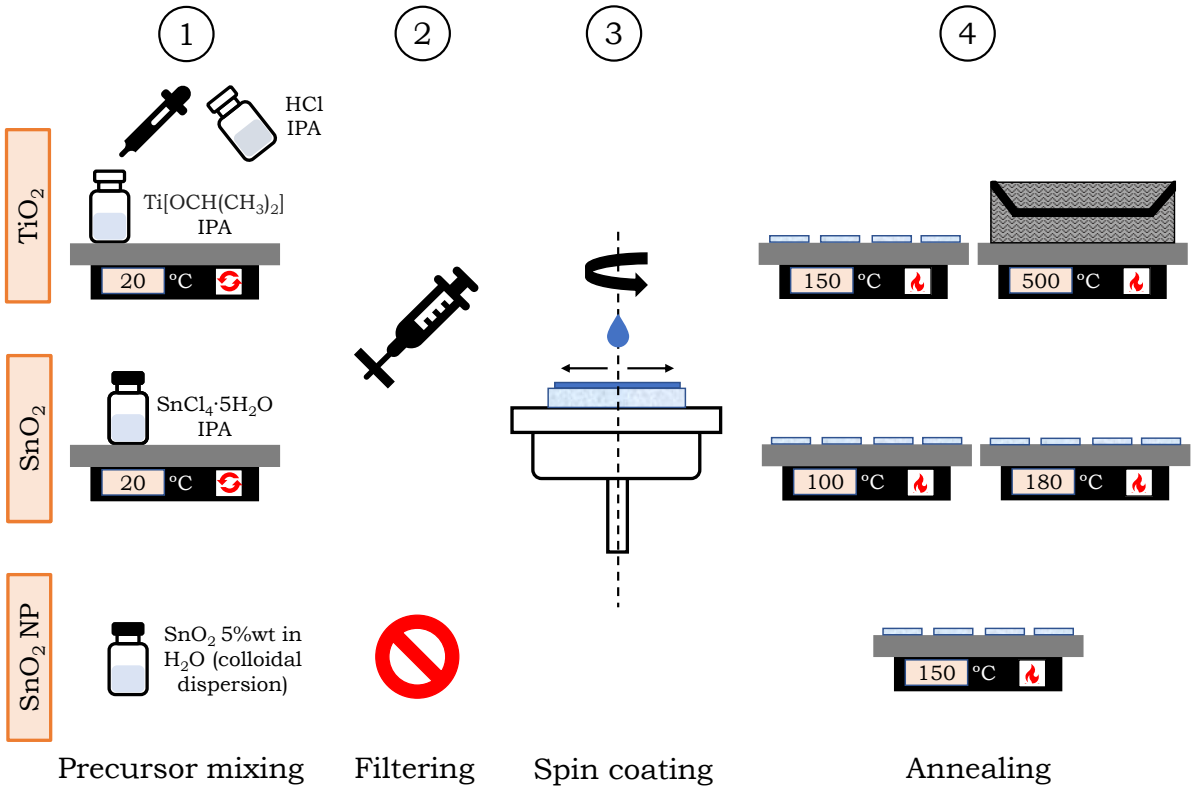

Figure 2.4: Compact ETL deposition process using a sol-gel solution of TiO_2 (top), SnO_2 (middle) and a 5 %wt colloidal SnO_2 aqueous dispersion (bottom).

A compact titanium dioxide (c-TiO_2) layer was deposited on the 3×3 blocks via dynamic spin coating a filtered sol-gel TiO_2 solution at 2000 rpm for 30 s followed by subsequent annealing at 500 °C for 45 min. For the TiO_2 sol-gel mixture, a 35 µL solution of 2 M HCl in 2-propanol was added drop-wise to a vigorously stirred 0.43 mM solution of titanium isopropoxide (Sigma Aldrich, 99.999 %) in dry 2-propanol (Acros Organics, 99.8 %, extra dry). After spin coating, solvents were evaporated from the substrates with a 10 min annealing step at 150 °C. The hot annealing was performed in a programmable high-temperature hot plate ramping up for 30 min to 500 °C and keeping that temperature for 45 min. When samples had cooled down slightly above 100 °C, they were cut into the 20×20 mm scribed pieces and stored in the glovebox to prevent moisture ingress.

For the sol-gel tin oxide layer, a 0.05 M solution of $SnCl_4{\cdot}5H_2O$ (Acros Organics, 98+ %) in anhydrous isopropanol was stirred for a minimum of 30 min before filtered and spin-coated on the FTO substrates at 3000 rpm for 30 s. The solvent was removed by annealing at 100 °C for 10 min and the Fermi levels of SnO_x were modified by a 1 h annealing at 180 °C. As in the case of the TiO_2, substrates were cut into the 20×20 mm samples and kept in the glovebox before depositing the perovskite layer.

The colloidal SnO_2 aqueous dispersion was diluted with deionized water to a 5 %wt from the precursor bottle solution (Tin (IV) oxide, 15 % in H_2O colloidal dispersion, Alfa Aesar). The FTO substrates were spin-coated with this solution at 4000 rpm for 30 s and annealed for 1 h at 150 °C, following the recipe from Liu et al.[172] After the annealing step, substrates were cut in the 20×20 mm samples and stored in the glovebox to prevent moisture ingress.

PCBM interlayer

Devices fabricated with a fullerene interlayer between the ETL and the perovskite incorporated a spin-coated solution of PCBM in chlorobenzene deposited at 1500 rpm for 40 s and annealed for 10 min at 100 °C. To improve the adhesion of the perovskite to the fullerene layer, a 50 µL/sample of a 0.2 %wt solution of Al_2O_3 nanoparticles in IPA was spin-coated at 2000 rpm for 30 s on top of the PCBM and annealed at 100 °C for 10 min.

Perovskite absorber

Following the perovskite film fabrication procedure reported in section 2.1.2, 1.25 M solutions of the perovskite absorber layer were spin-coated on top of the metal oxide layer after a 10-15 min O_2 plasma or UV-O_3 treatment. Once the annealing was done, the samples were ready for the deposition of the hole transporting material.

Hole transporting layer (HTL)

For the hole transporting layer (HTL), two different organic molecules were used: the state-of-the-art Spiro-OMeTAD and the novel and highly stable EDOT-Amide-TPA reported by Petrus et al.[229]

For the reference HTL, 75 mg of Spiro-OMeTAD (Borun Chemicals, 99.9 % sublimed grade) were dissolved in 1 mL of chlorobenzene (Acros Organics, 99.5 %, extra dry) and doped with 10 µL of 4-*tert*-Butylpyridine (tBP, Sigma Aldrich) and 30 µL of a 0.592 M solution of lithium bis(trifluoromethanesulfonimide) (Li-TFSI, Acros Organics, 99 %) in anhydrous acetonitrile (Alfa Aesar, >99.8 %). The solution was filtered and deposited on top of the perovskite layer by spin coating at 2000 rpm for 40 s inside a nitrogen-filled glovebox. As a final step, samples were left to oxidize inside a desiccator overnight before depositing the metal electrode.

The EDOT-Amide-TPA was synthesized in-house following the methods reported by Petrus et al.[229] and dissolved in a 1:4 volume ratio of chloroform (Acros Organics, 99.9 % extra dry):chlorobenzene at a concentration of 10 mg per mL of solvent mixture. For the doping, 10 µL mL^{-1} of tBP and 20 µL mL^{-1} of the above-mentioned Li-TFSI solution were added. To completely dissolve the powders, the solution was heated between 90 °C and 100 °C and then kept at 80 °C after hot filtering. Finally, it was spin-coated hot onto the perovskite layer at 1000 rpm for 45 s inside the glovebox. Then, the samples were left to

oxidize in a desiccator overnight. Due to the high volatility of the chlorobenzene at the above-mentioned temperatures, several vials of the amide solution were prepared in small quantities in order to limit the evaporation from each flask.

Metal evaporation

After oxidizing overnight, the perovskite layer was removed from the samples in the areas highlighted in figure 2.5, corresponding to the ground pins in the solar simulator measuring equipment. To do so, a cleaning solution made with a mixture of acetone, ethanol, isopropanol and deionized water was rubbed on the area with a cotton bud. Finally, 50 nm of gold were evaporated in a BOC-Edwards Auto thermal evaporator at a rate of 1 $Å s^{-1}$ at 10^{-6} Torr.

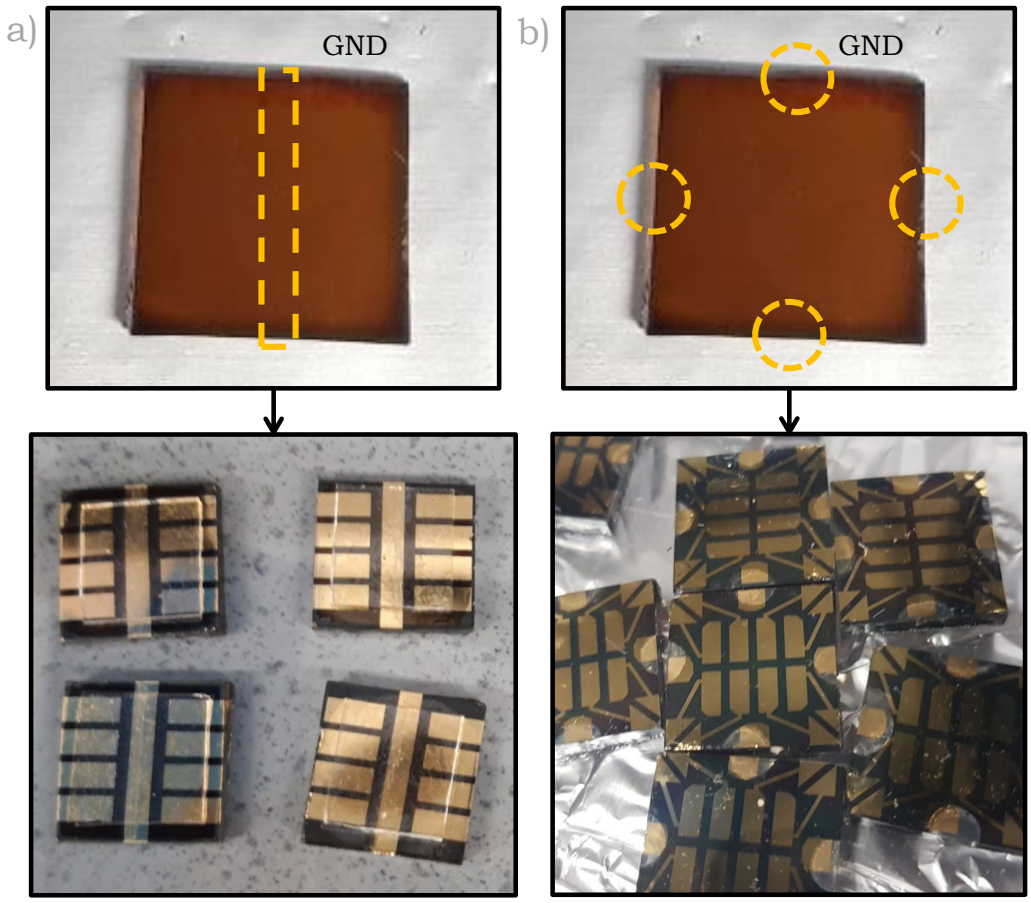

Figure 2.5: Ground (GND) cleaning areas (yellow) of the perovskite films and gold evaporation patterns on the solar cells for the vertical (a) and crossed (b) architectures.

2.3 Characterization techniques

2.3.1. X-ray diffraction (XRD)

X-ray diffraction (XRD) is a common material characterization technique that involves the use of X-ray radiation to determine the crystal structure of a sample. This measurement can retrieve a lot of useful information about the material's composition and properties such as their degree of crystallinity, orientation, size and strain of the crystallites.

Operational principle

In crystalline materials such as perovskites, their constituents (atoms and molecules) are arranged in a highly ordered microscopic structure forming, generally, a three-dimensional lattice. The best way to characterize this structure is to record the relative positions of the atoms in the smallest repeatable motif of the lattice: the unit cell. Here the distances between atoms can be described by the distances between planes (d) passing through the centres of the atoms. In figure 2.6 a, two sets of planes are represented in the unit cell of the inorganic $CsPbI_3$ perovskite. These planes are defined by the Miller indices (hkl), where the three integers denote the three points (a_1/h, a_2/k, a_3/l) where the plane intercepts the lattice vectors (a_1, a_2, a_3) defining the unit cell.

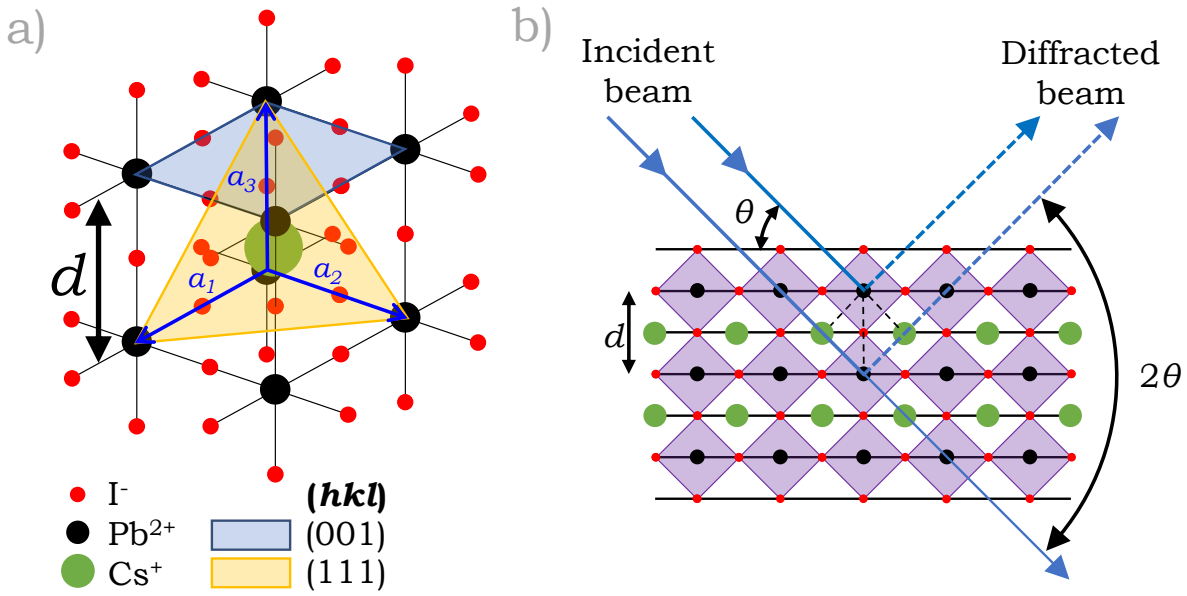

Figure 2.6: a) Representation of cubic $CsPbI_3$ unit cell with (001) and (111) planes highlighted. b) Schematics of X-ray diffraction on a cubic $CsPbI_3$ crystal.

The position of these atoms can be determined using X-ray diffraction. The physics behind this technique relies on the elastic scattering of the incident X-rays by the electrons bound to atoms in a sample. In the crystal structure, the information about the relative positions of the atoms can be obtained by recording the intensities of scattered waves reaching the detector with a relative phase shift. However, these signals can only

be detected if they form a constructive interference, that is if they satisfy Bragg's law. Diffraction peaks will appear when the distance between parallel planes in the crystal d is proportional to the wavelength of the X-ray λ, being n the diffraction order and θ the Bragg angle (equation 2.2, figure 2.6 b). It is worth noting that diffraction peaks only appear for crystalline materials as the disorder in amorphous solids prevents constructive scattering of the X-rays.

$$n\lambda = 2d\sin(\theta) \tag{2.2}$$

Instrumental details

XRD patterns were acquired with a *Bruker D8 advance* X-ray diffractometer. The functional part of the tool consists of a source and a detector mounted on a goniometer as shown in figure 2.7. Between them, two sets of optics boxes (primary and secondary) and a sample stage complete the design. Normally measurements are taken in a Bragg-Brentano geometry. Here, the sample is fixed in the centre, and both source and detector move with the beam keeping an average angle of incidence θ and diffracting at an angle of 2θ.

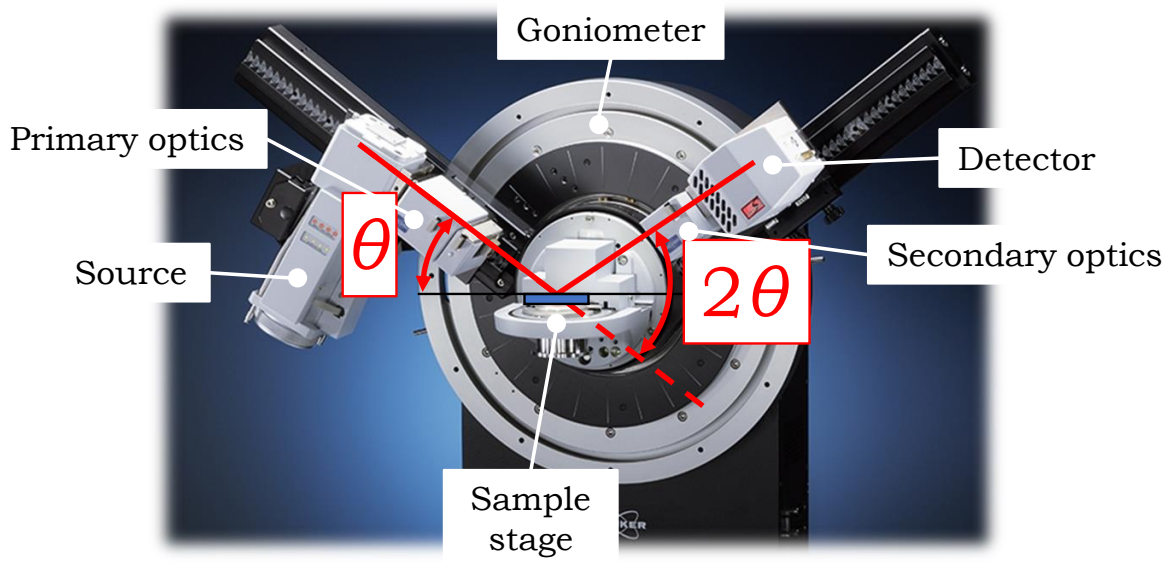

Figure 2.7: Parts of an X-ray diffractometer in a Bragg-Brentano setup. Incident (θ) and diffraction (2θ) angles are highlighted. Diffractometer image source from [57].

The emission of X-rays in the diffractometer is produced within the source which contains an X-ray tube. In this tube, electrons are emitted by a tungsten filament heated at high voltages (20-50 kV), accelerated and shot against a metallic anode. Copper is normally the target choice as it provides the best resolution. [52] When the bombarded electrons hit the Cu anode with energies below a certain threshold (about 8.5 kV) a continuous spectrum known as white radiation is produced. For higher energies, the shot electrons can eject an electron from one of the inner electron shells of the copper atoms.

As a consequence, an electron from a higher atomic level drops to the vacant level with the emission of an X-ray photon of either K_β or K_α energy. The α component is normally selected for the measurement because of its higher intensity. Various optical elements can be placed in the beam path to tailor its characteristics. For instance, a filter can be used to remove unwanted radiation (Cu K_β), a monochromator can select a particular wavelength (Cu $K_{\alpha 1}$) and a mirror can focus the beam. For our standard measurement, the K_β component was removed either with a 0.2 Ni filter in a Bragg Brentano setup or with a Göbel mirror when using a parallel beam configuration. Finally, the detector transforms the diffracted X-rays into an electrical signal either directly (silicon detectors) or with an intermediate conversion into photons before entering a photomultiplier tube (scintillation detectors).[52] The computer collects the data as a table of 2θ position and the respective number of counts.

In this thesis, the *Bruker D8 Advance* XRD diffractometer was operated in two of the most common setups for reflection mode: Bragg-Brentano and parallel beam. A diagram of these configurations can be seen in figure 2.8.

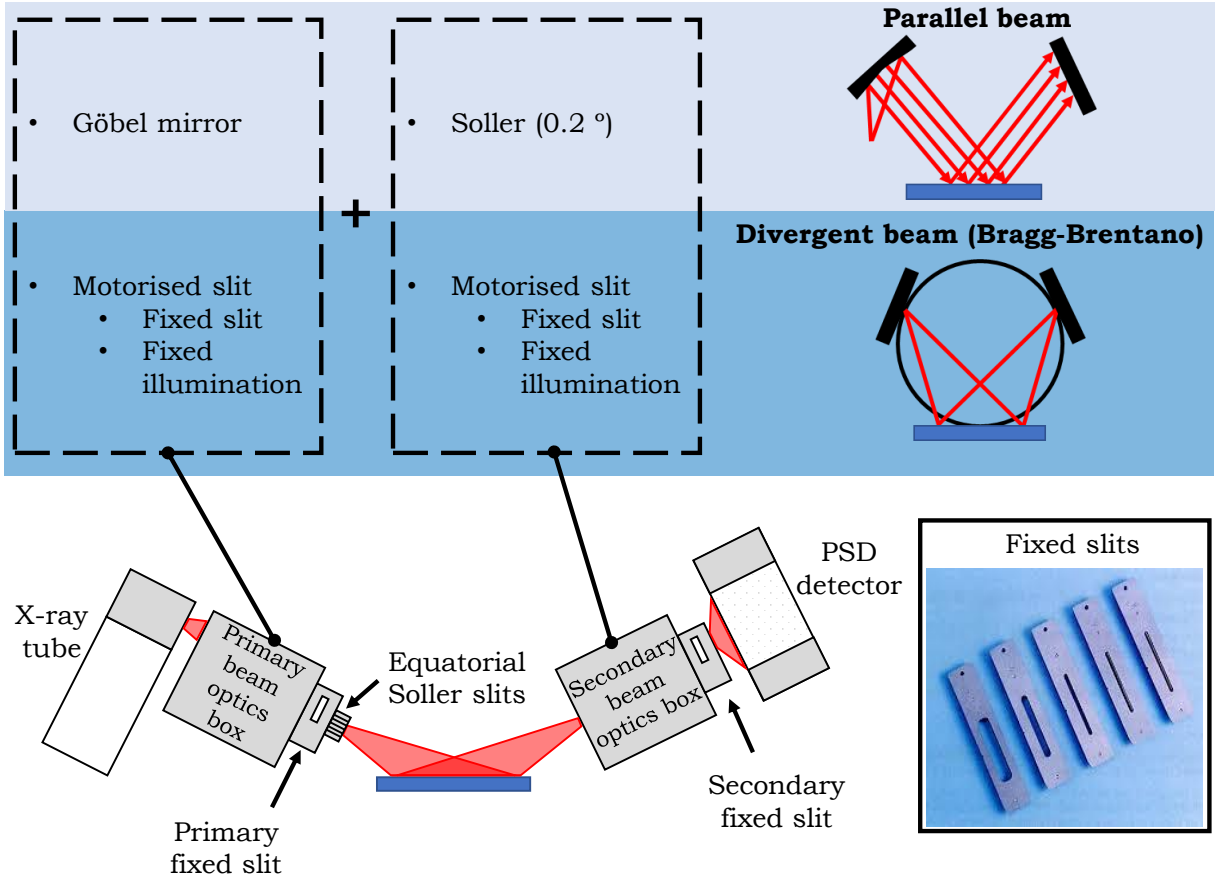

Figure 2.8: Diagram of a *Bruker D8 Advanced* XRD diffractometer in reflection mode. Details on the settings required both in the primary and secondary beam optics to change the beam configuration are represented at the top of the figure.

The main difference between them stems from the confinement of the beam. For the former, both the direct beam coming from the source and the diffracted beam coming from the sample will experience a considerable divergence in both the equatorial and the

axial planes. This induces defocussing effects that modify the final XRD profile. On the other hand, a parallel beam configuration reduces this instrumental effect by narrowing the optics to the expense of reducing the number of counts, which complicates the data acquisition of low-diffracting samples. Each setup adds alterations to the sample's diffraction pattern modifying the peaks' shape profile or position due to geometrical aberrations known as the instrumental contribution, similarly to what is depicted in figure 2.9.

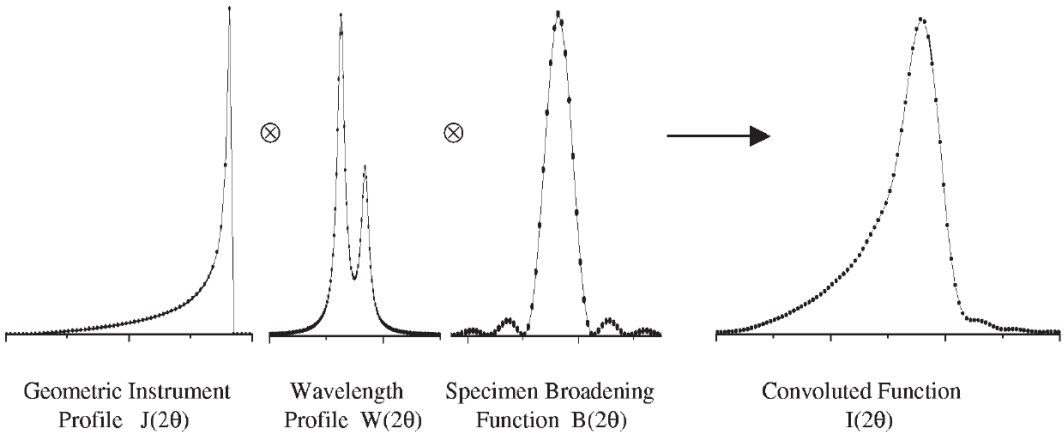

Figure 2.9: Convolution of the geometric instrument profile J(2θ), the wavelength profile W(2θ) and the specimen broadening function B(2θ) to produce the measured convoluted function I(2θ). Reproduced with permission from[39].

The errors associated with each setup are suitably described by Cheary and coworkers.[39] Given the conditions of our machine, the instrumental contributions affecting peak shape for a divergent beam configuration were limited to the following: finite width of the X-ray source, divergence coming from a flat specimen, beam penetration into the specimen (sample transparency), equatorial divergence associated with the finite width of the receiving slit, axial divergence of the beam and defocussing effects associated with a flat Silicon PSD detector. A summary of these, including the main shape modifications they induce in an XRD pattern, can be found in appendix A. In a parallel configuration, divergence errors are limited to the beam's axial divergence component.

XRD analysis

The direct result of this measurement is a two-dimensional plot with the abscissa signalling the diffraction angle (2θ) and the y-axis representing peak intensity in counts. The position and intensity of these peaks in a powder sample reveal information about the crystal structure and the elements that form the material. Hence a powder diffraction pattern can be seen as a fingerprint of a material.

However, before interpreting the results, a set of transformations needs to be applied to the data: the removal of the Cu K_α doublet and the 2θ displacement correction. For the set of measurements included in this thesis, corrections to the pattern were made with the X'pert Highscore Plus software. Cu $K_{\alpha 2}$ was removed employing the Rachinger

method and the vertical alignment were performed using the FTO peak at 26.53° as a reference. Additional background corrections were applied when necessary using the smoothing algorithm included in the program.

In a powder sample, all the possible planes fulfilling the Bragg condition are represented in the final diffraction pattern. On the contrary, polycrystalline films can carry a preferred orientation dependent on the crystallization conditions.[20] Therefore, some of the crystal planes will not be seen as only the planes that are parallel to the substrate satisfy the Bragg equation. An example of this behaviour can be seen in figure 2.10 a.

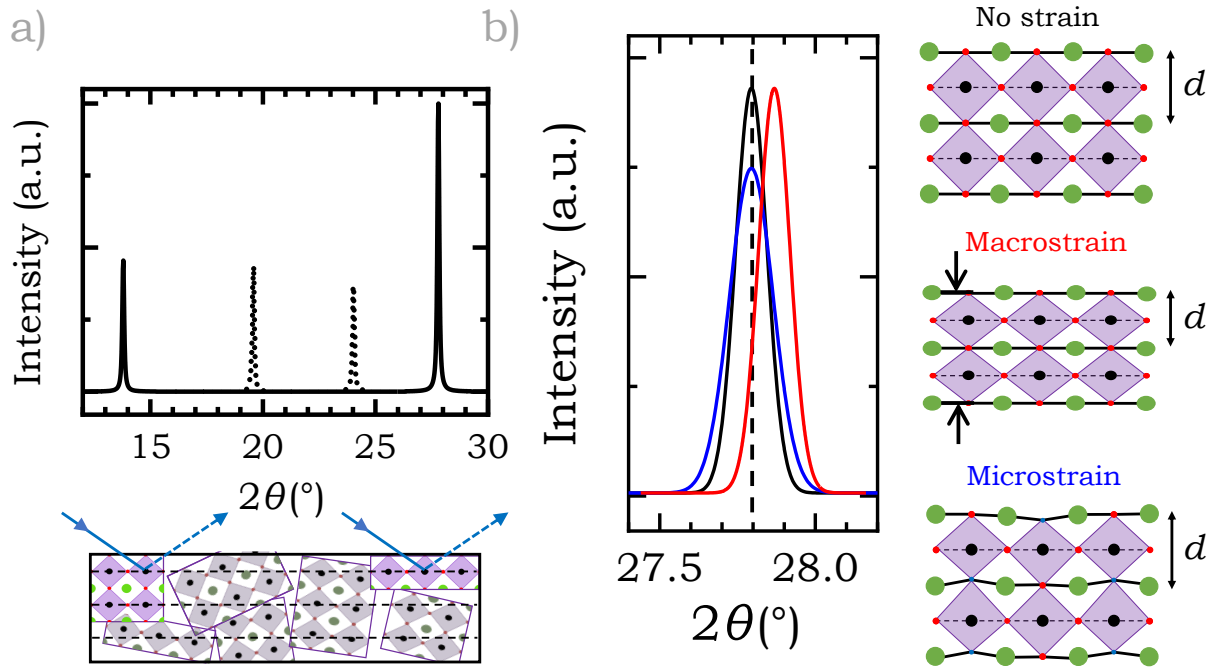

Figure 2.10: a) Representation of the diffraction of a perovskite polycrystalline sample. Only the aligned crystallites produce diffraction peaks. Dotted peaks represent the planes "unseen" by the XRD. b) Effects of lattice macro and micro strain in the line profile of an XRD peak. In red, the shift produced by macro stress, in blue, the peak broadening due to microstrain.

The peak profile contains information about the size and the strain of the crystallite that can be determined through peak broadening analysis.[20] [256] An assessment of the latter is particularly interesting in the study of perovskites as it provides an indication of their structural stability.[343,352,302]

First, it is crucial to make a distinction between two types of strain the material can be subjected to: macrostrain and microstrain. The first one takes into account the effect of tension or compression forces in the lattice which enlarges or shortens the d spacing, respectively.[94] As a result, the diffraction peaks show shifts that can be detected with a cradle stage in an out-of-plane measurement (figure 2.10 b). On the other hand, microstrain gives an indication of the existing distortions in the crystal lattice giving rise to contractions and expansions of the bond lengths. In this case, d is not a fixed value but a distribution of values, which translates into a broadening of the peak (figure 2.10 b).[94] Microstrain information can be obtained from standard Bragg Brentano measurements

by extracting the peak width either as the full width at half maximum ($FWHM$) or the integral breadth (β), defined as the area of the peak divided by its height.

XRD Microstrain: analytical methods

Microstrain can be obtained by deriving Bragg's law with respect to d and θ, with λ fixed. The result of this operation is the limit of resolution (equation 2.3),[94] which gives a relationship on the variation of interplanar distances with respect to the variation in the peak width.

$$\frac{\delta d}{d} = -\cot(\theta)\delta\theta \tag{2.3}$$

For microstrain analysis, the ratio between δd and d can be defined as the product of the root mean square strain $\varepsilon_{\mathrm{rms}}$ and a factor K_{D} dependent on the nature of the lattice distortion and the model of microstrain.[20] Taking that into consideration and defining the variation in 2θ as the peak broadening β, equation 2.3 can be seen as:

$$\beta = -2K_{\mathrm{D}}\varepsilon_{\mathrm{rms}}\tan(\theta) \tag{2.4}$$

However, the width of a peak is not just the product of strain but also includes the contribution of the crystallite size and an instrumental factor. The average crystal domain size (D) is normally estimated with the Scherrer equation (2.5), where K_{s} is a dimensionless factor accounting for the shape of the crystallite.[20] Standard diffractometers can detect size effects in crystallites measuring in the range of or less than 100 nm. Beyond that number, domain size effects can be hardly distinguished from the instrumental contribution.[20,302]

$$D = \frac{K_{\mathrm{s}}\lambda}{\beta\cos(\theta)} \tag{2.5}$$

There are several ways of estimating the combined contributions of size and strain. Yet, due to their simplicity, integral breadth (IB) methods are normally the tool of choice in the literature. Amongst them, the most common method is the Williamson-Hall (WH) plot (figure 2.11 a).[256,20] In it, the $FWHM$ or β of the peaks corresponds to the sum of the broadening due to crystallite size (β_{S}) and the lattice distortion (β_{D}) with ε representing the microstrain, as shown in equation 2.6. Williamson and Hall proposed multiplying both sides of the equation by $\cos(\theta)/\lambda$ and plotting $\beta\cos(\theta)$ versus $4\sin(\theta)$. In this way, the slope of the linear fit of the plot retrieves the strain value and the intercept, the average domain size (equation 2.7).

$$\beta = \beta_{\mathrm{S}} + \beta_{\mathrm{D}} = \frac{K_{\mathrm{s}}\lambda}{D\cos(\theta)} + 4\varepsilon\tan(\theta) \tag{2.6}$$

$$\beta\cos(\theta) = \underbrace{\frac{K_s\lambda}{D}}_{\text{size}} + \underbrace{4\varepsilon\sin(\theta)}_{\text{strain}} \tag{2.7}$$

Although simple to perform, the limitations of this method are manifold. First, the simple addition of the size and strain components assumes that both the size and the strain in the peak follow a Lorentzian distribution. However, it is experimentally known that Lorentzian peak profiles are associated only with the size component while Gaussian distributions are a better fit for strain. The method is also limited to small grain sizes so that the domains stay below the ~100 nm threshold.

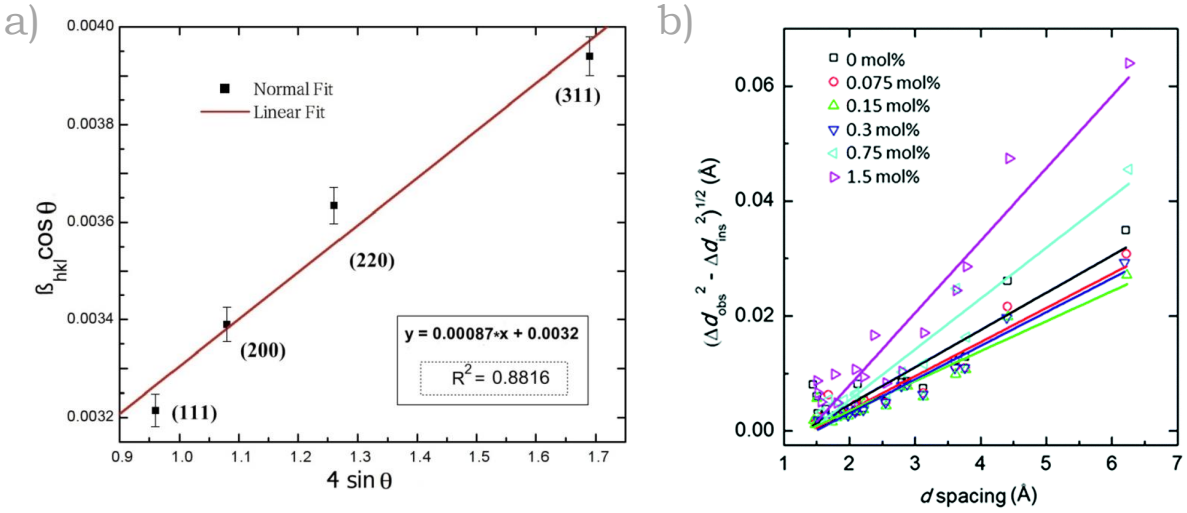

Figure 2.11: a) Williamson-Hall plot of CdSe nanoparticles. Reproduced with permission.[200] Copyright (2019) Elsevier B.V. b) Modified Williamson-Hall plot of Al^{3+} doped $MAPbI_3$ at different concentrations. Reproduced with permission from[302]. Copyright (2016) The Royal Society of Chemistry.

To overcome some of these limitations, it is common to use a modified version of the Williamson-Hall (mod-WH) plot in halide perovskite film studies, as depicted in figure 2.11 b.[302,352] Here the peak width contribution from crystallite size is rightfully ignored (due to the presence of large grains) and the microstrain is plotted as a function of the d-spacing. In this case, the only contributions to the observed width of the peak (Δd_{obs}) are the microstrain (Δd_ε) and the instrumental response (Δd_{ins}), as defined by equation 2.8,[302] following a Gaussian distribution.

$$\varepsilon = \frac{\Delta d_\varepsilon}{d} = \frac{\sqrt{\Delta d_{\text{obs}}^2 - \Delta d_{\text{ins}}^2}}{d} \tag{2.8}$$

Despite modifying the method, the WH plot is still designed for powder measurements. Therefore, its application in films can introduce further errors due to strain anisotropy induced by preferential orientation.[20] Hence, the interpretation of the data must be done with caution and considered in combination with other characterization techniques. Alternatively, to remove potential anisotropic effects from the result, the line analysis of the diffracted planes in the film can be done individually by fitting a Voigt function and

using the Gaussian component (β_G). In this way, the strain component can be obtained for each diffracted plane using equation 2.9.[20]

$$\varepsilon = \frac{\beta_G \cot(\theta)}{4} \tag{2.9}$$

Note that whether the peak width is obtained with a Voigt fit (V) (convolution of Lorentzian (L) and Gaussian (G) functions as defined in equation 2.10) or directly with a Gaussian, the instrumental contribution must be removed accordingly (equation 2.11).

$$\beta_V^2 = \beta_L \beta_V + \beta_G^2 \tag{2.10}$$

$$\beta_L = \beta_L^{obs} - \beta_L^{ins}, \quad (\beta_G)^2 = (\beta_G^{obs})^2 - (\beta_G^{ins})^2 \tag{2.11}$$

To obtain the instrumental width contribution a reference sample with known lattice constants is measured in the exact same conditions of the sample under study. Their diffraction peaks are fit and their widths are plotted as a function of the diffraction angle. These points are then fit by a smoothed curve, generally a polynomial, enabling the extraction of the aberration contribution at any 2θ angle to be subtracted from the original sample. The most common fitting functions are the Caglioti and the Langford fit, defined by equations 2.12 and 2.13, respectively.[30,149]

$$\beta_{ins}^2 = U \cdot \tan^2(\theta) + V \cdot \tan(\theta) + W \tag{2.12}$$

$$\beta_{ins}^2 = A \cdot \tan^2(\theta) + B + C \cdot \cot^2(\theta) + D \cdot \sin^2(\theta) \tag{2.13}$$

XRD Microstrain: program fitting

To calculate perovskite microstrain (MS) a Python-based application (*Multiple Voigt fit program - MICROSTRAIN CALCULATION*) was developed using the *tkinter* module to generate a graphical user interface (figure 2.12). Note that to perform the calculations, the XRD data was pre-treated (Cu$K_{\alpha 1}$ radiation, no background).

The Voigt function was used to fit the diffraction peaks following the definition from the *lmfit* module (equation 2.14). Here, the parameters correspond to amplitude (A), centre (μ), gamma (γ) and sigma (σ), with Re[$w(z)$] as the real part of the Faddeeva function evaluated for z and erfc() as the complementary error function. The γ value was constrained to be equal to σ. Microstrain was calculated individually for each peak using the previously defined equations 2.9 (ε, individual line profile analysis), 2.7 (Williamson-Hall plot) and 2.8 (modified Williamson-Hall plot). For the WH and mod-WH methods, both x and y coordinates of the plot were given.

$$f(x; A, \mu, \sigma, \gamma) = \frac{A\mathrm{Re}[w(z)]}{\sigma\sqrt{2\pi}}$$

$$z = \frac{x - \mu + i\gamma}{\sigma\sqrt{2}}, \quad w(z) = e^{-z^2}\mathrm{erfc}(-iz) \tag{2.14}$$

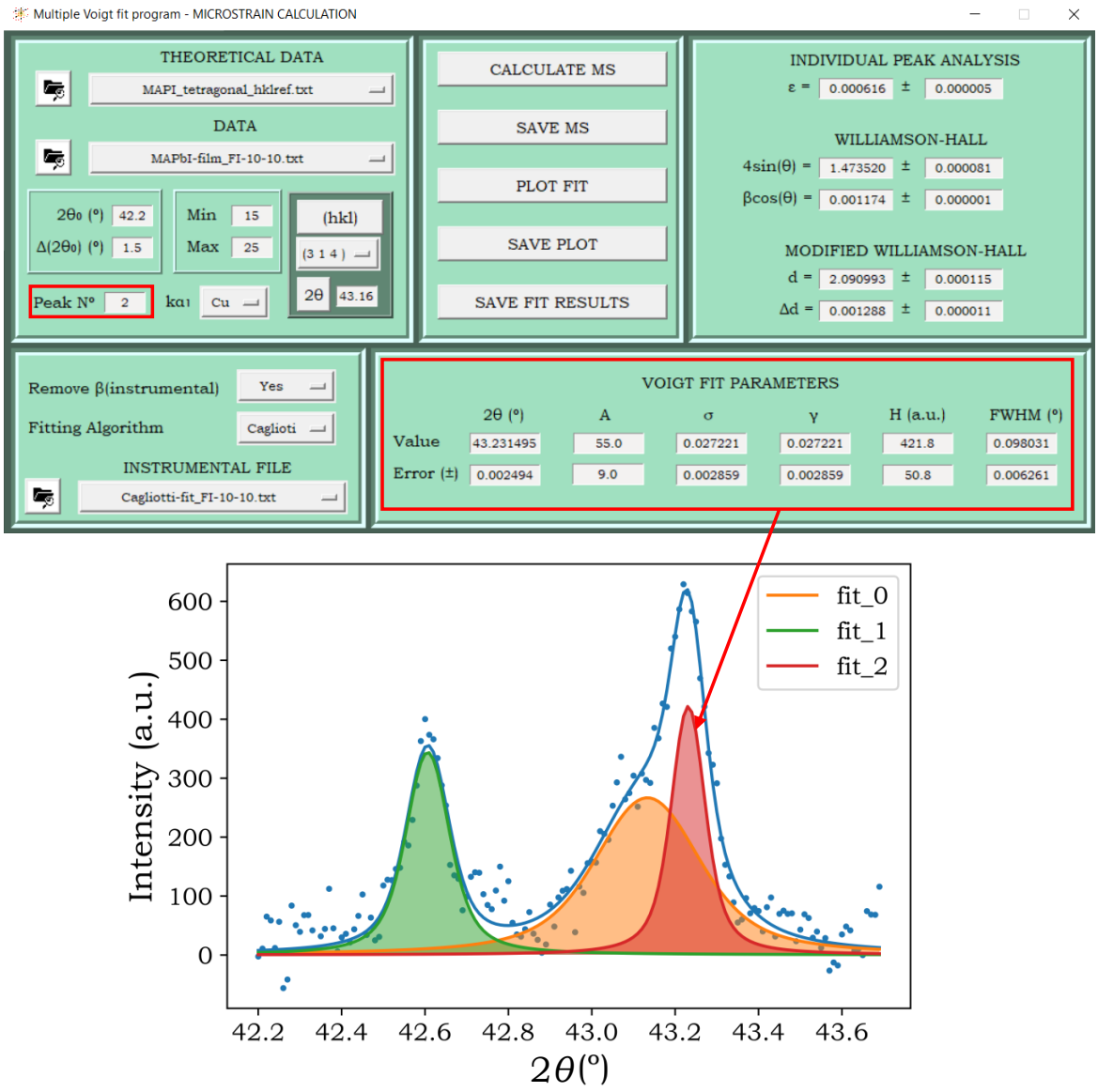

Figure 2.12: Python-based Microstrain calculator's user interface with the calculated Voigt fit parameters and microstrain of the (314) plane of a $MAPbI_3$ film sample. The generated multiple Voigt fit plot is represented at the bottom of the image.

The program was designed to provide a multiple peak fit using the peak search algorithm (*find_peaks_cwt*) in the signal processing module *scipy.signal*, using a similar approach as the one developed by Ostrouchov.[219] The peak search was constrained by the four parameters defined in figure 2.12: $2\theta_0$, $\Delta 2\theta_0$, Min and Max. The first two parameters defined the 2θ window where the peak search would be performed, while the

second two constrained the algorithm to find n peaks presenting widths between a minimum (Min) and maximum (Max) value, within the selected window. In order to provide the user with a reference to select the appropriate 2θ peak search window, the program displays the theoretical 2θ positions per (hkl) plane, provided the theoretical pattern for the studied sample is loaded. The theoretical pattern file can be obtained by exporting the calculated perovskite powder pattern from a *.cif* file in *Mercury* as a reflection list (*.hkl*) and transforming it to a *.txt* file. Both the Voigt fit parameters and the microstrain values are displayed for one peak at a time, as determined by the user in the *Peak N°* entry (figure 2.12). Microstrain calculations were performed by default using the Cu$K_{\alpha 1}$ wavelength, set at 1.54056 Å. However, the user can choose between a range of targets besides copper (Mo, Fe, Cr or Co).

The instrumental contribution was removed both in the Gaussian and Lorentzian components of the Voigt fit using equation 2.11. The instrumental peak width functions were calculated using either a Caglioti or a Langford fit by loading the instrumental file. The latter was calculated using a second *tkinter*-based application (*Instrumental fit program*), as depicted in figure 2.13.

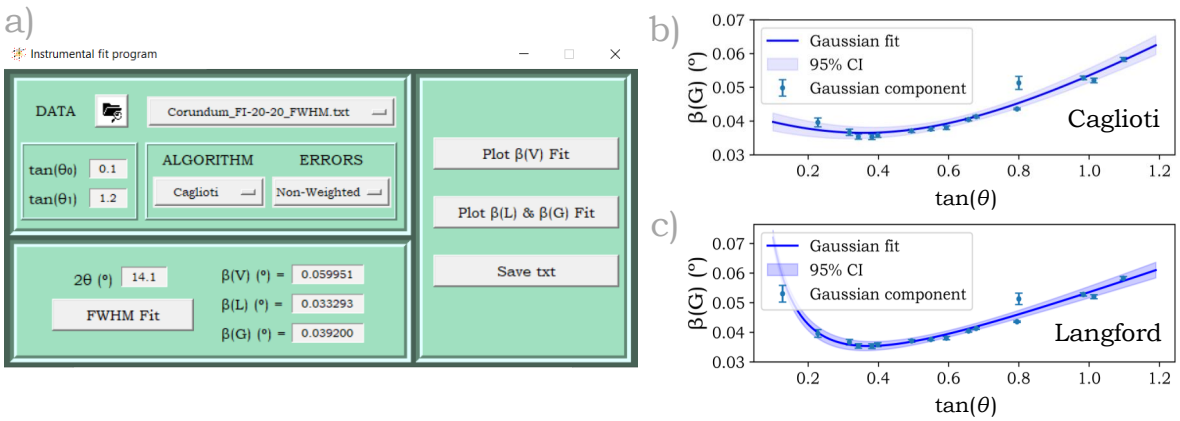

Figure 2.13: Python-based Instrumental fit's user interface (a) with Caglioti (b) and Langford (c) fit plots using the Gaussian component from the peaks fit of a Corundum reference sample.

The Caglioti and Langford fits were calculated for the instrumental reference sample using equations 2.12 and 2.13, respectively. Prior to this, the diffraction peaks in the reference sample were fit with a Voigt function using the application depicted in figure 2.12. The *Instrumental fit program* returned three fits per function. The first was calculated using the *FWHM* of the Voigt function, while the second and third used the Gaussian and Lorentzian components of the Voigt fit, respectively. Note that the fits could be obtained both with and without weighting the peak fit widths errors of the reference sample using the predetermined *numpy polyfit* function. Results could be visualized either as a full plot (figure 2.13 b and c) or as individual values using the calculator included at the bottom of the application (figure 2.13 a). Both the Caglioti and Langford function parameters were stored in a text file to be used in the *MICROSTRAIN CALCULATION* program.

Uncertainties in the microstrain values were obtained using the standard error propagation formulas by taking into consideration the error from the perovskite Voigt peak fit returned by *lmfit* and the error from the instrumental Caglioti or Langford fits, returned by the extremes of the 95 % confidence interval (CI). The CI was calculated following the formula from equation 2.15.[71] Here, the CI gives the 95 % probability of finding the mean response of new values at a specified $2\theta_0$ angle, with $T^{.975}$ as the 97.5$^{\text{th}}$ percentile of the Student's t-distribution with $(n-m)$ degrees of freedom and $\hat{\sigma}$ as the standard deviation of the instrumental fit (equation 2.16). Note that the degrees of freedom were determined by the number of data points considered (n) and the number of parameters of each fit (m), with m=3 for Caglioti and m=4 for Langford.

$$CI = T^{.975}_{(n-m)}\hat{\sigma}\sqrt{\frac{1}{n} + \frac{(\tan(\theta_0) - \overline{\tan(\theta)})^2}{\sum_{i=n}^{n}(\tan(\theta_i) - \overline{\tan(\theta)})^2}} \tag{2.15}$$

$$\hat{\sigma} = \sqrt{\sum_{i=n}^{n}\frac{(\beta_i - \hat{\beta})^2}{n-m}} \tag{2.16}$$

2.3.2. Ultraviolet-visible (UV-Vis) absorption spectroscopy

Ultraviolet-visible (UV-Vis) absorption spectroscopy is an analytical technique quantifying the absorption of light by solid or liquid samples within the 170 to 780 nm range. The absorption mechanism reflects the electronic transitions occurring within the sample which are characteristic of the material. In it, electrons from the ground state will be promoted to the excited state when struck by photons with enough energy.

To get the absorbance of a material, the intensity of light of a determined wavelength (λ) before (I_0) and after (I) passing through the sample is measured. The ratio between these two values corresponds to the transmission of light through the sample. A value of absorbance (A) is obtained by calculating the negative logarithm of this ratio as defined by the Beer-Lambert law (equation 2.17). The absorbance is proportional to the sample concentration (c), the sample extinction coefficient (ε) and the sample path length (ℓ).

$$A(\lambda) = -\log\left(\frac{I(\lambda)}{I_0(\lambda)}\right) = \varepsilon\ell c \tag{2.17}$$

For the study of perovskite semiconductors, the absorbance spectrum is normally transformed into a Tauc plot to obtain the optical band gap. In it, the abscissa is represented as the energy of light ($h\nu$) while the y-axis is the result of the product between the absorption coefficient and the energy of light to the power of a constant ($(\alpha h\nu)^{\frac{1}{r}}$). The exponent r denotes the nature of the transition and is equal to 1/2 for direct allowed transitions and 2 for indirect allowed transitions. The electronic band gap of the material corresponds to the intercept value of the linear region.

To acquire the absorption data a spectrophotometer is used: light is emitted by a deuterium lamp (UV) and/or a xenon lamp (visible) and shined through a sample and a reference (figure 2.14). Before hitting the targets, a monochromator separates the wavelengths of light and focuses each of them onto the photodetector sequentially, enabling the acquisition of absorbance values over the whole spectrum.

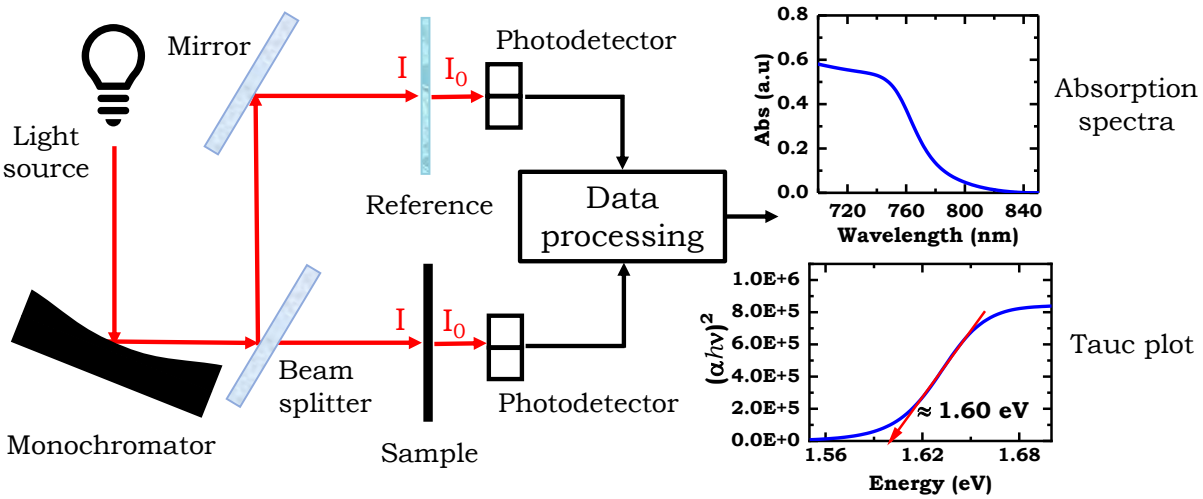

Figure 2.14: Schematic representation of the UV-Vis spectrometer setup with the recorded absorption curve. A Tauc plot can be obtained from the former.

The absorbance of perovskite films on glass was measured with a Shimadzu UV-1800 spectrophotometer. To calculate the absorbance of the sample, the absorbance of a glass slide was subtracted from the total measured absorbance.

2.3.3. Photoluminescence (PL) spectroscopy

Photoluminescence (PL) spectroscopy is a widely employed characterization technique that can be used to identify the electronic transitions occurring within a material by collecting the light it emits upon photon excitation.

In a semiconductor, the movement of electrons within electronic transitions can be divided into three main processes: excitation, relaxation and radiative recombination (figure 2.15 b). When a photon with enough energy strikes on the sample, an electron in an occupied valence state jumps to an empty conduction-band state, forming an electron-hole pair. This pair undergoes a relaxation process where the carriers transition to their respective ground states: the conduction and valence band edge states. Finally, the pair recombines generating a photon with a different wavelength from the incident light that can be collected and measured by the equipment.

Results are normally represented as a plot of emission wavelength versus light intensity at a specific excitation wavelength. The peak in this photoluminescence spectrum corresponds approximately to the energy difference between the conduction and valence band edges (band gap) of the semiconductor. In perovskite semiconductors, PL results are particularly useful in LED characterization as they provide the wavelength, band-

width and intensity of the emitted light, which are normally dependent on the halide composition.[180]

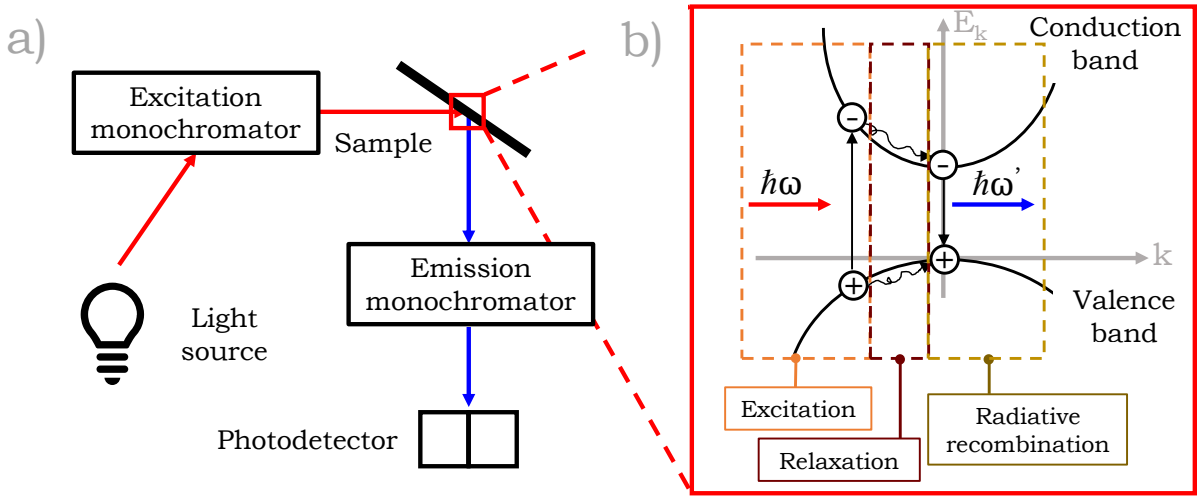

Figure 2.15: a) Schematic representation of a PL setup. b) Detail on the electronic transitions occurring within the sample between excitation and light emission. Here the energy of the carriers (E_k) is represented against their momentum (k), with $\hbar$ as the Planck constant and ω and ω' representing the excitation and emission angular frequencies, respectively. Adapted with permission from[181]. Copyright (2018), Springer International Publishing AG.

In a photoluminescence spectrometer light is filtered through a monochromator to select a group of excitation wavelengths to direct into a sample (figure 2.15 a). The light emitted from the sample is then filtered in a second monochromator to select the emission wavelength of interest and collected by a photodetector. Steady PL measurements were taken with a Shimadzu RF-6000 spectro fluorophotometer.

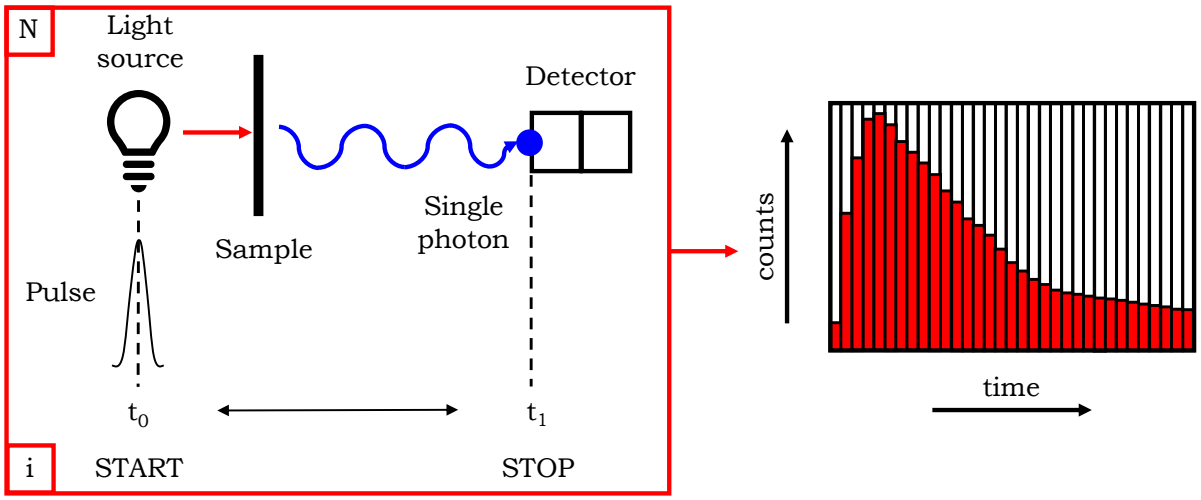

Figure 2.16: Schematic representation of the working principle behind a TCSPC measurement. The histogram is constructed with the accumulated data of N cycles.

The kinetics behind the electronic transitions occurring in a semiconductor can be further studied with a time-resolved setup. Here the main aim is to obtain the relaxation time and radiative recombination lifetime by exciting the sample with a laser pulse and

recording its PL emission as a function of time. One of the most common setups for this data acquisition is the time-correlated single-photon counting (TCSPC) technique. In it, the PL decay is measured in a series of start-stop sequences delimited by the emission of the excitation pulse (start) and the arrival of the first fluorescence photon at the detector (stop). The time between these two events is measured and the cycle is repeated millions of times to obtain a histogram of signal photon counts versus time (figure 2.16). This technique is particularly useful for obtaining the perovskite carrier lifetimes, which are extracted by fitting one or more exponential curves to the obtained histogram.[62,332] In this thesis, an Edinburgh Instruments FLS980 Spectrometer was used for time-resolved PL measurements.

2.3.4. Atomic force microscopy

Atomic force microscopy (AFM) is a high-resolution imaging technique where a small probe with a sharp tip is scanned across a sample to measure its topography with sub-nanometer resolution. Surface features are detected by the displacement of a laser beam over the cantilever, which stands on top of the sample either touching it (contact mode) or oscillating on top of it (non-contact mode) (figure 2.17).

In the contact mode, tip and sample are in direct contact. The feedback loop of the system keeps the tip-sample distance constant by moving and recording the z position with a piezo-stage. These height variations correspond to the topography of the sample.

For the non-contact mode, the cantilever is oscillating on top of the sample close to its free resonance frequency. When the tip approaches the sample, the interaction between both changes the resonance frequency of the cantilever, which translates into a change in the cantilever's amplitude. This is the signal introduced into the feedback loop to keep a constant distance between tip and sample and record the height variation as in contact mode.

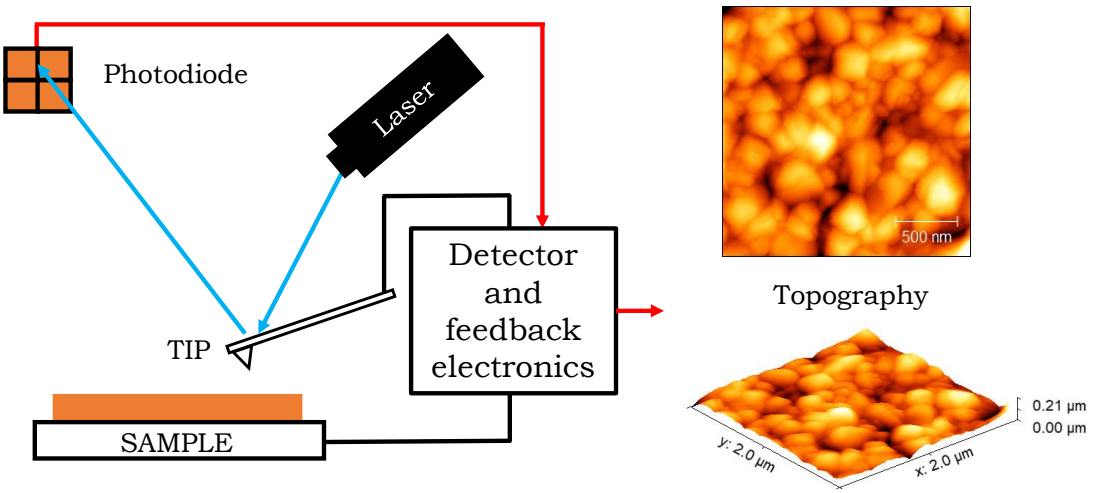

Figure 2.17: Schematic representation of an AFM setup with topography results.

There is a third mode in between the above-mentioned ones called tapping mode. Here the cantilever vibrates close to its resonant frequency at much larger amplitudes than in non-contact mode while lightly "tapping" on the sample surface during the scan. The feedback system detects the changes in the amplitude as a function of the tapping, which is used as a set point to adjust the height variation and map the surface.

As a general rule, non-contact is the most recommendable mode to use. It produces the least damage to the sample and the tip, as none of them is brought in contact. The topography of the studied perovskite films was acquired in this mode with a Park Systems XE-150 atomic force microscope. The obtained perovskite images were levelled in Gwyddion using a 2nd order polynomial and grain size was calculated using the watershed algorithm described by Klapetek et al.,[140] as depicted in figure 2.18.

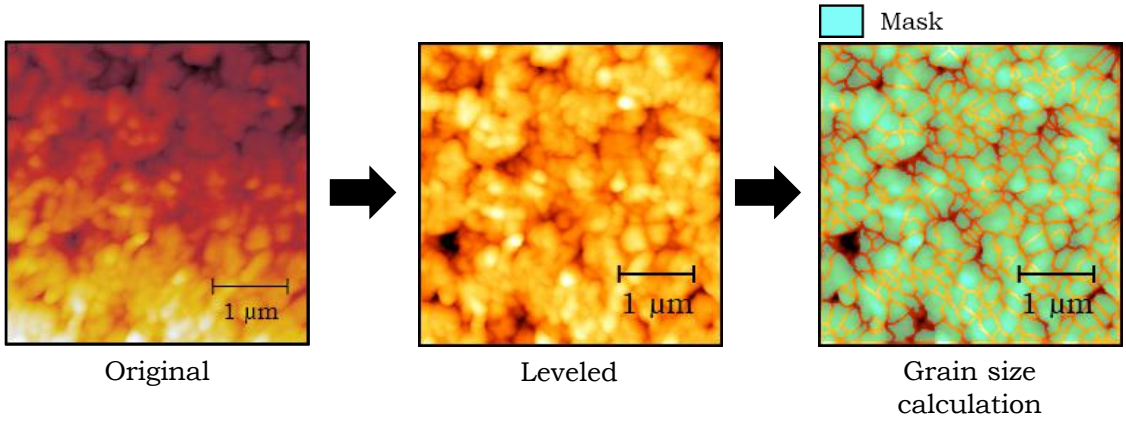

Figure 2.18: AFM image treatment process.

2.3.5. Current-voltage (IV) measurements

Solar cells are normally characterized by a current-voltage (IV) scan. For this measurement, the flow of current across the device is measured as a function of the applied voltage under illumination. Usually, the photocurrent is divided by the active area to plot values of current density (J).

The main characteristics of the solar cell are reported by the curve obtained when a light IV is performed under Standard Test Conditions (STC). That is, the scan is performed at an irradiance of $1000\,\mathrm{W\,m^{-2}}$ with an air mass of 1.5 (AM 1.5) spectrum and the sample at 25 °C.[111] These conditions were reproduced using the JV measuring equipment described in chapter 3. The main parameters obtained from this plot are highlighted in figure 2.19.

The current density at short-circuit (J_{SC}) is the current flowing through the solar cell at zero voltage bias. Its value is dependent both on environmental conditions such as light intensity and spectrum and the intrinsic properties of the materials: band gap, optical properties (absorption, reflection) and charge collecting performance.

The open-circuit voltage V_{OC} corresponds to the maximum voltage of the solar cell which occurs at zero current. It is equal to the difference in the quasi-Fermi levels of the majority carriers at the two terminals: electrons in the n-type portions and holes in the p-type portion. By definition, this parameter is susceptible to changes in the band gap and to charge recombination processes.

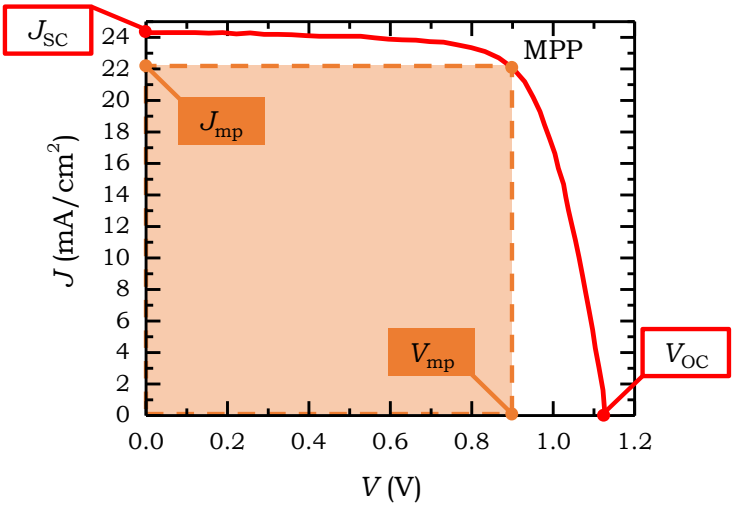

Figure 2.19: Solar cell JV scan plot with its characteristic parameters.

The product of J_{mp} and V_{mp} equals the maximum power output of the solar cell. This point is known as the maximum power point (MPP) and it is used to obtain both the Fill Factor (FF) and the Power Conversion Efficiency (PCE) of a solar cell.

The FF gives a measure of the quality of a solar cell. It is defined as the ratio between the maximum power and the product of J_{SC} and V_{SC} (equation 2.18). Graphically it describes the amount by which the J_{SC}-V_{OC} rectangle is filled by the J_{mp}-V_{mp} area. This factor is affected by the cell's series and shunt resistances.

$$FF = \frac{J_{mp}V_{mp}}{J_{SC}V_{OC}} \tag{2.18}$$

Finally, the PCE is defined as the power at the MPP divided by the incident illumination power (equation 2.19).

$$PCE = \frac{J_{SC}V_{OC}FF}{P_{in}} \tag{2.19}$$

An additional phenomenon of crucial importance in the specific characterization of perovskite solar cells is the electrical hysteresis. In these ionic semiconductor devices, it is common to find a mismatch between the measured JV curves taken in opposite scan directions. The hysteresis index (HI), defined in equation 2.20 can be used as a way to quantify this directional discrepancy. Note that this parameter has been deemed inadequate as an absolute metric, due to the large variability it presents depending on the scanning regimes.[92] However, it still represents a good relative quantification of the difference between scans when the scanning conditions are kept constant, as occurs in the experiments collected for this thesis.

$$HI = \frac{PCE_{\text{rev}}}{PCE_{\text{for}}} - 1 \tag{2.20}$$

2.3.6. Temperature-dependent conductivity

Extracting the ionic motion contribution in the charge transfer of perovskite solar cells is crucial to understanding the appearance of hysteresis in the devices. Although several mechanisms were ascribed to this phenomenon, such as ferroelectric or charge trapping and de-trapping effects,[274] ion migration stands out as the dominant factor.[244,73,158,113] Quantifying ion migration in halide perovskites is possible through the acquisition of temperature-dependent conductivity measurements. Plotting the values of conductivity over temperature (figure 2.20 b) highlights two regions: a conductivity-dominated one at low temperatures, where ions are frozen, and an ionic-dominated region at high temperatures, where both electrons and ions contribute to the total conductivity. The slope of the mixed conductivity region is often used to extract the activation energy for ionic motion.[32,329]

In this thesis, temperature-dependent conductivity measurements were performed using a cryostat in the setup described in figure 2.20 a. Fast current-voltage (IV) scans were performed to the lateral device described in the inset of figure 2.20 a, fabricated by spin coating a layer of perovskite on ITO etched glass substrate, where a 162 cm long by 75 µm width channel was carved. The values of conductivity were calculated using the resistance extracted from the IV (R_{IV}) scan performed between 180 K and 300 K, following equation 2.21. The parameter L equated the width of the channel and the cross-sectional area (A) corresponded to the product of the length of the carved channel multiplied by the thickness of the perovskite film.

$$\sigma_{\text{mixed}} = \frac{1}{R_{IV}} \cdot \frac{L}{A} \tag{2.21}$$

Using a similar methodology, Zhao et al. complemented the fast IV scans with a galvanostatic measurement (figure 2.20 c), extracting the value of electronic conductivity (σ_{e}) through the stabilized value of resistance obtained after supplying a very low current in the order of picoamps.[347] This enabled the extraction of the ionic component of conductivity (σ_{i}) using equation 2.22.

$$\sigma_{\text{mixed}} = \sigma_{\text{e}} + \sigma_{\text{i}} \tag{2.22}$$

Due to limitations in the acquisition speed of IV scans in the setup, the galvanostatic measurement was exclusively used to assess the electronic contribution without subtracting it to the mixed values. These were affected by slight hysteresis given the impossibility of performing scans in the range of $50\,\text{V}\,\text{s}^{-1}$, which retrieved lower mixed-conductivity values than the electronic values extracted from the galvanostatic scan.

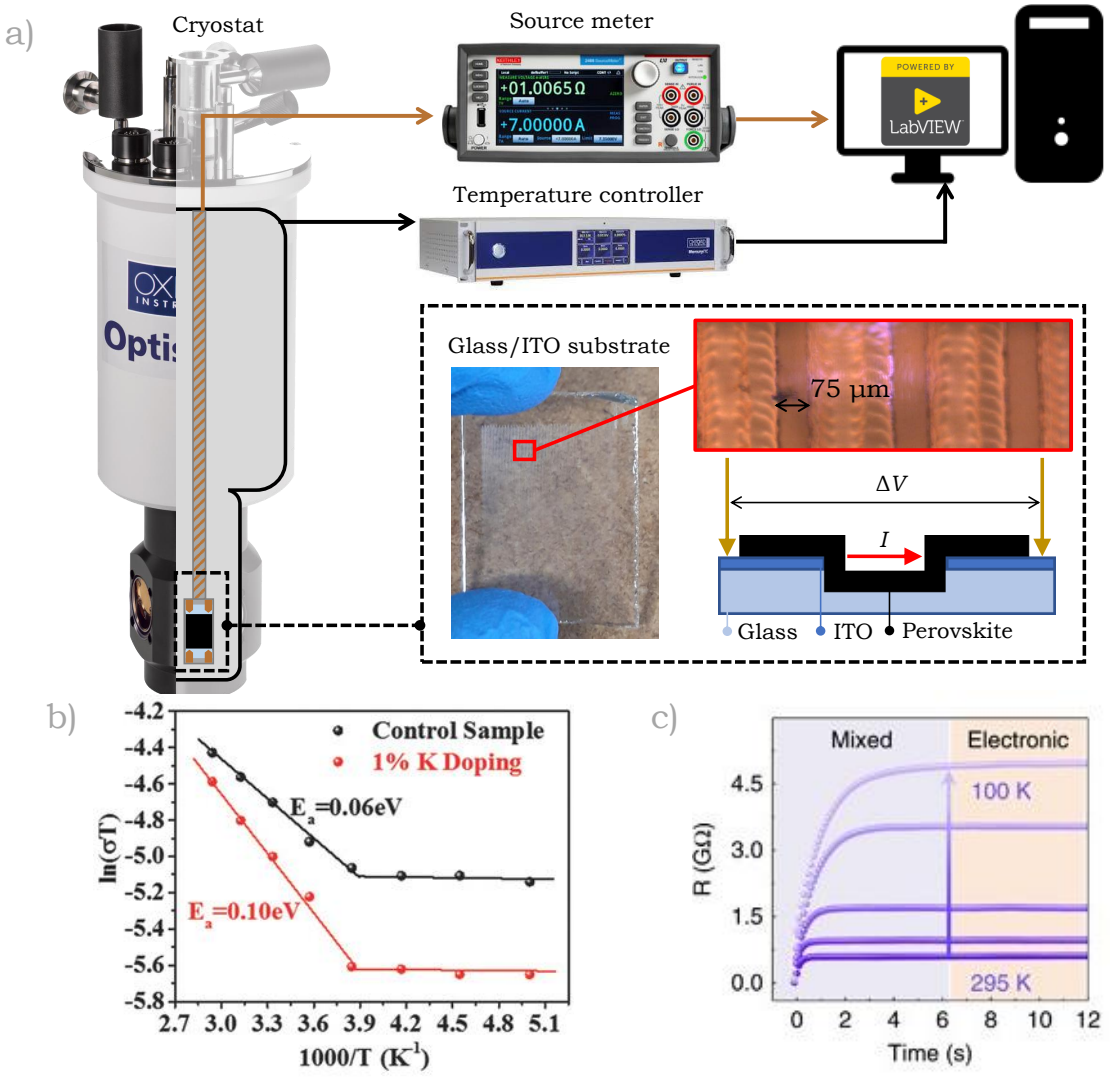

Figure 2.20: a) Ionic conductivity setup conformed by an Optistat DN cryostat paired with a Mercury ITC temperature controller from Oxford Instruments and a Keithley 2460 source meter, all of them controlled with a Labview program. b) Extraction of the activation energy from the temperature-dependent conductivity measurement of Cs/MA/FA perovskite and 1 % K^+-doped Cs/MA/FA perovskite from publication.[32] c) $MAPbI_3$ galvanostatic curves at different temperatures from publication.[347]

Chapter 3. Experimental setup

This chapter contains information on the design, fabrication and operational principles of three original in-house-built instruments for perovskite characterization. The chapter is divided into three sections corresponding to each instrument: an automated *JV* measuring equipment, a hydration chamber for X-ray diffraction and a colourimetry-based instrument for thermal degradation assessment named pixel colour tracking (PCT).

3.1 Automated *JV* measuring equipment

Solar cells are normally characterized by a current-voltage (*IV*) scan taken with a source meter under the light of a solar simulator. These two instruments are the minimum requirement to perform the measurement, yet their use without additional instrumentation poses a significant time constraint to the number of samples that can be measured per hour, given that each cell has to be changed and measured manually. Optimizing the measurement often involves the addition of a program able to control the source meter and a sample holder design that enables the automatic change between the solar cells contained in the same substrate. While low-cost versions of this currently exist in the market,[275] they are often limited to measuring one substrate at a time with a specific design pattern. Herein, two low-cost designs of automated *JV* measuring systems are presented. They enable the measurement of multiple samples containing 12 and 8 solar cells per substrate for two types of solar cell architectures.

3.1.1. Description and operational procedure

The measuring system was conceived, in its most basic form, as a set of a sample holder and a PCB connected to a source meter (Keithley 2410), a power source and a control board (Maxibee) directed by the computer to perform *IV* scans as shown in figure 3.1. The Maxibee executed the Labview commands coming from the computer to activate and deactivate each measuring pixel so that all solar cells in the sample could be measured either individually or sequentially. Additional features of the system included a motorized linear stage driven by the Stepper-bee control board which enabled the displacement of the stage. In this way, the user could re-position the holder to expose each sample to the HelioSim-CL60 solar simulator beam. Light intensity was calibrated using a BPW 21 OSRAM photodiode, with the principal characteristics detailed in the specification sheet

referenced here.[218]

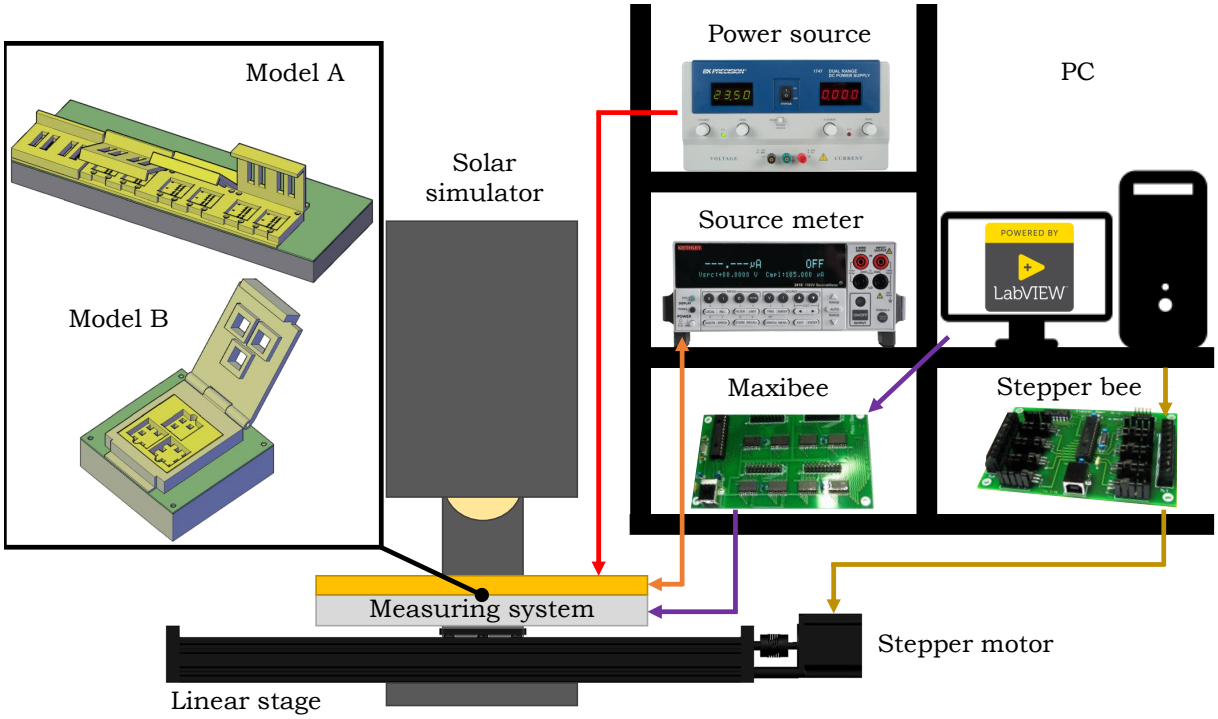

Figure 3.1: Automated *JV* measuring system layout.

In the following subsections, the two main models of automated *JV* measuring equipment with their correspondent solar cell designs are described.

3.1.2. Solar cell designs

Two models of the automated *JV* measuring equipment were designed and fabricated adapting to the size and layout of the two sample architectures highlighted in figure 3.2. For simplicity, the equipment and cell architectures will share names in this text as model A and model B, respectively. Both device types incorporated the absorber and charge carrier extraction layers in a planar architecture, with the main difference between them being the size and the distribution of the electrodes.

Model A devices displayed a standard solar cell design commonly found in the literature.[102,90] They were fabricated from a 12×12 cm FTO-glass sheet cut into 16 equal pieces. Thus, each was shaped as a square of 30 mm in side length. Before cutting, the transparent electrode sheet was etched leaving a central stripe of exposed glass to prevent a short circuit in the cells, in case the measuring pin pierced the top electrode. Each of the samples contained twelve devices, half of them mirrored along a vertical line of symmetry as displayed in figure 3.2. The ground pins were localized on the sides of the square and the measuring contacts, vertically along the centre. Each sample had a maximum active area of 0.1925 cm^2 which was reduced to 0.1024 cm^2 upon the incorporation of a shadow mask on top of the glass side of the sample.

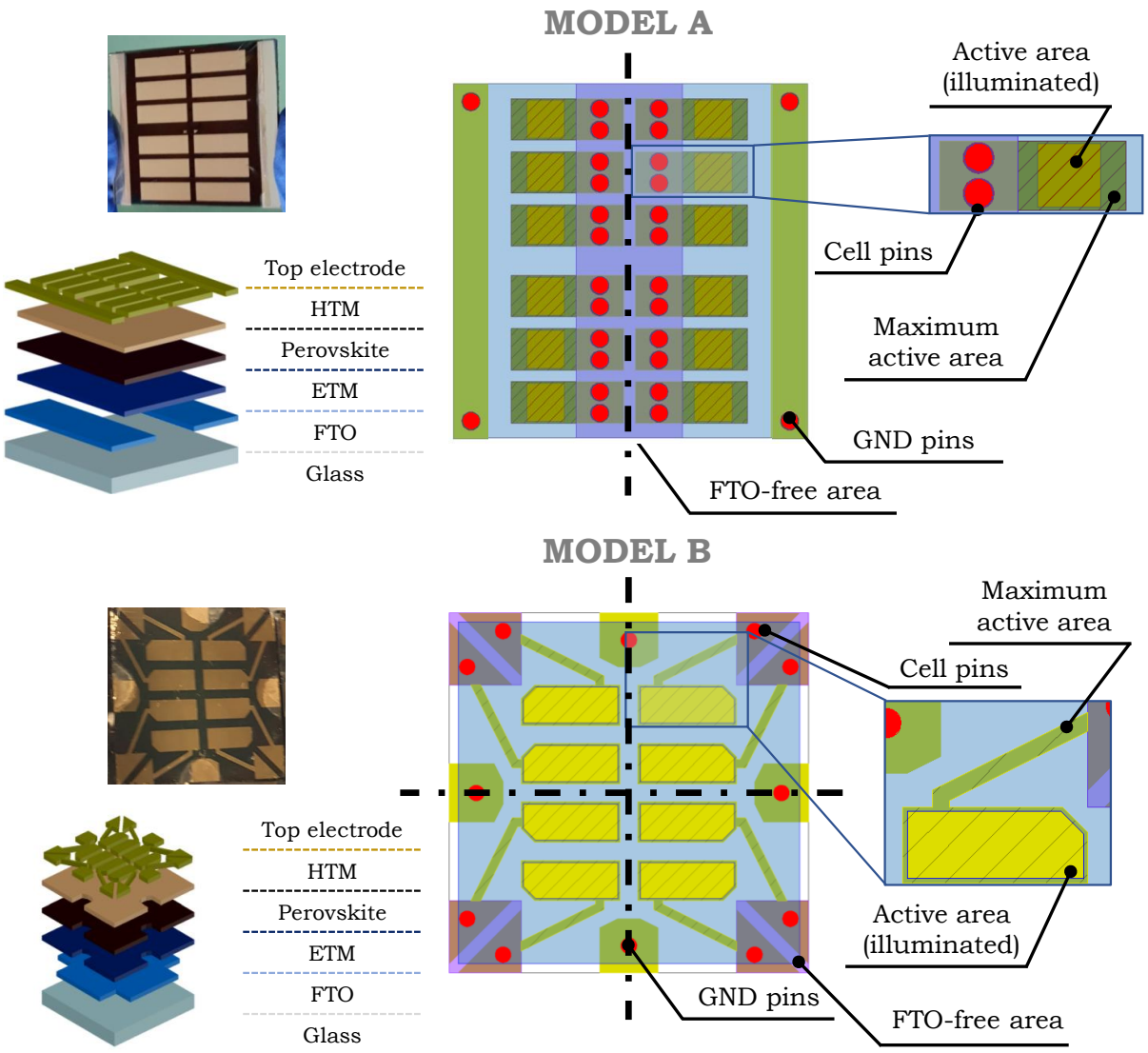

Figure 3.2: Solar cell architecture for model A (top) and model B (bottom).

Model B samples were originally designed to provide a larger number of devices per slide of FTO-glass sheet: 36 samples of 20 mm of square side length. In this architecture, the measuring pins were designed to contact the corners of the cell. Therefore, the FTO layer was patterned in a cross design, leaving etched corners of 4×4 mm. Each sample contained a total of 8 symmetrical cells along both the horizontal and vertical axis marked in figure 3.2. The four ground pins contacted the sample in the centre of each side of the square. The maximum active area of each device was measured to be 0.1471 cm^2 and the final illuminated area after covering the sample with a shadow mask, 0.1027 cm^2.

3.1.3. Model A: design, fabrication and development

The automated *JV* measuring equipment for model A was achieved through iterative cycles of testing and development, starting from the prototype described in figure 3.3 and finalising with the design described in figure 3.4.

For the initial prototype, the measuring base plate was conceived as a single sample holder with a close design to the existing machine at Ludwig-Maximilians-Universität (LMU), provided by Dr Docampo. Both the dimensions of the holder and the electrical design were modified and adapted to the rest of the equipment setup at Newcastle University. Figure 3.3 a shows the final assembly of the prototype. The sample holder was 3D printed in acrylonitrile butadiene styrene (ABS) and comprised two pieces: a base plate holder attached to the PCB and a flat lid bolted to the latter. The lid was conceived to apply even pressure on the sample, enabling a good contact between each solar cell and the electrical pins in the PCB. To ensure a correct fit between the holder and the linear stage, a custom-made box was 3D printed with an equivalent screw pattern to the linear stage gantry plate.

A layout of the printed circuit board is provided in figure 3.3 b. The design was conceived as a 4-wire system, which entangled duplicity of electrical components (pins and multiplexers). The connections between the measuring pins and the external electrical equipment were managed via a 12 wire-to-board terminal block. Power was provided to the ADG706 multiplexers via a 5 V power supply connected to the top 2 pins of the terminal block. Contacts 3 to 7 in the block were externally wired to the Maxibee control board and internally connected to two multiplexers.

The activation and deactivation of the pixels can be easily understood following the 2-wire schematics represented in inset 1 of figure 3.3 b. The multiplexer switched between measuring pixels after receiving a binary code from the Maxibee. Specifically, the EN port (orange line) switched the multiplexer on or off, while the A0, A1, A2 and A3 lines (magenta) provided the required code to open each measuring pin (green lines). When one of the green lines was active, current flowed from the positive pin in the cell to the multiplexer output (blue line) which was connected to the positive connector of the source meter. The circuit was closed by connecting the ground pins to the negative plug of the source meter (black line), allowing the acquisition of the *JV* scan. When operated in 4-wire, the second multiplexer activated the second set of pixels using the same logic described for the 2-wire system.

To comply with the electrical requirements of the multiplexers, their powering was done via a two-resistor voltage divider. In this way, the VDD port received a 2.5 V signal, the VSS port a -2.5 V signal and the ground (GND pin) corresponded to the connection between resistors as depicted in inset 2 from figure 3.3 b.

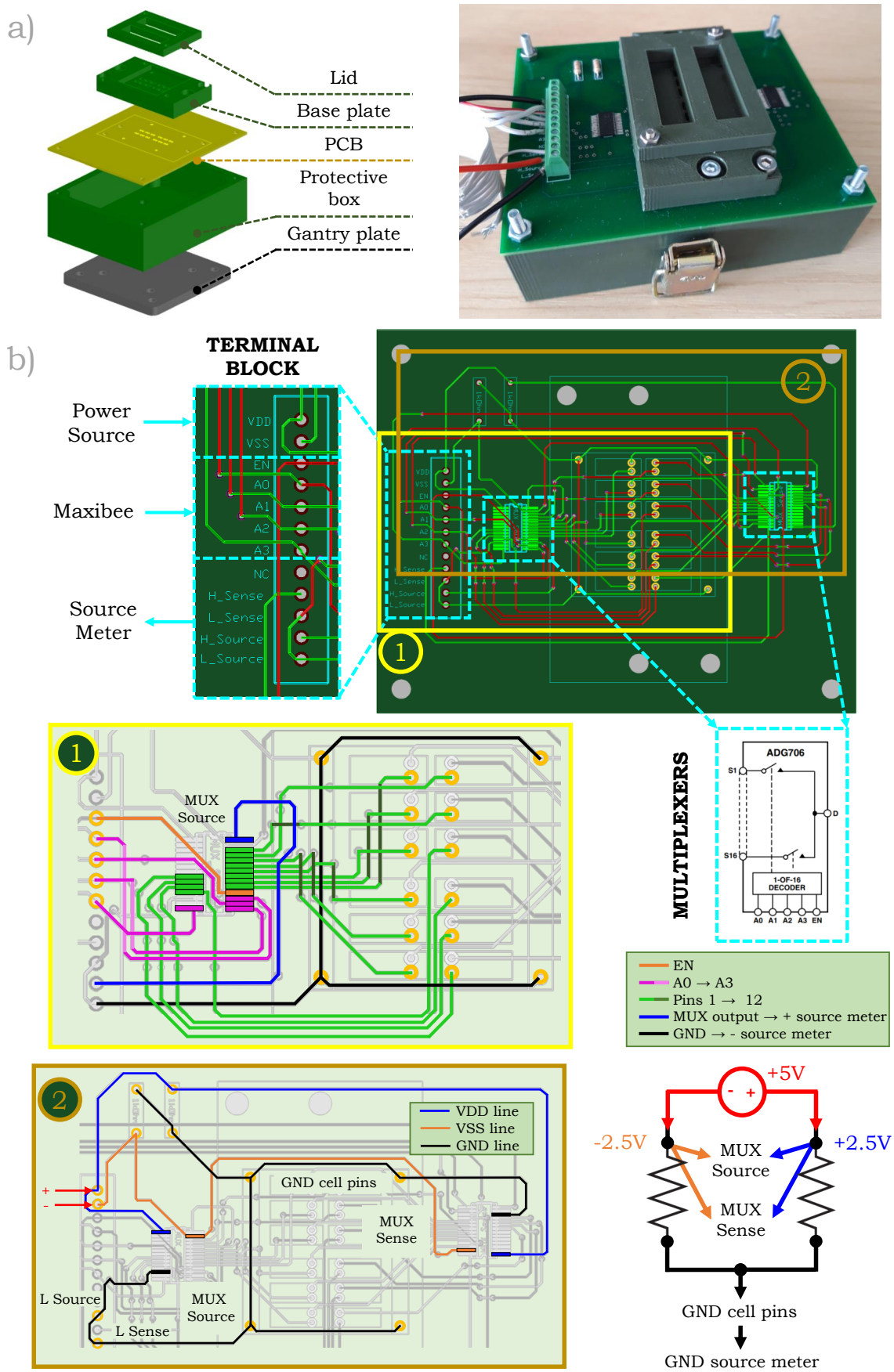

Figure 3.3: Model A prototype base plate (a) and printed circuit board layout (b). Inset 1-b highlights the main connections between the cells and measuring equipment. Inset 2-b describes the power lines in a voltage divider schematic.

In order to speed up the sample loading process, the lid design was modified. Instead of requiring to screw and unscrew the lid every time a sample was measured, the new system allowed the user to just open and close the lid through the combination of a hinge securing the lid to the base plate on one end, and a clasp enclosing the system on the other. The internal part of the lid was designed with an extrusion to provide even pressure between the sample and the measuring pins when fastened. This upgrade was the basis for the final design depicted in figure 3.4 a, where the sample holders were 3D printed in ABS and the protective box was fabricated in aluminium. Here, a modular approach was taken into consideration by designing the PCBs with two samples per board with a symmetric layout, so that several boards could be linked together. This allowed the possibility to scale up or down the system (adding or subtracting cells) depending on the availability of the resources. In this particular case, the linear stage was the limiting factor for the number of cells that could be measured, with eight being the top number to fit the stage's length.

Although the basis for the electrical circuitry was kept the same between the prototype and the final design, several modifications were required as noted in figure 3.4 b. Four individual modules were connected laterally and powered by an additional board called Diode PCB. In each individual module, the top part of the PCB was filled with a total of 19 active lines crossing the board from left to right supplying current to the rest of the modules. To control the activation of the multiplexers, the top lateral connectors (inset 1 in figure 3.4 b) provided eight EN lines intercepted by two 8-way DIP switches (one per sample). Sample numbers were assigned in the DIP switches, starting from left to right. The lower connectors (inset 2 in figure 3.4 b) supplied the multiplexers with four code-lines for the selection of the measuring pixel (A0 to A3), two power lines (VDD and VSS) and the ground line (GND). The final four active lines in the row connector conducted the signal from the cells to the source meter (H_source, L_source, H_sense, L_sense).

The signal of 19 active lines from the modular PCBs was supplied by the PCB-diode board, located at the right end of the conjunction. As seen in inset 3 from figure 3.4 b, direct connections were established to the Maxibee control board via the top three IDC20 connectors, a double power supply (in a voltage divider schematic) and the source meter. Additionally, a calibrating photo-diode was included in the setup to measure the sunlight intensity provided by the solar simulator before measuring the samples. This connection was controlled by the Maxibee and the calibration measurement was performed using the source line of the source meter (H_source).

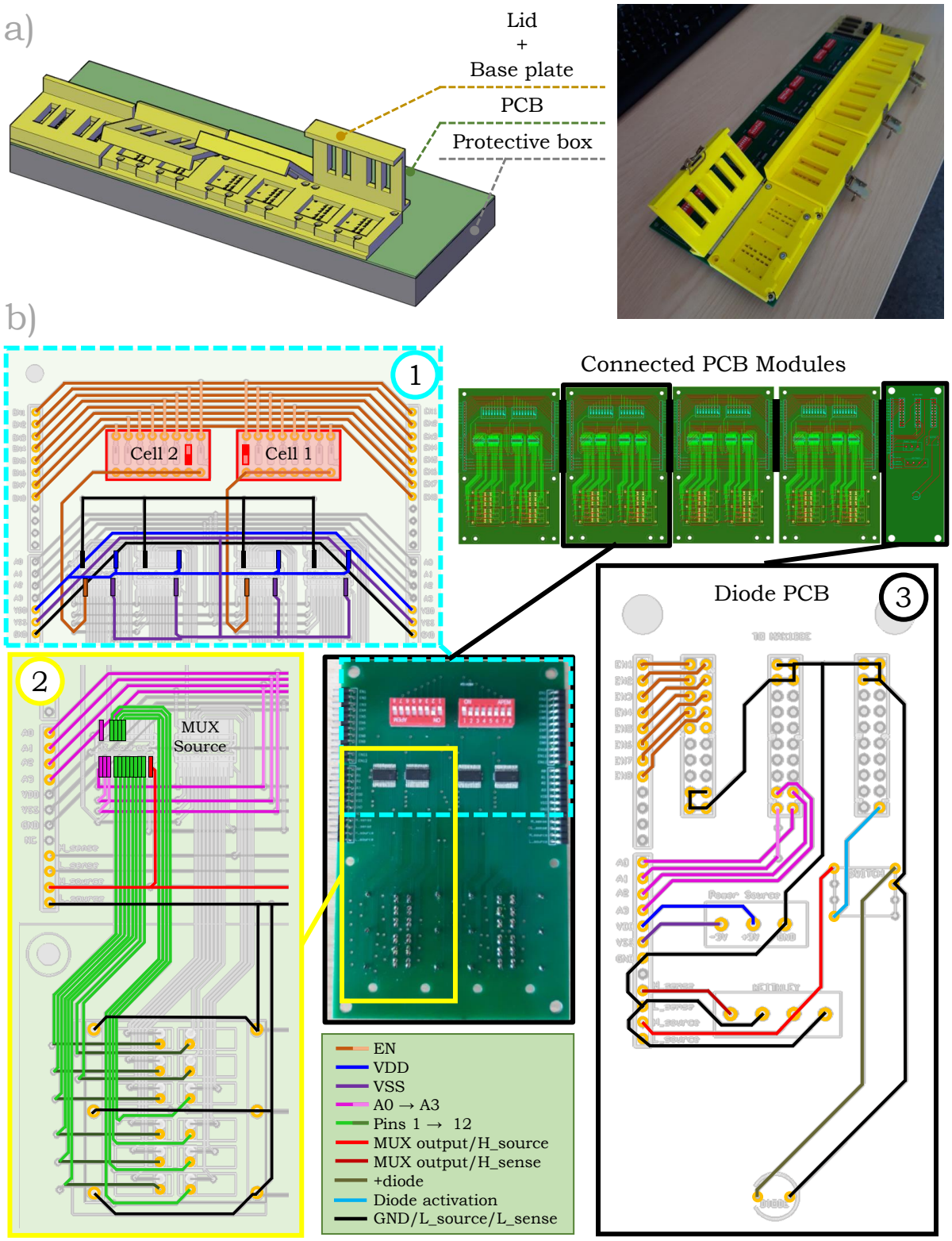

Figure 3.4: Model A final design of sample holder (a) and printed circuit boards (b). Insets b-1 and b-2 detail the connections to the cells. Inset b-3 incorporates a layout of the calibration diode module.

3.1.4. Model B: design, fabrication and development

Model B was conceived as an upgrade of both the cell design layout and the number of devices measured. By reducing the cell size, the number of devices per batch was raised from 192 to 288. To compensate for the increasing scanning time per batch associated with a higher sample number, the new measuring modules were adapted to scan 3 cells simultaneously with a Keysight U2722A source meter. This enabled the measurement of the full batch under 2 h at a rate below 4 min per module.

To address holder durability issues, the design was modified as depicted in figure 3.5 a. The base plate and the lid were redesigned with an in-built hinge system and fabricated from a block of aluminium which increased its bending resistance under normal operating conditions. To limit the weight and cost of this change in material as well as to increase the versatility of the design, the base plate was conceived as an attachable frame to the PCB. This enabled the fit of different 3D printed insets adaptable to a variety of cell layouts (figure 3.5 a).

In this new design, the electrical connections of the PCB were also reconsidered to increase the equipment's robustness and durability. The multiplexers were substituted by relay boards to reduce the failure risk due to a current spike. With a maximum switching current of 10 A, the relays provided a much more reliable cell switching system when compared to the 100 mA of maximum peak current of the multiplexers. To enable the activation and deactivation of the JV scan per sample, a second relay board controlled by the Maxibee was incorporated as outlined in figure 3.5 b. The Maxibee activated the first relay board, enabling three relays at a time, corresponding to the three samples included in the module. Then, the activated relays supplied current to three different relay boards with eight relays linked to each solar cell in the sample. The activation and deactivation of these secondary relays enabled the individual solar cell selection in each sample, with the aid of a second connection coming from the Maxibee control board.

3.1.5. Design challenges and future prospects

While 3D printing provided a faster and cheaper alternative to metal work in the manufacturing of Model A holders, the use of unoptimized parameters during the printing resulted in the creation of weak spots that compromised the equipment's durability when wrongly operated. In particular, the excess strain induced in the lid system when samples were misfitted in the base plate indentation (see figure 3.6), induced a progressive bending behaviour in the lid. This operation unevenly reduced the pressure applied to the sample resulting in a worsened contact between electrodes and measuring pins in certain areas. Eventually, the repeated operation weakened the joint over time leading to fracture.

Although the cause of the breakage could be traced to user malpractice, the incorporation of a stronger frame to the holder could have prevented the final rupture. Consequently, two main alternatives were considered to solve this issue. The first one involved

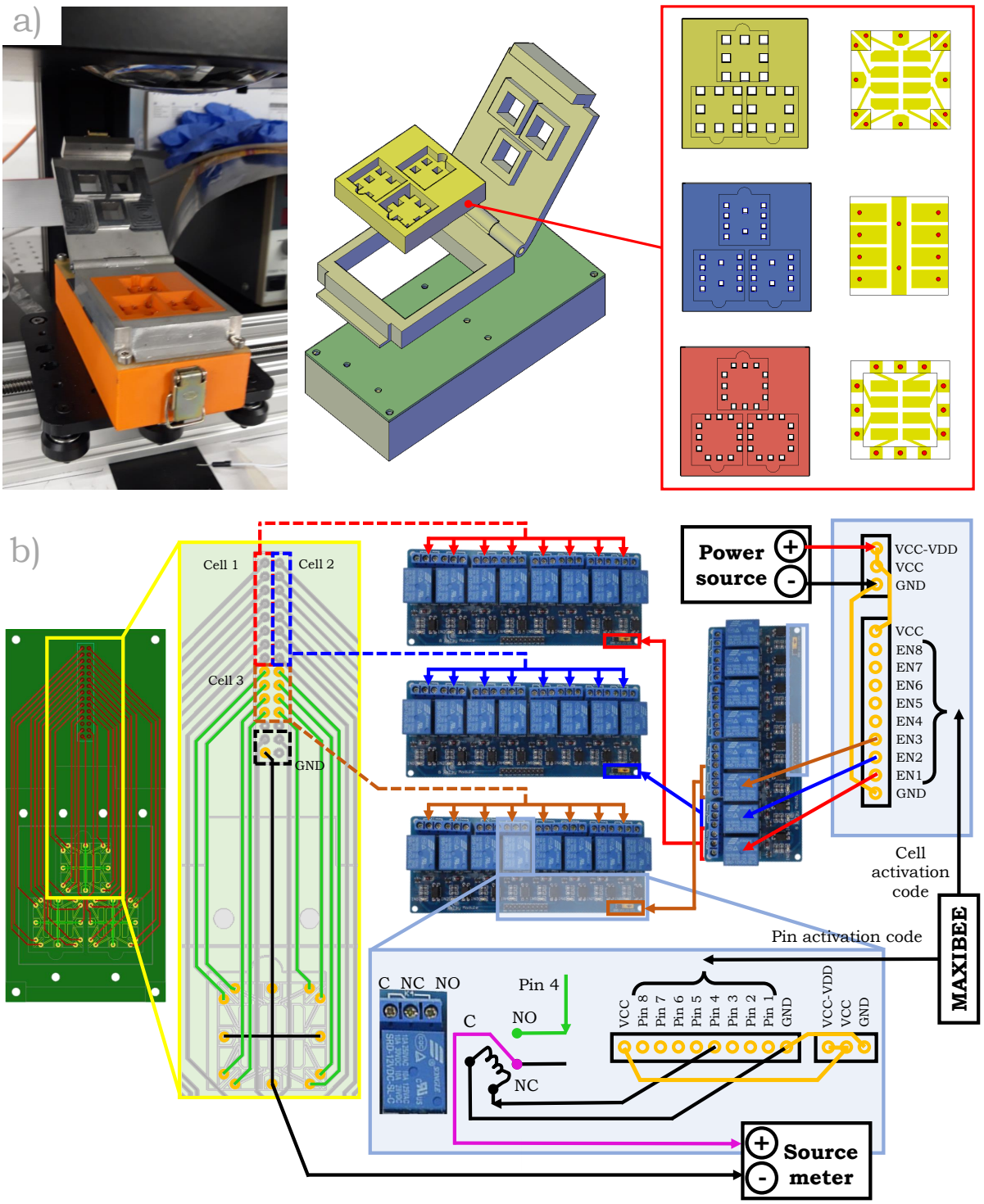

Figure 3.5: Model B holder design with adaptable insets for different solar cell configurations(a) and printed circuit board layout with main connections (b).

both increasing the depth of the base plate indentation and increasing the infill percentage of the 3D print. In this way, the chance of the user misfitting the sample would be reduced and the strength of the print enhanced. Alternatively, a change of material from plastic to aluminium could provide the required bending resistance without altering the design. Finally, a combination of a change in design and material was implemented in Model B.

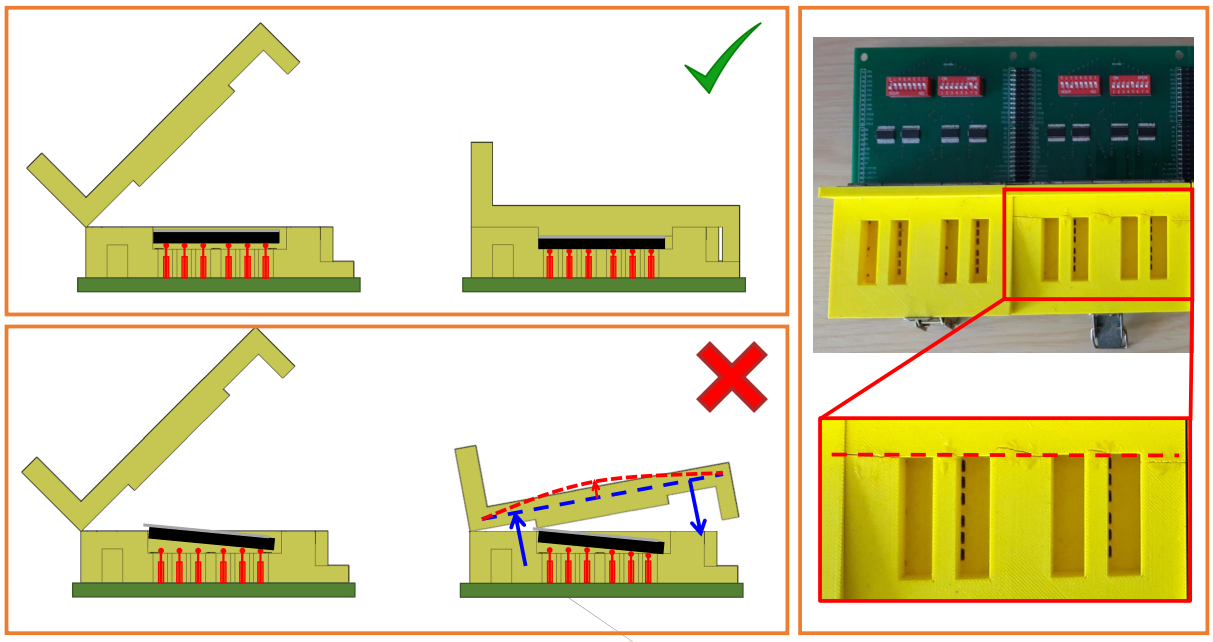

Figure 3.6: Operation of Model A sample holder and breakage points.

Model B represented a reasonable improvement of Model A's design of the measuring equipment. The increased number of devices using the same raw materials significantly incremented the number of variables that could be tested in each experiment while ensuring enough devices per variable. The symmetrical electrode design enabled the user to fit the device in the holder in four different positions (adapting to the shape and imperfections of the manually cut glass substrate) without affecting the final result. Additionally, the reinforcement of the lid at points of increased strain significantly dropped the chances of holder breakage while the substitution of multiplexers for relay boards reduced the chances of measuring malfunction due to current spikes. However, the design was not exempt from challenges.

Reducing the size of the sample hindered the etching and cutting steps during the fabrication process. A manual etching technique based on the use of commercial tape to cover the final FTO pattern added an error of approximately ± 0.5 mm on the etching line limits. Therefore, the precision of the user during the alignment of the etching line must be impeccable not to affect the final active area of the cells in the sample. Furthermore, the manual scribing and cutting of 3 mm thick glass increased the probability of damaging the corners of the sample, which held the contact area to the measuring pins. Size challenges were also observed in the requirements needed for the electronic design. The proximity between measuring contacts at the corner of the cells required a selection of thinner pogo pins to ensure enough distance between them, so as not to cause a short-circuit. The drawback of this action comprised the stability and durability of the measuring pins, which could bend more easily than their thicker counterparts when the applied pressure was not even.

Future prospects will necessarily require a significant improvement in the fabrication process to avoid the above-mentioned reproducibility issues. For instance, moving from a

manual etch and cut to a laser etch and scribing process would address the imperfections in the corners, leading to the successful measurement of all devices in the sample.

3.2 Hydration chamber

Water is a critical agent in the degradation of perovskite solar cells.[72] Therefore, tracking the evolution of the perovskite structure upon moisture exposure is crucial to assessing both the decomposition routes and the dynamics of the reaction. *In-situ* XRD is often the measurement of choice to explore these decomposition reactions through the use of commercial non-ambient XRD stages, which offer a myriad of measurement conditions (temperature, pressure, humidity, etc).[154,99] However, their elevated prices make the resource out of reach for many research groups. Herein, a simple and low-cost alternative is presented to quantify *in-situ*, the effects of high humidity environments in perovskite films. To do so, the simplest method for humidity control was used: the incorporation of deionized water into an enclosed atmosphere. The enclosed environment was achieved with the chamber's design, introduced in the following section.

3.2.1. Design, fabrication and operation

The design of the chamber was made to fit the spatial conditions of the equipment. As such, the chamber was fabricated in two main pieces: an indented base plate, vacuum-attached to the motorized stage of a *Bruker D8 Advance* diffractometer, and a tight-fitting semi-transparent lid to provide the enclosed atmosphere (figure 3.7 a). The chamber was entirely made of aluminium and a knife was included to remove the direct signal of the beam impacting the detector at low angles. Figure 3.7 b shows the equivalence in the obtained diffraction patterns of fluorine-doped tin oxide (FTO) at low angles with the chamber's knife and with the instrument's knife.

Although simpler designs can be used to create an air-tight atmosphere, such as reseal-able transparent plastic bags, they come with the disadvantage of providing an additional XRD print. This signal, although minor when analyzing highly diffractive samples such as $MAPbI_3$, can hinder the reflections less crystalline samples like $Cs_2AgBiBr_6$. Thus, a thin polyimide film (Kapton) was selected to cover the metallic frame of the chamber. This material, despite reducing the intensity of the diffraction peaks of a $Cs_2AgBiBr_6$ film on FTO, barely showed any contribution to the scan. On the other hand, polyethene terephthalate (PET) and high-density polyethene (HDPE) films significantly hid the sample's diffraction pattern (figure 3.7 c).

To perform the measurement a three-step method was implemented. First, the base plate was vacuum fixed to the motorized stage of the diffractometer and the sample fit into the base plate central indentation with double-sided tape. A vertical and tilting alignment of the sample and base plate conjunction was performed with the diffractometer stage as

routinely done for standard film samples. Secondly, the lid was fit on top and a first measurement was taken to record the initial XRD pattern. Then, the hydrating solution was introduced either in a vial lid or distributed across the metallic plate with a pipette, and the sample was enclosed. Finally, a recurring program of measurements was set in the diffractometer software to acquire XRD patterns over time.

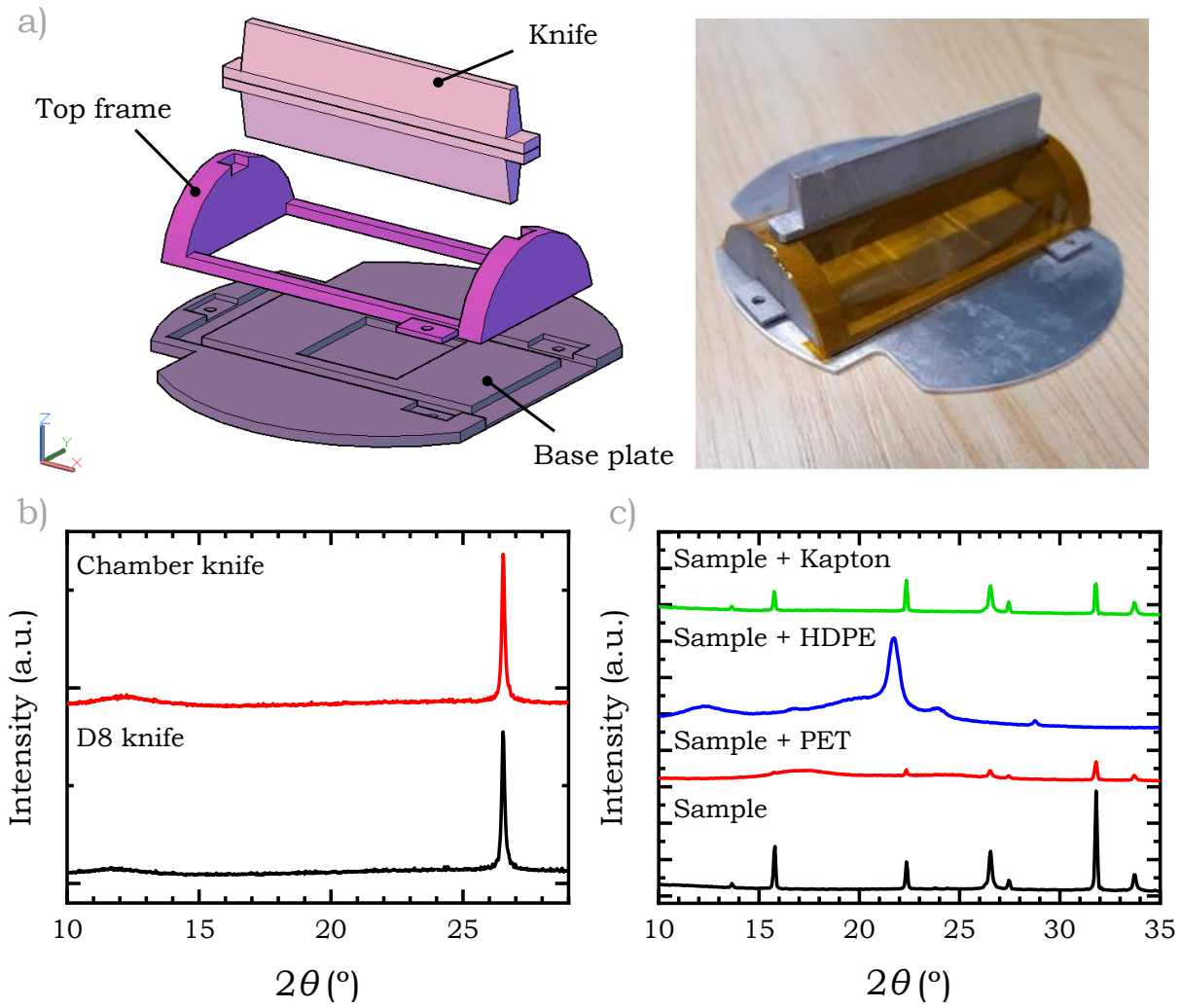

Figure 3.7: a) Hydration chamber setup. b) XRD pattern of FTO film with instrument knife and chamber knife. c) Comparison of XRD signal of $Cs_2AgBiBr_6$ film with PTE, HDPE and polyimide (Kapton) covers.

3.3 Pixel colour tracking (PCT)

Perovskite thermal degradation can be tracked by quantifying the amount of lead iodide appearing in a sample.[72] An accurate way of determining this is by observing the evolution of the sample's XRD pattern while exposing it to high temperatures over time.[178,138] However, the accessories required to perform this measurement in a standard diffractometer very often compromise the price of the resource. Alternatively, the formation of PbI_2 in black perovskites such as $MAPbI_3$ or $CsFAMAPb(IBr)_3$ can be tracked *in-situ* by quantifying the appearance and growth of its characteristic yellow spots without the need

for expensive XRD accessories.[168] Notwithstanding this, taking a final XRD scan of the degraded samples is recommended to ensure the proper distinction of side phases with similar chromaticity. Herein, a low-cost Arduino-based colourimetric instrument designed to track thermal degradation *in-situ* in perovskite films under different environments is presented.

3.3.1. Colourimetry and image processing

Before providing details on the instrument's characteristics, it is crucial to understand the insights of colour acquisition from a commercial phone camera and how it is digitally displayed. A digital image is formed through the conjunction of a minimum of three n x m arrays superimposed, representing the LED colours red (R), green (G) and blue (B). The number of columns (n) and rows (m) represent the width and height of the image using pixels as the counting unit as displayed in figure 3.8. Each array displays an intensity value ranging from 0 (least saturated) to 255 (most saturated). The superposition of the intensity values in each RGB array enables the formation of over 16 million colours in a digitally displayed image, providing a relatively good chromatic representation of reality.

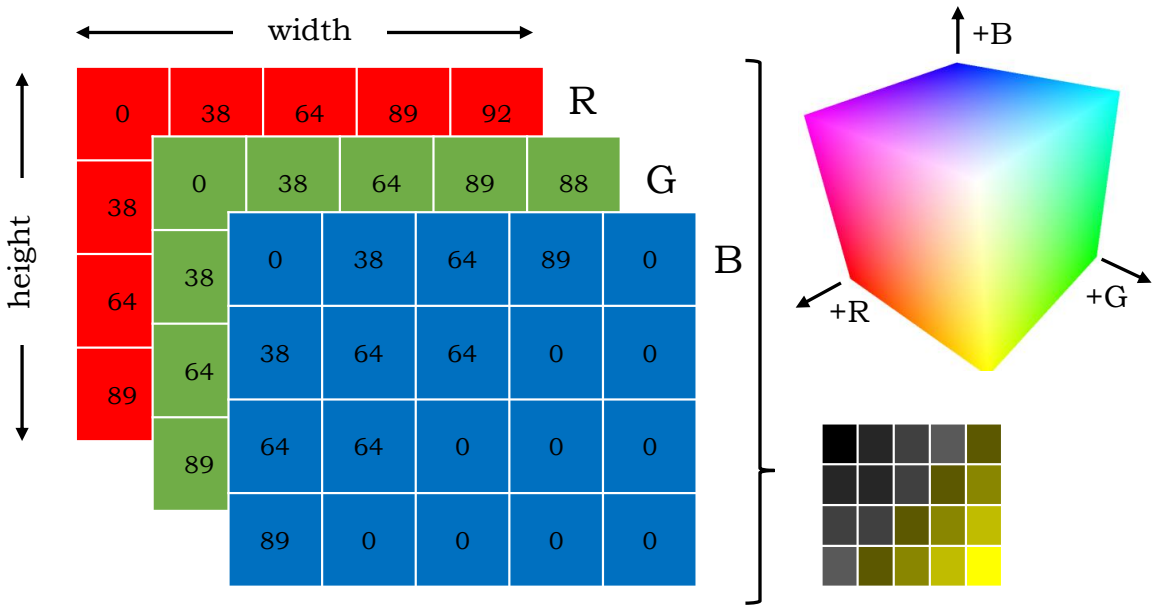

Figure 3.8: RGB scale and channel arrays. RGB cube adapted from[245].

The aim of this experimental setup was to capture the chromatic evolution of perovskite samples over time when exposed to a degrading agent (high temperature) as they transition from black to yellow (highlighting the presence of PbI_2). Although this change is visible to the naked eye, a more accurate approach can be taken by looking at the evolution of the above-mentioned intensity RGB values of each pixel in each frame, presuming they would evolve from (0,0,0) (black) to (255,255,0) (yellow). These intensity values in the samples are influenced by the light conditions of the image acquisition, the quality of the camera and the reflectivity of the samples. Therefore, this measurement was designed

to track relative changes in the colour of samples measured in the same or very similar conditions.

3.3.2. Description and operational procedure

The experimental configuration of the PCT equipment can be divided into two parts: a sensor that controls the optical degradation of the perovskite samples (phone camera) and a set of sensors that control the conditions of the degrading environment (temperature and humidity) as depicted in figure 3.9. The camera was configured to stream video to the computer via either Wifi and/or USB while the Arduino-controlled humidity and temperature sensors were configured to transmit the data to the computer via Bluetooth.

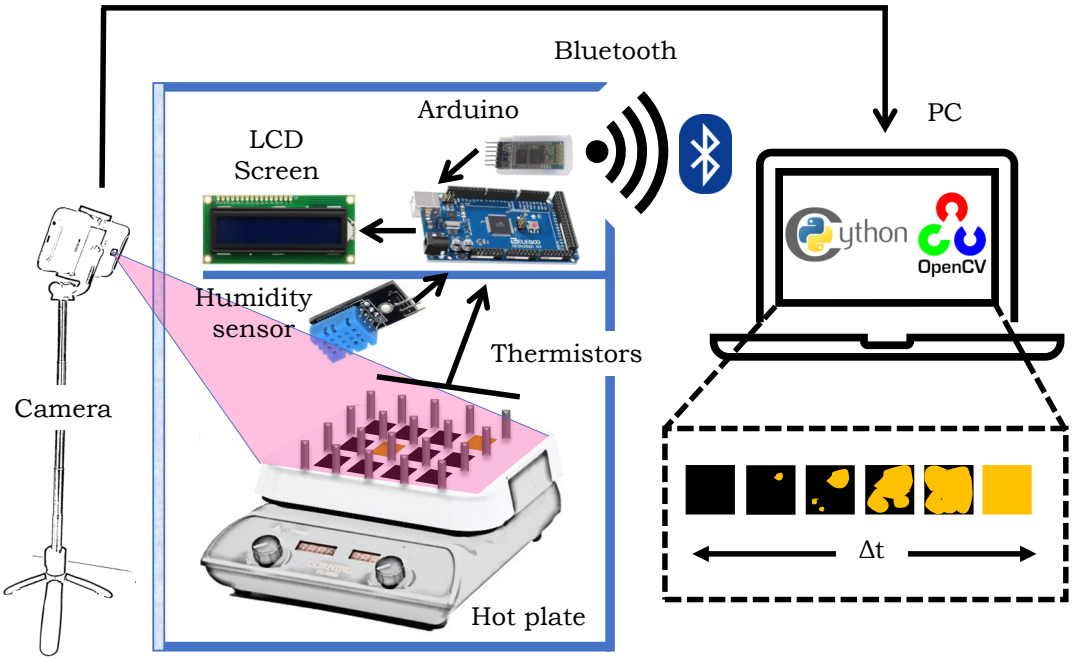

Figure 3.9: Experimental setup for pixel colour tracking (PCT).

The hardware was connected via a custom-designed PCB inserted on top of the Arduino board. The latter, represented in figure 3.10 a, was powered by a 9 V power supply connected to the Arduino power module and the printed board providing two voltage lines: a 3.3 V and a 5 V with shared grounds. The designed PCB incorporated a maximum of 12 thermistors connected via a 2-pin JST (Japan Solderless Terminal) connector, which enabled the easy replacement of the parts in case of device failure. The DHT11 sensor was also included in the design to provide relative humidity readings. To give the user an idea of the thermal variation within the hot plate and therefore provide guidance on where to place the samples, temperatures were displayed on the LCD screen. Both temperature and humidity values were sent via the hc05 Bluetooth module and printed to the Arduino serial monitor of the PC.

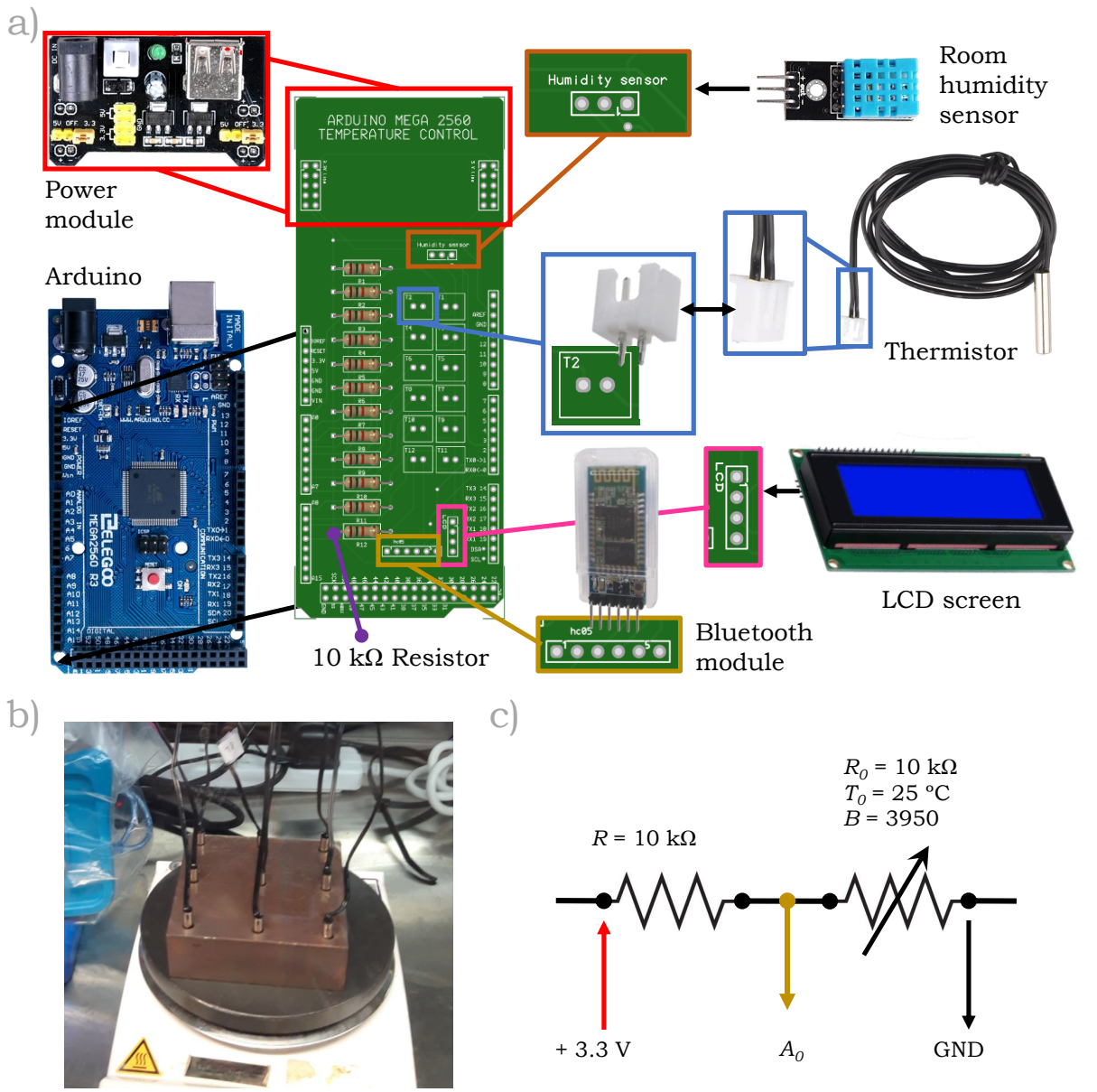

Figure 3.10: PCT Arduino general setup (a) and temperature control system composed of hot plate and NTC thermistor array (b) with functioning diagram (c).

A copper block was incorporated into the design to ensure a homogeneous distribution of the heat in the hot plate, which was measured by a 3×3 array of NTC thermistors inserted into the metal as shown in figure 3.10 b. The values of temperature were obtained from the NTC thermistors through their change of resistivity with heat. As the temperature increases, the resistance in the thermistors decreases, allowing more current to be passed through. Each of them was connected in series with a 10 kΩ resistor to the power supply from the Arduino in a voltage divider schematic, and the voltage drop was measured between the resistors via the analogue pin as shown in the diagram in figure 3.10 c. The micro-controller read this value (V_i) through a 10-bit analogue to digital converter (ADC), which can detect 1024 (2^{10}) discrete analogue levels. Hence, the ADC reading was the result of the operation in equation 3.1, being V_{Aref} the analogue reference voltage. For the given circuit, assuming the logic voltage (V_{cc}) is equal to the reference

(V_{Aref}), the terms cancel each other and the resistance value can be obtained as shown in equation 3.2.

$$ADC = V_i \cdot \frac{1023}{V_{\text{Aref}}} \tag{3.1}$$

$$ADC = \frac{R}{R + 10\,\text{k}\Omega} \cdot V_{\text{cc}} \cdot \frac{1023}{V_{\text{Aref}}} \Rightarrow ADC = \frac{R}{R + 10\,\text{k}\Omega} \cdot 1023 \tag{3.2}$$

The ADC reading was then transformed into a resistance value (R) and finally to temperature (T) with the Steinhart-Hart equation (3.3), a, b and c being the characteristic parameters of the device. Due to the complexity of this equation, an approximation was used with c=0 and the B parameter given by the manufacturer (equation 3.4). The latter is characteristic of the thermistor and is given for a temperature (T_0) of 25 °C and resistance (R_0) of 10 kΩ. To improve the quality of the readings, the B values were calibrated for all thermistors using an ice bath.

$$\frac{1}{T} = a + b \cdot \ln(R) + c \cdot \ln^3(R) \tag{3.3}$$

$$\frac{1}{T} = \frac{1}{T_0} + \frac{1}{B} \cdot \ln\left(\frac{R}{R_0}\right) \tag{3.4}$$

To increase the accuracy of the temperature readings, the thermistors were connected to the 3.3 V power line instead of the 5 V since it is generally subject to less noise and interference. Additionally, voltage readings were averaged every 10 ms to provide final temperature results displaying less variation.

The presence of ambient moisture was controlled through the DHT11 sensor, which included an 8-bit micro-controller that directly outputs values of relative humidity between 20-80 % with an accuracy of ±5 %. The underlying mechanism for this sensor was also based on a resistance change between two materials: two electrodes and a moisture-holding substrate. Variations in humidity changed the conductivity between the substrate and electrodes, generating a change in resistance that was measured and processed by the integrated circuit, which provided the final reading.

3.3.3. Data acquisition and processing

The data collection both from the Arduino-powered sensors and the camera was performed through a Python-based application. The user interface was created using the *tkinter* module, as depicted in figure 3.11 a. Here, the Bluetooth transmitted data was printed to the Arduino serial monitor, read and saved using the port provided by the user. Pressing the *Connect* button triggered three actions simultaneously. The first two enabled the reading of the serial port by Python and the identification of each sensor meter with a time stamp. The third one live-streamed the images captured by the phone camera to the PC via either USB or an IP address (Wifi) aided by the *DroidCam* App (figure 3.11 b),

while the Python module *OpenCV* stored the receiving video to a file. The *Save* button stopped the video and the sensor data acquisition while saving the received data to an *.avi* and *.txt* files, respectively. The Python app could then be exited by pressing the *Disconnect* button.

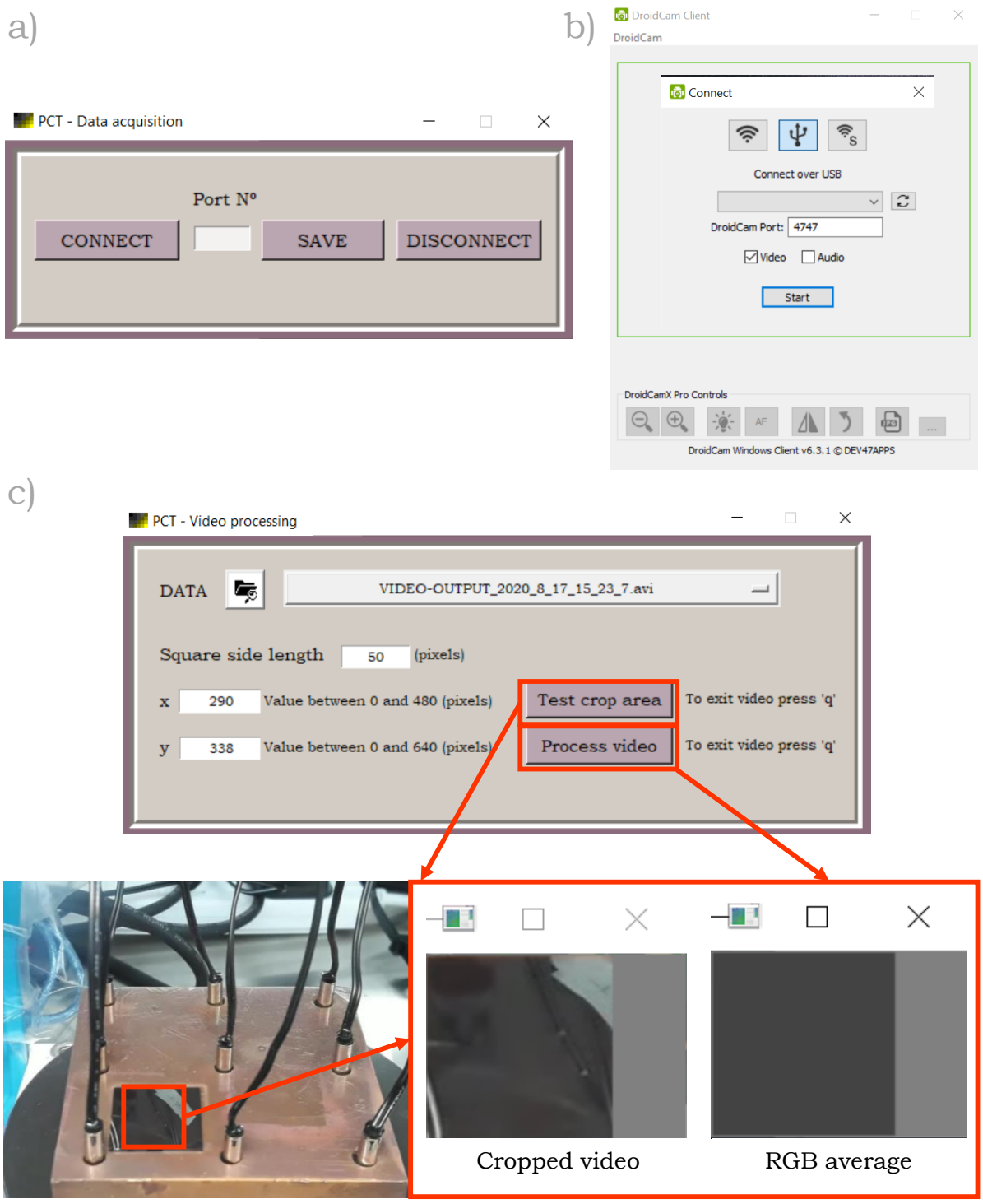

Figure 3.11: a) Python application for PCT data acquisition. b) *DroidCam* App. c) PCT video processing application with outputs.

Once the video was collected, a pre-treatment of the data was performed before analyzing the final RGB evolution. This was done using the second Python-developed application highlighted in figure 3.11 c. Here, the area of the studied sample was selected

using a square of a size determined by the user (in number of pixels) and the position of the top left corner of that square in x-y coordinates. To aid the user in this operation, the button *Test crop area* displayed the cropped video, providing a visual result to determine whether corrections in either the position or the size of the selecting square needed to be made. Once the user was satisfied with the selected area, the data was homogenized by clicking on the *Process video* button. Here, the program calculated the average value for each R, G and B channels for each frame. Average numbers for each channel were calculated first for each row of pixels and then for the set of rows. This operation simplified the data by returning only one colour per frame which was tracked with time. Additionally, this enabled the homogenization of colour within the sample to remove the contribution from defects in the spin coating of the perovskite film or from reflections on the sample's surface.

A third Python application compiled all the data collected from the sensors (temperature and humidity) and the processed video and displayed the degradation results in a comprehensive manner, providing the user with an overall idea of the sample degradation and the degrading environment as highlighted in figure 3.12.

The numerical analysis was performed through the application of three parameters provided by the user: the time at which the sample was placed on the hot plate (*t_start*), the desired time lapse between results (*t_interval*) and the time at which the user wanted to stop the analysis (*t_end*). Once these values had been introduced, the evolution with time of each RGB value was displayed by clicking the *Plot RGB-Grey* button. This action also returned an average of the three channels labelled as *Greyscale*. Additionally, the user could quantify the bleaching of the perovskite film by using the formula originally included in the publication from Lin et al. (equation 3.5).[168] In this paper, a similar approach to the quantification of perovskite degradation was used. They optically tracked the perovskite film degradation by detecting the RGB photobleaching when exposed to a light source of 4000 K with 1 sun intensity. The mentioned formula returned the evolution of the degradation process starting at RGB_0 (the initial value) and displaying the relative value of RGB at each time t (RGB_t). However, the use of this formula is restricted to the sample reaching a full bleached state, since the normalization of the result takes the degraded state as a reference (RGB_{deg}). To display the result of this operation the user had to introduce a reference value: either the original RGB_{deg} by writing 0 in the provided space or a specific colour value in greyscale (e.g. yellow (255,255,0) in greyscale = 170). All the above-mentioned results could be saved as a text file by clicking the buttons *Save RGB evolution*, *Save grey* and *Save degradation*, respectively.

$$\text{Optical degradation} = \frac{|RGB_t - RGB_{\mathrm{deg}}|}{|RGB_0 - RGB_{\mathrm{deg}}|} \tag{3.5}$$

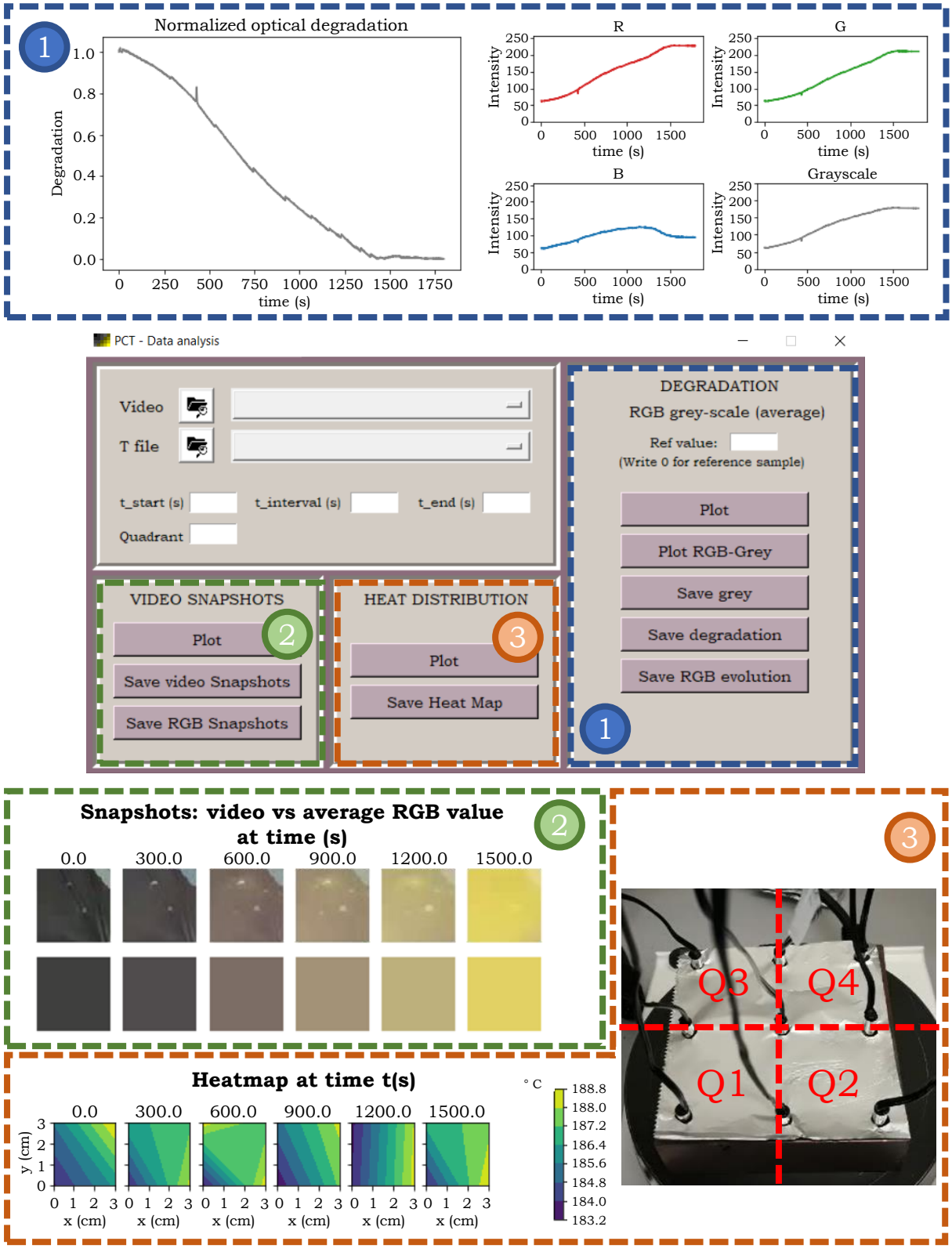

Figure 3.12: PCT data processing application with outputs.

To obtain visual results of the degradation process the program included a section to extract screenshots of both the original and the processed video every certain set of seconds determined by the variable *t_interval*. The user could either display these results on the screen by clicking the *Plot* button under the *VIDEO SNAPSHOTS* area or save them as *.jpg* files by pressing the *Save video Snapshots* and *Save RGB Snapshots* buttons.

Finally, the *HEAT DISTRIBUTION* section of the program enabled the user to plot

a heat map of the copper block area under the sample. To do so, the user would introduce the quadrant number in which the sample had been placed as depicted in figure 3.12. By pressing the *Plot* button, the program selected the data from four thermistors surrounding the sample and produced a temperature distribution map across the 3 cm by 3 cm area every *t_interval* seconds. This data could be saved as a text file by clicking the *Save Heat Map* button.

Chapter 4. Halide perovskite microstrain: Are we measuring correctly?

4.1 Introduction

Partial element substitutions in halide perovskites have been implemented over the years to improve the quality of the devices: from boosting their optoelectronic properties to increasing their stability. However, incorporating elements of different atomic sizes can induce micro distortions through the structure. The impact these distortions have on the lattice and their relationship with solar cell performance and phase stability is yet not fully understood.

Generally, higher microstrain values have been associated with larger defect concentrations. Snaith et al. correlated non-radiative recombination losses in devices with increased local distortions provoked by high proportions of Al^{3+}, Cl^- or Sn^{2+} in the perovskite structure.[302,253,141] Wu et al. reported a similar mechanism when doping $MAPbI_3$ with $Zr(Ac)_4$[316] and the equivalent behaviour has been seen in tin halide perovskites, where selectively mixing the A site to reduce microstrain retrieved better carrier mobilities.[206] However, the opposite has also been noted, where the incorporation of small amounts of Sr^{2+} and Mg^{2+} into the $MAPbI_3$ structure passivated the optoelectronic defects despite increasing their microstrain value.[233] It has been found that charged defects causing non-radiative recombination can be tracked to local heterogeneous-strain distributions induced by the processing conditions of perovskite films.[123] Yet, Frohna et al. pointed out the role of nanoscale strain variations to be of minor influence in the optoelectronic response of mixed perovskites compared to the effects of compositional disorder.[83] Thus, it is not clear whether a direct relationship between higher values of microstrain and a worsening of the optoelectronic properties can be made. In fact, mixed perovskites with similar values of microstrain have reported different optoelectronic responses depending on whether the substitution had been done on the A-site or the X-site.[279]

This dichotomy is also observed regarding the stability of perovskites with competing non-photoactive phases at room temperature. $FAPbI_3$ has been reported to present high values of microstrain in an anisotropic distribution, which has been thought to be the driving mechanism in the transformation from the α phase into the δ phase. In this case, the incorporation of elements such as Cs^+, MA^+, methylenediammonium (MDA^+), Cd^{2+}, Cl^-

or Br^- stabilized the photoactive phase by lowering the microstrain values.[343,352,325,136,252] Yet increasing the structural distortion in $CsPbI_3$ with Bi^{3+}, Eu^{3+} or excess CsBr also allowed the photoactive phase to last longer.[100,116,165]

Interesting hypotheses can arise from these contradictory results. Can the distribution of the microstrain along certain sets of crystallographic planes influence the optoelectronic properties of halide perovskites and/or their phase stability? Unravelling this conundrum, however, requires resolving a preceding question: can we trust the reliability of the state-of-the-art methods used in the calculation of halide perovskite microstrain?

In this work, the validity of the halide perovskite XRD microstrain results reported both in the literature and in the lab using integral breadth methods is analysed. The recurring presence of a significant error at low 2θ angles is highlighted: parallel planes displaying different values of microstrain; a clear breach of the constraint imposed by the Wilson-Stokes approximation. The origins of this disparity are explored by first minimizing the instrumental errors associated with the diffractometer configuration and then optimizing the fit of the instrumental curve using several reference materials. Despite the instrumental error minimization, the parallel plane decreasing microstrain trend in $MAPbI_3$, $MAPbBr_3$ and $CsFAMAPb(IBr)_3$ perovskite thin films was found to remain, suggesting the presence of non-linear microstrain distribution in these materials.

4.2 Integral Breadth (IB) methods and the Wilson-Stokes approximation

A material's microstrain (ε) reflects the existing distortions in the crystal lattice induced by defects in the structure. These non-uniform local distortions produce variations in the interplanar spacing, which along with crystallite size, manifest as a broadening of the diffraction peaks. Integral breadth methods (IB) use this peak broadening to determine the microstructural features following the methodology described in chapter 2. Due to their simplicity, they are the most common technique used in the literature to determine microstrain in halide perovskites, particularly, the Williamson-Hall (WH) plot.[100,325,352,302,14,233]

Limitations of the Williamson-Hall plot have been often discussed in the literature as the basic linear fit does not account for an anisotropic distribution of the strain along the different crystallographic planes. Stacking fault defects in the sample, which can be seen as "errors" in the stacking sequence of the atomic layers (figure 4.1 a), contribute to this anisotropy with peak shifts and a "size effect" type of line broadening that varies between different sets of (hkl) planes.[226,288] This type of anisotropic peak broadening has been observed in the WH plots of Ruddlesden–Popper layered perovskites (figure 4.1 b), due to the presence of stacking faults that increase with layer dimensionality.[288] Alternatives to the linear WH fit have been proposed in the literature to account for this limitation, such as the incorporation of elastic constants using the uniform deformation

stress (UDSM) or the uniform deformation energy density (UDEDM) models, amongst other modifications.[19,187,286]

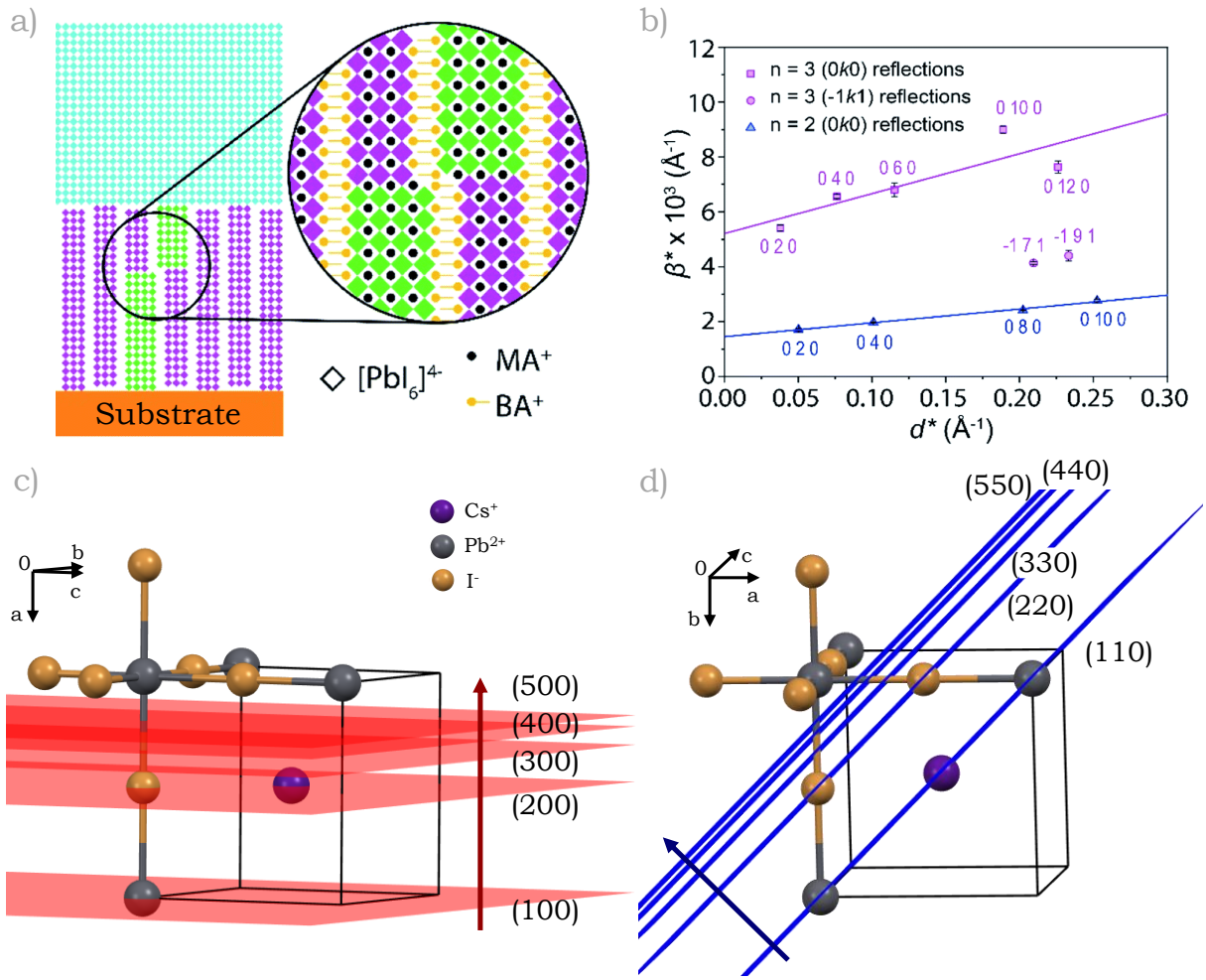

Figure 4.1: Representation of stacking faults in 2D perovskites (a) causing an anisotropic distribution of the microstrain in the WH plot with increasing layer dimensionality (b). Adapted with permission from[288]. Representation of two sets of crystallographic planes: *i·(100)* (c) and *i·(110)* (d) on a $CsPbBr_3$ cubic *Pm-3m* unit cell.

However, even for the case of samples with an isotropic distribution of the microstrain along the different crystallographic planes, IB methods are limited by one more assumption: the Wilson-Stokes approximation.[157] In simple terms, this constraint assumes that there is a negligible strain gradient in a stack of parallel planes such as the ones represented in figures 4.1 c and d. Therefore, the *FWHM* of each diffraction peak is assumed to increase linearly with the order of reflection, which experimentally manifests as parallel planes retrieving similar values of microstrain. This equivalence between parallel planes has been successfully observed in the 1980s in metal film samples using IB methods and standard laboratory diffractometers, reporting differences between them below a 10 % of the value.[61] Given those results, one could assume that the applicability of the method holds for the modern diffractometers used today, provided the compliance of the samples with the Wilson-Stokes approximation. Unfortunately, microstrain values of perovskite films and powders reported in the literature return differences between parallel planes of-

ten above 50 % of their initial value without addressing this disparity,[186,9,14,352,279] which will be discussed in the following subsection.

4.2.1. Non-compliance with the Wilson-Stokes approximation in halide perovskites

Non-compliance with the Wilson-Stokes approximation can be directly observed in the literature when single-line profile methods are used.[186,333] An example of this is displayed in figure 4.2 a, where the microstrain in plane (220) is approximately half the value of the (110) in a $MA_{0.57}FA_{0.38}Rb_{0.05}PbI_3$ perovskite film.[186] For the majority of the literature, however, these changes remain visually hidden in the form of Williamson-Hall plots.[9,14,352,279] Provided the fit with a Gaussian function, microstrain values obtained with the single-line profile formula (equation 4.1) are proportional to the individual data points in the WH plot, as evidenced in equation 4.2. By applying these changes, the WH plot can be transformed into a bar plot of the individual values of microstrain per indexed crystallographic plane.

$$\varepsilon_{(hkl)} = \frac{\beta_{G_{(hkl)}}}{4\tan(\theta)_{(hkl)}} \tag{4.1}$$

$$\Delta d_{(hkl)} = d_{(hkl)} \cdot \varepsilon_{(hkl)} = d_{(hkl)} \cdot \frac{\beta_{G_{(hkl)}}}{4\tan(\theta)_{(hkl)}} \tag{4.2}$$

When the above-mentioned transformation is applied to the WH plots in figures 4.2 b and c, an equivalent trend to the one displayed in 4.2 a can be observed in 4.2 d and e: microstrain in parallel planes decreases with increasing diffraction angle (2θ) (or equivalently, with decreasing d). Interestingly, these results replicate over the literature independently of the type and crystal structure of the perovskite (e.g. $MAPbI_3$ tetragonal versus cubic/pseudo-cubic multi-mixed perovskites) or the format of the sample (thin film versus powder).[186,9,14,352,279] It is important to note that most publications report a thorough application of the standard microstrain calculation procedure, correctly removing the instrumental contribution with the NIST recommended LaB_6 reference sample.[352,279] Therefore, individual malpractice could be excluded as a cause of the observed disparities between parallel planes.

Perovskite degradation upon X-ray beam exposure can also be excluded from being a fundamental cause of the observed microstrain disparities. Although perovskites have been found to degrade proportionally to the X-ray fluence in a synchrotron, this parameter needed to be above 10^{16}-10^{17} photons cm^{-2} to produce damage in the films.[285] Top performing laboratory diffractometers offer X-ray flux densities substantially below $6{\cdot}10^{13}$ photons $cm^{-2}\,s^{-1}$,[272] which reported minimal degradation over a period of an hour in Svanström et al.'s work.[285] Given that a standard scan of the perovskite film requires less than 15 min of exposure to the beam, the effects of X-ray-induced degradation can be

deemed negligible. In accelerated degradation conditions, such as the exposure of a bare $MAPbI_3$ film to a >90 % RH environment, samples only showed the formation of degradation products (hydrate or PbI_2) after 75 min of exposure with XRD scans taken every 5 min (figure B.1, Appendix B). Moreover, the breach of the Wilson-Stokes approximation seems to prevail independently of the perovskite composition both in the literature and in the experimental results contained in this work, which is a critical factor in the appearance of degradation upon heat, moisture, and X-ray exposure.[124,125,295,99,154,285]

Despite the concealment displayed by the WH plots, the effects of microstrain non-equivalence between parallel planes in the final results are critical. This disparity not only affects the average value of microstrain extracted from the slope of the linear fit but also the physical meaning of the result, particularly when negative slopes are obtained.[9,84,269]

A negative slope in a Williamson-Hall plot represents a physically meaningless result: negative microstrain.[16] The slope of the linear fit, provided isotropy in the sample, can be seen as an average of the microstrain contributions from the different crystallographic planes crossing the unit cell. These micro-distortions are extracted from the width of the diffraction peaks in the XRD scan, representing the spread of the distribution of the interplanar distances (d values) for each crystallographic plane. Thus, this must always be a positive value given that a distribution of values can be very narrow, yet never negative.

Often, when negative WH slopes are obtained, researchers tend to attribute the negative sign to a contraction of the interplanar distance.[9,84,348] Although strain can affect the interplanar distance for certain crystallographic orientations, this is not manifested as a broadening of the peak but as a peak shift in the 2θ scale that can, effectively, be identified as a compression of the unit cell (shift to higher angles) or an expansion (shift to lower angles).[127]

Stacking faults are a common explanation behind the appearance of negative WH slopes in the literature.[16] Yet, herein the non-compliance with the Wilson-Stokes approximation is identified as a significant driving factor of negative WH slopes in halide perovskites, as reflected in figures 4.2 b and d. In the original plot (figure 4.2 b), the authors obtained a negative slope in the linear fit of four data points, corresponding to planes (110), (220), (310) and (224) in several samples of $MAPbI_3$ nanowires.[9] Note that the x-axis of the plot was labelled as $4\sin(\theta)$, yet the results correspond to $4\sin(2\theta)$. This change, however, does not affect the relative differences in microstrain between planes nor the sign of the slope, as the microstrain result is mainly driven by the *FWHM* (on the y axis). The transformed plot of one of the samples (figure 4.2 d) points out a reduction in the microstrain value of almost 60 % between the parallels (110) and (220), significantly driving the linear fit in figure 4.2 b to provide a negative slope. Beyond this, other factors can contribute to the obtainment of a negative slope, such as the fact that only half of the peaks in the diffraction pattern were included in the WH plot.[9]

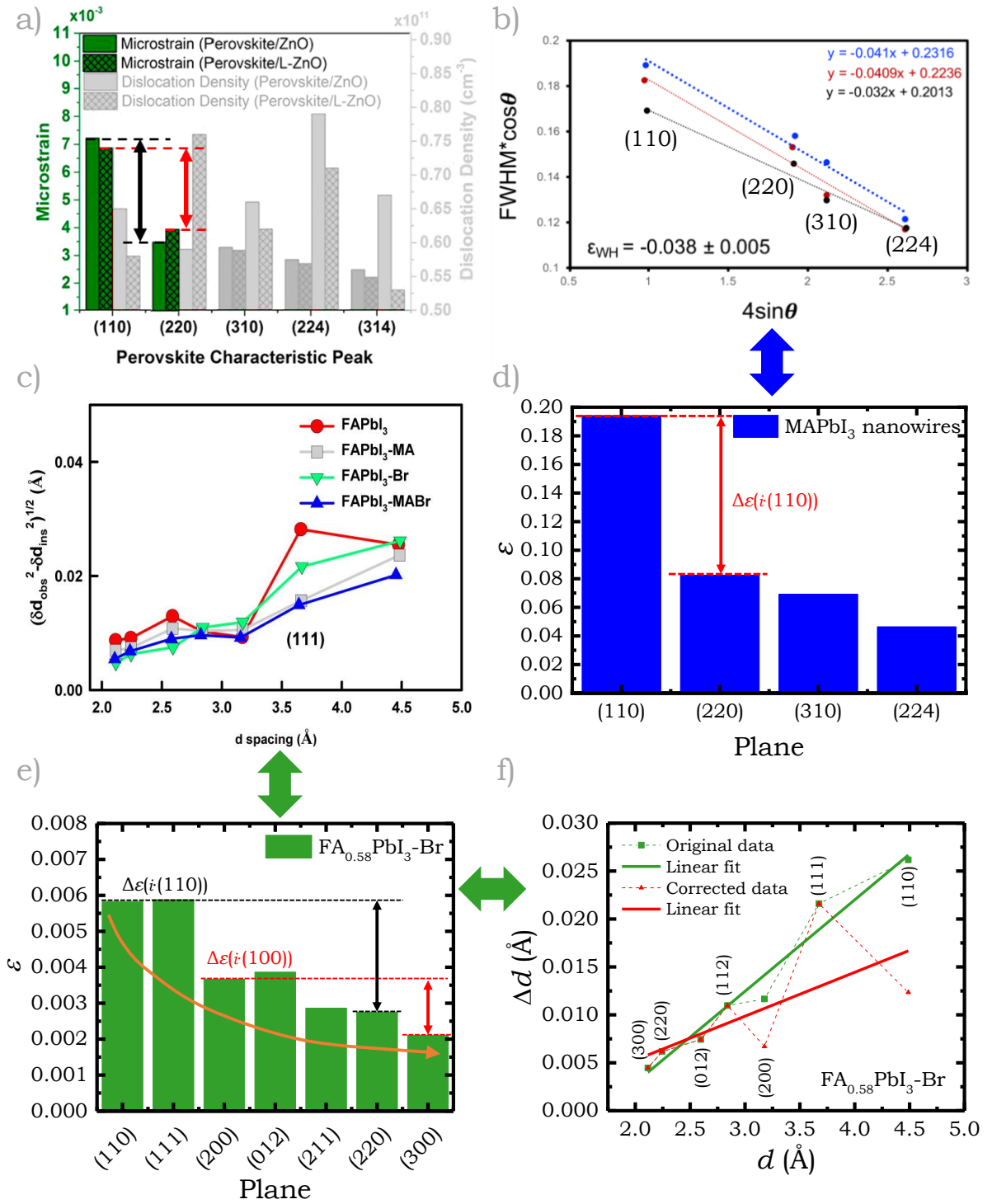

Figure 4.2: a) Highlighted difference in microstrain between parallel planes of $MA_{0.57}FA_{0.38}Rb_{0.05}PbI_3$ perovskite/ZnO and perovskite/Li-doped ETL films. Adapted with permission from[186]. Copyright 2017 American Chemical Society. b) WH plots of axial heterojunction $MAPbI_3$ perovskite nanowires. Adapted with permission from[9] (supporting information). Copyright 2018 American Chemical Society. c) Original WH plot from a $FAPb(IBr)_3$ film. Adapted with permission from[352]. Copyright 2016 American Chemical Society. d) Re-plotted microstrain values (ε) per indexed crystallographic plane of blue sample in (b). e) Re-plotted microstrain values (ε) per indexed crystallographic plane of the $FAPbI_3$-Br sample in (c). f) Original (green) and corrected (red) WH plot of the $FAPb(IBr)_3$ film sample in (c).

Another potential reason impacting the final result could be the resolution of the scan, having an effect on the quality of the peaks at higher angles, where intensity gets reduced and most peak overlapping occurs. In this particular example, no mention had been made to the removal of the instrumental contribution, which could be a reason behind the parallel-planes disparity.[9]

Lastly, the obtainment of positive slopes in the WH plot using its modified version does not guarantee compliance with the Wilson-Stokes approximation nor does it reduces the impact on the results, as evidenced by figures 4.2 c, e and f. The latter shows a correction of the data points (red) of the $FAPb(IBr)_3$ sample from figure 4.2 c (green) by equalizing the ε values for the tuples $i\cdot(110)$ and $i\cdot(100)$, using the numbers of the highest diffraction order. Changes were exclusively made to the planes that clearly reported differences with their parallels, that is the (110) and the (200). Thus, the planes in the graph without a visible parallel ((111), (012),(211)) have been kept constant. As a result of the correction, the average microstrain obtained from the slope got reduced to less than half its original value, from $9.55\cdot10^{-3} \pm 8.7\cdot10^{-4}$ down to $4.58\cdot10^{-3} \pm 2.33\cdot10^{-3}$. Note that the increase in the error for the second fit stems from the large variation between the corrected and non-corrected planes, particularly at low angles.

Considering the previous analysis, two main hypotheses were raised: (i) either the microstrain values in halide perovskites are the result of an accumulated error in the widths of the peaks at low 2θ angles (which tends to be an error-prone diffraction region in standard XRD diffractometers) or (ii) the values are reliable and halide perovskite samples show a microstrain distribution which is truly non-compliant with the Wilson-Stokes approximation. Solving this conundrum is essential to discern whether or not IB methods are suitable for the microstrain analysis of halide perovskites. Samples with a non-linear distribution of *FWHM* along the order of reflection require the use of more complex methods where the Wilson-Stokes simplification is not taken into account, such as the Warren-Averbach, which is based on the application of Fourier transforms of the peak profiles.[20] It is to be noted, that this method is also not exempt from limitations, particularly for complex crystallographic structures with overlapping diffraction lines,[157] such as is the case for halide perovskite samples. Hence, to discern between the aforementioned avenues of thought, the origin of the halide perovskite parallel-plane disparity in the following sections was explored by minimizing instrumental error contributions stemming from (a) the configuration of the XRD diffractometer and (b) the removal of the instrumental contribution with a standard reference sample.

4.3 Results and discussion

4.3.1. Impact of the diffractometer's configuration

As summarized in chapter 2, the diffractometer's configuration affects the profile of the instrumental contribution, which is dependent on the angle of diffraction, the size of the beam (limited by fixed or variable slits) and the quality or format of the sample (sample transparency). For a standard Bragg-Brentano scan, at mid to low angles the contributions to the profile associated with axial divergence, a flat specimen and the width of the detected beam (finite width of receiving slit) are maximum.[39] This reinforces the hypothesis that the origin of the microstrain disparity between parallel planes at low-to-mid angles could lay in the ineffective removal of instrumental aberrations.

Although these could be modelled and removed by deconvolution following a fundamental parameters approach (FPA),[39,193] most of the functions were thought for powder patterns,[80] which limits the function suitability in preferentially oriented thin films. Hence, to specifically assess the impact of the various instrumental aberrations on the peak profiles and microstrain of halide perovskites, samples were scanned in both Bragg-Brentano and parallel beam geometries using various slit configurations.

To compare experimental results with the microstrain values observed in the literature, a first standard Bragg-Brentano XRD scan of a $MAPbI_3$ film deposited on FTO and covered in PMMA was taken. The Cu $K_{\alpha 2}$ wavelet and the background were removed from the pattern as described in chapter 2. Diffraction peaks were individually fitted with a Voigt function and the microstrain was calculated using the Gaussian component of the *FWHM* fit. Calculations were performed without removing the instrumental contribution in order to assess the data as obtained from the instrument. The results were plotted in figure 4.3.

Based on the number of counts, the quality of the scan and the microstrain value, three regions could be identified in the XRD pattern, coloured from lighter (I) to darker (III) blue in figure 4.3 a. The first region was selected between 10° and 22°, the second region was roughly enclosed between 22° and 36° and the higher angle region from 36° until the end of the scan. The $MAPbI_3$ sample was measured at room temperature and therefore it was presented in a tetragonal phase, as highlighted by the presence of the (211) diffraction peak at 23.63°. Perovskite grains crystallized with preferential orientation as revealed by the superior number of counts of the (110) and (220) planes in comparison with the other peaks. This behaviour is characteristic of film depositions. Setting aside the effect of preferential orientation, it was evident that the intensity of the perovskite peaks decreased with the angle of diffraction. With it, the quality of the fit worsened as the peak shapes became less defined. This effect was particularly acute in the third region, where diffraction peaks start to overlap, requiring the use of multiple fits as depicted in figure 4.3 d.

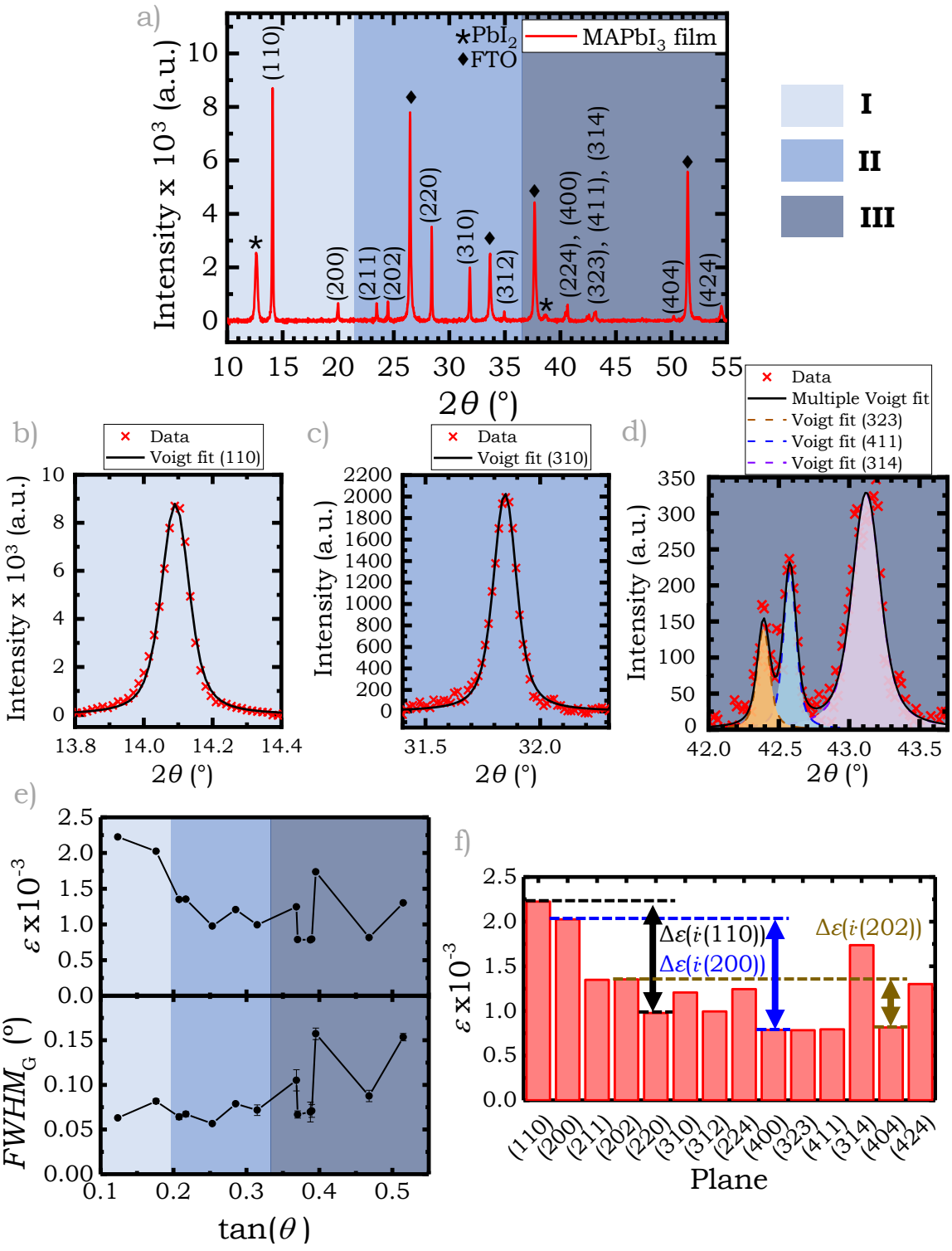

Figure 4.3: a) XRD pattern of $MAPbI_3$ film on FTO divided in three regions (I to III) from light to darker blue. Detail from figure a: XRD profiles of peak (110) (b), (310) (c) and the convolution of peaks (323), (411) and (314) (d) fitted with a Voigt function. e) Evolution of the peaks *FWHM* and microstrain over 2θ from the XRD pattern in figure a, coloured by region. f) Microstrain values from the XRD pattern in figure a, plotted by indexed crystallographic plane. Microstrain disparities between parallel planes are highlighted.

While regions I and II shared similar fit qualities to the naked eye (figures 4.3 b and c), a distinction between them could be made when observing the evolution of the microstrain. Figure 4.3 e represents the *FWHM* and the microstrain of each perovskite peak with the tangent of θ, with the correspondent regions highlighted in the background. Here, it is clear how peak widths remained fairly similar between the low and mid angles, which forced the microstrain to be unusually large at the beginning of the scan. In region III, the uncertainty in the *FWHM* calculation increased as highlighted by the larger error bars, coinciding with the peak overlapping regions. However, microstrain values could be averaged to values similar to the ones in region II. The difference in microstrain between parallel planes is highlighted in figure 4.3 f, where microstrain values are plotted against each indexed plane. Note how the difference between the tuples is much larger between planes whose first peak lays within the first region, such as the (110)-(220) and the (200)-(400), versus peaks starting in the middle region like the (202)-(404). The observed trend (coincidental with results from the literature) pointed to the low angle region as a potential defective zone. Here, several optical effects affecting the beam often contribute to the enlargement of peak widths through the addition of a left tail peak asymmetry.

To assess the impact of asymmetry, a film sample of $MAPbI_3$ deposited on FTO and covered in PMMA was scanned in two configurations: Bragg-Brentano and parallel beam (figure 4.4 a). After removing the Cu $K_{\alpha 2}$ wavelet and the background from the XRD pattern, diffraction peaks were individually fit with a Voigt and a skewed Voigt function to extract peak height and *FWHM*. The asymmetry was quantified by the parameter skew, which reported negative values associated with asymmetry at the left tail of the peaks. In order to facilitate the fitting of the skewed function, the analysis excluded the higher angle region. This was done to avoid areas of high overlapping which can induce additional error when distinguishing asymmetries in partially convolved multiple peaks. To facilitate the comparison in the goodness of the fit (GOF) between peaks of the same pattern with significantly different intensity values, the chi-squared value of the fit (χ^2) normalized to the intensity of each peak (I_{peak}) was used as defined by equation 4.3. Lower numbers indicate a better fit as the disparity between the data values and the fit decreases.

$$GOF = \frac{\chi^2}{I_{peak}} = \frac{\Sigma \frac{(data-fit)^2}{data}}{I_{peak}} \tag{4.3}$$

Peak asymmetry in Bragg-Brentano can be attributed to two instrumental effects: flat sample and axial divergence. Defocusing effects due to sample transparency can be discarded in $MAPbI_3$ given that its linear attenuation coefficient is well above $200\,cm^{-1}$ at the diffractometer's radiation energy (8.04 keV).[310] The scans were taken in fixed slit mode, which kept the angle of divergence of the source beam constant over the diffraction angle. Therefore, both flat sample and axial divergence functions were expected to produce maximum asymmetry at the left tail of the peaks at low 2θ values and decrease with

increasing diffraction angle.[39] In practice, results showed that the evolution of asymmetry in the perovskite film XRD peaks over the diffraction angle differed from the theoretical expectation.

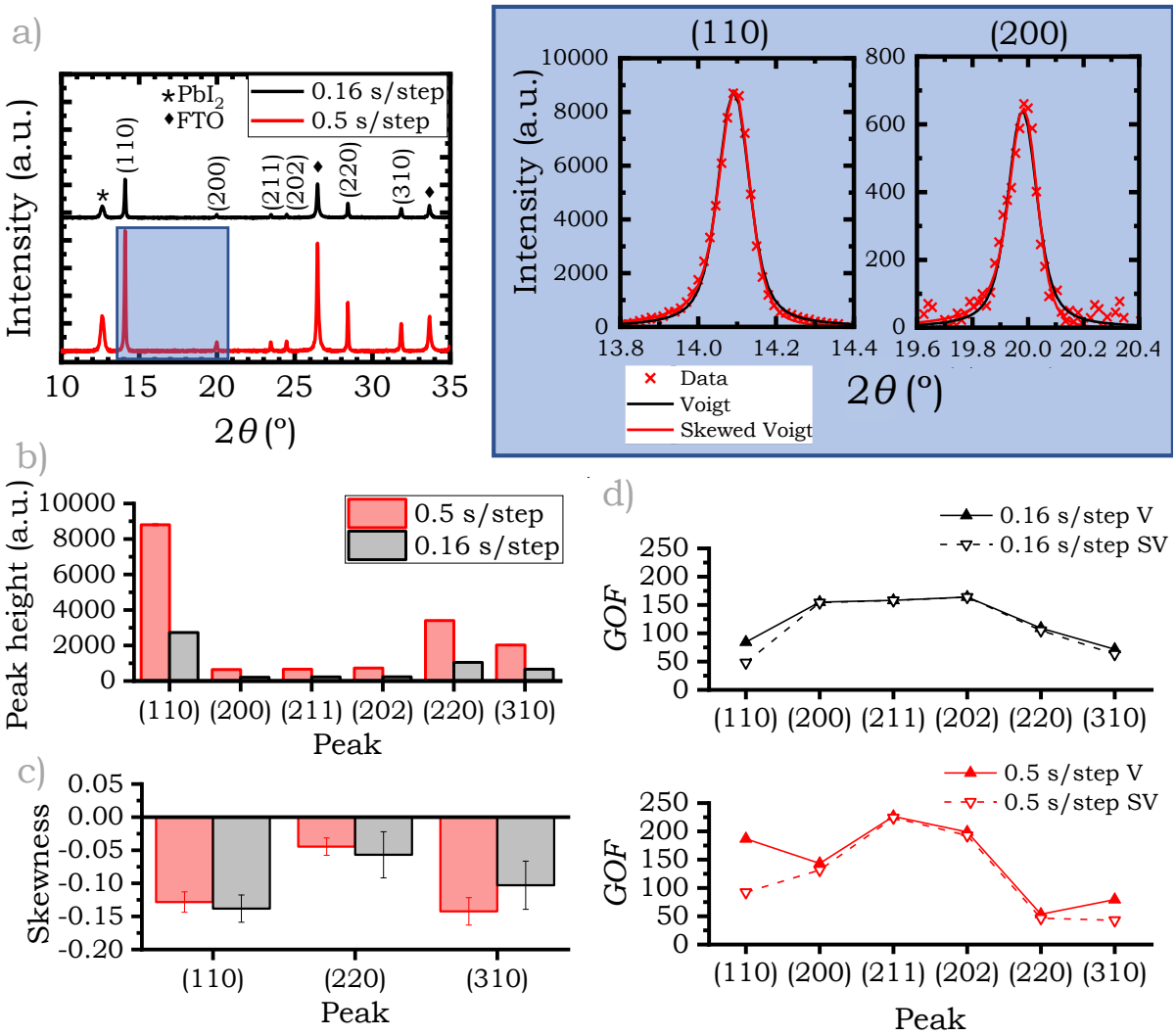

Figure 4.4: a) XRD patterns of $MAPbI_3$ film on FTO taken at a 0.16 s/step (black) and 0.5 s/step (red) scan rate in a Bragg-Brentano configuration. Detail on the data fit with a Voigt and a skewed Voigt function for peaks (110) and (200) in the 0.5 s/step scan. b) Peak height extracted from a Voigt fit of the perovskite diffracting peaks in figure a, plotted per indexed crystallographic plane. c) Skew value obtained from the skewed Voigt fit of the most intense peaks from the diffraction pattern represented in figure a. d) Plot of the goodness of fit (*GOF*) per indexed crystallographic plane using a Voigt (V) and a skewed Voigt (SV) function for peaks in the 0.16 s/step (top) and the 0.5 s/step (bottom) scans from figure a.

The degree of asymmetry in the peak resulted to be more dependent on the number of counts than on the 2θ position. In fact, this behaviour got reinforced when performing longer scans, where longer exposures to the beam increased the number of counts as shown in figure 4.4 b. Figure 4.4 d provides a comparison of the *GOF* in the peaks between a Voigt and a skewed Voigt function both for the 0.5 s/step and the 0.16 s/step scan patterns. Note how peaks of relatively low intensities located at the mid 2θ angles

reported almost identical values. The similitude in the *GOF* parameter between the Voigt and skewed-Voigt fits highlights the lack of asymmetry in the region by deeming unnecessary the use of the skew parameter.

On the other hand, the difference in *GOF* for the strongest peaks between the symmetric and asymmetric fits increased with increasing scan time, demonstrating that, in general, the higher the peak intensity, the closer the shape to a skewed function. An exception to the trend was reported by the (310) peak, as highlighted in figure 4.4 c. Here, the skew values for the strongest peaks in both time scans were plotted. The degree of asymmetry got reasonably reduced with increasing 2θ angle, as depicted by the reduction in the skew value for the (220) peak at 28.42° compared to the (110), located at 14.09°. However, the (310) peak presented a skew comparable to the (110) despite being much further away in the 2θ scale (31.84°) and presenting a lower intensity than the (220).

Yet, the high degree of asymmetry in the (310) does not necessarily account for instrumental effects. As one gets closer to the third region of the graph, the diffraction peaks in the pattern start to overlap. This might hamper the precision of most fitting algorithms, which can interpret the presence of a very small peak as an asymmetry. In perovskite films, preferential orientation during crystallization can reduce or even hinder the diffraction of certain peaks. In the theoretical $MAPbI_3$ powder pattern two peaks overlap significantly at 32°: the (222) recorded at 31.979° and the (310) at 32.114°. The 0.135° difference between them makes distinguishing the convolution between a small (222) peak at 31.71° and the (310) at 38.85° from an asymmetric peak, virtually impossible at low scan rates (figure B.1, Appendix B).

Similar correlations between asymmetry and peak intensity were observed when different parameters of the measurement were changed to boost the number of counts as shown in figure B.2 from Appendix B. For instance, the inclusion of a knife to reduce the background noise at lower angles limited the divergence of the incident beam while plummeting the number of counts in the pattern, which resulted in a reduction of peak asymmetry, as predicted by theory. Further modifications affecting the beam width, such as reducing the size of the secondary slit, were also able to fully remove the asymmetry, yet at the expense of reducing the quality of the signal for the less intense peaks.

On the other hand, in a parallel beam configuration, instrumental effects get reduced to the axial divergence contribution. As expected, this setup removed the asymmetry in all peaks to the expense of heavily reducing the number of counts as highlighted in figure 4.5 a. To achieve a reasonable intensity, the acquisition rate for the parallel beam setup was increased to 3 s/step instead of the 0.16 s/step of the Bragg-Brentano scan. Additionally, the number of data points was increased by reducing the step size from 0.015°/step to 0.010°/step. Figures 4.5 a-c highlight the asymmetry removal for the (110) peak both in the skew and *GOF* values.

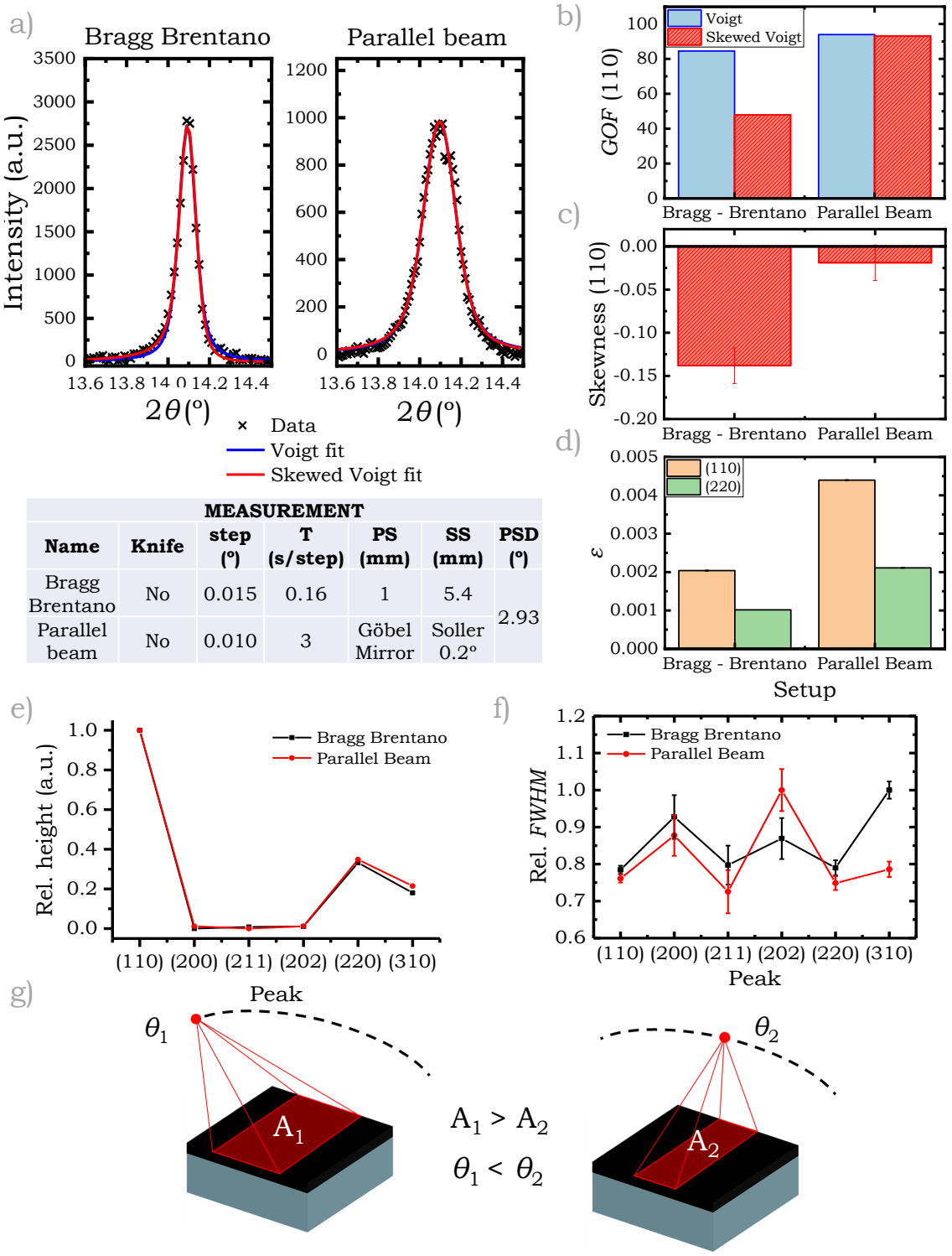

MEASUREMENT						
Name	**Knife**	**step (°)**	**T (s/step)**	**PS (mm)**	**SS (mm)**	**PSD (°)**
Bragg Brentano	No	0.015	0.16	1	5.4	2.93
Parallel beam	No	0.010	3	Göbel Mirror	Soller 0.2°	

Figure 4.5: XRD Results of a $MAPbI_3$ film sample scanned in Bragg-Brentano versus parallel beam configuration. a) (110) diffraction peak fit with a Voigt and a skewed Voigt function. Details of the measurement conditions are located at the bottom of the figure (PS = primary slit, SS = secondary slit, PSD = position-sensitive device detector). b) Plot of the goodness of fit (*GOF*) for peak (110), using a Voigt and a skewed Voigt function. c) Skew parameter for peak (110), fit with a skewed Voigt. d) Microstrain values for peaks (110) and (220). Relative peak height (e) and *FWHM* (f) extracted from the Voigt fit, plotted per indexed crystallographic plane. g) Diagram of the illuminated area of a sample operated with a diffractometer in fixed slit configuration.

Removing the asymmetry, however, did not solve the disparity between parallel planes as reported in figure 4.5 d. Here, the microstrain in the (220) plane remained approximately half the value of the (110) both for the scan in Bragg-Brentano and parallel beam setup. This concluded that the small modifications in the *FWHM* fit caused by asymmetry alone can not be blamed for the huge disparity between parallel planes in the mid to low angles. On the other hand, the difference in the absolute values of microstrain between measurements was attributed to the change in both scan rate and beam configurations.

Interestingly, the microstrain trend similarity displayed between divergent and parallel beam geometries was partnered with an equivalent distribution of the peak intensities and widths despite the significant difference in the number of counts, as shown in figures 4.5 e and f. Note that the main differences between the relative *FWHM* of the scan configurations occurred in the central peaks, which generally displayed lower intensities and a much lower signal-to-noise ratio, particularly for the parallel beam scan. Considering the observed strong correlation between asymmetry and peak intensity in the different scan configurations, the relationship between the peak intensity distribution and the peak widths was questioned.

Peak intensity is related to the amount of material diffracting in a sample and therefore to the scanned area. For both of the above-studied measurements, fixed slits were used, which involved a reduction in the scanned area as the goniometer increased the angle of diffraction, increasing the penetration depth simultaneously (figure 4.5 g). This effect played a significant role in the detection of intensity at the higher angles, which started to decay as the illuminated area decreased. In films, the impact is even more acute since the thickness of the samples rarely surpasses 250 nm. To avoid it, the diffractometer can be set up to provide a relatively fixed illuminated area, that is, the slits will increase their opening degree as 2θ increases to compensate for the narrowing of the beam. Given the stronger correlation that asymmetry displayed with peak intensity, the relationship between intensity and *FWHM* over 2θ was explored by keeping the scanned area constant. To do so, measurements were repeated on the $MAPbI_3$ perovskite film and the results of a Bragg-Brentano fixed slit versus a fixed illumination length configuration were compared using the same scanning conditions of step size and acquisition rate.

By keeping the scanned area constant, the peak intensity distribution along the 2θ axis can be changed (figure 4.6 b). Bragg reflections at low angles, such as the (110) plane, experienced a drastic reduction in height while peaks located further along the pattern, such as its parallel the (220), increased this parameter (figure 4.6 c). Inset of figure 4.6 a highlights how this change improved the definition of the features located at the end of the scan, where most overlapping between peaks occurs. While fixing the illumination area did not fully eliminate the disparity in microstrain values between the parallel planes (110) and (220) (figure 4.6 e), their difference got slightly reduced as the *FWHM* decreased for the 110 and increased for the 220 (figure 4.6 d).

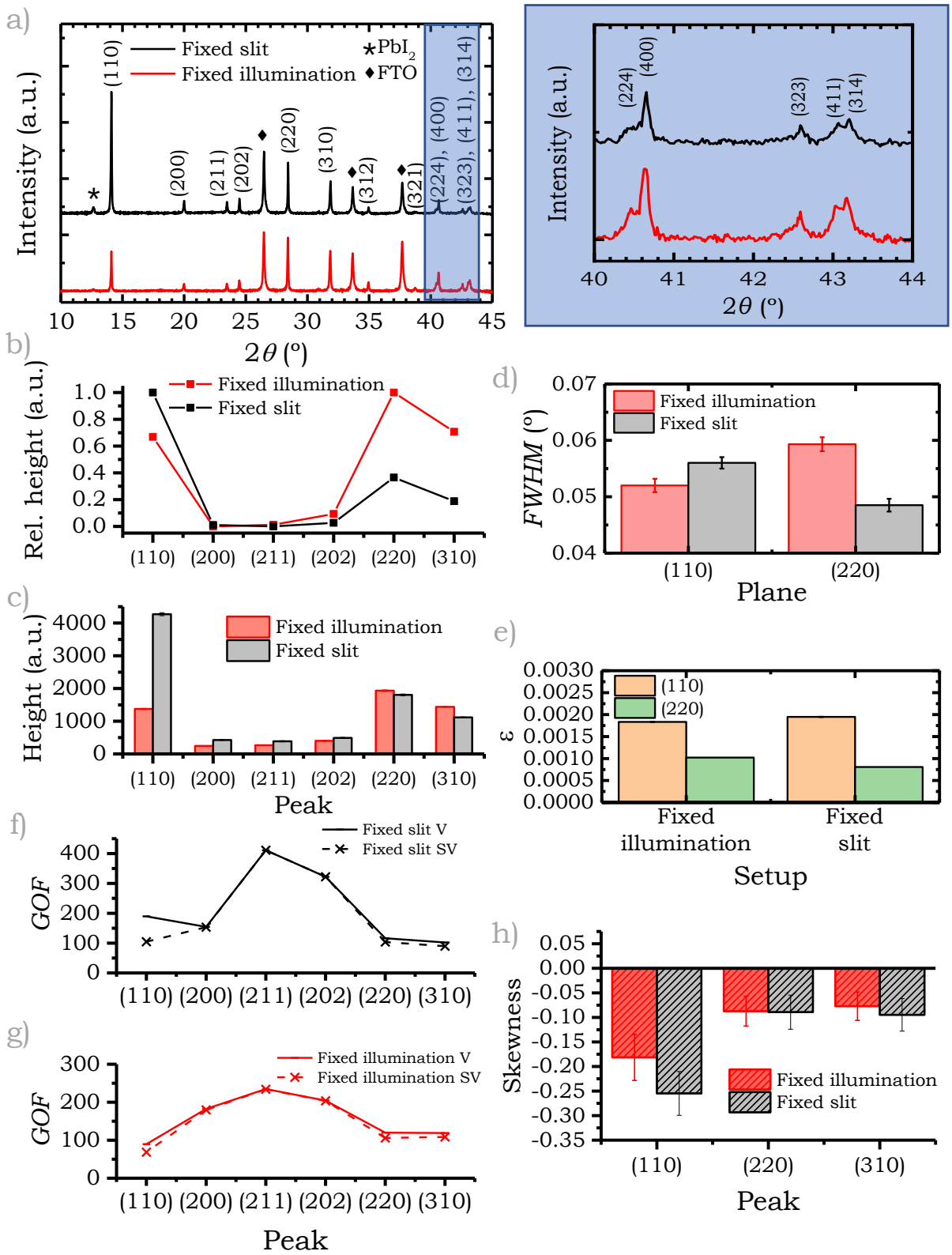

Figure 4.6: a) XRD patterns of $MAPbI_3$ film sample on FTO scanned in fixed slit and fixed illumination length configurations. Inset of the peak profiles at higher angles is depicted on the right side of the figure. Derived parameters from the pattern are plotted per indexed crystallographic plane: absolute (c) and relative (b) Voigt peak heights, *GOF* of Voigt (V) (f) and skewed Voigt (SV) (g) fits with skew parameter (h). Gaussian *FWHM* of Voigt function (d) and microstrain values (e) from peaks (110) and (220) of the $MAPbI_3$ film scanned in fixed slit and fixed illumination length configurations.

The reduced intensity at low angles achieved with a fixed illumination scan was accompanied by a reduction of the skew at low angles as shown in figure 4.6 h. This effect was compatible with the change of shape of the function describing the flat specimen aberration. When the divergence angle is fixed, flat specimen effects are maximum at low angles and decrease with 2θ. However, in a fixed illumination length configuration, this contribution is minimum at low angles and reaches its maximum at 90°.[39] Therefore, asymmetry at low angles can be reduced to the effects of axial divergence. It is also important to note the overall improvement of the symmetric fit across the whole pattern (figures 4.6 f and g).

While the complete removal of the instrumental aberrations from the peak profiles at low angles could not be achieved, their effects in the *FWHM* of parallel planes were reduced by operating the scan in a Bragg-Brentano set up with fixed illumination length. Using this configuration, the methods for instrumental contribution removal were assessed in the following section.

4.3.2. Removal of the instrumental contribution

Removing the instrumental contributions from the sample measurement is a crucial step to correctly determining the microstrain of crystalline materials. The most common empirical technique used for instrumental removal in powder XRD is the external calibration method. Here, the instrumental contribution is extracted by measuring a material with known lattice constants (ideally a certified NIST standard) in the same conditions of the sample under study, before or after performing the sample scan. This reference sample should share characteristics with the nanocrystalline specimen such as a similar mass absorption coefficient, atomic weight and packing density.[277] Additionally, the standard should present a rigid-lattice structure with strong chemical bonding, cover the 2θ range of the sample to analyze and, in the case of line profile analysis, present negligible crystallite size or microstrain contributions to the profile.[52]

Selecting an appropriate standard is a complex assignment given the multiple requirements an ideal reference sample must comply with. Doing so at low angles is deemed an even more daunting task since the diffraction range of most reference materials tends to start above 20°. The accuracy of the method in determining the instrumental error is known to be heavily limited at the lower angle region, and so having a lower number of points to fit in the standard can force systematic errors to pile up when fitting the mathematical models.[6] Mica is one of the few NIST-certified materials with diffracting peaks at low angles, with the first reflection starting at 8.853°.[108] However, its elevated price becomes a limitation for many research groups.[170]

Alternatively, silver behenate ($AgC_{22}H_{46}O_2$) has been proposed as an adequate peak position reference at lower angles due to its large layer spacing (58.38 Å), with the advantage of costing one-twentieth of the mica standard price.[52,271] However, the soft bonding nature of commercial silver behenate powder translates into peak shape irregularities that

discard them as a good line profile calibration standard (figure B.3, Appendix B).

Instead, a two-dimensional halide perovskite $(PEA)_2PbI_4$ was selected as a potentially good reference material given its wide diffraction range and the good resolution of its diffraction peaks, as highlighted in figure 4.7 a. To perform the scans, the large ellipsoidal single crystal of approximately 3 mm width, 7 mm length and 25 µm thickness depicted in the same figure was selected.

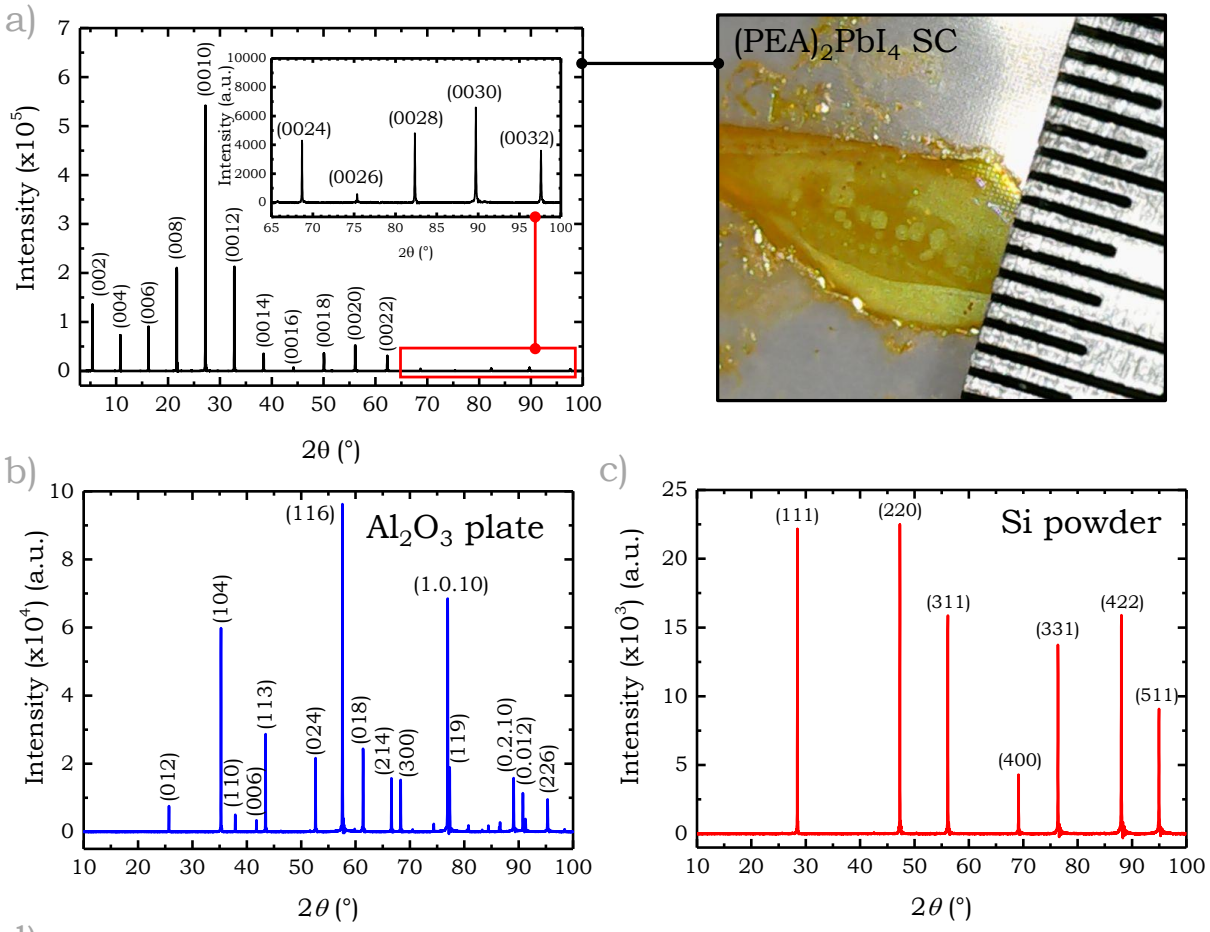

d)

	REFERENCE MATERIAL			PEROVSKITE SAMPLES		
PROPERTY	$(PEA)_2PbI_4$	Al_2O_3	Si	$MAPbI_3$	$MAPbBr_3$	$CsFAMAPb(IBr)_3$
Molar mass (mg/mmol)	959.19	101.96	28.09	619.98	478.98	627.08
Mass attenuation coefficient (µ/ρ) (cm^2/g)	203.37	31.8	64.06	253.87	143.18	245.68

Figure 4.7: Indexed XRD patterns of the 2D perovskite $(PEA)_2PbI_4$ (a), the corundum sintered plate (Al_2O_3) (b) and silicon powder (Si) (c). d) Molar mass and mass attenuation coefficients of several perovskite samples and the reference materials. Mass attenuation coefficient curves are provided in Appendix C.

Commercial silicon pellets milled into a very thin powder were used to compare the effects of a more distant diffraction range between sample and reference (figure 4.7 c), with a diffraction starting point coincidental with the NIST 640f standard at 28.441°.[95] A 25.6 mm diameter ground sintered plate of corundum (Al_2O_3, NIST SRM-1976) was chosen as a reference, presenting a relatively similar diffraction range to the state-of-the-

art LaB_6, commonly used in the literature (figure 4.7 b).[352,279]

Prior to the calculation of microstrain, the impact of the measurement conditions and fitting algorithms on the calibration scan of the selected reference materials was studied in order to rank their suitability. Several scans were taken in a Bragg-Brentano fixed illumination configuration at increasing illumination lengths (2, 5, 10 and 20 mm) and the calibration curves were plotted in figure 4.8, using the Langford and Caglioti fits.

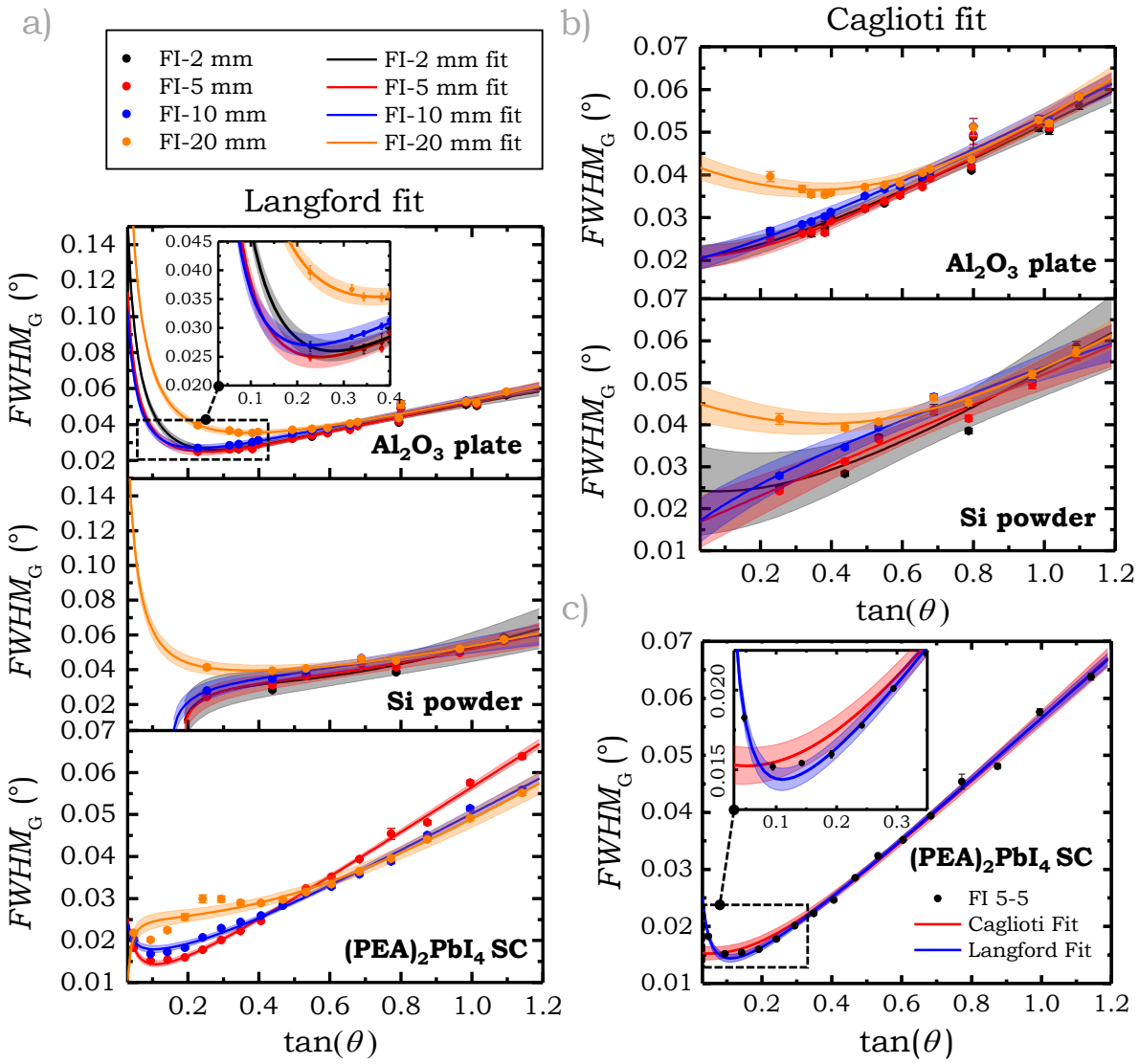

Figure 4.8: Langford (a) and Caglioti (b) curve fits of the Gaussian widths ($FWHM_G$) of the reference samples XRD peaks, scanned in fixed illumination configuration (FI) at different primary and secondary illumination length apertures: 2, 5, 10 and 20 mm. Coloured areas represent the 95 % confidence interval of the fits. c) Comparison of Langford vs Caglioti fit for the $(PEA)_2PbI_4$ single crystal taken with a 5 mm illumination length aperture.

Note that the curve fits were performed following the original methods without weighting the errors of each individual peak to prevent the curves to retrieve senseless shapes under the influence of the outliers at low apertures (figure B.4, Appendix B).[30,149] The scans for the different apertures were taken consecutively, keeping the rest of the parame-

ters intact and without altering the position of the samples. The individual Voigt fits for each peak and scan type are included in Appendix B (figures B.5 to B.19).

As reported in the literature, the use of the Langford formula significantly improved the quality of the fits as evidenced by the reduction of the error range in the curves for all tested materials.[20] Interestingly, the change in the shape of the calibration curves below 70° ($\tan(\theta) \approx 0.7$) was not proportional to the increase in illumination length, which highlighted the complexity of the *FWHM* response at low 2θ angles.

Independently of the selection of the fitting algorithm, both the diffraction angle range and the number of peaks were of great importance for the achievement of a calibration curve with a low error range, particularly at low 2θ angles. The lower number of diffraction points presented in silicon compared to Al_2O_3 increased the confidence interval of the fit, highlighting a much higher error range than in the previous standard (figure 4.8 b). In the case of the Langford fits, the lack of fitting points in the silicon sample below 28° retrieved not only a significantly larger uncertainty range but also incorrect shapes in the majority of the curves (figure 4.8 b). While the Si fit at the maximum illumination length displayed a reasonable shape, the correspondent diffraction peaks were heavily influenced by asymmetry at low angles (figure B.14, Appendix B), as occurs with the corundum reference at large illumination lengths (figure B.9, Appendix B).

On the other hand, the instrumental fit of the 2D perovskite single crystal matched almost perfectly to the Langford formula even at low angles, when scanned in a fixed illumination configuration with a 5 mm illumination length, as shown in figure 4.8 c. Yet, the size of the scanned area in this particular reference sample played a significant role in the overall fit. Very small openings (2 mm) retrieved diffraction peaks that were impossible to fit at high angles (figure B.16, Appendix B), while the larger openings deformed the shape of the fit between 0.1 and 0.5 $\tan(\theta)$ (figure 4.8 a). The presence of this bump in the curve can be traced to the enhanced asymmetry displayed by the most intense peaks (figure B.19, Appendix B), similarly to what occurs in $MAPbI_3$. This defocusing effect could also be influenced by having a larger scanning area in the case of the 10 mm and 20 mm beam length scan configurations than the size of the single crystal.

The format of the reference material was also found to be a significant parameter in the removal of the instrumental contribution, particularly when large differences in thickness existed between the standard and the perovskite films. In a fixed illumination setup, this difference in thickness encompasses a significant change in the amount of material that is being measured depth-wise, which can translate into the overshadowing of the standard over the sample, as occurs in figure 4.9. Here, the Al_2O_3 plate, the $(PEA)_2PbI_4$ single crystal and a 15×15 mm $MAPbBr_3$ film were measured in a 5 mm length fixed illumination setup, ensuring that a similar surface area of material was scanned in all samples. The significant difference in thickness between the 2.2 mm depth of the corundum sample and the approximate 250 nm of the $MAPbBr_3$ film forced the instrumental fit to

overshadow the perovskite XRD width response, which did not occur with the thin 2D $(PEA)_2PbI_4$ single crystal reference. On the other hand, when scanning a $MAPbBr_3$ single crystal of approximately 2 mm thickness, the width of the peaks was proportionally raised compared to the corundum reference sample, highlighting thickness as a critical parameter to take into account when removing the instrumental contribution. For this specific measurement, it is crucial to note that the observed intensity of the (100) peak was significantly lower in the single crystal than in the film (figure 4.9 b) and reported an outstandingly large *FWHM* after performing a Voigt fit on the particularly irregular peak (figure B.21, Appendix B). This response is hypothesized to be the result of the visible surface imperfections presented by the single crystal.

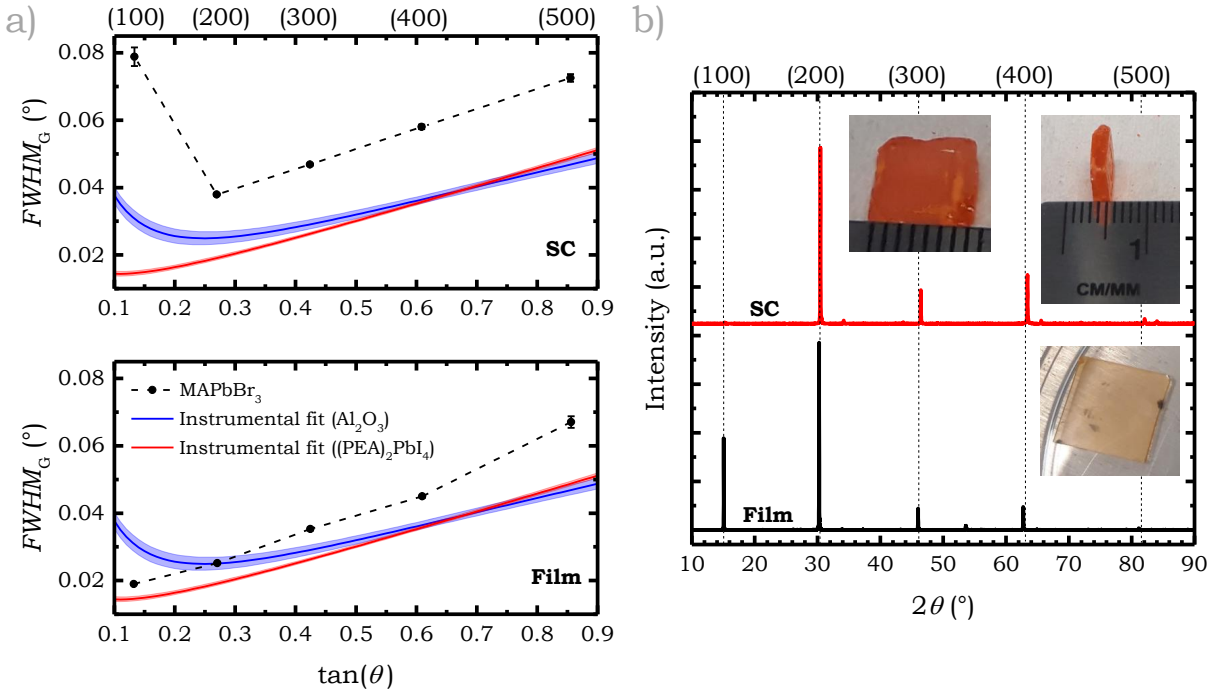

Figure 4.9: a) Gaussian widths ($FWHM_G$) extracted from the fitted diffraction peaks of the *i·(100)* plane set of a $MAPbBr_3$ single crystal (SC) (top) and film (bottom). Langford instrumental curves of the corundum NIST SRM-1976 standard (blue) and the $(PEA)_2PbI_4$ single crystal (red) are included in each plot. b) Correspondent XRD diffraction patterns of the $MAPbBr_3$ SC and film with images of the samples.

Considering the above, the use of a $(PEA)_2PbI_4$ single crystal as a reference material for the removal of the instrumental contribution evidenced a notorious success in the analysis of 3D perovskite films compared to the state-of-the-art standards. On the one hand, this low-cost material fulfilled the premise of sharing characteristics with the specimens under study such as a similar mass absorption coefficient and atomic weight (figure 4.7 d). Its well-resolved diffraction peaks covered the full 2θ range of the 3D perovskites, which enabled a superior fitting of the instrumental functions at low angles compared to the Al_2O_3 or Si reference samples. Additionally, its synthesis into a large single crystal guaranteed both a similar thickness to the films under study and the elimination of the size broadening component from the profile, given the large size of the crystallite. Notwithstanding

this, the existence of a small microstrain remains possible due to the soft bonding nature of the $(PEA)_2PbI_4$ SC. These potential interplanar variations were small enough not to alter substantially the instrumental profile when compared to state-of-the-art standards like corundum and silicon. Yet, the softness of the $(PEA)_2PbI_4$ structure can be identified as a disadvantage regarding its long-term stability, justifying the material's sensitivity to air, moisture and light.[77,258,330]

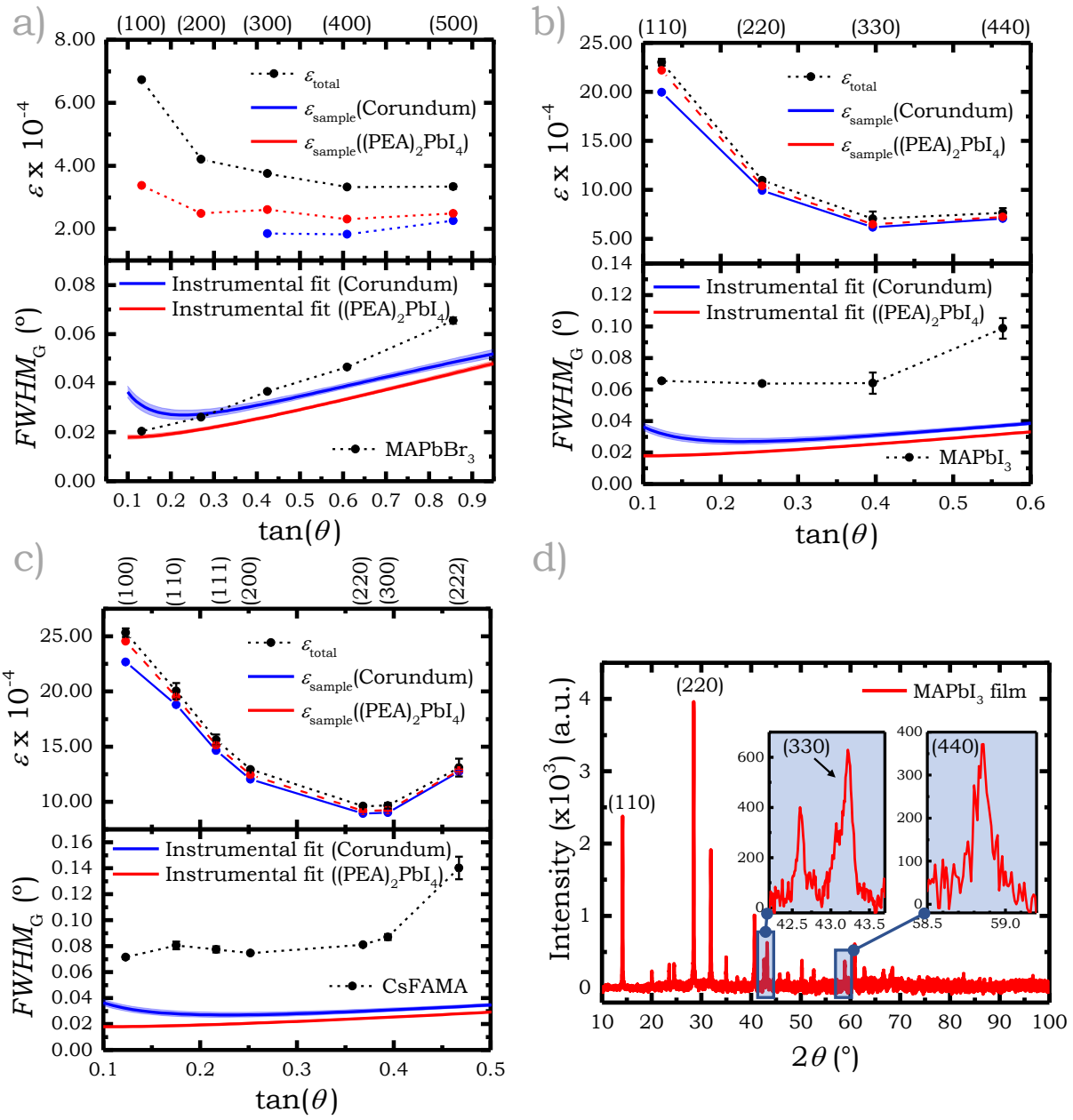

Figure 4.10: Microstrain parameters extracted from the diffraction peaks of the *i·(100)* set of planes of a $MAPbBr_3$ film (a), the *i·(110)* set of planes of a $MAPbI_3$ film (b) and the *i·(100)*, *i·(110)* and *i·(111)* sets of planes of a $CsFAMAPb(IBr)_3$ film (c). Parameters are plotted in a stacked graph with: Gaussian width ($FWHM_G$) of the perovskite sample with the instrumental fits obtained with corundum (blue) and $(PEA)_2PbI_4$ (red) as reference samples (bottom); Perovskite microstrain before (ε_{total}) and after removal of instrumental contribution (ε_{sample}) (top). d)XRD pattern of the scanned $MAPbI_3$ film.

Finally, the *FWHM* and microstrain from three different perovskite films using the 2D perovskite standard were plotted in figure 4.10 to evidence the impact of the instrumental contribution removal. The calibration curves of the corundum and the $(PEA)_2PbI_4$ were included for $MAPbBr_3$ (4.10 a), $MAPbI_3$ (4.10 b) and $CsFAMAPb(IBr)_3$ (4.10 c), as well as their microstrain with ($\varepsilon_{\text{total}}$) and without the instrumental contribution ($\varepsilon_{\text{sample}}$). The individual Voigt peak fits of the perovskite samples were plotted in figures B.23, B.24 and B.25 in Appendix B, respectively. To ensure an adequate beam coverage of the perovskite samples, the scans were taken in a 10 mm fixed illumination length setup for the 15×15 mm perovskite thin films, using the same scan conditions for the reference samples, respectively. For simplicity the strongest sequence of parallel planes was selected, corresponding to the $i \cdot (100)$ in cubic $MAPbBr_3$, the $i \cdot (110)$ in tetragonal $MAPbI_3$, and the *i·(100)*, *i·(110)* and *i·(111)* in the cubic triple cation. Note that the parallel reflections in the iodide sample start to disappear earlier than in the bromide samples and are subject to peak overlapping in plane (330) as reflected by the XRD pattern included in figure 4.10 d, increasing the error bar of the Gaussian *FWHM*.

Overall, barely any difference was observed in the microstrain shape before and after the removal of the instrumental contribution for the iodide-rich perovskite samples independently of the reference material. In all samples, the progressive decrease in the microstrain tended to equalize above 43° ($\tan(\theta) \approx 0.4$). Yet, the films still presented a general decreasing shape, instead of deploying the characteristic constant microstrain of samples compliant with the Wilson-Stokes approximation. Notwithstanding this, the use of the $(PEA)_2PbI_4$ thin single crystal as a reference sample was successful for the complete removal of the instrumental contribution of the $MAPbBr_3$ thin film, which was hampered at low angles by the unoptimized thickness of the corundum reference (figure 4.10 a).

In $MAPbI_3$ and $CsFAMAPb(IBr)_3$ the difference in thickness with the reference sample did not seem to play a critical role, since they reported both a significantly higher general microstrain and higher microstrain disparity between sets of parallel planes than the bromide film.

The observed evidence raises the question of whether microstrain non-linearity is a characteristic of halide perovskites and if, indeed, it is dependent on perovskite composition, given the lower variability in microstrain between parallel planes reported by $MAPbBr_3$ films versus the iodide-containing samples. Additionally, the observed decreasing microstrain trend over 2θ with higher differences between parallels at the lower angles could be compatible with a hypothetical microstrain model presenting a decreasing strain in the direction of the order of diffraction, as schematically plotted in figure 4.11. Here, the existence of a decreasing microstrain gradient between the centre and the corners of the cube directly proportional to the distance deploys a larger difference in microstrain between the first and the second planes compared to the difference between the fourth and fifth diffraction orders.

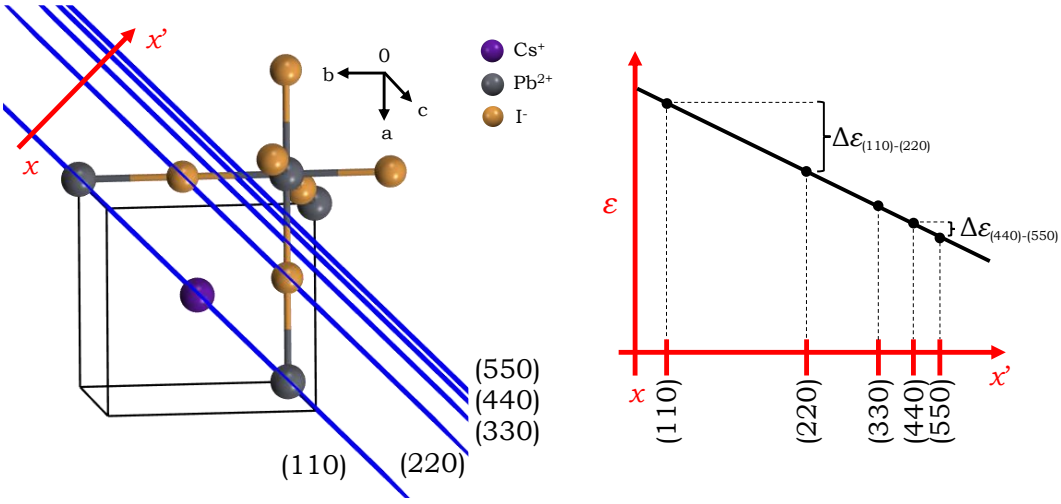

Figure 4.11: Hypothetical microstrain model with decreasing strain with increasing order of diffraction.

Interestingly, a similar yet opposite non-linear type of line broadening behaviour across the order of reflection has been reported for low-temperature Ni_3Sn_2 powder.[156] Here, the integral breadths of parallel planes increased in a non-linear fashion with upward curvature with the order of reflection, therefore demonstrating increased microstrain with diffraction order.[156] They correlated this unusual microstrain broadening to inhomogeneities at the nanoscale, which lead to small phase shifts of the scattered radiation from different locations.[156] In Jones et al. work, a complex local heterogeneity strain variation was evidenced for $MAPbI_3$ perovskite films at different scales using advanced diffraction techniques such as μXRD and synchrotron nano-XRD measurements: from long-range super-grain clusters to grain-to-grain and sub-grain nanoscale.[123] Although non-explicitly, their observations using high-resolution XRD could be compatible with the hypothesized microstrain gradient dependent on the order of diffraction, observable with a standard laboratory diffractometer.

On the one hand, by selecting the right scan configuration significantly good fits of the perovskite diffraction peaks were achieved at low to mid angles (see figures B.22 to B.24 from Appendix B), which discards errors in the extraction of the *FWHM* to be due to a poor fit. Additionally, the use of $(PEA)_2PbI_4$ as a reference material provided a perfect fit with the instrumental function even at the lowest diffraction angles, discarding the quality of the instrumental function fit as the reason behind the large perovskite parallel plane microstrain disparity.

On the other hand, several factors could contribute to the inclusion of additional non-evaluated errors into the pattern. For instance, the occurrence of peak overlapping at high angles in certain perovskites like $MAPbI_3$ or even the natural intensity decrease of the peaks with the order of reflection introduces more errors in the Voigt fit. Moreover, post-acquisition treatments such as the mathematical removal of the Cu $K_{\alpha 2}$ doublet due to the absence of a monochromator in our diffractometer setup, or the background removal are additional sources of error. Therefore, the direct interpretation of these results

as definitive proof of the existence of a microstrain gradient between parallel planes in perovskites should be contrasted by performing further studies using theoretical modelling of XRD patterns and higher precision instruments with different sources of radiation, or synchrotron-based correlative measurements such as nXRD.[240,146]

Interestingly, the perception of non-linearity can be enhanced by the selection of the scan configuration, as shown in figure 4.12.

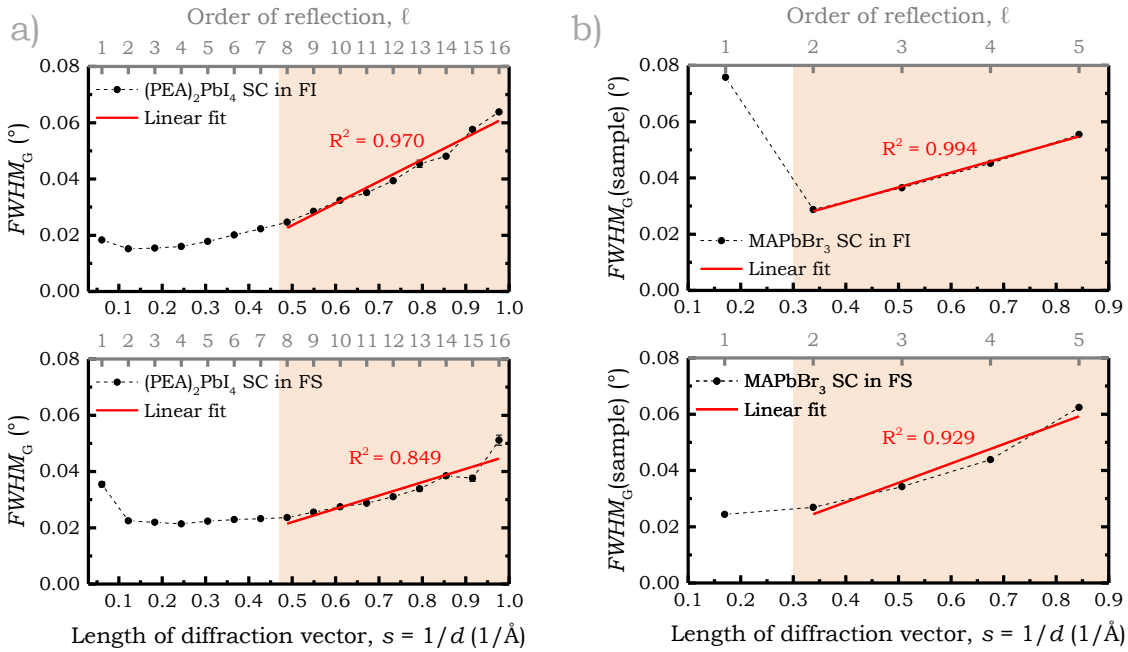

Figure 4.12: Gaussian widths ($FWHM_G$) of the $(PEA)_2PbI_4$ (a) and $MAPbBr_3$ (b) SC diffraction peaks plotted as a function of the length of the diffraction vector and the order of reflection for a scan taken in fixed illumination (FI) (top) and a fixed slit (FS) setup (bottom). The linear fit of the high angle diffraction region with the correspondent R^2 parameter is included in all graphs.

At mid to high angles, both the total Gaussian *FWHM* of the $(PEA)_2PbI_4$ sample (4.12 a) and the sample's Gaussian *FWHM* of the $MAPbBr_3$ single crystal (4.12 b) displayed a lesser degree of linearity in a fixed slit configuration compared to the scan operated in a fixed illumination, as demonstrated by the improved quality of the linear fit. Note that the lower *FWHM* of the first reflection of the $MAPbBr_3$ single crystal scanned in fixed slit corresponds to a better-defined peak (figure B.20, Appendix B) than the one observed in fixed illumination. This is speculated to be the result of a larger illuminated area at low angles in the fixed slit scan, which could have compensated for the narrower and likely more defective area scanned in fixed illumination, given the observed rough surface of the crystal.

4.4 Conclusions

In this work, the suitability of IB methods for the microstrain analysis of halide perovskite thin films using a standard X-ray diffractometer has been studied by exploring the origins of the observed non-compliance of results in the literature with the Wilson-Stokes approximation. The inherent variation in the scanned area over 2θ in the standard Bragg-Brentano-fixed-slit diffractometer configuration has been observed to critically reduce the XRD peak widths at mid to high angles, retrieving a false non-linear response of the *FWHM* over 2θ. Thus, the use of a fixed illumination setup is pointed out to be primordial in obtaining accurate line-profile patterns. In addition, using the appropriate diffractometer configuration, the selection of a $(PEA)_2PbI_4$ single crystal as a reference sample to remove instrumental contribution was key to improving the quality of the instrumental curve fit. Yet, this was not sufficient to alter the decreasing shape of the perovskite microstrain curves of $MAPbI_3$, $MAPbBr_3$ and $CsFAMAPb(IBr)_3$ films, suggesting the presence of a microstrain gradient across the order of diffraction in these materials. Given the limitations of commercial diffractometers, further studies are required to confirm the presence of this behaviour in perovskites with more precise instrumentation and different radiation wavelengths. Nevertheless, the use of IB methods is encouraged to be discarded for microstrain analysis in halide perovskites in favour of either (i) methods that do not require the compliance with the Wilson-Stokes approximation, such as the Warren-Averbach, provided peak width non-linearity of the materials or (ii) given linearity, the use of more precise equipment or techniques that minimize data acquisition errors at low angles.

Chapter 5. Entropic stabilization of mixed lead-antimony halide perovskites

5.1 Introduction

Halide perovskite solar cells are a promising technology in the field of photovoltaics. In slightly over a decade, the efficiency of single-junction devices has grown from 3.8 % in 2009 up to a certified 25.2 % in 2021, returning comparable results to the ones obtained by crystalline silicon.[142,120,210] However, perovskites severely degrade under operational conditions when they are exposed to light, heat, moisture and oxygen.[67,72] Appropriate encapsulation can prevent exposure to water and oxygen and even reduce the thermal outgassing of the volatile perovskite components.[153,242,267,182] Yet, long-term exposure to operational temperatures, which can range up to 85 °C, is unavoidable.

One of the most common and successful routes employed to increase the thermal decomposition threshold of perovskites is rooted in entropic stabilization: mixing multiple elements to increase the number of microstates (Ω). A perfect example of the success of this strategy is multi-mixed perovskites based on the triple cation $CsFAMAPb(IBr)_3$ (abbreviated as CsFAMA), which is commonly established as a reference due to the optimal combination of stability and performance reported in the literature.[255,48,98,47] While other mixed perovskites have reported better thermal stability by primarily excluding MA, such as $CsFAPbI_3$ or $RbCsFAPbI_3$,[295] CsFAMA is still widely used in the fabrication of solar cells with *PCE*s above 21 %, deeming it a well-consolidated perovskite within the research landscape.[255,48]

The limits of entropic stabilization have been pushed beyond the CsFAMA system usually by further mixing on the A or X sites, for example in RbCsFAMA, KCsFAMA and KRbCsFAMA perovskites.[254,189,29,351] However, maximizing the number of microstates involves not only mixing various elements but doing so in even proportions. Unfortunately, this last approach often encounters structural challenges related to unoptimized tolerance factors. In fact, the incorporation of proportions of caesium or bromide into the structure above 15 %, has been reported to trigger the phase segregation of mixed perovskites.[144,42]

Although less common than the A or X site mixing, structural instabilities in perovskites have been successfully addressed by mixing on the B site. In fact, the photoactive α-$CsPbI_3$ has been successfully stabilized through the partial substitution of Pb^{2+} by

Bi^{3+},Sb^{3+},Ca^{2+} or Eu^{2+} and Eu^{3+}.[100,317,150,116] Beyond phase stability, the partial substitution of lead with Sr^{2+}, Ba^{2+}, Mn^{2+} or Cu^{2+} has also improved the thermal stability of inorganic caesium-based perovskites.[151,283,355,17] This thermal stability improvement was also observed in hybrid organic-inorganic perovskites such as $MAPbI_3$, where the addition of strontium at the B site increased its thermal decomposition threshold.[262,337]

Considering the above, in this chapter B-site partial substitution is proposed as a strategy to increase the thermal stability of triple cation CsFAMA perovskites by maximizing the entropy of the system without compromising their structural stability. To do so, a mixture of Pb-Sb is reported to increase the thermal stability of the perovskite films, even for combinations containing MA^+ and larger proportions of I^- than the CsFAMA reference. Additionally, the optical and morphological effects of Sb incorporation into the structure are studied, as well as the interaction of the $CsFAMAPbSb(IBr)_3$ systems with moisture.

5.2 Thermally stable perovskites: a symbiosis between entropy and tolerance factor

As introduced in chapter 1, the formation of highly thermally stable perovskites involves the careful selection of a mix of elements that would bond strongly between them and provide a high number of microstates to compensate for the enthalpic cost of stronger bonds. In other words, a reduction of the Gibbs free energy (ΔG) of the perovskite (equation 5.1) can only be achieved if the change in entropy of the system (ΔS) is large enough to overcome the potential increase, if any, in the change in enthalpy (ΔH) of the system.

$$\Delta G = \Delta H - T\Delta S \tag{5.1}$$

The enthalpy is the sum of the internal energy and the product of the pressure and volume of a thermodynamic system.[191] The internal energy contains components that are often unknown or not easily accessible, and so the total enthalpy of a system cannot be measured directly. Thus, changes in enthalpy are commonly measured in chemical reactions to simplify the description of energy transfer.

The change in enthalpy of the reaction ($\Delta_r H^0$) equates to the change of enthalpy of the products at equilibrium minus the change in enthalpy of the reactants (equation 5.2).[205] A negative value is indicative of an exothermic process, where the enthalpy of the products is lower than that of the reactants, and hence, more thermodynamically stable.[205] In chemical reactions, the term enthalpy of formation is often used to describe the enthalpy change observed in a constituent of a thermodynamic system when one mole of a compound is formed from its elementary antecedents and marked by the f subscripts and the 0 superscripts.[205] It is also accompanied by the prefix standard, evidencing that this

change in enthalpy is calculated in standard conditions: 1 atm, 298.15 K, 1.0 M concentration (if the element or compound is in solution) and with the elements or compounds in their normal physical states.[205] The enthalpy of formation of a large number of atoms, free radicals, ions, clusters and compounds is available from multiple websites and text books.[207,53,248]

$$\Delta_r H^0 = \Delta_f H^0{}_{\text{products}} - \Delta_f H^0{}_{\text{reactants}} \tag{5.2}$$

Assuming the reaction occurs at constant pressure, the definition of enthalpy can be seen in equation 5.3. For most chemical reactions, the second term $p\Delta V$ is much smaller than the internal energy change ΔU. Thus, reaction enthalpies are often analysed in terms of bond energies.[228]

$$\Delta H = \Delta U + p\Delta V \tag{5.3}$$

The Born-Haber cycle is traditionally used for the analysis of the energies required for breaking the bonds of the precursors and forming the bonds of the product. It allows to break the formation energy into the main following components: atomisation enthalpy, ionisation enthalpy, and lattice enthalpy.[350] Zheng et al. extended the Born-Haber cycle to the analysis of energy components of the reaction enthalpies for various perovskite structures using density functional theory (DFT) without including environmental factors such as degradation in water or oxidation in air (figure 5.1).[350]

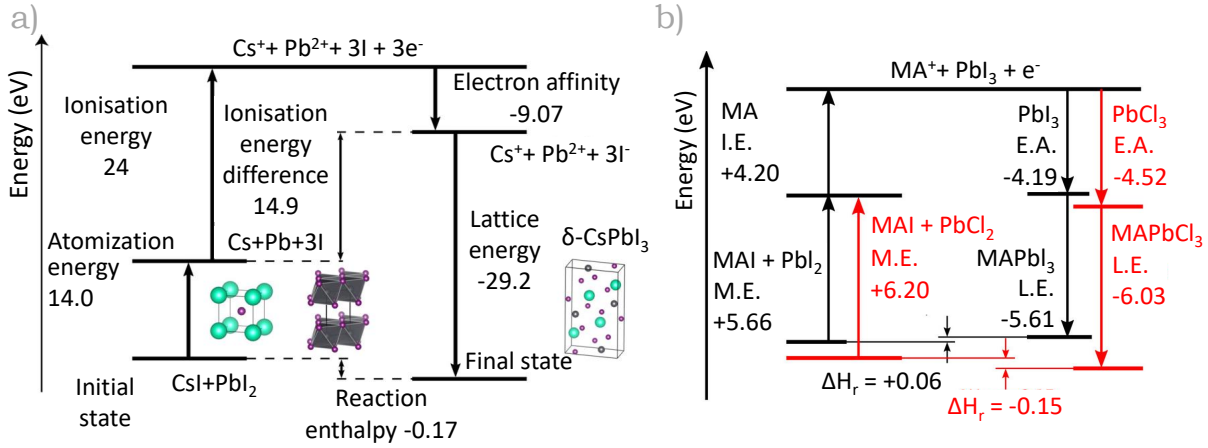

Figure 5.1: Born–Haber cycle of halide perovskites. a) Caesium lead iodide obtained with Cs^+, Pb^{2+}, and I^- ions as elementary species. b) Comparison between $MAPbI_3$ and $MAPbCl_3$. The following components are shown: the molecularization energy (M.E.), the ionisation energy (I.E.), the electron affinity (E.A.), and the lattice energy (L.E.). (a) and (b) adapted with permission from[350]. Copyright 2017 American Chemical Society.

According to their studies, achieving a chemically stable hybrid halide perovskite required both favourable geometrical factors and a low ionisation energy, since the molecularization and lattice energies largely cancelled each other.[350] This could be achieved via two routes: (i) using a cation with a low ionisation energy or (ii) selecting an inorganic

cage with a low electron affinity. Figure 5.1 b evidences how switching halides in the complex ions from $[PbI_3]^-$ to $[PbCl_3]^-$ lowers their electron affinity, leading to the lower total ionisation energy.[350] A similar trend can be observed in experimental studies, where the enthalpy of formation obtained from calorimetry or Knudsen effusion-mass spectrometry (KEMS) and Knudsen effusion mass loss (KEML) techniques becomes more negative with the increase in bond strength between the Pb and the halide.[198,112,28]

An extrapolation from simple to complex systems is tempting to make following Hess's law, where the enthalpies of formation will be the sum of all contributing elements. In principle, a mixed perovskite containing both Br and I ions (e.g. $MAPbI_{(1-x)}Br_x$) would have an intermediate enthalpy of formation (and equivalently bond strengths) between the iodide ($MAPbI_3$) and the bromide ($MAPbBr_3$) simpler compositions. Notwithstanding this, mixed halide perovskites often undergo reversible halide segregation upon light illumination, which renders them an example of pseudo-binary mixtures.[26,44,306,110] Thus, the enthalpic contribution must also include the enthalpy of mixing. In the case of the $MAPbI_{(1-x)}Br_x$ mixed perovskite, first principle calculations retrieved a positive enthalpic term due to chemical strain originating from the ionic size mismatch between the I and Br.[110] Yet, the enthalpic cost of straining the bonding environment was offset by the gain in configurational entropy, rendering a negative Gibbs free energy value.[110]

This beneficial compensation brings light to the second term of the Gibbs free energy equation: the change in entropy. Unlike the standard enthalpy of formation, the standard molar entropy (S^0) is an absolute number. This value is dependent on the temperature and is 0 for a perfect crystal at 0 K. Equivalently to changes in enthalpy, changes in entropy can be accounted as the entropy of the products minus the entropy of the reactants (equation 5.4) and are associated with phase changes and chemical reactions.[301]

$$\Delta_r S^0 = \Delta S^0{}_{\text{products}} - \Delta S^0{}_{\text{reactants}} \tag{5.4}$$

Absolute entropy values can also be found in tabulated registries from books or websites and changes in entropy can be experimentally acquired using calorimetry.[207,53,248,260,217] Equivalently to the enthalpy of mixing, the entropy of mixing also plays a role in mixed perovskite compositions and is mainly determined by the number of microstates(Ω) (equation 5.5). Therefore, maximizing Ω would maximize the total entropy.

$$S = k_B \ln(\Omega) \tag{5.5}$$

However, maximizing the entropic contribution encounters structural limitations related to disparities in size between the host lattice and the incorporated atoms, resulting in the creation of two or more different phases. These geometrical limitations are a representation of the increase in the enthalpy of formation of the mixed perovskite, which, as seen before, needs to be compensated by the entropic contribution.[198,110] In other words, increasing the number of microstates must comply with the structural constraints of the

Goldschmidt tolerance factor to achieve both phase and thermal stability.

Maximizing the number of microstates in perovskite is as simple as introducing a mixture of elements in the structure in even proportions. This can be easily observed by extracting the number of microstates (Ω) of different perovskite systems using combinatorial mathematics. To simplify the concept, the contributions of rotations and translations of the molecules and atoms around their positions or defects in the structure have been ignored. Thus, given a perovskite with structure ABX_3, the number of possible microstates was determined by the product of the variations (V) without repetition of each possible permutation (P) in positions A, B and X (m_A, m_B, m_X) such as:

$$\Omega = \mathrm{V}_{\mathrm{A}_1}^{m_\mathrm{A}} \mathrm{V}_{\mathrm{B}_1}^{m_\mathrm{B}} \mathrm{V}_{\mathrm{X}_1}^{m_\mathrm{X}}$$

$$\mathrm{V}_{\mathrm{A}_1}^{m_\mathrm{A}} = \frac{m_\mathrm{A}!}{(m_\mathrm{A}-1)!}, \quad \mathrm{V}_{\mathrm{B}_1}^{m_\mathrm{B}} = \frac{m_\mathrm{B}!}{(m_\mathrm{B}-1)!}, \quad \mathrm{V}_{\mathrm{X}_1}^{m_\mathrm{X}} = \frac{m_\mathrm{X}!}{(m_\mathrm{X}-1)!} \tag{5.6}$$

Simultaneously, each permutation was considered without repetition at each A, B, X site. Mixing elements involves incorporating n atoms of k different elements in A (A_1, $A_2 \ldots A_k$), in B (B_1, $B_2 \ldots B_k$) and in X (X_1, $X_2 \ldots X_k$) with $k < n$. Mathematically this is expressed as:

$$\begin{aligned} m_\mathrm{A} &= \mathrm{P}_{\mathrm{A}_{n_\mathrm{A}}}^{n_{\mathrm{A}_1}, n_{\mathrm{A}_2} \ldots n_{\mathrm{A}_k}} = \frac{n_\mathrm{A}!}{n_{\mathrm{A}_1}! n_{\mathrm{A}_2}! \ldots n_{\mathrm{A}_k}!} \\ m_\mathrm{B} &= \mathrm{P}_{\mathrm{B}_{n_\mathrm{B}}}^{n_{\mathrm{B}_1}, n_{\mathrm{B}_2} \ldots n_{\mathrm{B}_k}} = \frac{n_\mathrm{B}!}{n_{\mathrm{B}_1}! n_{\mathrm{B}_2}! \ldots n_{\mathrm{B}_k}!} \\ m_\mathrm{X} &= \mathrm{P}_{\mathrm{X}_{n_\mathrm{X}}}^{n_{\mathrm{X}_1}, n_{\mathrm{X}_2} \ldots n_{\mathrm{X}_k}} = \frac{n_\mathrm{X}!}{n_{\mathrm{X}_1}! n_{\mathrm{X}_2}! \ldots n_{\mathrm{X}_k}!} \end{aligned} \tag{5.7}$$

The number of microstates obtained with these formulas is plotted in figure 5.2, where a total of 9 ABX_3 units were considered per perovskite system. Just by replacing a single Pb^{2+} ion with an Sb^{3+} ion in $MAPbI_3$, the number of possible spatial configurations increases from 1 to 9 (5.2 a). When balancing the proportions of the triple cation system (5.2 b), the number of microstates reaches a maximum. Mixing iodide with bromide further boosts the number of microstates between 7 and 10 orders of magnitude compared to the single ABX_3 configuration (5.2 c) and introducing a new B-site element such as Sb^{3+} can rise Ω beyond 12 orders of magnitude (5.2 d).

Yet, achieving this maximized number of microstates in triple cation mixed halide perovskites is structurally hampered by the tolerance factor, as depicted in figure 5.3 a. Note how in $Cs_x[FA_{0.83}MA_{0.17}]_{(1-x)}Pb(I_{(1-y)}Br_y)_3$ the incorporation of additional caesium results in a tolerance factor decrease that can not be compensated by the inclusion of more bromide atoms, justifying the experimentally observed phase segregation of triple cation perovskites with high proportions of Cs.[144,42] Here, the octahedral cages formed

between the Pb^{2+} (119 pm), I^- (220 pm) and Br^- (196 pm) atoms can not shrink the lattice enough to comfortably fit the Cs^+ atoms (167 pm),[263] which present a much smaller size than their organic counterparts MA^+ (~217 pm) and FA^+ (~253 pm).[135]

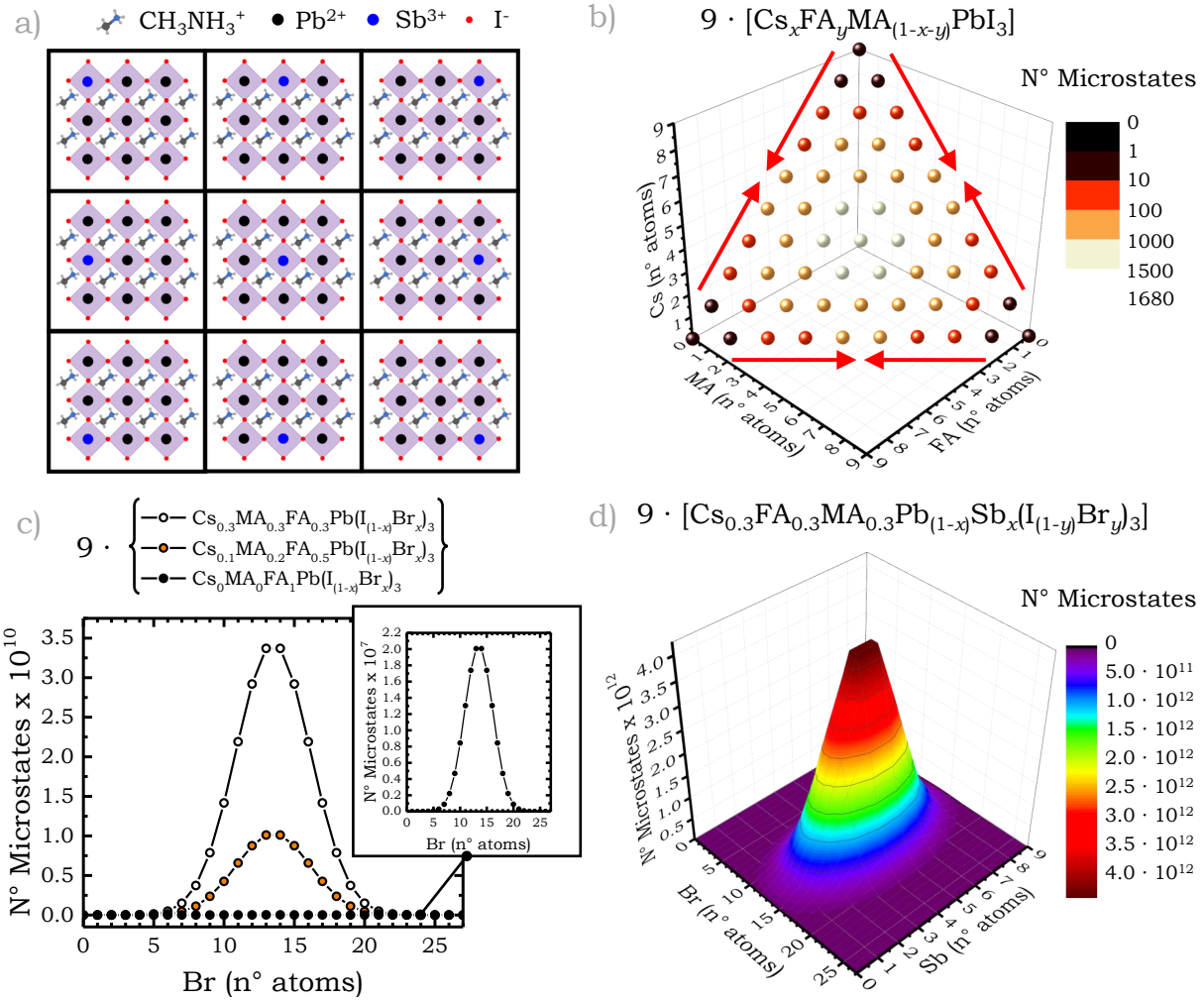

Figure 5.2: a) 2D Diagram of the possible microstates of $MAPbI_3$ when 1 atom of Pb^{2+} is substituted by Sb^{3+}, for a set of 9 B cations. Distribution of the number of microstates of 9 stoichiometric perovskite units when mixing different proportions of elements at the A-site (b); A and X-sites (c); and A,B and X-sites (d).

On the other hand, when partially substituting the B-site element (Pb^{2+}) with the smaller Sb^{3+} ion (figure 5.3 b), the tolerance factor increases by decreasing the size of the B-X octahedral cages, allowing a better fit of the smaller elements (Cs, Br) in positions A and X. Hence, increasing levels of Sb enable the incorporation of larger amounts of Cs at the A site while keeping the tolerance factor of the state-of-the-art $Cs_{0.05}[FA_{0.83}MA_{0.17}]_{0.95}Pb(I_{0.83}\ Br_{0.17})_3$ (Cs_5) constant at a value of 0.969 without the need to increase the bromide content (figure 5.3 c), which normally entangles a less favourable band gap enlargement.[209] Likewise, Ω can be effectively maximized in the triple cation mixed halide perovskite, since even proportions of A, B and X become compatible with a cubic tolerance factor when Sb surpasses the 31 % of the B-site (figure 5.3 d).

Interestingly, the partial substitution of lead with antimony alone in a simpler system, such as $MAPbI_3$, does not necessarily predict a structural reinforcement, as reflected

in figures 5.3 e and f. Here, a 2D map was built to compare the evolution of several compositions of CsFAMAPb(IBr)$_3$-Sb defined in table 5.1, and MAPbI$_3$-Sb, plotting the tolerance factor on the x-axis and the octahedral factor on the y-axis.

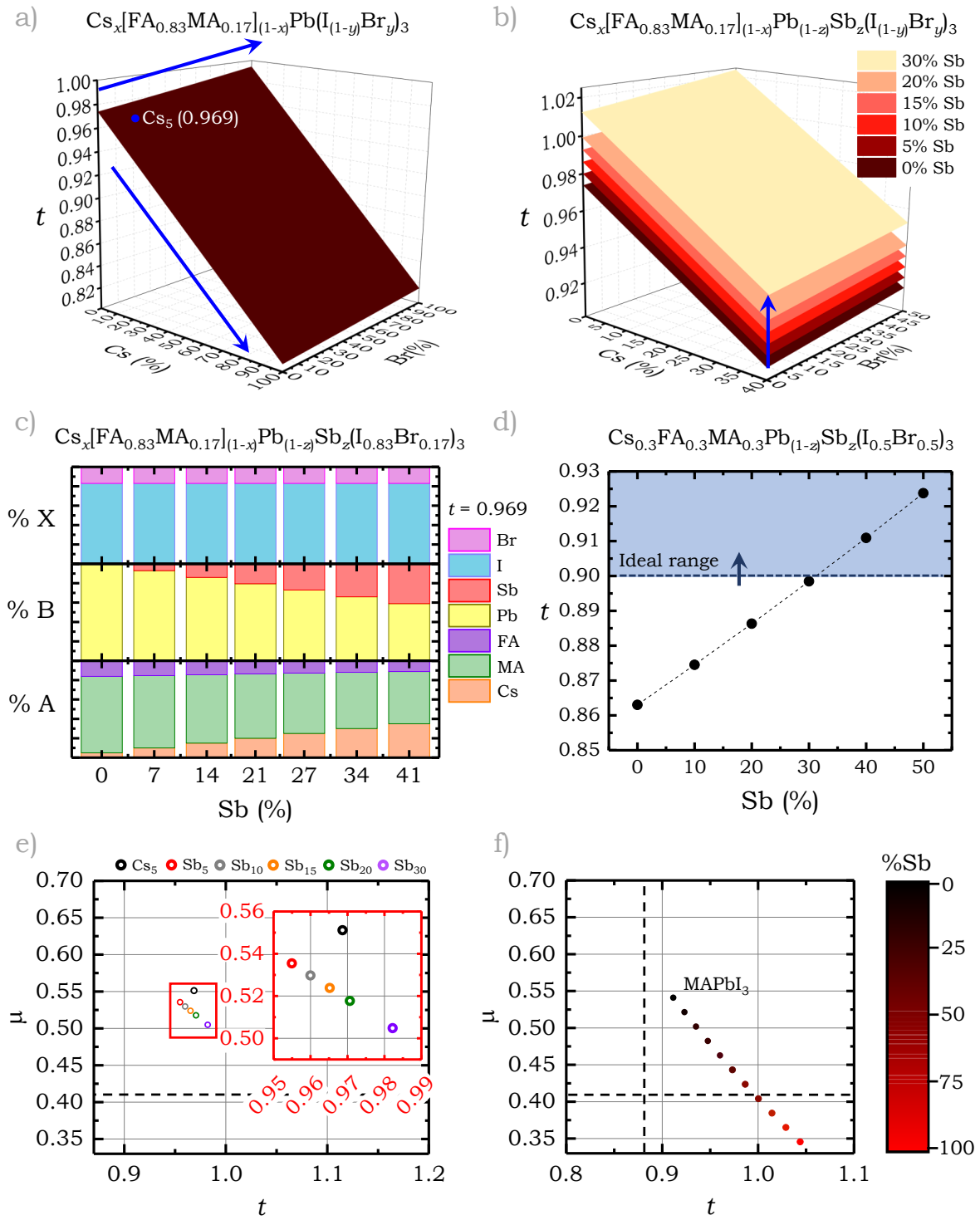

Figure 5.3: Evolution of the tolerance factor with increasing proportions of Cs and Br for the mixed perovskite $Cs_x[FA_{0.83}MA_{0.17}]_{(1-x)}Pb_{(1-z)}Sb_z(I_{(1-y)}Br_y)_3$ without (a) and with (b) different proportions of Sb at the B-site. c) Distribution of the A, B and X elements in the $Cs_x[FA_{0.83}MA_{0.17}]_{(1-x)}Pb_{(1-z)}Sb_z(I_{(1-y)}Br_y)_3$ perovskite for a fixed tolerance factor of 0.921. d) Evolution of the triple cation mixed halide perovskite tolerance factor with increased amounts of Sb, when Ω is maximized at A and X. 2D map of tolerance and octahedral factors for different CsFAMA-Sb compositions (e) and MAPbI$_3$-Sb (f).

The tolerance factor was calculated using Shannon's revised effective ionic radii for the inorganic ions and the effective radii of molecular cations (MA and FA) from Kieslich et al.'s work.[263,135] The octahedral factor, defined as the ratio between the ionic radius of the B site cation and the X site anion (equation 5.8) provides a fitting condition for the B element into the halide octahedral cage and is commonly used to compensate for the stability prediction limitations of the tolerance factor.[159,292]

$$\mu = \frac{r_{\mathrm{B}}}{r_{\mathrm{X}}} \tag{5.8}$$

	% A			% B		% X	
	Cs	**FA**	**MA**	**Pb**	**Sb**	**I**	**Br**
Cs_5	5	78.9	16.1	100	0	83.0	17.0
Sb_5	7.5	76.8	15.7	95	5	92.6	7.4
Sb_{10}	15.0	70.6	14.4	90	10	85.5	14.5
Sb_{15}	22.5	64.3	13.2	85	15	78.6	21.4
Sb_{20}	30.0	58.1	11.9	80	20	71.9	28.1
Sb_{30}	45.0	45.7	9.3	70	30	59.1	40.9

Table 5.1: Composition of triple cation mixed halide perovskite combinations with increasing percentage of antimony. The 0 % Sb perovskite combination corresponds to the reference Cs_5.

The vertical and horizontal dotted lines in figures 5.3 e and f represent the lower limits for perovskite formation of the tolerance factor (t=0.875) and octahedral factor (μ=0.41) respectively, following a similar assessment to the ones reported in the literature.[159,292]

According to the maps, the incorporation of high proportions of Cs and Br into the antimony mixed triple cation perovskite structure is supported by a low variability of both their tolerance and octahedral factors (figure 5.3 e), as opposed to what occurs in the $MAPbI_3$-Sb system (figure 5.3 f). Here, the dots represent the different percentages of Sb incorporation into the structure in 10 % steps, ranging from pure $MAPbI_3$ in black to a hypothetical $MASbI_3$ in bright red. Antimony substitutions above a theoretical 67 % lower the octahedral factor beyond the minimum, suggesting the octahedral cages to be too distorted to fit large proportions of the smaller antimony atoms.

Considering the improvements predicted above by the tolerance factor, B-site partial substitution in complex systems could open the door to further stabilization of multiple cation mixed halide perovskites. Hence, in the following sections, the evolution of the thermal and environmental stability of $CsFAMAPb(IBr)_3$ perovskite films will be investigated upon the addition of the Sb^{3+} cation. Given the inherent complexities of introducing variable proportions of all three A, B and X site elements, the impact of B-site substitution alone will be addressed using a simpler system: $MAPbI_3$-Sb. While the addition of Sb^{3+} to $MAPbI_3$ solar cells has been previously studied,[338,38,215,216,175] this work aims to unveil the entropic and environmental stability implications of its B-site partial substitution, which remain hitherto unexplored.

5.3 Incorporation of antimony into the perovskite structure

Aiming to further stabilise the triple cation perovskite, Pb^{2+} was partially substituted for Sb^{3+} into the B-site by combining the hexagonal $Cs_3Sb_2Br_9$ with the cubic $FAMAPbI_3$ perovskite following the steps reported in chapter 2. For an easier understanding of the figures, samples with increasing amounts of $Cs_3Sb_2Br_9$ were labelled based on their antimony proportions, following the relative stoichiometry of the compounds defined in table 5.1. Note that the I-Br ratio was calculated assuming the incorporation of the excess halide into the structure. Cs_5 was selected as the reference, given the favourable combination of efficiency and stability of devices reported in the literature, which renders it as an established perovskite.[255,48,98,47]

XRD scans were acquired for the optimized films and plotted in figure 5.4 a. The distribution of the diffraction peaks reveals that all tested combinations shared the same cubic crystal structure as the reference sample. The introduction of the smaller elements Cs^+ (167 pm), Sb^{3+} (76 pm) and Br^- (196 pm) into the perovskite structure compared to their ABX counterparts $FAMA^+$ (253 pm, 217 pm), Pb^{2+} (119 pm) and I^- (220 pm) was highlighted by the shifting of the peaks towards larger diffraction angles. The insets from figure 5.4 a expose the right shift of the (200) diffraction peaks with increasing amounts of $Cs_3Sb_2Br_9$, keeping the reference FTO peak fixed at 26.53°. Considering the limitations the incorporation of large amounts of caesium and bromide reported in the literature for the triple cation mixed halide perovskite,[144,42] the inclusion of antimony into the lattice could be inferred both from the reduction of the lattice parameters and, particularly, from the lack of phase segregation in the highly mixed perovskite patterns.

However, the observed right shifts in the pattern could be induced by the incorporation of caesium and bromide alone, concealing the presence of antimony at the interstices. In fact, lattice expansion was observed as a left peak shift in the triple cation Sb_5 sample XRD pattern when compared to a triple cation perovskite film with equivalent nominal caesium (7.5 %) and bromide (7.4 %) proportions ($Cs_{7.5}$) (figure 5.4 b). The presence of alkali cations with a similar effective ionic radius to Sb^{3+} (Li^+,76 pm) has been detected at the interstices of multi-mixed perovskites.[32] Nonetheless, the observed lattice expansion can be attributed to a lower assimilation of bromide into the structure in the antimony sample, since the Sb_5 contained excess Br by default to compensate for the antimony 3^+ charge, whereas the $Cs_{7.5}$ reference was prepared in stoichiometric conditions. These excess bromide ions are likely to sit at the interstices,[296] which further expands the unit cell volume.

To prove the feasibility of Sb accommodation into the B-site of the perovskite structure, the incorporation of antimony into the simpler system $MAPb_{(1-x)}Sb_xI_{(3+x)}$ was studied.

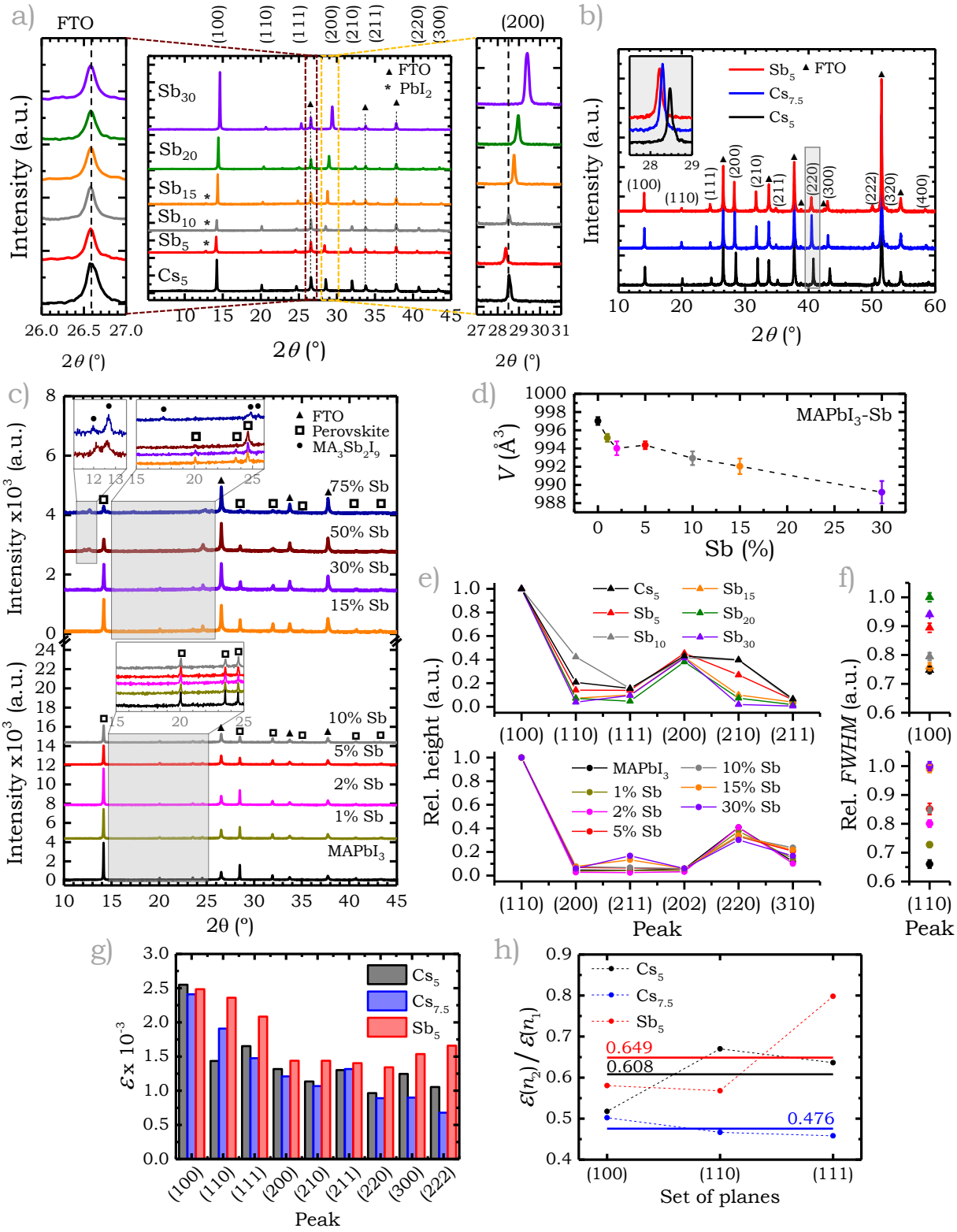

Figure 5.4: XRD patterns of $Cs_{1.5x}FA_{0.83(1-1.5x)}MA_{0.17(1-1.5x)}Pb_{(1-x)}Sb_xI_{(3-3.5x)}Br_{4.5x}$ (a) and $MAPb_{(1-x)}Sb_xI_{(3+x)}$ perovskite films (c) with increasing contents of Sb. b) XRD patterns of Sb_5, $Cs_{7.5}$ and Cs_5 perovskite films. d) Unit cell volume of $MAPbI_3$-Sb perovskite combinations per increasing percentage of antimony. e) Relative height of the diffraction peaks of CsFAMA-Sb (top) and $MAPbI_3$-Sb (bottom) films, normalized to the strongest reflection. f) Relative *FWHM* of the strongest peak in (e). Microstrain (ε) per indexed crystallographic plane (g) and microstrain ratio between the second (n_2) and the first order of diffraction (n_1) of the sets of parallel planes (h) of the perovskite films from (b).

Here, the substitution of up to 30 % of PbI_2 with SbI_3 resulted in a decrease in the unit cell volume with increasing proportions of antimony as reflected in figure 5.4 d, which lies in agreement with similar $MAPbI_3$-Sb reports.[338,215] This volume was obtained from the calculation of the a and c lattice parameters by XRD unit cell refinement assuming the characteristic $MAPbI_3$ *I4/mcm* symmetry, evidenced by the appearance of the (211) peak at 23.63° in figure 5.4 c. As occurs in the literature, high concentrations of Sb in the solution showed the appearance of peaks in the film compatible with the hexagonal *P6$_3$/mmc* $MA_3Sb_2I_9$.[338,336]

An additional argument for the successful B-site incorporation of Sb in multi-mixed perovskites can be made by comparing the crystallinity of the XRD perovskite peaks between systems and the formation of side phases. High crystallinity in perovskite films is represented by the sharpness of the diffraction peaks, involving both high intensity and low *FWHM*. In both cases, the incorporation of antimony widened the perovskite peaks, which can be correlated with an increase in the lattice microstrain upon the mixture of elements into the B-site. Yet, the increase in the CsFAMA system was lower than in the $MAPbI_3$-Sb as revealed by the normalized *FWHM* of the strongest perovskite diffraction peak in figure 5.4 f, and not exclusively proportional to the increase in antimony content. Additionally, high proportions of Sb in the $MAPbI_3$ system progressively reduced the intensity of the peaks to the point where side phases were observable. On the other hand, CsFAMA perovskites experienced a substantial increase of peak intensity above 15 % Sb beyond the observable reorientation of the crystallites upon Cs, Sb and Br incorporation, which contributed to the enlargement of the (100) and (200) peaks (figure 5.4 e). The enhancement of crystallinity paired with a lack of side phases, which are common in triple cation perovskites with more than 15 % Cs,[144,42] points to the successful incorporation of Sb into the B-site. Moreover, these observations are geometrically coherent with the worsening of the tolerance and octahedral factors of Sb partially substituted $MAPbI_3$, which have significantly lower variability in the studied CsFAMA-Sb perovskites.

Next, the structural stability of the triple cation Sb_5 perovskite was evaluated through XRD microstrain analysis. The incorporation of antimony was found to induce an overall higher degree of distortion in the average interplanar distances as demonstrated by the increased microstrain values obtained for each crystallographic plane represented in figure 5.4 g. Despite the individual increase for each plane, the microstrain distribution was significantly more isotropic than the one observed in both the Cs_5 or $Cs_{7.5}$ films. A more uniform distribution of strain between families of planes suggests improved structural stability in the antimony-based samples, similar to what occurs in $FAPbI_3$ when Cs, MA or Br are introduced into the structure.[343,352] Notwithstanding this, mixed Sb samples still presented a significant difference in microstrain between parallel planes, similar to their full Pb counterparts, deeming the use of integral breadth methods rather unsuitable for microstrain analysis as discussed in chapter 4.

Intriguingly, the average difference in microstrain between parallel planes seemed to decrease with the incorporation of antimony as depicted in figure 5.4 h. Here, the microstrain ratio between the second order of diffraction ($n = 2$) and the first order of diffraction ($n = 1$) was plotted for three sets of parallels ($n(100)$, $n(110)$ and $n(111)$) exposing a lower microstrain gradient (or equivalently higher isotropy) within the order of diffraction for the Sb_5 sample than the Cs_5 or $Cs_{7.5}$ samples. Given the successful correlation observed between structural and thermal stability in perovskite compounds with higher interplanar isotropy,[343,352] an equivalent hypothesis could be made where a more balanced distribution of strain across the order of diffraction could contribute to the enhanced structural stability of Sb mixed perovskites.

Regarding the perovskite morphology, the incorporation of antimony into the structure reported a progressive increase of the average grain size in both $MAPbI_3$-Sb and CsFAMA-Sb systems as revealed by AFM measurements included in figure D.1 from Appendix D. Annealing the films at their optimized temperatures, which were higher than the standard 100 °C to prevent the formation of side phases, also contributed to the grain enlargement.[70,18] However, the inclusion of Sb was accompanied by an increase in the surface roughness of the films, which produced a loss of packing density and the formation of more pinholes, especially in low-doped $MAPbI_3$-Sb samples. It has been found that the addition of optimal amounts of HI can improve the quality of $FAPbI_3$ perovskite films, while excess iodide ions contribute to more pinholes.[137] Therefore, the incorporation of excess iodide is hypothesized to be partially healing the morphological irregularities induced by the antimony addition between 2 % and 10 % of SbI_3, progressively worsening the regularity of the surface above that threshold. On the other hand, both the variation in film roughness and grain size between the various CsFAMA-Sb samples was relatively low, equivalently to the observations made by Jacobsson et al. on mixed perovskites, where large variations in the proportions of A and X elements remained surprisingly similar, especially while compared to the diversity of surfaces found in the literature for $MAPbI_3$ alone.[121]

5.4 Optical properties

Often, the inclusion of new elements into the perovskite lattice encompasses a change in its optoelectronic properties such as the band gap and the charge recombination lifetimes, which are parameters of critical importance for the attainment of high-performing solar cells. Hence, the optical features of the phase pure fabricated films of both CsFAMAPb $(IBr)_3$-Sb and $MAPbI_3$-Sb perovskite series were investigated by acquiring their absorption and photoluminescence (PL) steady-state spectra (figure 5.5 c, e and f). Note how in both perovskite systems, the colouration of the films became slightly red-tinted as higher proportions of Sb were incorporated into the structure (figures 5.5 a and b).

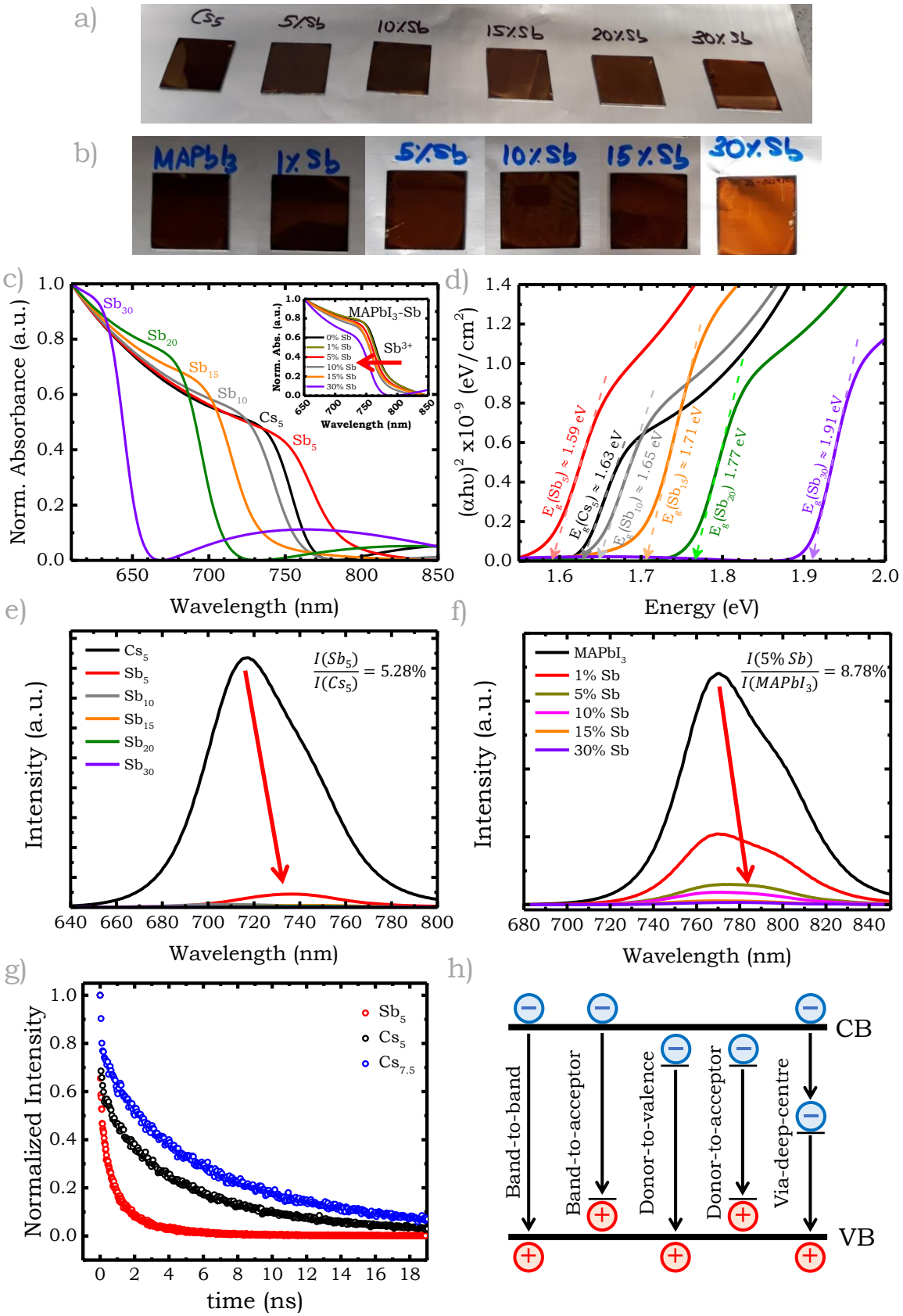

Figure 5.5: Images of $CsFAMAPb(IBr)_3$-Sb (a) and $MAPbI_3$-Sb films (b). c) Normalized absorption spectra of mixed Sb perovskite films. d) Tauc plot of $CsFAMAPb(IBr)_3$-Sb films. Steady-state photoluminescence spectra (PL) of $CsFAMAPb(IBr)_3$-Sb (e) and $MAPbI_3$-Sb films (f). g) TRPL measurements of Cs_5, $Cs_{7.5}$ and Sb_5 films. h) Radiative recombination processes in a semiconductor.

The optical band gaps of the triple cation perovskites were calculated using the Tauc plot represented in figure 5.5 d. In the steady PL measurements, the excitation wavelength was selected at 540 nm and a 555 nm filter was included in the detector to avoid interference from the primary beam. Similarly to reports in the literature, the incorporation of antimony into the $MAPbI_3$ perovskite showed a slight blue shift of the absorption spectra, being particularly noticeable for Sb contents above 30 %.[338,38] A similar effect was observed in the absorption spectra of the triple cation mixtures, where the impact of Sb was not clearly noticeable below a 30 % content. Here, the blue shift was much stronger than in $MAPbI_3$-Sb, primarily driven by the addition of Cs and Br, in agreement with previous studies.[255,145,163]

Note that the quality of these scans was altered by the light scattering of morphologically uneven films as evidenced in the Sb_{30}, Sb_{20} and the Cs_5 curves, due to the lack of an integrating sphere in the spectrometer setup.

To confirm the impact of B-site mixing in the absorption shift of the triple cation films, the band gaps of $CsFAMAPb(IBr)_3$ perovskites with and without antimony were compared. To do so, the band gap of the lead perovskite references was calculated using the optimized linear regression (LR) model reported by Li et al., and compared to the Sb-mixed experimental values.[163] This algorithm was selected due to its facile applicability and the high prediction accuracy revealed by the machine learning experiments performed on triple cation mixed halide perovskites.[163] The results, included in table 5.2, highlighted higher differences between the experimental Sb-Pb mixes and the predicted $CsFAMAPb(IBr)_3$ values when the content of Sb reached 30 %, equivalently to what was experimentally observed in the $MAPbI_3$-Sb system. Additionally, the likely lower inclusion of bromide into the lattice previously showcased by the Sb_5 reinforces the hypothesis that the slight band gap increase in the multi-mixed systems was rooted in the incorporation of antimony.

	Cs (%)	**Br (%)**	$\boldsymbol{E_g}$**(Pb)$_{\mathbf{Calc}}$**	$\boldsymbol{E_g}$**(Pb-Sb)$_{\mathbf{Exp}}$**	$\boldsymbol{\Delta E_g}$
Cs_5	5	17.0	1.61	1.63	0.02
5 % **Sb**	7.5	7.4	1.55	1.59	0.04
10 % **Sb**	15.0	14.5	1.61	1.65	0.04
15 % **Sb**	22.5	21.4	1.66	1.71	0.05
20 % **Sb**	30.0	28.1	1.72	1.77	0.05
30 % **Sb**	45.0	40.9	1.82	1.91	0.09

Table 5.2: Predicted band gap values of $CsFAMAPb(IBr)_3$ and experimental band gap values of $CsFAMAPb(IBr)_3$-Sb perovskite films, per equivalent proportions of A cations and X anions.

Several transitions can occur within the photoluminescent process in perovskites giving rise to different types of radiative recombination as illustrated in figure 5.5 h. Whether or not the recombination follows a free carrier process or a bound exciton recombination, that is, where the exciton gets trapped in a near band-edge defect, is determined by the experimental conditions such as the temperature and by the sample itself, given

the exciton binding energy.[298] The latter is defined as the transition energy difference between the excitonic emission and the free carrier recombination process.[298] Decreasing this value is highly desirable to limit the inefficient optical generation of charges. Deep-trap recombination is also an undesired process that occurs when charges recombine with traps located mid-gap.

In both cases, the increase of Sb^{3+} in the mixture reported an exponential reduction of the photoluminescence intensity. This observation, in agreement with the literature for Sb-doped $MAPbI_3$, correlates the reduction of the PL peak with an increase in mid-trap states, leading to potentially higher charge recombination rates in devices.[338] Deep trap recombination is likely the dominant agent behind the PL peak quenching, as occurring with similar heterovalent doped systems ($MAPbBr_3$-Bi and $MAPbI_3$-Bi). Here, the reduction in the PL peak was enhanced in the bismuth incorporated samples, while the below-gap infrared PL emission was increased.[296,14] Unfortunately, equipment limitations in the wavelength range detection both for absorption and photoluminescence did not allow for measurement in the IR region of the Sb mixed systems studied in this thesis.

Although the addition of Sb^{3+} has been pointed to as the main cause of the trap increase,[338] this effect could also be enhanced by the excess halide incorporated in the mixtures via the SbI_3 and $Cs_3Sb_2Br_9$ precursors. In fact, for the bismuth doped $MAPbBr_3$ system, Ulatowski et al. proposed that the halide excess associated with $BiBr_3$ addition incorporates into the interstices, enhancing the electron trapping.[296] Moreover, the inclusion of low proportions of antimony through an acetate source ($Sb(Ac)_3$) to stoichiometric $MAPbI_3$ resulted in a superior enhancement of PL intensity and carrier lifetimes compared to the incorporation through the halide source (SbI_3).[175]

Interestingly, the PL intensity drop experienced by the addition of 5 % of Sb into the triple cation was higher than in the $MAPbI_3$-Sb system, decreasing to 5.28 % of the intensity of the reference compared with the 8.78 % showcased by the $MAPb_{0.95}Sb_{0.05}I_{3.05}$ perovskite. This observation contrasts with the findings of Angelis et al.'s work, where the substitution of iodide interstitials with bromide in $MAPbI_3$ reduced the trap's depth,[192] which suggests a lower formation of halide interstitial defects in the $MAPbI_3$-Sb system compared to the CsFAMA-Sb.

The impact of bound excitonic transitions within the band-edge is often analysed through a fitting of the band-edge absorption spectra following Elliot's theory, where a value for the exciton binding energy can be extracted.[59,296] At room temperature, the exciton binding energy of halide perovskites tends to be small (around 8 meV),[59] and the Elliott analysis of similar systems ($MAPbBr_3$-Bi) did not observe changes in that energy upon the heterovalent substitution.[296] Unfortunately, the excessive light scattering present in the UV-Vis absorption measurements hampered this type of analysis near the band-edge of the perovskite samples contained in this thesis. However, a similar behaviour is expected of the antimony mixed samples given the similarities in the PL response between Sb and Bi partially substituted perovskites.[338,296,14]

TRPL measurements further supported the hypothesis of deep-trap increase in the antimony mixed triple cation perovskites by showcasing a critical plummeting of the charge recombination lifetimes, as evidenced in figure 5.5 g. Here, the inclusion of antimony and excess halide deployed a much faster decay of the PL emission of the Sb_5 film compared to the stoichiometric Cs_5 reference and $Cs_{7.5}$ film, fabricated with a more similar composition.

Overall, given the observed optoelectronic results, it was clear that lower values of antimony will be preferable for the fabrication of devices to enhance the absorption of photons and limit the number of defects acting as recombination sites.

5.5 Enthalpy and crystallization dynamics of Sb-Pb mixtures

The enthalpy of the synthesized Sb-Pb perovskite systems was evaluated indirectly by observing their crystallization and degradation dynamics with temperature. To do so, $MAPbI_3$-Sb and $CsFAMAPb(IBr)_3$-Sb perovskite films were fabricated with increasing amounts of SbI_3 and $Cs_3Sb_2Br_9$, respectively, and annealed under an inert atmosphere for 10 min at increasing temperatures. To prevent excessive bleaching of the perovskite films, the time was reduced to 3 min for annealing temperatures above 200 °C in the triple cation perovskites and above 180 °C in the single cation system. Note that a higher set of temperatures was selected for the triple cation due to its superior thermal stability.

The XRD scans of each perovskite series with increasing Sb content and annealing temperature are included in figures D.2 and D.3 from Appendix D, respectively. The evolution of the crystalline phase with temperature was assessed by tracking the intensity of the strongest perovskite diffraction peak in the pattern relative to the intensity of the FTO substrate (at 26.53°). Additionally, temperature-induced degradation was analysed by extracting the intensity ratio between the main degradation product (PbI_2 peak at 12.7°) and the strongest perovskite peak in the pattern. Both metrics are represented for the $MAPbI_3$-Sb and $CsFAMAPb(IBr)_3$-Sb perovskites in figures 5.6 a and c, and 5.6 b and d, respectively.

After the incorporation of antimony into the perovskite structure, films required higher temperatures to achieve a highly crystalline phase, compared to the Sb-free reference. In $MAPbI_3$, the (110) diffraction peak located at 14.16° reached its maximum height in the sample annealed at 100 °C, while the maximum for the B-site mixed samples was delayed to 150 °C when less than 2 % Sb was incorporated, to 160 °C in the 5 % Sb mixture and to 170 °C in the 10 % Sb film (figure 5.6 a). Likewise, the maximum height of the (100) diffraction located between 14.1° and 14.6° in the triple cation series was generally displaced towards the higher end of the temperature range: 200 °C for Sb contents below 20 % and 220 °C for the Sb_{30} film (figure 5.6 b). Exceptionally, the 10 % mixture (Sb_{10}) showcased its highest intensity when annealed at 220 °C. Yet, the peak height obtained

at 200 °C was relatively close to it.

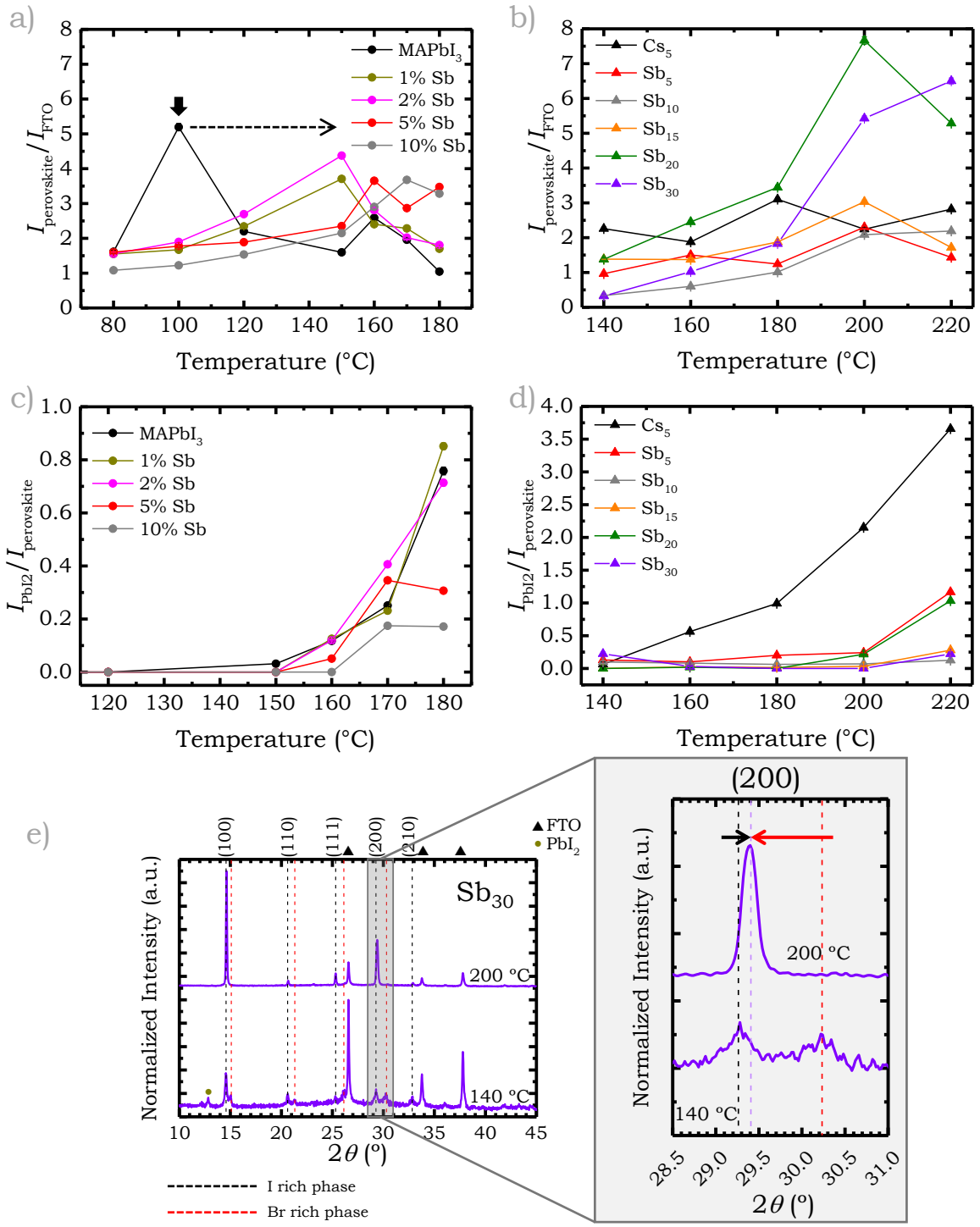

Figure 5.6: $(110)_{perovskite}$/FTO (a) and $PbI_2/(110)_{perovskite}$ (c) peak intensity ratios extracted from the XRD patterns of $MAPbI_3$-Sb samples annealed between 80 °C and 180 °C. $(100)_{perovskite}$/FTO (b) and $PbI_2/(100)_{perovskite}$ (d) peak intensity ratios extracted from the XRD patterns of $CsFAMAPb(IBr)_3$-Sb samples annealed between 140 °C and 220 °C. e) Indexed XRD pattern of $Cs_{0.45}FA_{0.46}MA_{0.09}Pb_{0.7}Sb_{0.3}I_{1.95}Br_{1.35}$ samples annealed at 140 °C and 200 °C. The inset on the right highlights the peak changes in the (200) reflection between temperatures.

Interestingly, the formation of lead iodide was only successfully reduced in the triple cation systems containing antimony, even in samples fabricated with much lower propor-

tions of bromide than the reference (Sb_5) (figure 5.6 d). $MAPbI_3$-Sb perovskites displayed a similar PbI_2 formation curve to the reference, only showcasing less amount of the degradation product at 180 °C when the content of Sb surpassed the 5 % (figure 5.6 c).

In both perovskite systems, requiring higher temperatures to form a highly crystalline perovskite phase suggested an increase in the enthalpy of formation, the activation energy of the reaction or both.

On the one hand, partially substituting Pb^{2+} with a smaller ion with a higher charge (Sb^{3+}) increases the strength of the B-X bonds. This is reflected in the bond lengths of the precursors: PbI_2 shows a separation between the metal and the halide of 3.28 Å,[290] while in SbI_3, the iodide ions are pulled closer to the Sb at an average distance of 3.06 Å.[291] Changes in the bond strength of precursors and products modify the lattice and the atomisation enthalpies. Yet, these contributions often cancel each other in halide perovskites.[350] Thus, the increase in the bond strength between the metal and the halide is expected to be beneficial for the reduction of the ionisation energy of the halide cage, and hence the reduction of the final enthalpy.[350]

On the other hand, strain associated with the size disparity between the B-site ions increases the enthalpy of formation by increasing the enthalpy of mixing.[110] This increase needs to be offset by the entropic component to render the crystalline structure stable.

This balance did not seem to be achieved in the antimony mixed $MAPbI_3$ perovskites, especially when high proportions of antimony were introduced into the structure, making the formation of the 3D phase less favourable compared to other compounds. In fact, higher substitutions of SbI_3 in $MAPbI_3$ showcased the presence of the $MA_3Sb_2I_9$ at low temperatures, which disappeared in samples annealed at higher temperatures. This was the case for the 30 % Sb mixed samples, which showed the formation of the dimer phase between 100 °C and 150 °C (figure D.4-a, Appendix D), disappearing in the 160 °C annealed film. For higher contents, such as the 50 % Sb mix, this phase remained present in the 160 °C annealed film (figure D.4-b, Appendix D). The existence of the dimer phase at low annealing temperatures highlighted a lower enthalpy of formation of $MA_3Sb_2I_9$ compared to the mixed perovskite.

On the other hand, the potential increase in enthalpy associated with higher contents of $Cs_3Sb_2Br_9$ precursor in the triple cation solution was not necessarily correlated with a drop in thermal stability, since the formation of PbI_2 in the films was critically reduced. In this case, more thermal energy was required to form the crystalline phase as induced by the evolution of the Sb_{30} diffraction patterns between 140 °C and 200 °C (figure 5.6 e). In this case, lower temperatures allowed the formation of two cubic perovskite compounds: one richer in smaller elements highlighted by the red dotted lines and the other one, presumably richer in the larger ions (MA, FA, I), pointed by the black dotted lines. By increasing the annealing temperature up to 200 °C, the bromide-rich phase disappeared, and the left peaks shifted towards the higher angles, forming the final non-segregated perovskite phase. Once formed and cooled down, no phase segregation or

formation of degradation products were observed at room temperature under inert conditions, highlighting the entropic contribution to the decrease in free energy. The need for more heat suggested an increase in the activation energy of the reaction, often linked to the type of intermediate species formed with the solvents before the annealing step.[105] It is to note, that intermediate chemistry of halide perovskites is a complex process that significantly affects the kinetics and thermodynamics of perovskite formation,[105] which analysis extends beyond the focus of this thesis.

Additionally, samples with lower contents of antimony, such as the 10 % mixture, showcased the presence of traces of additional side phases at low temperatures compatible with the 2D $CsPb_2Br_5$ perovskite diffraction pattern. Previous reports have shown that this compound can be formed along with $CsPbBr_3$, where an excess of $PbBr_2$ facilitates the transformation from the 3D into the 2D phase at low temperatures.[346]. In this particular case, the excess of bromide incorporated through the $Cs_3Sb_2Br_9$ precursor is hypothesized to sustain the formation of the $CsPb_2Br_5$ traces. As shown in figures D.4-c and D.4-d in Appendix D, this secondary phase was successfully removed by increasing either the annealing time or the temperature.

5.6 Thermal degradation of Sb-Pb mixed perovskites

To assess the thermal stability of the Pb-Sb perovskites, the evolution of their colouration over time was tracked as they were exposed to high temperatures on a hot plate under an inert atmosphere *in-situ*, using the PCT setup described in chapter 3.

Perovskite degradation was quantified based on the average colour of a selected area in each film. As time passed, the area changed from black (perovskite) to yellow, as the characteristic colouration of the final degradation product (PbI_2). To simplify the analysis, the intensity in the RGB channels was transformed to grey-scale, where degradation was identified by the increase of the average intensity over time (ΔI), corresponding to the progressive bleaching of the film. Note that the difference between ΔI after full beaching varied between samples since each measurement was dependent on the illumination conditions. Hence, pictures of the films over time were included in figure 5.7 c to support the grey-scale curves of the triple cation and single cation systems, plotted in figures 5.7 a and b, respectively.

Two different temperatures were used for the systems: $MAPbI_3$-Sb samples were heated at 180 °C while CsFAMAPb$(IBr)_3$-Sb samples were exposed to 200 °C. Despite selecting a lower temperature for the single cation systems, degradation occurred at a much faster rate than their mixed counterparts, as reflected by the plateau of most of the curves after 20 min of heat exposure and a full yellow colouration of the films after 25 min. This lies in agreement with the observations in the literature since the A and X elements in $MAPbI_3$ present much higher volatility than the ones employed in the mixed perovskite combinations (such as FA, Cs or Br).[124,125,295]

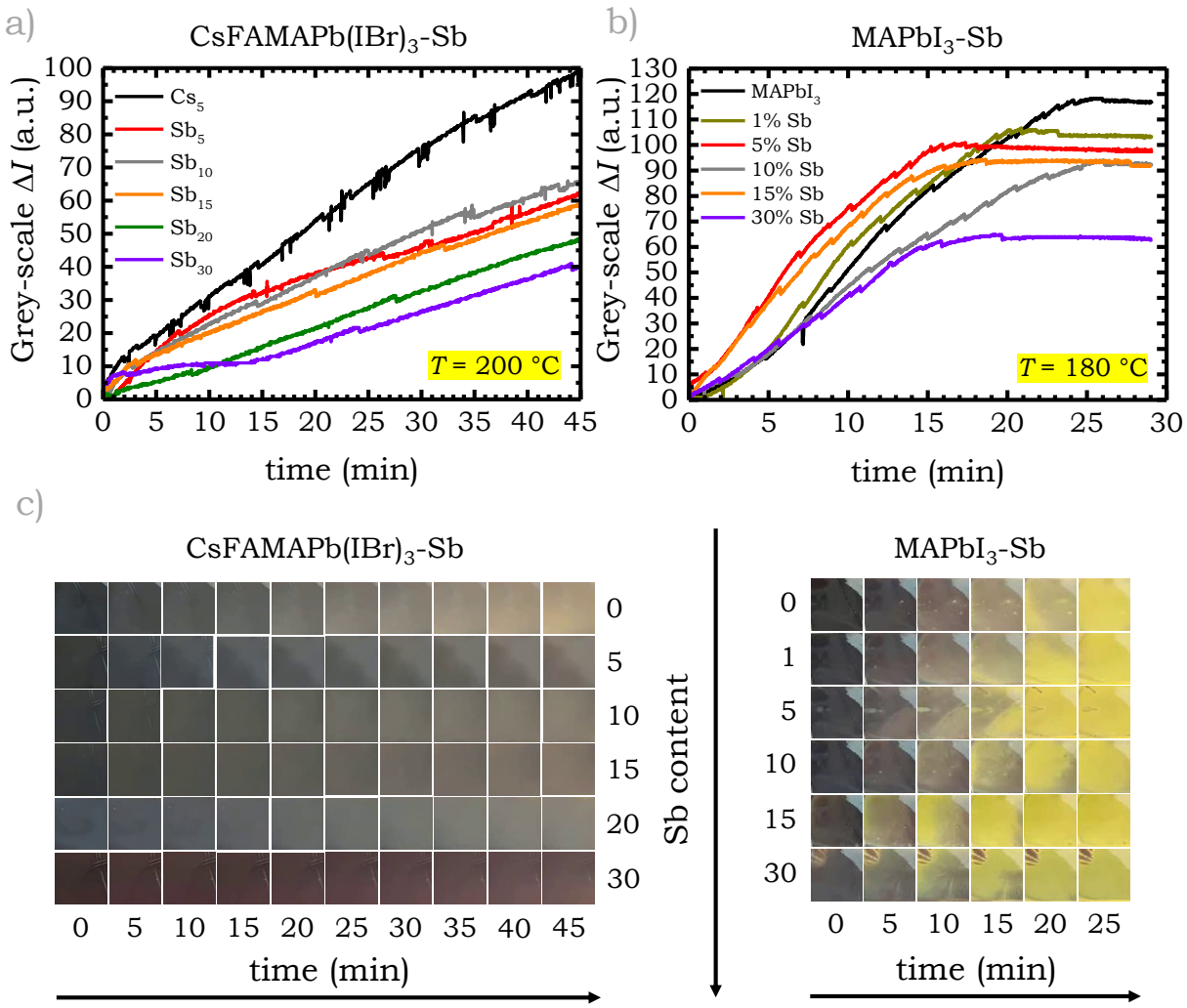

Figure 5.7: Evolution of the grey-scale intensity over time of $CsFAMAPb(IBr)_3$-Sb (a) and $MAPbI_3$-Sb (b) films upon heat exposure under a N_2 atmosphere. c) Images of the heated Pb-Sb perovskite films over time.

The thermal degradation dynamics between systems upon Sb substitution showed opposite behaviours. Increasing percentages of Sb in the single cation perovskite resulted in faster degradation of the films despite increasing the number of microstates. Thermal decomposition in $MAPbX_3$ perovskites is primarily dominated by the sublimation of the organic and halide components followed by the thermal decomposition of the remaining metals at much higher temperatures (equation 5.9).

$$MAPbX_3(s) \rightarrow PbX_2(s) + CH_3NH_2(g) + HX(g) \tag{5.9}$$

This reaction is often independent from the chemical stability of $MAPbX_3$ determined by their enthalpy of formation. For instance, $MAPbCl_3$ has the lowest enthalpy of formation and its degradation occurs earlier when heated than the bromide or iodide analogues because of the lower onset temperature for the sublimation of MACl compared to MAI.[234] This suggests that an increase in the strength of the perovskite halide cage would not critically modify its thermolysis given that the formation of a gaseous product significantly

increases the entropy of the degradation products. However, some substitutions, such as the partial replacement of Pb^{2+} with Sr^{2+}, have been found to increase the onset temperature for thermal degradation of the perovskite.[262] Interestingly, the experimental results revealed the opposite: an accelerated decomposition linked to the incorporation of antimony. This can be attributable to a higher formation of surface defects with the incorporation of antimony stemming from the addition of excess halide. Defects at the surface with much lower energetic barriers to decomposition are thought to accelerate the decomposition in $MAPbI_3$ upon thermal exposure even for temperatures below its TGA-determined decomposition onset.[21]

On the other hand, the progressive incorporation of less volatile cations like Cs into the perovskite structure aided by Sb resulted in the creation of significantly more thermally stable systems, as reflected in figures 5.7 a and c. Here, the bleaching speed of the reference sample (Cs_5) was significantly higher than the one experienced by the Pb-Sb combinations, which decreased with increasing proportions of antimony (combined with Cs and Br). Interestingly, Sb_5 films, while having similar relative proportions of A cations to Cs_5, surpassed the thermal stability of the reference despite containing a much lower percentage of Br. This ion usually enhances perovskite stability and enables the incorporation of higher proportions of the more thermally stable Cs in multi-mixed systems without phase segregation.[11,42] Therefore, the increase in thermal stability upon antimony incorporation is rooted in the ability of Sb to provide a better fit for the smaller but more thermally stable Cs cation into the halide cage without the need of incorporating large proportions of Br. It is to note, that the triple cation perovskite follows a thermal degradation process initiated by the decomposition of the MA organic cation,[287] therefore an increase in the proportions of stronger A cations is desirable to delay the thermal decomposition.

Solar cell operational conditions involve the exposure of the material to heat in combination with oxygen and humidity, which have proven to be detrimental to the stability of halide perovskite devices.[67] Hence, the combined effects of heat, oxygen and water on the Pb-Sb perovskite samples were assessed by reproducing the previous experiment under air at a relative humidity between 60-70 %. The temperature of the hot plate was kept at 180 °C for the $MAPbI_3$-Sb systems and 220 °C for the triple cation mixtures. The average colouration intensity of $MAPbI_3$-Sb and the $CsFAMAPb(IBr)_3$-Sb films with and without a PMMA protective layer were plotted as a function of time in figures 5.8 a, b and c, respectively.

Overall, the exposure to a combination of heat, oxygen and water resulted severely detrimental to the perovskite films containing larger amounts of antimony, independently of the complexity of the system. The negative effects were particularly acute for the $MAPbI_3$-Sb films, where samples with 30 % of Sb fully degraded within the first 10 min of heat exposure. Some samples experienced recrystallization triggered by the combination of heat with ambient moisture before degrading,[320] as marked by the initial decrease of the grey-scale curve. This drop corresponds to a darkening of the film as exposed in figure

D.5 in Appendix D. Progressively lower proportions of antimony delayed the degradation onset from 4 min in the highest substituted sample up to 20 min for the 1 % Sb sample.

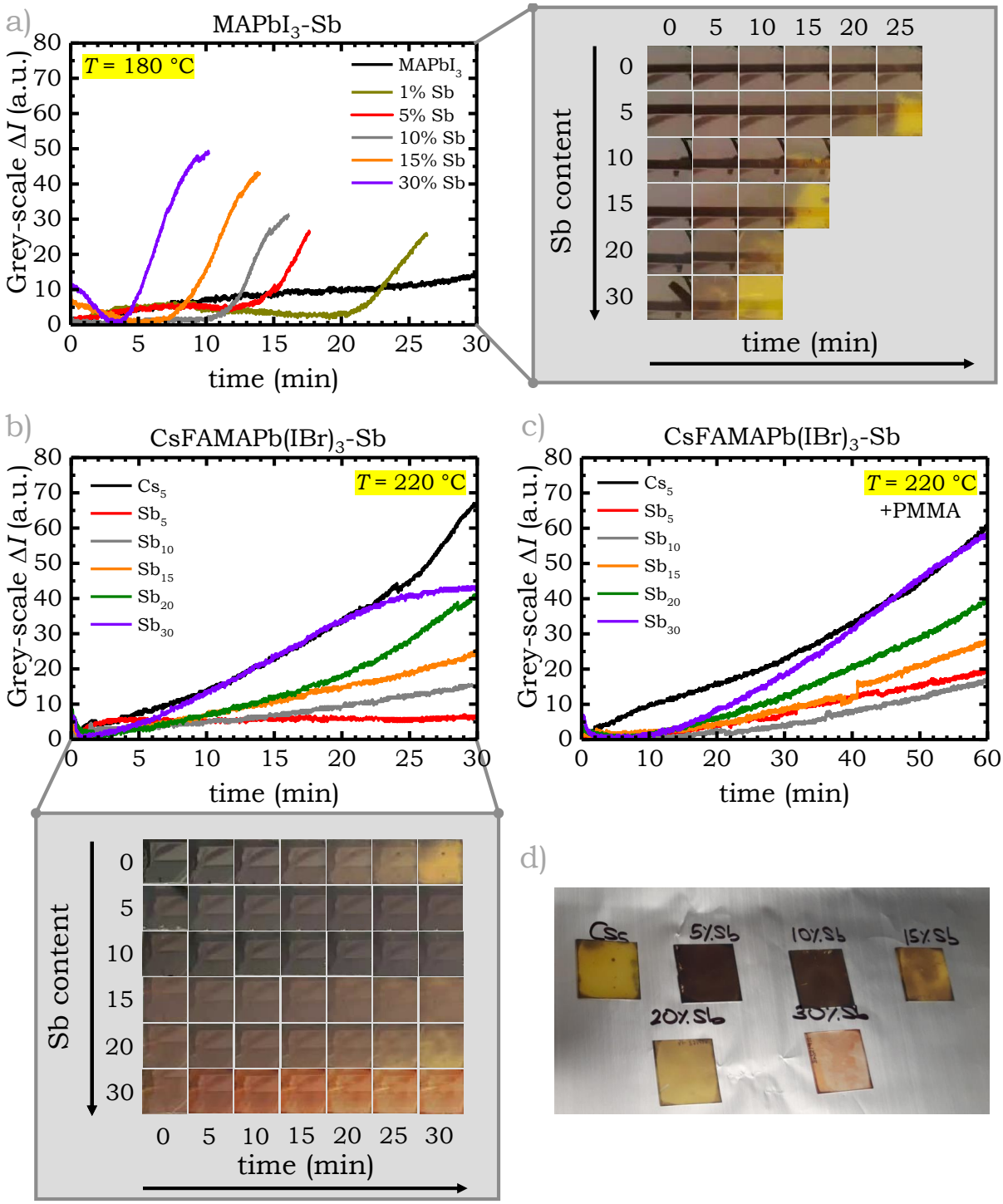

Figure 5.8: Evolution of the grey-scale intensity over time of $MAPbI_3$-Sb (a) and $CsFAMAPb(IBr)_3$-Sb films with (c) and without (b) a PMMA protective layer, upon heat exposure under room conditions (air, 60-70 % RH). Images of the progressive bleaching of the triple and single cation films without PMMA are included at the right and bottom of each graph, respectively. d) $CsFAMAPb(IBr)_3$-Sb films without PMMA after 30 min of exposure to 220 °C.

Normally, reinforcing the structural stability of the perovskite by reducing the halide cage size reduces the percolation of the water molecules through the structure and delays

the degradation.[21] However, the hypothesized presence of surface defects in the $MAPbI_3$-Sb mixtures in combination with the heat might favour the incorporation of water, as revealed by the potential recrystallization experienced by the films, and hence accelerated the degradation process.

Note how the reference $MAPbI_3$ did not show significant bleaching after 30 min of heat exposure, degrading at a much slower rate than in the experiments performed under nitrogen. This peculiarity is ascribed to the experimental conditions. Samples degraded under air were subject to the continuous air re-circulation of the fume hood, only experiencing heat through the substrate. On the other hand, samples degraded in the purge box were affected by a lower re-circulating flow of N_2, which in combination with the hot plate heat in an enclosed atmosphere, created a hotter environment that contributed to the faster thermal decomposition of the films.

In the triple cation system, the effects of oxygen and water played a significant role in the thermal stability of the samples containing high proportions of antimony. While they all performed better than the Cs_5 reference sample upon heat exposure, their bleaching worsened in proportion to their antimony content. Adding a protective PMMA layer only delayed the process, showing similar values of degradation after one hour.

The change in colouration of the triple cation samples without PMMA after 30 min of heat exposure can be seen in figure 5.8 d. Note how the Sb_5 and Sb_{10} samples barely reported any significant bleaching in comparison to an almost fully yellow Cs_5. On the other hand, samples with proportions of antimony above 15 % demonstrated significant bleaching proportional to the amount of Sb. Note how the 30 % Sb retrieved a red-tinted colouration, suggesting a different degradation route than the one experienced by the other compositions, which primarily transformed into PbI_2.

The similar colouration results experienced by both Pb-Sb perovskite systems upon the exposure to a combination of heat, oxygen and moisture pointed to antimony as the primary reason behind the increased sensitivity of the materials to the environment. Chonamada et al. studied the degradation mechanisms of $Cs_3Sb_2I_9$ when exposed to both heat, light, oxygen and moisture. Their study highlighted the formation of various antimony oxides when samples were exposed to water and a combination of oxygen and light.[49] The formation of an oxide phase upon exposure to a 75 % RH atmosphere for a week was also observed in $MA_3Sb_2I_9$.[87] Atmospheric oxygen can be introduced into the halide perovskite lattice contributing to the formation of superoxide species and the degradation of the perovskite. However, this incorporation occurs primarily upon illumination.[259] In a similar manner, the photodecomposition of SbI_3 only occurs when the compound is exposed to both light and oxygen.[78] Given that the experiments were not performed under an intense light source, water is suggested as the primary degradation agent of the Sb-rich mixed perovskite films.

Therefore, to understand the effects of water in the mixed Pb-Sb films, a 10 % Sb triple cation film was subjected to a highly humid atmosphere (>90 % RH) for one day.

In-situ XRD measurements were performed after 1 h, 3 h, 5 h, 12 h and 24 h using the hydration chamber setup described in chapter 3 (figure 5.9). Here, the scans revealed a degradation route where phase segregation dominated over the formation of PbI_2, which is the predominant byproduct in the interaction of state-of-the-art mixed perovskites with water.[99,3]

After only one hour of moisture exposure, the perovskite peaks started to shift towards the lower angles, as highlighted by the (200) reflection from the inset of figure 5.9. The observed shift demonstrated enlargement of the cubic lattice driven by the migration of the smaller elements (Cs, Sb or Br) out of the structure as water molecules permeated through. After 3 h of moisture exposure, peaks compatible with a yellow δ-phase of Cs-rich $CsFAMAPb(IBr)_3$ started to appear in the diffraction pattern, similar to what Abdi-Jalebi et. al observed in triple cation mixed halide perovskite films when exposed to a 50 % RH atmosphere.[3] Equivalently to the interaction between $MA_3Sb_2I_9$ and $Cs_3Sb_2I_9$ perovskites and water observed in the literature,[87,49] the formation of antimony oxide species was preferred over PbI_2. The peaks at 26.7°, 29.9° and 31.5° were correlated with the (123), (025), and (124) reflections of $Sb_3(IO_4)$ arranged in the monoclinic $P12_1/c1$ system. Thus, oxygen is hypothesized to interact with the perovskite as occurring in $Cs_3Sb_2I_9$,[49] permeating through the structure aided by the water-induced lattice separation.

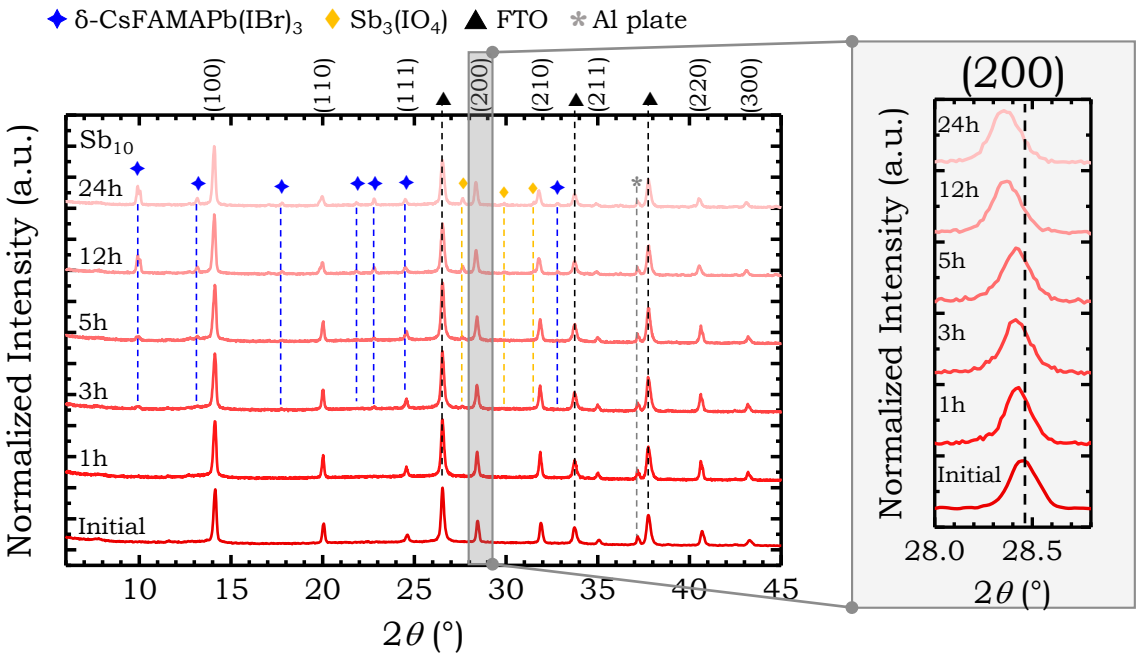

Figure 5.9: *In-situ* XRD indexed patterns of a $Cs_{0.15}FA_{0.71}MA_{0.14}Pb_{0.9}Sb_{0.1}I_{2.65}Br_{0.45}$ film exposed to a >90 % RH atmosphere for 24 h. Peaks corresponding to the formed side phases, FTO substrate and the aluminium base plate are highlighted.

5.7 Conclusion

In this work, the fabrication of mixed Pb-Sb perovskite films both in single and multiple cation systems was achieved, proving the maximization of the number of microstates aided by B-site partial substitution as an effective strategy to form more thermally stable perovskites. The incorporation of a combination of Sb, Cs and Br into the triple cation mixed halide perovskites enhanced their structural stability by providing a more isotropic distribution of the microstrain both across the different crystallographic planes and their order of diffraction, enabling the formation of perovskites with large proportions of caesium and bromide (above 25 %) without phase segregation. This structural reinforcement enabled a higher incorporation of less volatile cations, which in turn, slowed the degradation of the perovskite films when exposed to high temperatures. On the other hand, the use of large amounts of Sb^{3+} posed a challenge to the fabrication of high-performing solar cells due to the creation of more trap states, as revealed by PL measurements. Hence, further exploration of these perovskite combinations in solar cells is required to unveil whether the observed thermodynamic improvement is compatible with high electronic performance.

Chapter 6. Performance and degradation of triple cation antimony-lead mixed halide perovskite solar cells

6.1 Introduction

In the previous chapter, more thermally stable Pb-Sb mixed CsFAMA perovskite films were successfully achieved via ionic partial substitution on the B-site. However, the effects of mixing new elements into the system go beyond mere stability improvement, often altering the optoelectronic properties. For instance Cs, K or Rb have been shown to act as trap passivators and to modify the crystallization process of mixed perovskites, which are key contributions to the final solar cell performance.[101,254,29,351]

Electronic alterations in the perovskite layer can be tailored further to increase solar cell efficiency through heterovalent substitutions on the B-site to attain n-doping, which favours larger open-circuit voltages. Although n-doping is not always easily achievable through the partial substitution of Pb^{2+} with 3^+ elements,[45,2] it has been found to occur in both Bi^{3+} and Sb^{3+} partially substituted $MAPbX_3$ perovskites despite the increased number of defects and trap states observed in these systems.[296,203,69,338,38,104] In particular, the partial substitution of Pb with Sb in $MAPbI_3$ solar cells has reported an overall improvement of the photovoltaic parameters, achieving a record open-circuit voltage of 1.13 V through effective tailoring of the crystallization conditions.[338,38] Similar improvements associated with n-doping were observed in ETL-free 2 % Sb substituted $MAPbI_{(3-x)}Cl_x$ solar cells and in HTL-free Sb-$CsPbI_3$ carbon-based devices.[104,317] Even the incorporation of Sb^{3+} in very low proportions retrieved improved performances in $Cs_{0.1}FA_{0.9}PbI_3$ cells, with a stabilized record *PCE* of 21.04 %, a high fill factor of 0.84 and small hysteresis.[238] In a more recent publication, Liu et al. achieved improved device performance and thermal stability of stoichiometric $MAPbI_3$ when small proportions of antimony acetate were incorporated as an additive.[175] Here, antimony-containing solar cells reported a 25 % increase in the degraded *PCE* compared to the reference after being heated in air at 85 °C for 55 days.[175] Hence, the incorporation of Sb into the triple cation suggests interesting prospects both from the performative and stability points of view.

Ultimately, the long-term thermal stability of perovskite solar cells is also dependent on the endurance of the charge extraction layers, especially of the hole transporter in *n-i-*

p device architectures,[117,171,195] for which many record stable devices discard the use of Spiro-OMeTAD.[8,189,13] Hence, exploring the device stability of Pb-Sb mixed perovskites with different extraction layers is critical to ensure an effective translation of the thermal endurance of films into devices.

In this chapter, the performative and stability effects of the partial substitution of Pb for 5 % Sb in CsFAMA perovskite solar cells will be studied. To do so, the impact the addition of trivalent ions has on the conductivity and ionic mobility of the Sb mixed perovskite layer will be first investigated. Then, the potential n-doping effects on the performance and hysteresis rates of the solar cells will be assessed in conjunction with the band alignment of the perovskite absorber with different ETLs, HTLs and interlayers. Finally, the stability of the planar heterojunction devices will be evaluated through dark storage and heat ageing tests in comparison to the state-of-the-art Cs_5.

6.2 Characteristics of the Pb-Sb solar cells

Partially substituting Pb^{2+} with Sb^{3+} in multi-mixed perovskites substantially raised the thermal decomposition onset of state-of-the-art CsFAMA films. In the previous chapter, this enhanced stability was linked to the suitable combination of increased entropy with the presence of stronger bonds in the system, inherent to the incorporation of an element with a smaller ionic size and larger valency. A stronger structural bonding within the perovskite structure should encompass a reduction of ionic movement upon voltage bias or light illumination, which is attributed to be the main mechanism behind the appearance of damaging hysteresis in perovskite solar cells.[129,158,299,73,244] To determine the impact of ionic motion in the novel antimony mixed devices, the mixed and electronic conductivity of both Cs_5 and 5 % Sb substituted CsFAMA (Sb_5) films was studied between 188 K and 295 K using the lateral device described in chapter 2. The conductivity of the films at various temperatures was extracted from the *JV* scans taken under dark conditions (figures E.1 and E.2, appendix E) and was plotted in figure 6.1 a.

Two slopes were identified in each data set corresponding to the regions with a dominance of the ionic (high temperatures) and electronic (low temperatures) conduction mechanisms, transitioning at a similar temperature to the one observed in the literature for CsFAMA perovskites.[32,329] Note that the linear fits excluded the points marked with a star since they were the result of an unexpected change in the speed of the scan rate, triggered by an error in the source meter programming. The activation energy (E_a) of the ionic-dominated region was extracted from the first linear fit using the Nernst–Einstein relation:

$$\sigma(T) = \frac{\sigma_0}{T} \cdot e^{\frac{-E_a}{kT}} \tag{6.1}$$

where k is the Boltzmann's constant, σ_0 is a constant, and T is the temperature.[32,329]

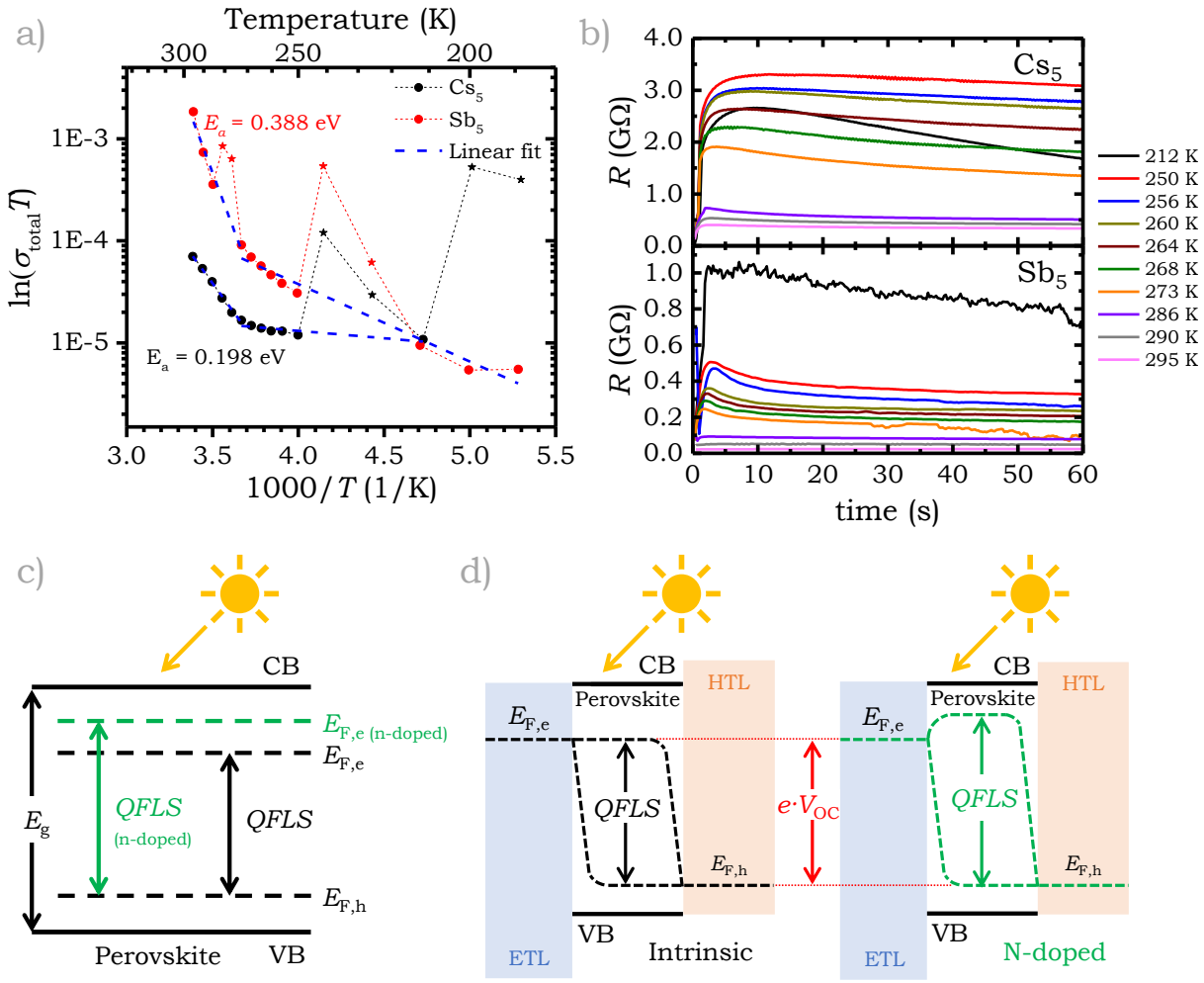

Figure 6.1: a) Temperature-dependent mixed conductivity plot of Cs_5 and Sb_5 films with the correspondent linear fit for the ionic and electronic regions. b) Galvanostatic measurements of Cs_5 and Sb_5 perovskite films performed between 212 K and 295 K. Effects of n-type doping on the quasi-Fermi levels of a perovskite semiconductor upon illumination (c) and in the open-circuit voltage of a solar cell (d). For simplicity, the effects of the interfaces have been ignored in the diagram, assuming perfect alignment of charge transport layers and perovskite in the intrinsic case.

The results confirmed the stronger bonding of the Sb_5 perovskite compared to the Cs_5 by almost doubling the activation energy for ion migration. The Cs_5 film presented an activation energy of 0.198 eV in the ionic dominant region, which laid within the range of values reported in the literature,[32,329] while the Sb_5 film reported an energy barrier of 0.388 eV, substantially hampering the ionic movement. Similarly, the slope of the linear fit belonging to the electronic conductivity region in the antimony mixed sample was found to be steeper than the one observed in the reference sample. This linear region is often associated with defect ionization.[347] Hence, the increased slope displayed by the Sb_5 sample was compatible with the partial substitution of Pb^{2+} with an ion with higher ionisation energies such as Sb^{3+}.[167]

Beyond ionic motion, the temperature-dependent scans revealed a higher conductivity of the antimony mixed films, which was also observable in the galvanostatic measurements

performed in the dark at different temperatures and plotted in figure 6.1 b. Here, the resistance of the reference sample decreased with increasing temperature displaying similar magnitudes to the ones observed in lead-based perovskites.[347] While the trend was kept in the antimony-mixed film, the resistance values were significantly lower, which pointed to the presence of more electrons in the system inherent to the substitution of bivalent lead for trivalent antimony.

The incorporation of more electrons in a semiconductor lattice is known as n-doping and can be particularly beneficial for improving the performance of solar cells. Under illumination, n-doping raises the quasi-Fermi level for electrons ($E_{\mathrm{F,e}}$) in a semiconductor, which represents the density of free photogenerated electrons in the conduction band. As represented in figure 6.1 c, an increase in $E_{\mathrm{F,e}}$ enlarges the distance with the quasi-Fermi level for holes ($E_{\mathrm{F,h}}$), representing the population of holes. This distance, known as the quasi-Fermi level splitting ($QFLS$), is proportional to the open-circuit voltage of the perovskite solar cell when there is no bending of the quasi-Fermi levels and each of them aligns with the respective electrode work function (figure 6.1 d).[34] However, the expected n-doped induced $QFLS$ increase in Sb_5 solar cells will not be observed in the device V_{OC} if the band alignment between the charge extraction layers and the perovskite worsens, as represented in figure 6.1 d, or if there is a heavy compensation from the intrinsic defects observed upon Sb incorporation.

Intriguingly, the increase in the Fermi level associated with the observably higher electron concentration in the Sb_5 perovskite films did not result in an enhancement of the solar cell open-circuit voltage, as revealed in figure 6.2 a. Here, the average photovoltaic parameters of several batches of solar cells fabricated in a planar heterojunction structure with FTO/TiO_2/Perovskite/Spiro-OMeTAD/Au revealed similar average performances between the Cs_5 and Sb_5 devices.[1]. Yet, the large drop in open-circuit voltage manifested by the antimony mixed samples critically limited the performance of the record cells as evidenced in figure 6.2 b.[2]

An increase in the Fermi level of the perovskite associated with n-doping with antimony was previously reported by Zhang et. al and Chatterjee et al. both through experimental and DFT calculations in the $MAPbI_3$-Sb system.[338,38] However, the improvement in open-circuit voltage was only observed in devices with relatively low proportions of antimony, particularly in *n-i-p* architectures.[338] Devices fabricated with proportions of Sb^{3+} superior to a 10 % of molar content reported a significant reduction in the V_{OC} which was mainly attributed to the trap increase induced by the Sb 5p state.[338] Similarly, the PL results exposed in chapter 5 revealed a significant increase of trap states in the perovskite films which was more acute for the triple cation system than for the $MAPbI_3$-Sb. Hence, trap-assisted recombination is pointed as a critical agent behind the reduction of the open-circuit voltage in the Sb_5 devices compared to the Cs_5, given that the difference

[1] JV scans were acquired at 0.76 sun illumination. Plotted results display the conversion of values to 1 sun ($J_{\mathrm{SC\text{-}0.76\,sun}}/0.76$)

[2] See footnote 1

in band gap between perovskites only reduces the V_{OC} in 0.04 eV.

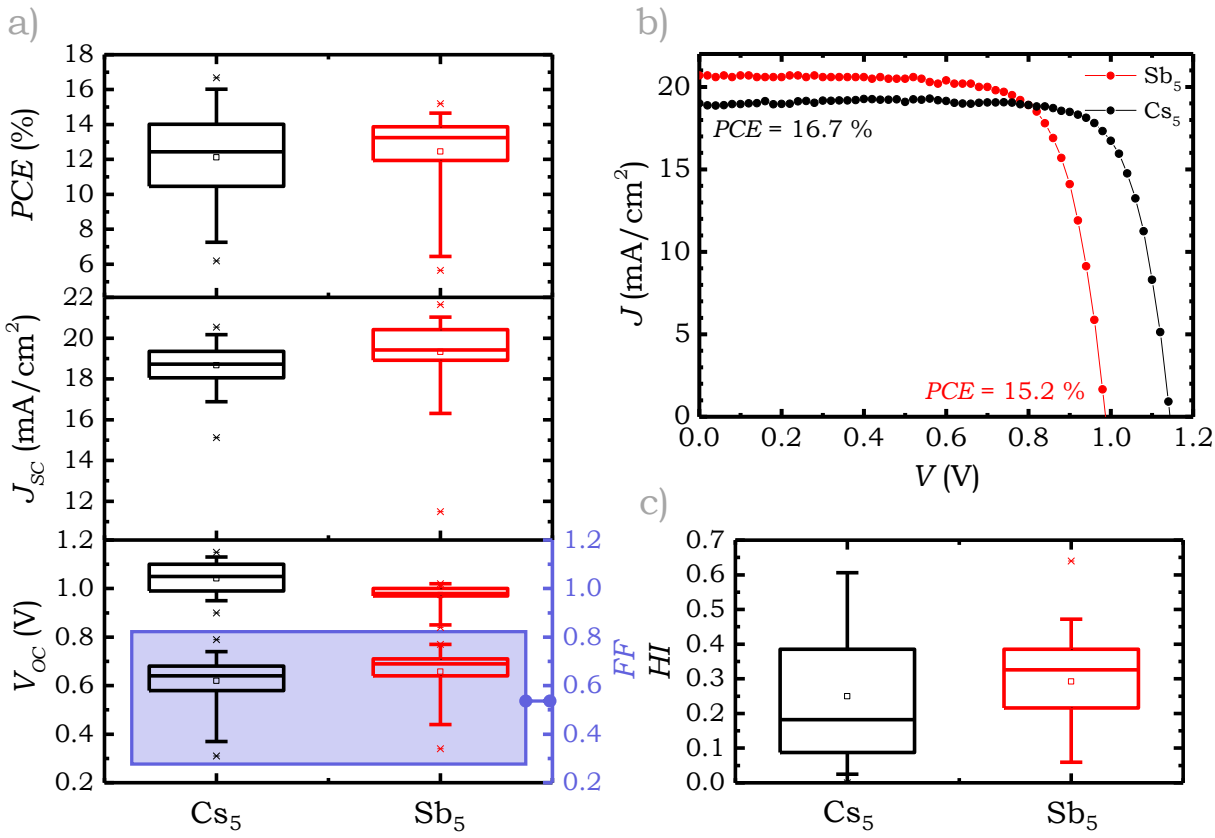

Figure 6.2: Box plot statistics of the photovoltaic parameters in the reverse scan (a) and hysteresis index (c) of several batches of optimized Cs_5 and Sb_5 solar cells with *JV* scans of record devices (b).

Interestingly, the decrease in V_{OC} due to Sb-induced recombination in solar cells with large proportions of Sb^{3+} reported in the literature was also accompanied by a reduction in the short-circuit current, which was not observed in the antimony mixed devices from this work.[338] On the contrary, Sb_5 solar cells highlighted a significant improvement in both the average and maximum J_{SC} compared to the reference. High J_{SC} values were observed in Sb_5 solar cells independently of the thickness of the perovskite layer, providing the complete crystallization of the film at high temperatures (140 °C for 1 h) as evidenced in figures E.3 and E.4 from appendix E. Although a reasonable improvement in the short circuit current was attributable to the lower band gap of the Sb_5 perovskite (1.59 eV) compared to the Cs_5 (1.63 eV), the detrimental effects observed in J_{SC} values of Sb_5 devices fabricated with excess PbI_2 pointed at the ETL/perovskite band alignment as a significant playing factor in the improvement of charge injection (figure E.4-b, appendix E). Contrarily to what occurs with the Cs_5 devices, where the introduction of excess PbI_2 is beneficial for the performance since it acts as a trap passivator at the interfaces,[266,222,194] its presence in the Sb_5 solar cells significantly hampered the charge extraction by acting as a barrier between the antimony clusters in the perovskite and the TiO_2. An enhanced charge injection between the TiO_2 and the Sb_5 perovskite was

likely caused by the hybridization between the Sb 5s and I 2p states and the I 6p and Ti 3d states reported by Qiao et al., which was reduced in the lead-based systems.[238] In their work, the introduction of small amounts of antimony favoured the performance of $Cs_{0.1}FA_{0.9}PbI_3$ solar cells by improving both the charge injection and the fill factor, which was also observable in the Sb_5 solar cells.[238] Likewise, a closer band alignment between the TiO_2 layer and the Sb_5 perovskites is also hypothesized to contribute to the charge extraction improvement.

Notwithstanding the increased charge extraction and the reduced ionic mobility of the antimony mixed devices, similar rates of hysteresis to the ones displayed by the Cs_5 cells were observed, with a higher average than the reference (figure 6.2 c). The hysteretic behaviour displayed by perovskite solar cells is commonly explained in the literature through the presence of ferroelectricity,[41,311] charge trapping and de-trapping,[152,299] and ionic migration.[244,73,113] While these factors usually coexist, ion migration and interfacial recombination have been suggested as the main contributors to the hysteresis in devices, both of them primarily manifesting at the interfaces between the perovskite and the charge extraction layers.[129,158,299,73,244] Given that the Sb_5 perovskites have demonstrated a higher activation energy for ionic motion than the Cs_5 and increased traps, in the following section, the role that interfacial recombination played in the performance and hysteresis rates of antimony-mixed perovskite cells is studied using different ETLs and interlayers.

6.3 Band alignment and charge accumulation at the perovskite/ETL interface

In regular *n-i-p* planar heterojunction solar cells, charge accumulation occurs at the ETL/perovskite interface due to the bulk low electron mobility of TiO_2 (0.1-4 $cm^2\,V^{-1}\,s^{-1}$) in comparison with the hole extraction rate at the HTL.[349,326] This accumulation can be reduced by selecting an ETL with a higher bulk electron mobility such as SnO_2 (250-450 $cm^2\,V^{-1}\,s^{-1}$).[173,224,115] Its wide band gap and deep conduction and valence bands usually provide a better alignment with the perovskite layer, which translates into the high V_{OC} and *PCE* values observed in the literature.[169,132] Additionally, its good optical and chemical stability as well as its lower temperature fabrication compared to TiO_2, pose SnO_2 as a promising candidate ETL to commercially produce highly stable devices.[323]

Considering the aforementioned,the effects of introducing SnO_2 as the electron transporting layer were studied in both the hysteresis rate and device performance of Sb_5 solar cells. To do so, compact and colloid-based SnO_2 layers were prepared for the fabrication of Sb_5 and Cs_5 solar cells and their performance and hysteresis rates compared against reference TiO_2 devices in figure 6.3.[3]

[3]See footnote 1

Despite the large performance variability displayed by the Cs_5 devices in this batch, the record cells showcased a similar trend to the ones reported in the literature. Solar cells fabricated with compact SnO_2 slightly raised both the open-circuit voltage and fill factor compared to TiO_2 due to an improved band alignment in the perovskite/ETL interface as illustrated in subfigures 6.3 c1 and c2 and achieved lower rates of hysteresis thanks to the improved electron mobility of the ETL. On the other hand, the SnO_2-NP cells showed a slight performance decrease in comparison with the TiO_2 reference devices, driven by a lower open-circuit voltage and fill factor. This behaviour is hypothesized to be the result of the low annealing temperature used during the synthesis of the SnO_2-NP layer, which dropped the Fermi level below the TiO_2 one and worsened the perovskite/ETL band alignment.[10] Additionally, the slightly lower J_{SC} values observed in the compact SnO_2 are speculated to be the result of a more irregular morphology of the spin-coated SnO_2 layer compared to more surface homogeneous methods like ALD.[323,223]

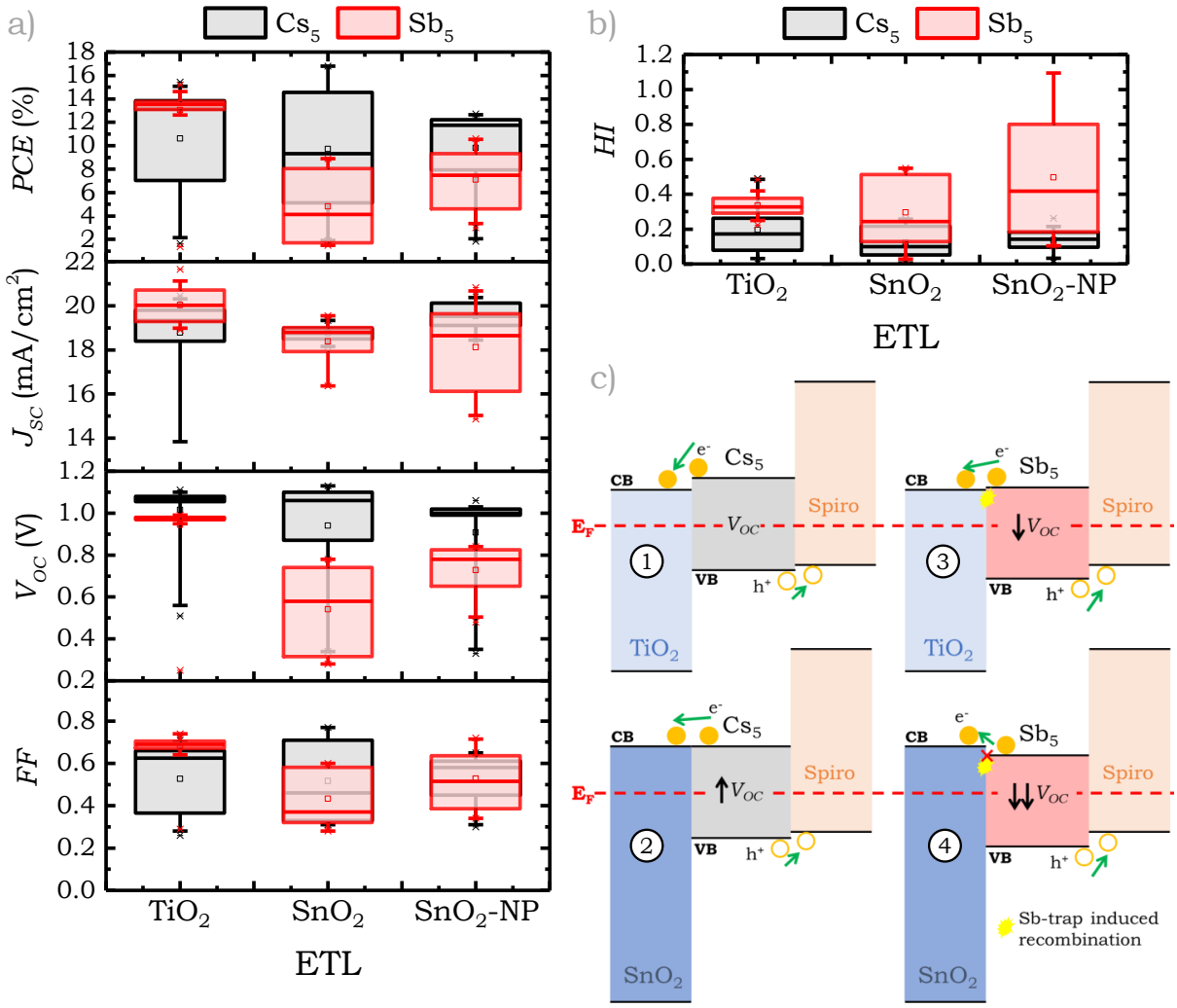

Figure 6.3: Box plot statistics of the photovoltaic parameters in the reverse scan (a) and hysteresis index (b) of Cs_5 and Sb_5 solar cells fabricated on compact TiO_2, compact SnO_2 and nanoparticle-based (NP) SnO_2 ETLs. c) Hypothetical band energy position of the Cs_5 and Sb_5 perovskite solar cells prepared with TiO_2 versus compact SnO_2. For simplicity, interface effects have been ignored in the diagram.

Surprisingly, Sb_5 solar cells fabricated with tin oxide showcased a particularly adverse response, both in their overall performance and hysteresis rates. The standard SnO_2 layer, which showed a favourable response in the Cs_5 samples, reported the lowest-performing devices due to a critical drop in V_{OC} and *FF*. This behaviour is hypothesized to be the result of a worsened band alignment between the ETL and the perovskite driven by a drop in the valence band maximum (VBM) of the Sb_5, similar to the one observed by Qiao et al. in their antimony doped $CsFAPI_3$ films and by Huang et. al in Sb partially substituted $MAPbI_{(3-x)}Cl_x$ films.[238,104]

A VBM drop paired with a slightly increased perovskite Fermi level induced by n-doping is compatible with a closer position between the conduction bands of the Sb_5 and the TiO_2 (figure 6.3 c3), favouring the extraction of charge as demonstrated by the superior J_{SC} values observed in the devices. Conversely, this hypothetical drop worsens the alignment of the perovskite VB and the HOMO level of the Spiro-OMeTAD, slowing the extraction of holes and therefore generating additional V_{OC} losses to the inherent charge trapping induced by Sb. Following the same hypothesis, a raised Fermi level in the SnO_2 compact layer can form a slight energy barrier to charge extraction when paired with the perovskite VBM drop (figure 6.3 c4). This induces an accumulation of electrons at the interface that recombine with the holes in the valence band, provoking the larger V_{OC} and *FF* losses observed in the Sb_5 SnO_2 devices. On the other hand, the considerable performance improvement observed in the Sb_5 SnO_2-NP cells compared to the compact ones likely responds to the lower position of the Fermi level of the colloid-based ETL. In this case, the superior alignment observed with the TiO_2 is not achieved, yet it is sufficient to reduce the device recombination compared to the compact SnO_2.

It is crucial to note that although the VBM drop hypothesis is able to coherently explain the device behaviour reported in figure 6.3, this VBM change should be confirmed by ultraviolet photoelectron spectroscopy (UPS) or scanning tunnelling spectroscopy measurements (STS).

An additional consequence of the worsened band alignment in SnO_2 Sb_5 devices was the presence of a larger number of charges accumulating at the interfaces, which worsened the hysteresis rates beyond the Sb-induced charge trapping and de-trapping, as highlighted in figure 6.3 b. The significantly larger hysteresis index of the nanoparticle-based SnO_2 devices is attributed to the presence of deeper traps in the SnO_x layer formed during the unoptimized temperature annealing, similarly to what was concluded by Aygüler et al.[10] Here, they explored the tunability of the Fermi level of ALD SnO_x layers by thermal annealing the ETL at different temperatures, highlighting that temperatures below and above the optimal for the process (180 °C) were correlated with higher trap energy at the SnO_x/perovskite interface, leading to enhanced recombination and higher *HI*.[10] Charge transport in metal oxides is based on a trapping-de-trapping mechanism which is slowed down with trap depth.[66,10] A slower mobility of the electrons in the SnO_2 layer induces higher charge accumulation at the perovskite/ETL interface, especially in

the n-doped system, which justifies the larger difference in *HI* observed between SnO_2 devices fabricated with Sb_5 versus Cs_5.

The minor contribution of ion migration to the hysteresis of Sb_5 solar cells compared to the Cs_5 was further evidenced by the inclusion of an interlayer between the perovskite and the TiO_2 (figure 6.4). Often, a successful reduction of hysteresis is achieved in planar architectures through the incorporation of thin fullerene-based interlayers such as PCBM (phenyl-C_{61}-butyric acid methyl ester).[322,183,353] Zhong et al. proposed that the permeation of the PCBM molecules through the grain boundaries of the $MAPbI_3$ perovskite layer immobilized iodide defects, limiting ionic migration and reducing the device hysteresis.[353] Additionally, a thin layer of PCBM is often used to tune the energy level alignment between TiO_2 and perovskite, given the higher working function of the fullerene molecule (figure 6.4 c).[183,119]

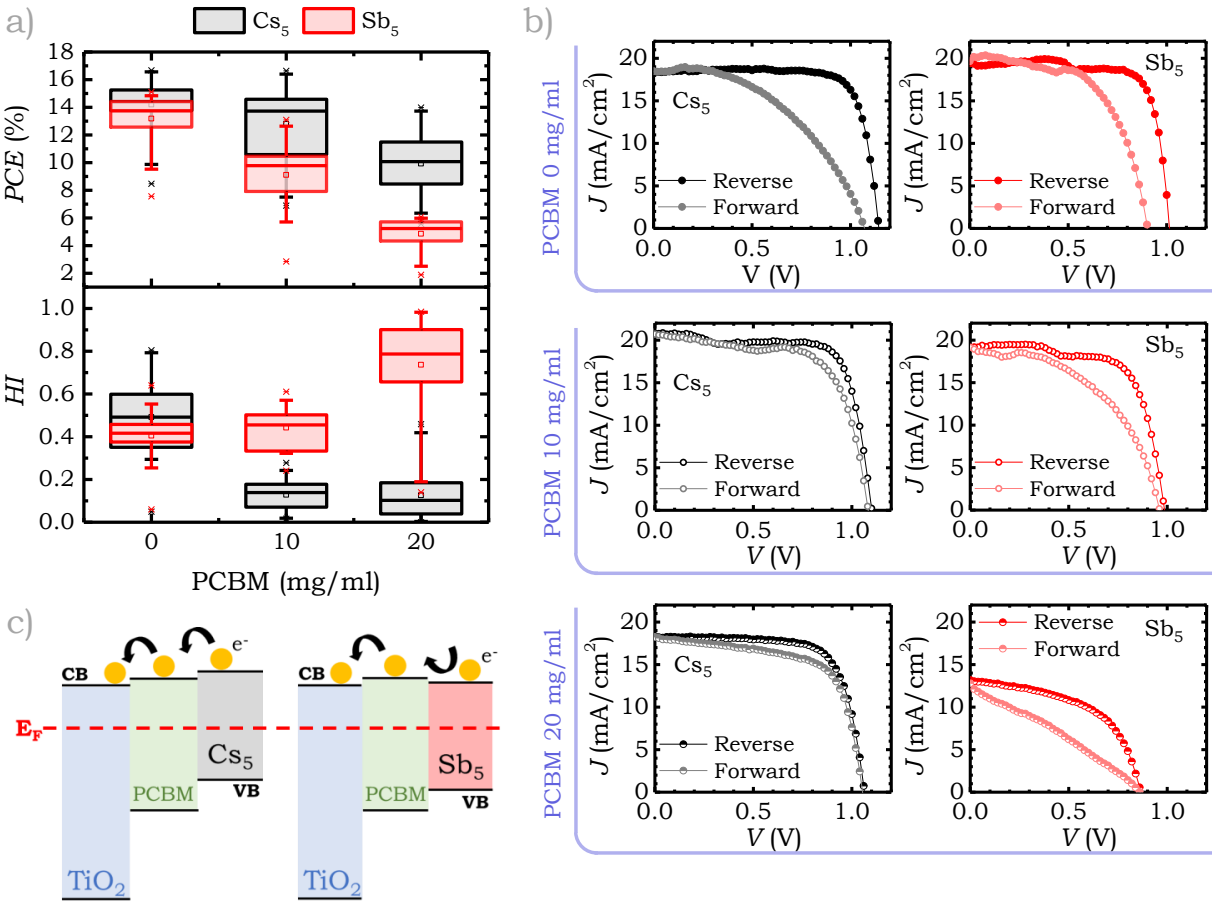

Figure 6.4: a) Box plot statistics of the reverse scan performance and hysteresis index of Cs_5 and Sb_5 solar cells fabricated with a layer of PCBM with various concentrations of the fullerene molecule between the ETL and absorber layers. b) Difference between the reverse and forward scans of the cells in (a). c) Diagram of the conduction band positions for Cs_5 and Sb_5 with a PCBM interlayer (interface effects have been ignored).

The successful reduction of hysteresis was observed in the Cs_5 devices fabricated with an interlayer with two concentrations of PCBM in comparison with the fullerene-free cells,

as highlighted in figure 6.4 a. [4] Here, the inclusion of an excessively thick PCBM layer ($20\,\mathrm{mg\,mL^{-1}}$) was still beneficial for the reduction of the *HI* parameter despite reducing the maximum *PCE* in almost a 3 % compared to the reference device.

On the other hand, the incorporation of the fullerene layer in the Sb_5 perovskite severely hampered the charge extraction by acting as a barrier between the hybridized Sb clusters from the perovskite and the TiO_2,[238] resulting in a much higher solar cell performance drop. This effect coalesced with a conduction band misalignment between the Sb_5 and the PCBM induced by the VBM drop (figure 6.4 c). While the difference in open-circuit voltage between the reverse and the forward scans of the antimony mixed devices was reduced (figure 6.4 b), limiting the charge extraction with a thick PCBM layer induced higher charge accumulation at the interface, which skyrocketed the *HI* index (figure 6.4 a).

It is indisputable that an appropriate band alignment tuning between the antimony mixed perovskite, ETL and in-between layers is critical to optimize the charge extraction and limit the voltage losses. However, a simplified picture has been presented here, addressing only the quasi-steady state of the system under illumination. Under real conditions, transients induced by light or by the application of an external voltage bias affect the ionic distribution, as summarized in figure 6.5.[74]

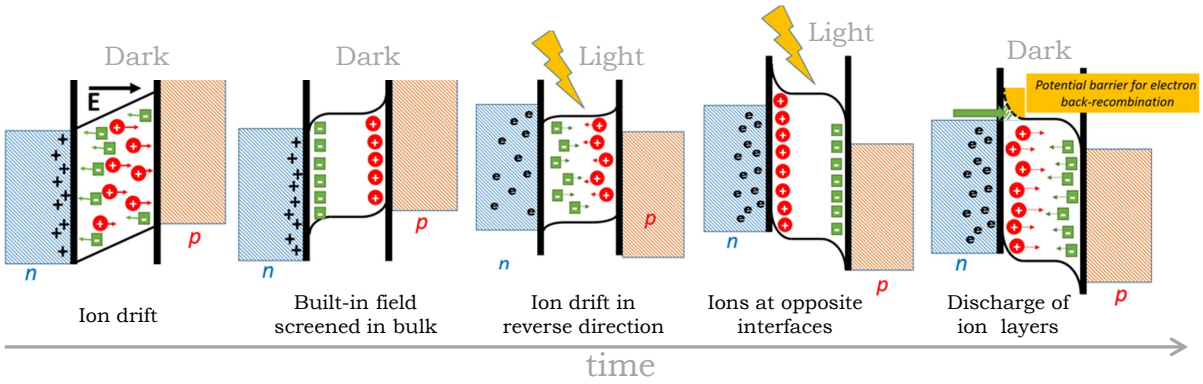

Figure 6.5: Evolution of the perovskite energy diagram at open circuit from left to right: after contact in dark, in equilibrium in dark, after light illumination, in equilibrium under light and after light soaking in dark. Adapted with permission from[74].

When the PSC layers are put in contact in the dark, the energy levels align creating a built-in voltage that will be subsequently screened in the bulk as the ions drift towards the interfaces.[235,74] Immediately after illumination, the appearance of a photovoltage creates an electric field opposite in sign to the built-in voltage that drifts the ions towards the opposite interfaces within tens of seconds until reaching equilibrium.[235] In this condition, the PSC V_{OC} is determined as the sum of the built-in potential and the electrostatic potential.[74] Switching the light off triggers ion movement again to re-establish the dark equilibrium condition.[235]

[4] See footnote 1

This ionic movement has been suggested to reduce recombination in PSCs by reducing the capture cross section as electronic charges are screened, and by stabilizing filled traps.[235] Therefore, the observed changes in the Sb_5 activation energy for ionic movement will likely have an impact on the trap-assisted recombination, which is increased compared to the Cs_5 reference, as observed in the TRPL scans. Additionally, ion migration modifies the band offsets and local band bending as reflected in figure 6.5 depending on the nature of the contact. For instance, in "hard" inorganic ETLs like TiO_2 and SnO_2, the mobile vacancies can become adsorbed at the interface introducing surface dipoles that affect charge injection, whereas in "softer" layers like PCBM, the mobile ions can permeate into the contact.[235] The complex dynamics between ion mobility and charge extraction and recombination cannot be deconvoluted using dynamic measurements like JV scans, where the presence or absence of hysteresis is not always a good measure of the effects of ion motion.[31] Thus, performing alternative measurements using electrochemical impedance spectroscopy (EIS), Intensity Modulated Photovoltage Spectroscopy (IMVS) or Open Circuit Photovoltage Decay (OCVD) techniques is highly desirable to properly unveil the effects of ionic distribution and traps displayed by the Sb_5 system.

6.4 Modification of the HTL

While the thermal stability of the antimony mixed perovskite films has proven to overcome that of the Cs_5 reference, guaranteeing the long-term thermal endurance of solar cells requires the coalescence of multiple factors beyond a good heat tolerance of the absorber layer. Normally, the first signs of device thermal degradation are linked to the decomposition of the hole transporter and the migration of the metal electrode into the perovskite.[195,117,68]

Spiro-OMeTAD (2,2',7,7'-tetrakis(N,N-di-p-methoxyphenylamine)-9,9'-spirobifluorene) is one of the most used organic hole transporting materials in perovskite solar cells. However, it suffers from a low conductivity and intrinsic hole-mobility in a pristine state, requiring the addition of dopants (lithium bis(trifluoromethane sulfonyl)imide (Li-TFSI) and 4-tert-butyl pyridine (tBP)) to improve its p-type conductivity.[1,305,93] Li-TFSI is introduced to promote the oxidation of Spiro-OMeTAD by O_2 in a reaction described by Abate et al.[1] while tBP enhances the charge extraction at the interface by acting as a morphology controller, uniformly distributing the lithium salts over the HTL.[305,93]. Unfortunately, tBP evaporates from the surface of the HTL above 85 °C, leading to the accumulation of the lithium salts that, due to their hygroscopic nature, introduce water into the device, decomposing the perovskite layer.[305,195,304]

A wide range of materials have been presented as an alternative to Spiro-OMeTAD, yet their complexity and cost of fabrication stand out as a considerable limitation for large-scale fabrication.[229] Alternatively, a low-cost, highly stable and outperforming hole transporting material was introduced by Petrus et al. as the first HTM for perovskite

solar cells with an amide-based backbone.[229] In their publication, the use of EDOT-Amide-TPA as the HTM in perovskite solar cells improved the long-term stability of the devices by reducing the amount of Li-TFSI and limiting the detrimental migration of the additives thanks to the ability of the amide bonds to coordinate with the lithium ions.[229] Hence, the performative suitability of this HTM was tested with the Sb_5 perovskite in the standard FTO/TiO_2/perovskite/HTL/Au architecture, using Cs_5 as a reference. The photovoltaic parameters of several batches and the record cell JV scans were plotted in figure 6.6.[5]

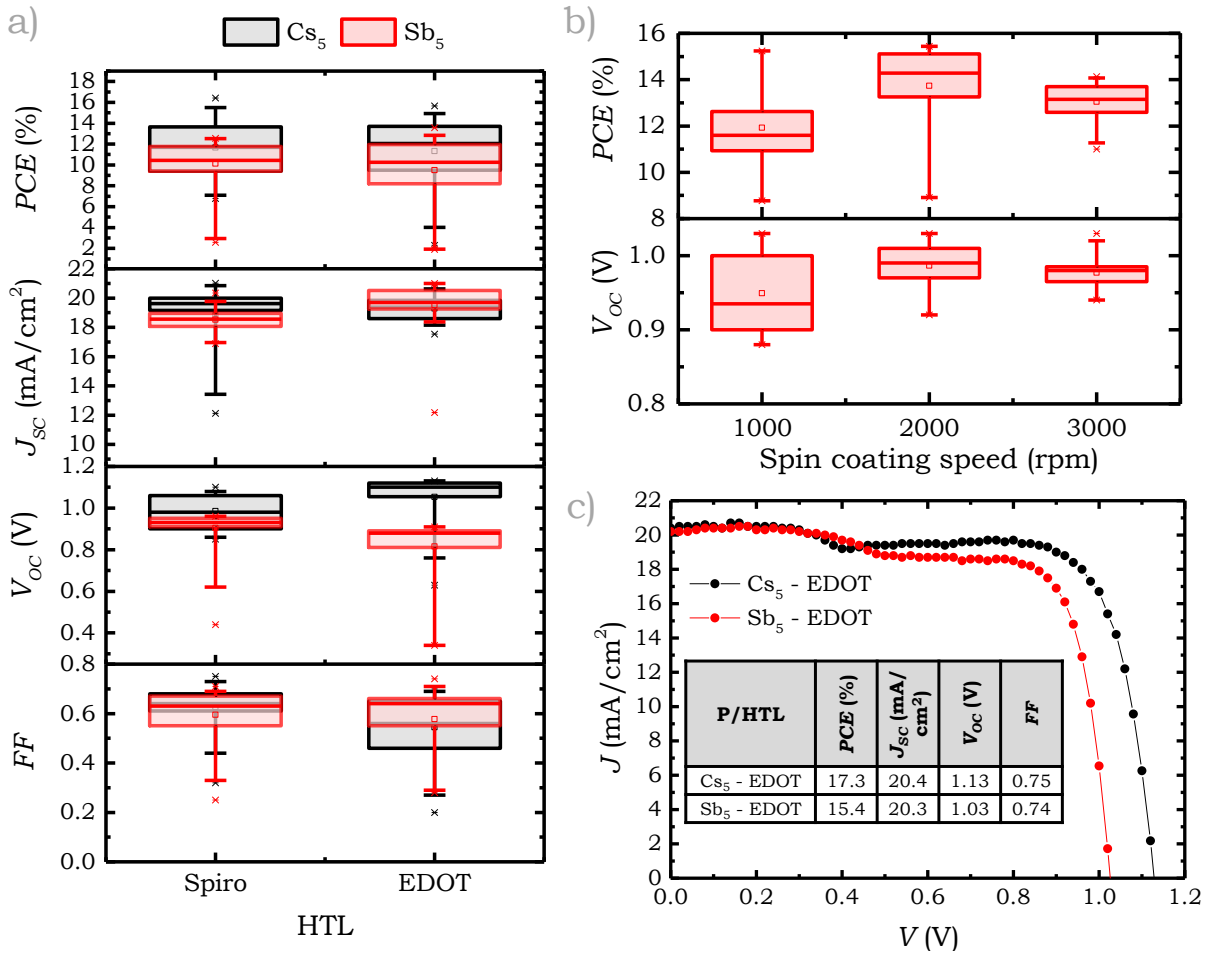

Figure 6.6: Box plot statistics of the photovoltaic parameters in the reverse scan of Cs_5 and Sb_5 solar cells fabricated with Spiro-OMeTAD and EDOT-Amide-TPA as the HTL. b) Dependence of PCE and V_{OC} with the EDOT layer thickness, as a function of spin coating speed. c) JV scans of Cs_5 and Sb_5 record cells fabricated with EDOT-Amide-TPA.

Similar average performance values between Spiro-OMeTAD and EDOT-Amide-TPA were reported for both perovskite systems. The increase in the open-circuit voltage of Cs_5 devices employing EDOT as the HTL lay in agreement with the observations reported by Petrus et al.,[229] thanks to the slightly deeper HOMO energy level of the amide-based HTM. However, the V_{OC} response of the Sb_5 devices in the batch did not showcase this

[5]See footnote 1

improvement. This result is attributable to the variability of the batch-to-batch ambient conditions affecting the speed of the HTL oxidation reaction since subsequent batches showcased a favourable improvement of the V_{OC}. Figure 6.6 b also evidenced the impact the thickness of the EDOT layer had on the open-circuit voltage of a second batch of Sb_5 solar cells, which directly affected the device performance. Record devices of antimony mixed perovskite paired with EDOT-Amide-TPA revealed the improved band alignment at the valence band, obtaining a maximum V_{OC} of 1.03 V, 70 mV above the Spiro record device in the comparative batch.

Note that the performance of the record devices was altered by the accumulation of charge at the interface between the absorber and the extraction layers in both Cs_5 and Sb_5 devices, manifesting as a jump in the JV curves at 0.3 V that resulted in a falsely larger J_{SC} (figure 6.6 c).

6.5 Device degradation

With an optimized recipe for both perovskite systems, degradation tests were performed on the solar cells to discern whether the improved stability of the Sb_5 films was translatable to devices. Initially, dark storage ageing tests were performed on unsealed devices fabricated both with Spiro-OMeTAD and EDOT-Amide-TPA, following a similar protocol to the ISOS-D-1 test conditions described in the literature.[134] Samples were stored in air, in the dark in a low humidity environment (<10 % RH) for a total of 1025 h and JV scans were acquired periodically at room conditions of temperature and humidity (18-22 °C, 60-70 % RH).

After 1025 h of dark storage testing, all samples showcased the presence of δ-$FAPbI_3$ and PbI_2 (figure 6.7 a), which pointed to the combination of light and moisture during the repeated device testing as a crucial source of degradation. As observed in the previous chapter, the formation of lead iodide was reduced in the antimony systems compared to the Cs_5. Interestingly, traces of SbI_3 were detected in the Sb_5 devices, which were likely segregated from the perovskite as a result of moisture permeation in combination with light. The formation of these degrading products over time was key to the progressive electrical average decay of the best 6 devices per variable, plotted in figure 6.7 b. Note that a general performance drop was observed in all samples close to the 400 h mark. This was attributable to the presence of solvents at the contact area between the gold and the measuring pin coming from the layer of silver paste, added after 359 h to preserve a good electrical contact over time. The progressive evaporation of those solvents justified the subsequent partial recovery observed in all devices.

Under dark ageing conditions, the electronic degradation of the solar cells was primarily dominated by the formation of the above-mentioned side phases at the interfaces, rather than a decay triggered by the decomposition of the hole transporting material. In fact, a faster degradation was observed in Cs_5 solar cells fabricated EDOT, which show-

cased a lower average performance after 1025 h of testing (42.5 % of initial *PCE*) than the less stable Spiro system (50 % of initial *PCE*). This performance drop in the EDOT samples was even more acute when compared to the top efficiency, which was reached after 48 hours due to delayed oxidation of the HTL.

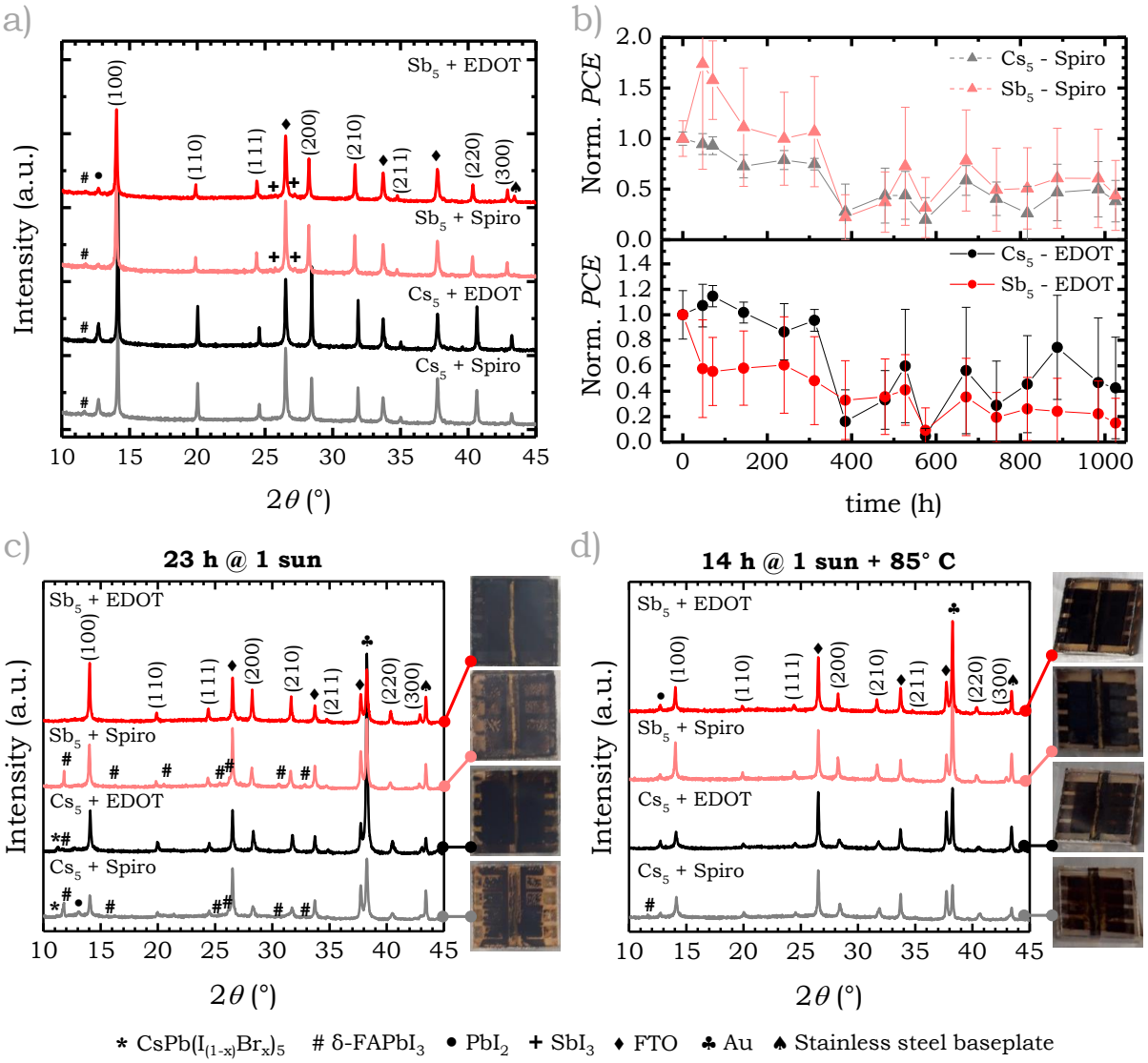

Figure 6.7: a) XRD patterns of the Cs_5 and Sb_5 devices fabricated with Spiro-OMeTAD and EDOT-Amide-TPA after 1025 h of dark storage. b) Average normalized *PCE* from the reverse *JV* scans of the top 6 devices per variable of Cs_5 and Sb_5 perovskite solar cells fabricated with Spiro-OMeTAD (top) and EDOT-Amide-TPA (bottom) over time. XRD patterns of Cs_5 and Sb_5 perovskite solar cells after 23 h exposure to 1 sun (c) and 14 h exposure to 1 sun at 85 °C (d). Images of the degraded devices are included next to their corresponding diffraction pattern.

The observed results pointed at a worsened alignment between the perovskite and the EDOT interface upon formation of side phases, as induced by the dominance of V_{OC} losses in these devices compared to the Spiro ones (figures E.6-a and E.6-b, appendix E). The open-circuit voltage decay was even stronger in the EDOT-Sb_5 solar cells, critically dropping the average *PCE* after only 24 h of dark storage and returning a final perfor-

mance of 14.9 % of the initial *PCE*. The faster electrical decay displayed by the antimony mixed devices was attributable to the formation of SbI_3 over PbI_2, as opposed to what occurred in the Cs_5 cells. Moderate presence of lead iodide has been found to passivate defects at the interfaces,[266,222,194] which is not expected in a compound containing large amounts of Sb^{3+}, given the significant increase in trap states associated with its addition to perovskite. On the other hand, the delayed oxidation of the Spiro in the Sb_5 cells provoked a significant increase in performance after 24 h of the first *JV* scan, which was not observed with the EDOT system. This large increase compensated for the decay of the average performance of the antimony mixed solar cells, which reached similar values of *PCE* drop to the reference Cs_5 after 1025 h.

Next, to solely quantify the effects of light soaking, a fresh batch of Sb_5 and Cs_5 solar cells was exposed to 1 sun LED white light for 23 h at room temperature and 14 h at 85 °C. To prevent moisture ingress, samples were encapsulated using glass slides and a thermoplastic ionomer resin film (surlyn). The results revealed that the combination of light with minimal amounts of ambient moisture able to percolate through the seal was sufficient to degrade the perovskite layer in hours, as highlighted by the XRD patterns in figures 6.7 c and d. At room temperature, the formation of δ-$FAPbI_3$ was stronger in the devices prepared with Spiro due to the hygroscopicity of the lithium salts, which were incorporated into the HTM in higher proportions than in the EDOT-Amide-TPA. Notably, the higher stability of the antimony mixed perovskite was highlighted by the lack of additional side phases that appeared in the Cs_5 such as PbI_2 or the two-dimensional $CsPb_2(I_{(1-x)}Br_x)_5$, which is often observed in CsFAMA perovskites after moisture exposure.[99] On the other hand, the incorporation of heat into the degrading process reduced the inclusion of water molecules into the devices, which limited the formation of the 2D phase in the perovskite layer of Spiro-fabricated devices, leaving PbI_2 as the predominant degradation product in all cells (figure 6.7 d).

Notwithstanding this, the combination of very small amounts of water with light was enough to provoke the electronic death of all devices exposed to light soaking as revealed by figure E.5 in appendix E. The complete loss of performance was ascribed to the degradation of the perovskite/ETL interface induced by the combination of moisture with charges generated during illumination and trapped along the grain boundaries, similarly to what was proposed by Ahn et al.[4] Here, using a similar device architecture, they found the complete performance loss of $FA_{0.4}MA_{0.4}PbI_{2.9}Br_{0.1}$ unencapsulated solar cells after only 6 h of light soaking due to the decomposition of the perovskite layer at the TiO_2 interfaces, demonstrating the irreversible degradation of the perovskite film along the grain boundaries when both moisture and trapped charges coexisted.[4]

Finally, the high-temperature stability of Sb_5 and Cs_5 encapsulated solar cells was tested over time using Spiro-OMeTAD and EDOT-Amide-TPA. The devices were heated in the dark at 85 °C for 999 h and *JV* scans were measured periodically, following the ISOS-D-2 test conditions described elsewhere.[134] The average normalized *PCE* from the

reverse *JV* scans of the best 6 cells per variable, device colouration and XRD patterns after heat exposure were plotted in figure 6.8.

The inherent structural strength of the Sb_5 perovskite layer was visibly demonstrated by the slower bleaching of the devices compared to the Cs_5 (figure 6.8 a), independently of which hole transporting material was used. On the other hand, for the less thermally stable perovskite, the selection of a more durable HTL with a lower amount of dopants was critical to slow the decomposition rate over time. In the Spiro samples, higher proportions of water molecules were driven into the structure by the larger amount of hygroscopic Li-TFSI present in the film, accelerating the degradation of the Cs_5 compared to the EDOT layer. This observation was repeatable in multiple batches, where the formation of $CsPb_2(I_{(1\text{-}x)}\ Br_x)_5$ was detected after 165 h of heat exposure (figure 6.8 c) and manifested as large bleached spots underneath the Au-covered areas after 120 h (figure 6.8 b). This bleaching was not observed in the more resistant Sb_5 devices which, equivalently, did not showcase alternative side phases beyond lead iodide. Additionally, the (100) perovskite XRD peak height displayed a significantly lower reduction than the one observed in the Cs_5 devices (figure 6.8 c). After almost 1000 h of heat exposure, the XRD patterns of the solar cells (figure 6.8 d) unveiled how the perovskite segregation was significantly higher in the Cs_5, which presented large proportions of $CsPb_2(I_{(1\text{-}x)}Br_x)_5$ beyond the formation of the expected PbI_2 byproduct.

The fast decomposition under humid conditions of the Cs_5 was likely enhanced by the presence of excess PbI_2 in the perovskite stoichiometry.[174,270,247,103,293] However, this variation is not considered to be paramount to the device degradation, given the inferior thermal stability in room conditions displayed by stoichiometric Cs_5 compared to Sb_5 films.

Similarly to the perovskite layer degradation, the electronic decay of the solar cells was significantly impacted by the stability of the HTL. As expected, the average performance of Cs_5 samples prepared with Spiro-OMeTAD critically dropped over 90 % of the initial *PCE* after only 12 h of exposure (figure 6.8 e). This decay was driven by the loss of conductivity of the hole transporter after evaporation of the additives,[195,305] which contributed to the morphological decay of both the Spiro and the perovskite/HTL interface.[195,117] This initial performance loss was also observed in the EDOT-based devices, yet the percentage was significantly less acute.

After 2 days of heat exposure, the slight recovery showcased by all samples is hypothesized to be related to a change in the morphology of the perovskite grains, likely experiencing an enlargement favoured by the combination of small amounts of water permeating through the seal and the high temperature of the hot plate.[320] Notwithstanding this, the inclusion of ambient moisture into the device was a critical accelerator of the heat-induced degradation in both HTM-based cells.

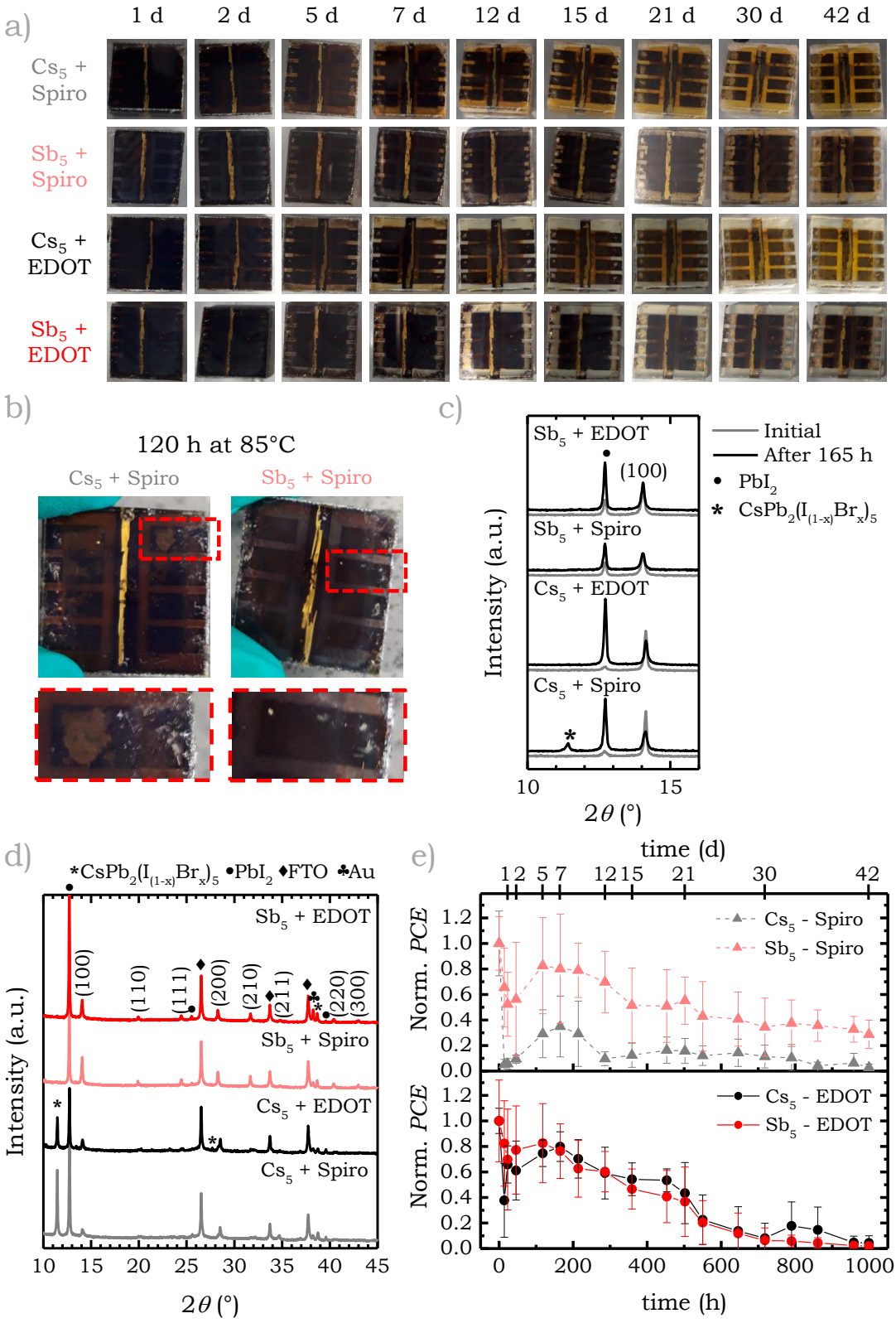

Figure 6.8: a) Images of encapsulated Cs_5 and Sb_5 exposed to 85 °C over time. b) Difference in colouration of Spiro devices after 120 h of heat exposure. XRD patterns of Cs_5 and Sb_5 solar cells after 165 h (c) and 999 h (d) of heat exposure. e) Average normalized *PCE* from the reverse *JV* scans of encapsulated Cs_5 and Sb_5 perovskite solar cells fabricated with Spiro-OMeTAD (top) and EDOT-Amide-TPA (bottom) and exposed to 85 °C over time.

In these experiments, the average performance of EDOT cells reached the T_{80} mark after 5 to 7 days of heat exposure, a much faster thermal degradation rate than the ones reported in the literature by mixed perovskites without Spiro.[229,189]

In addition to the evaporation of the Spiro additives, the accumulation of iodine coming from the Cs_5 perovskite layer exposed to high temperatures has been found to cause a reduction in the HOMO level of Spiro-OMeTAD, creating an energy barrier for the extraction of holes and hence reducing the J_{SC}.[294] On the other hand, a deeper HOMO level in the Spiro layer allows a better alignment with the assumed deeper VBM of the Sb_5 perovskite. Hence, the Spiro HOMO level drop reported by Tumen-Ulzii et al. is hypothesized to contribute to the slower photocurrent decay observed in the antimony mixed devices,[294] which was found to drive the performance loss of the Cs_5 Spiro samples (figure E.6-c, appendix E). On the other hand, the performance drop in the EDOT-based devices was primarily driven by the loss of V_{OC} and FF (figure E.6-d, appendix E), highlighting interface degradation due to the combination of heat, moisture and light.

Although further studies with reinforced encapsulation are necessary to properly unveil the electronic decay of antimony mixed devices, these preliminary results highlight the potential of the Sb_5 solar cells to display improved overall stability compared to the state-of-the-art triple cation perovskites.

6.6 Conclusion

In this work more thermally stable CsFAMA solar cells were successfully fabricated aided by the partial substitution of Pb with a 5 % of Sb, displaying close performances to the reference devices. Electronically, the introduction of trivalent antimony on the B-site acted as a double-edged sword. On the one hand, the improved conductivity achieved through the inclusion of the Sb^{3+} ions favoured the charge extraction in devices, displaying high J_{SC} values, while the enhanced bond strength of the system reduced ion migration, as revealed by the higher activation energy of Sb_5 films. On the other hand, an optimum band alignment between the perovskite and the charge extraction layers was found to be critical to limiting V_{OC} losses caused by the trap-inducing nature of the Sb-mixed compositions, which became the dominant mechanism behind device hysteresis. Overall, antimony mixed solar cells have demonstrated a slower structural decay of the absorber layer when exposed to a combination of heat, light and moisture than their lead counterparts. However, the unavoidable percolation of water into the devices in these experiments triggered a fast performance decay in both Cs_5 and Sb_5 perovskites, limiting the electronic decay analysis. Although further studies with reinforced encapsulation are necessary to unveil the properties and degradation pathways of CsFAMA-Sb mixed devices, this study points to B-site mixing on triple cation mixed halide perovskites as a promising approach to improve long-term device stability, bringing perovskite solar cells a step closer to commercialization.

Chapter 7. Conclusions and future outlook

In conclusion, this thesis focused on the reduction of structural and thermal instabilities of metal halide perovskite solar cells through the tailored compositional engineering of the B-site and questioned, for the first time, the applicability of the Wilson-Stokes approximation in the analysis of XRD halide perovskite microstrain.

Successfully creating more thermally stable perovskite compositions requires inherent stability of the structural arrangement, which is often linked to the distribution of microstrain. Yet, the impact of this property on the solar cell stability and performance and, more importantly, its origin and characteristics are still not clear. In the first part of this thesis, the limitations researchers face when analysing perovskite microstrain results via unsuitable state-of-the-art methods were pointed out. Integral breadth techniques, while easy to apply, result invalid for the extraction of halide perovskite microstrain since the results breach the Wilson-Stokes approximation constraint: parallel *hkl* planes do not report the required equivalent values of microstrain. Through careful optimization of the diffractometer setup and a meticulous selection of a reference sample to minimize data acquisition errors, the persistence of this anomaly is still observed. This suggested the existence of a hitherto unreported microstrain gradient across the order-of-diffraction in halide perovskites. In light of these results, the use of IB methods is encouraged to be discarded for the analysis of microstrain in halide perovskites in favour of analytical techniques that do not require compliance with the Wilson-Stokes approximation, such as the Warren-Averbach.

In the second part of the thesis, more thermally stable multi-mixed CsFAMA perovskite compositions were fabricated by maximizing the number of microstates through a B-site partial substitution of lead with antimony. The co-addition of a combination of 5 % Sb, 7.5 % Cs and 7.4 % Br to $FAMAPbI_3$ improved the perovskite structural stability by enhancing the bond strength and providing a more isotropic distribution of the microstrain both across the different crystallographic planes and their order of diffraction. This translated into a higher thermal decomposition onset and improved stability against moisture, showcased by slower bleaching of the colouration of perovskite films and the presence of lower proportions of side phases in their XRD diffraction patterns in comparison with the state-of-the-art Cs_5. Moreover, the progressive co-addition of the smaller Cs, Br and Sb ions also enabled the assimilation of proportions of Cs and Br above the limit for phase segregation. On the downside, the use of large amounts of Sb^{3+} reported more

trap states and lower carrier recombination lifetimes as revealed by TRPL measurements, which posed a challenge to the fabrication of high-performing devices.

Notwithstanding the challenges, the partial replacement of 5 % antimony in CsFAMA mixed perovskite solar cells reproduced relatively close performances to the reference devices, yet its inclusion acted as a double-edged sword. On the one hand, the n-doping properties of Sb increased the conductivity of the perovskite while its stronger bonding substantially rose the activation energy for ion migration, as revealed by temperature-dependent conductivity measurements. This translated into higher device photocurrent values and lower ion migration. On the other hand, the change in the Fermi levels of the Sb-mixed perovskite required an optimum band alignment with the charge extraction layers to limit V_{OC} losses. Open-circuit voltage drops were caused by the trap-inducing nature of the antimony mixed compositions, which became the dominant mechanism behind device hysteresis. Finally, the improved stability observed in the antimony mixed perovskite films was reproduced in devices, which demonstrated a slower formation of side phases when exposed to a combination of heat, light and moisture than their lead counterparts.

Overall, the results in this thesis pointed out the importance of creating a synergy between structural stability and high entropy in multi-mixed perovskite compositions for the successful achievement of long-lasting solar cells. However, more efforts should be invested to understand the effects of structural strain in multi-mixed perovskites and its relationship to thermal stability, as well as to address the limitations of this work.

On the one hand, further investigations employing theoretical modelling of XRD patterns and higher precision synchrotron-based correlative instruments are required to confirm the presence of the observed halide perovskite microstrain parallel plane gradient. Elucidating the origin and potential effects of this microstructural phenomenon could provide useful insights into the still unclear relationship between the microstrain, structural stability and optoelectronic behaviour of halide perovskites.

On the other hand, more studies on the antimony mixed triple cation mixed halide perovskites are required to elucidate whether the complex interplay between a higher number of traps and a stronger structural arrangement effectively translates into long-lasting operational devices. For this, further studies involving the use of transient photovoltage and photocurrent techniques are needed to provide information on charge transport and recombination in devices. Additionally, the use of UPS or STS techniques is fundamental to determining the Fermi level position of the Sb mixed perovskites, which would enable device performance optimization through effective tailoring of the band alignment with suitable charge extraction layers. Finally, ageing studies of devices with reinforced encapsulation under illumination are necessary to properly unveil the electronic decay of CsFAMA-Sb mixed solar cells.

Ultimately, this thesis pointed at B-site mixing on triple cation mixed halide perovskites as a promising approach to improve long-term solar cell stability. Hence, the

study of the partial replacement of lead by alternative B-site elements in multi-mixed perovskites that were proven successful stability-wise in simpler compositions such as Sr^{2+},[151,337,262] Ba^{2+},[283,12] or Eu^{2+},[318,116,240] stand out as a promising route to drive perovskite solar cells a step closer to commercialization.

List of Contributions

Publications

Halide Perovskite Microstrain: Are we measuring correctly?
Susana Iglesias-Porras, Nathan Hill, Dumitru Sirbu, Pablo Docampo and Noel Healy,
Manuscript in preparation

Entropic Stabilization of Mixed Lead-Antimony Perovskite Solar Cells
Susana Iglesias-Porras, Dumitru Sirbu, Pablo Docampo and Noel Healy,
Manuscript in preparation

Wide-Band-Gap Metal-Free Perovskite for Third-Order Nonlinear Optics
Dumitru Sirbu, Hei Chit Leo Tsui, Naseem Alsaif, Susana Iglesias-Porras, Yifeng Zhang, Ming Wang, Mingzhen Liu, Anna C. Peacock, Pablo Docampo and Noel Healy, ACS Photonics, 2021, 8, 8, 2450-2458

Posters and Oral presentations

Double perovskite optoelectronics (poster)
Susana Iglesias-Porras, Pablo Docampo and Noel Healy
ARC 2018, Newcastle University, Newcastle Upon Tyne

The influence of water vapour on the crystal structure and stability of $Cs_2AgBiBr_6$ perovskite solar cells (oral presentation)
Susana Iglesias-Porras and Pablo Docampo
ARC 2019, Newcastle University, Newcastle Upon Tyne

XRD microstrain analysis: a non destructive technique to assess the structural stability of perovskite solar cells (oral presentation)
Susana Iglesias-Porras
SAgE PGR conference 2020, Newcastle University, Online

References

[1] Abate, A., Leijtens, T., Pathak, S., Teuscher, J., Avolio, R., Errico, M. E., Kirkpatrik, J., Ball, J. M., Docampo, P., McPherson, I. and Snaith, H. J. [2013], 'Lithium salts as "redox active" p-type dopants for organic semiconductors and their impact in solid-state dye-sensitized solar cells', *Phys. Chem. Chem. Phys.* **15**, 2572–2579.

[2] Abdelhady, A. L., Saidaminov, M. I., Murali, B., Adinolfi, V., Voznyy, O., Katsiev, K., Alarousu, E., Comin, R., Dursun, I., Sinatra, L., Sargent, E. H., Mohammed, O. F. and Bakr, O. M. [2016], 'Heterovalent Dopant Incorporation for Bandgap and Type Engineering of Perovskite Crystals', *The Journal of Physical Chemistry Letters* **7**(2), 295–301.

[3] Abdi-Jalebi, M., Andaji-Garmaroudi, Z., Pearson, A. J., Divitini, G., Cacovich, S., Philippe, B., Rensmo, H., Ducati, C., Friend, R. H. and Stranks, S. D. [2018], 'Potassium- and Rubidium-Passivated Alloyed Perovskite Films: Optoelectronic Properties and Moisture Stability', *ACS Energy Letters* **3**(11), 2671–2678.

[4] Ahn, N., Kwak, K., Jang, M. S., Yoon, H., Lee, B. Y., Lee, J.-K., Pikhitsa, P. V., Byun, J. and Choi, M. [2016], 'Trapped charge-driven degradation of perovskite solar cells', *Nature Communications* **7**(1), 13422.

[5] Akbulatov, A. F., Frolova, L. A., Tsarev, S. A., Zhidkov, I., Luchkin, S. Y., Kurmaev, E. Z., Stevenson, K. J., Aldoshin, S. M. and Troshin, P. A. [2020], 'Film Deposition Techniques Impact the Defect Density and Photostability of $MAPbI_3$ Perovskite Films', *The Journal of Physical Chemistry C* **124**(39), 21378–21385.

[6] Allmann, R. [2008], General data reduction, *in* 'Powder Diffraction. Theory and practice', RSC Publishing, chapter 4, pp. 89–133.

[7] Alta-Devices [2018], 'GaAs best cells'. Last accessed 18 October 2021.
URL: *https://optics.org/news/9/12/19/AltaDecember2018*

[8] Arora, N., Dar, M. I., Hinderhofer, A., Pellet, N., Schreiber, F., Zakeeruddin, S. M. and Grätzel, M. [2017], 'Perovskite solar cells with CuSCN hole extraction layers yield stabilized efficiencies greater than 20%', *Science* **358**(6364), 768–771.

[9] Ashley, M. J., Kluender, E. J. and Mirkin, C. A. [2018], 'Fast Charge Extraction in Perovskite-Based Core–Shell Nanowires', *ACS Nano* **12**(7), 7206–7212.

[10] Aygüler, M. F., Hufnagel, A. G., Rieder, P., Wussler, M., Jaegermann, W., Bein, T., Dyakonov, V., Petrus, M. L., Baumann, A. and Docampo, P. [2018], 'Influence of Fermi Level Alignment with Tin Oxide on the Hysteresis of Perovskite Solar Cells', *ACS Applied Materials & Interfaces* **10**(14), 11414–11419.

[11] Aziz, A., Aristidou, N., Bu, X., Westbrook, R. J. E., Haque, S. A. and Islam, M. S. [2020], 'Understanding the Enhanced Stability of Bromide Substitution in Lead Iodide Perovskites', *Chemistry of Materials* **32**(1), 400–409.

[12] Bahadur, J., Ghahremani, A. H., Gupta, S., Druffel, T., Sunkara, M. K. and Pal, K. [2019], 'Enhanced moisture stability of $MAPbI_3$ perovskite solar cells through Barium doping', *Solar Energy* **190**, 396 – 404.

[13] Bai, S., Da, P., Li, C., Wang, Z., Yuan, Z., Fu, F., Kawecki, M., Liu, X., Sakai, N., Wang, J. T.-W., Huettner, S., Buecheler, S., Fahlman, M., Gao, F. and Snaith, H. J. [2019], 'Planar perovskite solar cells with long-term stability using ionic liquid additives', *Nature* **571**(7764), 245–250.

[14] Bartolome, J., Climent-Pascual, E., Redondo-Obispo, C., Zaldo, C., Alvarez, A. L., de Andres, A. and Coya, C. [2019], 'Huge Photostability Enhancement in Bismuth-Doped Methylammonium Lead Iodide Hybrid Perovskites by Light-Induced Transformation', *Chemistry of Materials* **31**(10), 3662–3671.

[15] Becquerel, A. E. [1839], 'Mémoire sur les effets électriques produits sous l'influence des rayons solaires', *Comptes Rendus de l'Académie des Sciences* **9**, 561.

[16] Beyerlein, K. R., Snyder, R. L., Li, M. and Scardi, P. [2010], 'Application of the Debye function to systems of crystallites', *Philosophical Magazine* **90**(29), 3891–3905.

[17] Bi, C., Wang, S., Li, Q., Kershaw, S. V., Tian, J. and Rogach, A. L. [2019], 'Thermally Stable Copper(II)-Doped Cesium Lead Halide Perovskite Quantum Dots with Strong Blue Emission', *The Journal of Physical Chemistry Letters* **10**(5), 943–952.

[18] Bi, D., Luo, J., Zhang, F., Magrez, A., Athanasopoulou, E. N., Hagfeldt, A. and Grätzel, M. [2017], 'Morphology Engineering: A Route to Highly Reproducible and High Efficiency Perovskite Solar Cells', *ChemSusChem* **10**(7), 1624–1630.

[19] Biju, V., Sugathan, N., Vrinda, V. and Salini, S. L. [2008], 'Estimation of lattice strain in nanocrystalline silver from X-ray diffraction line broadening', *Journal of Materials Science* **43**(4), 1175–1179.

[20] Birkholz, M. [2006], Line profile analysis, *in* 'Thin Film Analysis by X-Ray Scattering', John Wiley & Sons, Ltd, chapter 3, pp. 85–141.

[21] Boyd, C. C., Cheacharoen, R., Leijtens, T. and McGehee, M. D. [2019], 'Understanding Degradation Mechanisms and Improving Stability of Perovskite Photovoltaics', *Chemical Reviews* **119**(5), 3418–3451.

[22] *BP Statistical Review of World Energy 2018* [2019], Online edition, British Petroleum Company. (1981), London.

[23] *BP Statistical Review of World Energy 2019* [2020], Online edition, British Petroleum Company. (1981), London.

[24] *BP Statistical Review of World Energy 2020* [2021], Online edition, British Petroleum Company. (1981), London.

[25] Breitburg, D., Levin, L. A., Oschlies, A., Grégoire, M., Chavez, F. P., Conley, D. J., Garçon, V., Gilbert, D., Gutiérrez, D., Isensee, K., Jacinto, G. S., Limburg, K. E., Montes, I., Naqvi, S. W. A., Pitcher, G. C., Rabalais, N. N., Roman, M. R., Rose, K. A., Seibel, B. A., Telszewski, M., Yasuhara, M. and Zhang, J. [2018], 'Declining oxygen in the global ocean and coastal waters', *Science* **359**(6371), eaam7240.

[26] Brennan, M. C., Draguta, S., Kamat, P. V. and Kuno, M. [2018], 'Light-Induced Anion Phase Segregation in Mixed Halide Perovskites', *ACS Energy Letters* **3**(1), 204–213.

[27] Brenner, P., Glöckler, T., Rueda-Delgado, D., Abzieher, T., Jakoby, M., Richards, B. S., Paetzold, U. W., Howard, I. A. and Lemmer, U. [2017], 'Triple cation mixed-halide perovskites for tunable lasers', *Opt. Mater. Express* **7**(11), 4082–4094.

[28] Brunetti, B., Cavallo, C., Ciccioli, A., Gigli, G. and Latini, A. [2016], 'On the Thermal and Thermodynamic (In)Stability of Methylammonium Lead Halide Perovskites', *Scientific Reports* **6**, 31896.

[29] Bu, T., Liu, X., Zhou, Y., Yi, J., Huang, X., Luo, L., Xiao, J., Ku, Z., Peng, Y., Huang, F., Cheng, Y.-B. and Zhong, J. [2017], 'A novel quadruple-cation absorber for universal hysteresis elimination for high efficiency and stable perovskite solar cells', *Energy Environ. Sci.* **10**, 2509–2515.

[30] Caglioti, G., Paoletti, A. and Ricci, F. [1958], 'Choice of collimators for a crystal spectrometer for neutron diffraction', *Nuclear Instruments* **3**(4), 223 – 228.

[31] Calado, P., Telford, A. M., Bryant, D., Li, X., Nelson, J., O'Regan, B. C. and Barnes, P. R. [2016], 'Evidence for ion migration in hybrid perovskite solar cells with minimal hysteresis', *Nature Communications* **1**.

[32] Cao, J., Tao, S. X., Bobbert, P. A., Wong, C.-P. and Zhao, N. [2018], 'Interstitial Occupancy by Extrinsic Alkali Cations in Perovskites and Its Impact on Ion Migration', *Advanced Materials* **30**(26), 1707350.

[33] Cao, K., Li, H., Liu, S., Cui, J., Shen, Y. and Wang, M. [2016], '$MAPbI_{3-x}Br_x$ mixed halide perovskites for fully printable mesoscopic solar cells with enhanced efficiency and less hysteresis', *Nanoscale* **8**, 8839–8846.

[34] Caprioglio, P., Stolterfoht, M., Wolff, C. M., Unold, T., Rech, B., Albrecht, S. and Neher, D. [2019], 'On the Relation between the Open-Circuit Voltage and Quasi-Fermi Level Splitting in Efficient Perovskite Solar Cells', *Advanced Energy Materials* **9**(33), 1901631.

[35] Castro-Méndez, A.-F., Hidalgo, J. and Correa-Baena, J.-P. [2019], 'The Role of Grain Boundaries in Perovskite Solar Cells', *Advanced Energy Materials* **9**(38), 1901489.

[36] CEA/Toyobo [2020], 'An organic solar cell with 25% efficiency'. Last accessed 18 October 2021.
URL: *https://www.pv-magazine.com/2020/03/24/an-organic-solar-cell-with-25-efficiency/*

[37] Chang, X., Li, W., Zhu, L., Liu, H., Geng, H., Xiang, S., Liu, J. and Chen, H. [2016], 'Carbon-Based $CsPbBr_3$ Perovskite Solar Cells: All-Ambient Processes and High Thermal Stability', *ACS Applied Materials & Interfaces* **8**(49), 33649–33655.

[38] Chatterjee, S., Dasgupta, U. and Pal, A. J. [2017], 'Sequentially Deposited Antimony-Doped $CH_3NH_3PbI_3$ Films in Inverted Planar Heterojunction Solar Cells with a High Open-Circuit Voltage', *The Journal of Physical Chemistry C* **121**(37), 20177–20187.

[39] Cheary, R., Coelho, A. and Cline, J. [2004], 'Fundamental Parameters Line Profile Fitting in Laboratory Diffractometers', *Journal of research of the National Institute of Standards and Technology* **109**(1), 1–25.

[40] Chen, C., Xu, Y., Wu, S., Zhang, S., Yang, Z., Zhang, W., Zhu, H., Xiong, Z., Chen, W. and Chen, W. [2018], 'CaI_2: a more effective passivator of perovskite films than PbI_2 for high efficiency and long-term stability of perovskite solar cells', *J. Mater. Chem. A* **6**, 7903–7912.

[41] Chen, H.-W., Sakai, N., Ikegami, M. and Miyasaka, T. [2015], 'Emergence of Hysteresis and Transient Ferroelectric Response in Organo-Lead Halide Perovskite Solar Cells', *The Journal of Physical Chemistry Letters* **6**(1), 164–169.

[42] Chen, L., Tan, Y.-Y., Chen, Z.-X., Wang, T., Hu, S., Nan, Z.-A., Xie, L.-Q., Hui, Y., Huang, J.-X., Zhan, C., Wang, S.-H., Zhou, J.-Z., Yan, J.-W., Mao, B.-W. and Tian, Z.-Q. [2019], 'Toward Long-Term Stability: Single-Crystal Alloys of Cesium-Containing Mixed Cation and Mixed Halide Perovskite', *Journal of the American Chemical Society* **141**(4), 1665–1671.

[43] Chen, P.-Y., Qi, J., Klug, M. T., Dang, X., Hammond, P. T. and Belcher, A. M. [2014], 'Environmentally responsible fabrication of efficient perovskite solar cells from recycled car batteries', *Energy Environ. Sci.* **7**, 3659–3665.

[44] Chen, Z., Brocks, G., Tao, S. and Bobbert, P. A. [2021], 'Unified theory for light-induced halide segregation in mixed halide perovskites', *Nature Communications* **12**(1), 2687.

[45] Cheng, X., Jing, L., Yuan, Y., Du, S., Zhang, J., Zhan, X., Ding, J., Yu, H. and Shi, G. [2019], 'Fe^{2+}/Fe^{3+} Doped into $MAPbCl_3$ Single Crystal: Impact on Crystal Growth and Optical and Photoelectronic Properties', *The Journal of Physical Chemistry C* **123**(3), 1669–1676.

[46] Chhillar, P., Dhamaniya, B. P., Dutta, V. and Pathak, S. K. [2019], 'Recycling of Perovskite Films: Route toward Cost-Efficient and Environment-Friendly Perovskite Technology', *ACS Omega* **4**(7), 11880–11887.

[47] Chi, W. and Banerjee, S. K. [2021], 'Stability Improvement of Perovskite Solar Cells by Compositional and Interfacial Engineering', *Chemistry of Materials* **33**(5), 1540–1570.

[48] Choi, K., Lee, J., Kim, H. I., Park, C. W., Kim, G.-W., Choi, H., Park, S., Park, S. A. and Park, T. [2018], 'Thermally stable, planar hybrid perovskite solar cells with high efficiency', *Energy Environ. Sci.* **11**, 3238–3247.

[49] Chonamada, T. D., Dey, A. B. and Santra, P. K. [2020], 'Degradation Studies of $Cs_3Sb_2I_9$: A Lead-Free Perovskite', *ACS Applied Energy Materials* **3**(1), 47–55.

[50] Chu, W., Zheng, Q., Prezhdo, O. V., Zhao, J. and Saidi, W. A. [2020], 'Low-frequency lattice phonons in halide perovskites explain high defect tolerance toward electron-hole recombination', *Science Advances* **6**(7), eaaw7453.

[51] Chung, J., Shin, S. S., Hwang, K., Kim, G., Kim, K. W., Lee, D. S., Kim, W., Ma, B. S., Kim, Y.-K., Kim, T.-S. and Seo, J. [2020], 'Record-efficiency flexible perovskite solar cell and module enabled by a porous-planar structure as an electron transport layer', *Energy Environ. Sci.* **13**, 4854–4861.

[52] Cockcroft, J. K. and Fitch, A. N. [2008], Experimental setups, *in* 'Powder Diffraction. Theory and practice', RSC Publishing, chapter 2, pp. 20–57.

[53] *CODATA KEY VALUES FOR THERMODYNAMICS* [n.d.]. Last accessed 19 September 2022.
URL: *http://www.codata.info/resources/databases/key1.html*

[54] Colella, S., Mosconi, E., Fedeli, P., Listorti, A., Gazza, F., Orlandi, F., Ferro, P., Besagni, T., Rizzo, A., Calestani, G., Gigli, G., De Angelis, F. and Mosca, R. [2013], 'MAPbI$_{3-x}$Cl$_x$ Mixed Halide Perovskite for Hybrid Solar Cells: The Role of Chloride as Dopant on the Transport and Structural Properties', *Chemistry of Materials* **25**(22), 4613–4618.

[55] Conings, B., Drijkoningen, J., Gauquelin, N., Babayigit, A., D'Haen, J., D'Olieslaeger, L., Ethirajan, A., Verbeeck, J., Manca, J., Mosconi, E., Angelis, F. D. and Boyen, H.-G. [2015], 'Intrinsic Thermal Instability of Methylammonium Lead Trihalide Perovskite', *Advanced Energy Materials* **5**(15), 1500477.

[56] Correa-Baena, J.-P., Saliba, M., Buonassisi, T., Grätzel, M., Abate, A., Tress, W. and Hagfeldt, A. [2017], 'Promises and challenges of perovskite solar cells', *Science* **358**(6364), 739–744.

[57] *D8 ADVANCE Eco - powder diffraction* [n.d.]. Last accessed 01 April 2020.
URL: *https://www.bruker.com/products/x-ray-diffraction-and-elemental-analysis/x-ray-diffraction/d8-advance/eco.html*

[58] Dagar, J., Fenske, M., Al-Ashouri, A., Schultz, C., Li, B., Köbler, H., Munir, R., Parmasivam, G., Li, J., Levine, I., Merdasa, A., Kegelmann, L., Näsström, H., Marquez, J. A., Unold, T., Többens, D. M., Schlatmann, R., Stegemann, B., Abate, A., Albrecht, S. and Unger, E. [2021], 'Compositional and Interfacial Engineering Yield High-Performance and Stable p-i-n Perovskite Solar Cells and Mini-Modules', *ACS Applied Materials & Interfaces* **13**(11), 13022–13033.

[59] Davies, C. L., Filip, M. R., Patel, J. B., Crothers, T. W., Verdi, C., Wright, A. D., Milot, R. L., Giustino, F., Johnston, M. B. and Herz, L. M. [2018], 'Bimolecular recombination in methylammonium lead triiodide perovskite is an inverse absorption process', *Nature Communications* **9**, 293.

[60] De Angelis, F. [2021], 'The Prospect of Lead-Free Perovskite Photovoltaics', *ACS Energy Letters* **6**(4), 1586–1587.

[61] De Keijser, T. H., Langford, J. I., Mittemeijer, E. J. and Vogels, A. B. P. [1982], 'Use of the Voigt function in a single-line method for the analysis of X-ray diffraction line broadening', *Journal of Applied Crystallography* **15**(3), 308–314.

[62] De Marco, N., Zhou, H., Chen, Q., Sun, P., Liu, Z., Meng, L., Yao, E.-P., Liu, Y., Schiffer, A. and Yang, Y. [2016], 'Guanidinium: A Route to Enhanced Carrier Lifetime and Open-Circuit Voltage in Hybrid Perovskite Solar Cells', *Nano Letters* **16**(2), 1009–1016.

[63] De Wolf, S., Holovsky, J., Moon, S.-J., Löper, P., Niesen, B., Ledinsky, M., Haug, F.-J., Yum, J.-H. and Ballif, C. [2014], 'Organometallic Halide Perovskites: Sharp

Optical Absorption Edge and Its Relation to Photovoltaic Performance', *The Journal of Physical Chemistry Letters* **5**(6), 1035–1039.

[64] Deng, Y., Dong, Q., Bi, C., Yuan, Y. and Huang, J. [2016], 'Air-Stable, Efficient Mixed-Cation Perovskite Solar Cells with Cu Electrode by Scalable Fabrication of Active Layer', *Advanced Energy Materials* **6**(11), 1600372.

[65] Deretzis, I., Smecca, E., Mannino, G., La Magna, A., Miyasaka, T. and Alberti, A. [2018], 'Stability and Degradation in Hybrid Perovskites: Is the Glass Half-Empty or Half-Full?', *The Journal of Physical Chemistry Letters* **9**(11), 3000–3007.

[66] Docampo, P., Guldin, S., Steiner, U. and Snaith, H. J. [2013], 'Charge Transport Limitations in Self-Assembled TiO_2 Photoanodes for Dye-Sensitized Solar Cells', *The Journal of Physical Chemistry Letters* **4**(5), 698–703.

[67] Domanski, K., Alharbi, E. A., Hagfeldt, A., Grätzel, M. and Tress, W. [2018], 'Systematic investigation of the impact of operation conditions on the degradation behaviour of perovskite solar cells', *Nature Energy* **3**(1), 61–67.

[68] Domanski, K., Correa-Baena, J.-P., Mine, N., Nazeeruddin, M. K., Abate, A., Saliba, M., Tress, W., Hagfeldt, A. and Grätzel, M. [2016], 'Not All that Glitters Is Gold: Metal-Migration-Induced Degradation in Perovskite Solar Cells', *ACS Nano* **10**(6), 6306–6314.

[69] Du, K.-z., Wang, X., Han, Q., Yan, Y. and Mitzi, D. B. [2017], 'Heterovalent B-Site Co-Alloying Approach for Halide Perovskite Bandgap Engineering', *ACS Energy Letters* **2**(10), 2486–2490.

[70] Dualeh, A., Tétreault, N., Moehl, T., Gao, P., Nazeeruddin, M. K. and Grätzel, M. [2014], 'Effect of Annealing Temperature on Film Morphology of Organic–Inorganic Hybrid Perovskite Solid-State Solar Cells', *Advanced Functional Materials* **24**(21), 3250–3258.

[71] Duarte, M. [n.d.], 'Curve fitting'. Last accessed 15 November 2020.
URL: *https://nbviewer.jupyter.org/github/demotu/BMC/blob/master/notebooks/CurveFitting.ipynb*

[72] Dunfield, S. P., Bliss, L., Zhang, F., Luther, J. M., Zhu, K., van Hest, M. F. A. M., Reese, M. O. and Berry, J. J. [2020], 'From Defects to Degradation: A Mechanistic Understanding of Degradation in Perovskite Solar Cell Devices and Modules', *Advanced Energy Materials* **10**(26), 1904054.

[73] Eames, C., Frost, J. M., Barnes, P. R. F., O'Regan, B. C., Walsh, A. and Islam, M. S. [n.d.], 'Ionic transport in hybrid lead iodide perovskite solar cells', *Nature Communications* **6**(1), 7497.

[74] Ebadi, F., Aryanpour, M., Mohammadpour, R. and Taghavinia, N. [2019], 'Coupled Ionic-Electronic Equivalent Circuit to Describe Asymmetric Rise and Decay of Photovoltage Profile in Perovskite Solar Cells', *Scientific Reports* **9**(1), 11962.

[75] Eperon, G. E., Paternò, G. M., Sutton, R. J., Zampetti, A., Haghighirad, A. A., Cacialli, F. and Snaith, H. J. [2015], 'Inorganic caesium lead iodide perovskite solar cells', *J. Mater. Chem. A* **3**, 19688–19695.

[76] EPFL [2021], 'Grätzel solar cell with 13.5% efficiency, high open-circuit voltage'. Last accessed 18 October 2021.
URL: *https://www.pv-magazine.com/2021/03/23/gratzel-solar-cell-with-13-5-efficiency-high-open-circuit-voltage/*

[77] Fang, H.-H., Yang, J., Tao, S., Adjokatse, S., Kamminga, M. E., Ye, J., Blake, G. R., Even, J. and Loi, M. A. [2018], 'Unravelling Light-Induced Degradation of Layered Perovskite Crystals and Design of Efficient Encapsulation for Improved Photostability', *Advanced Functional Materials* **28**(21), 1800305.

[78] Fasoli, H. J., Yonni, F. and Testa, J. J. [2017], 'Properties of antimony triiodide photodecomposition and lewis acidity', *Educación Química* **28**(1), 11–13.

[79] Fedeli, P., Gazza, F., Calestani, D., Ferro, P., Besagni, T., Zappettini, A., Calestani, G., Marchi, E., Ceroni, P. and Mosca, R. [2015], 'Influence of the Synthetic Procedures on the Structural and Optical Properties of Mixed-Halide (Br, I) Perovskite Films', *The Journal of Physical Chemistry C* **119**(37), 21304–21313.

[80] Finger, L. W., Cox, D. E. and Jephcoat, A. P. [1994], 'A correction for powder diffraction peak asymmetry due to axial divergence', *Journal of Applied Crystallography* **27**(6), 892–900.

[81] First-Solar [2016], 'First Solar Hits Record 22.1% Conversion Efficiency for CdTe Solar Cell'. Last accessed 18 October 2021.
URL: *https://www.greentechmedia.com/articles/read/first-solar-hits-record-22-1-conversion-efficiency-for-cdte-solar-cell*

[82] Fritts, C. E. [1883], 'On a new form of selenium cell, and some electrical discoveries made by its use', *American Journal of Science* **s3-26**(156), 465–472.

[83] Frohna, K., Anaya, M., Macpherson, S., Sung, J., Doherty, T. A. S., Chiang, Y.-H., Winchester, A. J., Dani, K. M., Rao, A. and Stranks, S. D. [2021], 'Nanoscale Chemical Heterogeneity Dominates the Optoelectronic Response over Local Electronic Disorder and Strain in Alloyed Perovskite Solar Cells', *Nat Nanotechnol* . PMID:34811554.

[84] Fru, J., Nombona, N. and Diale, M. [2021], 'Growth and degradation of methylammonium lead tri-bromide perovskite thin film at metal/perovskite interfaces', *Thin Solid Films* **722**, 138568.

[85] Fu, F., Pisoni, S., Jeangros, Q., Sastre-Pellicer, J., Kawecki, M., Paracchino, A., Moser, T., Werner, J., Andres, C., Duchêne, L., Fiala, P., Rawlence, M., Nicolay, S., Ballif, C., Tiwari, A. N. and Buecheler, S. [2019], 'I_2 vapor-induced degradation of formamidinium lead iodide based perovskite solar cells under heat–light soaking conditions', *Energy Environ. Sci.* **12**, 3074–3088.

[86] Gao, P., Grätzel, M. and Nazeeruddin, M. K. [2014], 'Organohalide lead perovskites for photovoltaic applications', *Energy Environ. Sci.* **7**, 2448–2463.

[87] Giesbrecht, N., Weis, A. and Bein, T. [2020], 'Formation of stable 2D methylammonium antimony iodide phase for lead-free perovskite-like solar cells', *J. Phys. Energy* **2**(2), 024007.

[88] *Glasgow Climate Pact* [2021], UN Treaty, United Nations.

[89] Goldschmidt, V. M. [1926], 'Die Gesetze der Krystallochemie', *Naturwissenschaften* **14**(21), 477–485.

[90] Greul, E., Petrus, M., Binek, A., Docampo, P. and Bein, T. [2017], 'Highly stable, phase pure $Cs_2AgBiBr_6$ double perovskite thin films for optoelectronic applications', *J. Mater. Chem. A* **5**, 19972–19981.

[91] Głowienka, D., Zhang, D., Di Giacomo, F., Najafi, M., Veenstra, S., Szmytkowski, J. and Galagan, Y. [2020], 'Role of surface recombination in perovskite solar cells at the interface of HTL/$CH_3NH_3PbI_3$', *Nano Energy* **67**, 104186.

[92] Habisreutinger, S. N., Noel, N. K. and Snaith, H. J. [2018], 'Hysteresis Index: A Figure without Merit for Quantifying Hysteresis in Perovskite Solar Cells', *ACS Energy Letters* **3**(10), 2472–2476.

[93] Habisreutinger, S. N., Noel, N. K., Snaith, H. J. and Nicholas, R. J. [2017], 'Investigating the Role of 4-Tert Butylpyridine in Perovskite Solar Cells', *Advanced Energy Materials* **7**(1), 1601079.

[94] Hammond, C. [1997], X-ray diffraction of polycrystalline materials, *in* 'The basics of crystallography and diffraction', Oxford University Press, chapter 10, pp. 252–282.

[95] Holbrook, R. D. and Choquette, S. J. [2019], Standard Reference Material 640f, Line Position and Line Shape Standard for Powder Diffraction (Silicon Powder), Certificate, National Institute of Standards and Technology, Gaithersburg, MD 20899, USA.

[96] Hollemann, C., Haase, F., Schäfer, S., Krügener, J., Brendel, R. and Peibst, R. [2019], '26.1%-efficient POLO-IBC cells: Quantification of electrical and optical loss mechanisms', *Progress in Photovoltaics: Research and Applications* **27**(11), 950–958.

[97] Hu, S., Sprintall, J., Guan, C., McPhaden, M. J., Wang, F., Hu, D. and Cai, W. [2020], 'Deep-reaching acceleration of global mean ocean circulation over the past two decades', *Science Advances* **6**(6), eaax7727.

[98] Hu, W., Zhou, W., Lei, X., Zhou, P., Zhang, M., Chen, T., Zeng, H., Zhu, J., Dai, S., Yang, S. and Yang, S. [2019], 'Low-Temperature In Situ Amino Functionalization of TiO_2 Nanoparticles Sharpens Electron Management Achieving over 21% Efficient Planar Perovskite Solar Cells', *Advanced Materials* **31**(8), 1806095.

[99] Hu, Y., Aygüler, M. F., Petrus, M. L., Bein, T. and Docampo, P. [2017], 'Impact of Rubidium and Cesium Cations on the Moisture Stability of Multiple-Cation Mixed-Halide Perovskites', *ACS Energy Letters* **2**(10), 2212–2218.

[100] Hu, Y., Bai, F., Liu, X., Ji, Q., Miao, X., Qiu, T. and Zhang, S. [2017], 'Bismuth Incorporation Stabilized α-$CsPbI_3$ for Fully Inorganic Perovskite Solar Cells', *ACS Energy Letters* **2**(10), 2219–2227.

[101] Hu, Y., Hutter, E. M., Rieder, P., Grill, I., Hanisch, J., Aygüler, M. F., Hufnagel, A. G., Handloser, M., Bein, T., Hartschuh, A., Tvingstedt, K., Dyakonov, V., Baumann, A., Savenije, T. J., Petrus, M. L. and Docampo, P. [2018], 'Understanding the Role of Cesium and Rubidium Additives in Perovskite Solar Cells: Trap States, Charge Transport, and Recombination', *Advanced Energy Materials* **8**(16), 1703057.

[102] Hu, Y., Schlipf, J., Wussler, M., Petrus, M. L., Jaegermann, W., Bein, T., Müller-Buschbaum, P. and Docampo, P. [2016], 'Hybrid Perovskite/Perovskite Heterojunction Solar Cells', *ACS Nano* **10**(6), 5999–6007.

[103] Hu, Z., An, Q., Xiang, H., Aigouy, L., Sun, B., Vaynzof, Y. and Chen, Z. [2020], 'Enhancing the Efficiency and Stability of Triple-Cation Perovskite Solar Cells by Eliminating Excess PbI_2 from the Perovskite/Hole Transport Layer Interface', *ACS Applied Materials & Interfaces* **12**(49), 54824–54832.

[104] Huang, L., Bu, S., Zhang, D., Peng, R., Wei, Q., Ge, Z. and Zhang, J. [2019], 'Schottky/p-n Cascade Heterojunction Constructed by Intentional n-Type Doping Perovskite Toward Efficient Electron Layer-Free Perovskite Solar Cells', *Solar RRL* **3**(2), 1800274.

[105] Huang, X., Cheng, F., Wu, B. and Zheng, N. [2022], 'Intermediate Chemistry of Halide Perovskites: Origin, Evolution, and Application', *The Journal of Physical Chemistry Letters* **13**(7), 1765–1776.

[106] Huang, Y., Li, Y., Lim, E. L., Kong, T., Zhang, Y., Song, J., Hagfeldt, A. and Bi, D. [2021], 'Stable Layered 2D Perovskite Solar Cells with an Efficiency of over 19% via Multifunctional Interfacial Engineering', *Journal of the American Chemical Society* **143**(10), 3911–3917.

[107] Huang, Y., Wu, S., Chen, R., Fang, S., Zhang, S., Wang, G. and Chen, W. [2019], 'Efficient Methylamine-Containing Antisolvent Strategy to Fabricate High-Efficiency and Stable $FA_{0.85}Cs_{0.15}Pb(Br_{0.15}I_{2.85})$ Perovskite Solar Cells', *ACS Applied Materials & Interfaces* **11**(20), 18415–18422.

[108] Hubbard, C. [1982], Standard Reference Material 675, Low 2θ (Large d-spacing) Standard for X-ray Powder Diffraction, Certificate, National Institute of Standards and Technology, Washington, D.C. 20234, USA.

[109] Hubbard, S. [2016], *Recombination*, John Wiley & Sons, Ltd, chapter 2.4, pp. 39–46.

[110] Hutter, E. M., Muscarella, L. A., Wittmann, F., Versluis, J., McGovern, L., Bakker, H. J., Woo, Y.-W., Jung, Y.-K., Walsh, A. and Ehrler, B. [2020], 'Thermodynamic Stabilization of Mixed-Halide Perovskites against Phase Segregation', *Cell Reports Physical Science* **1**(8), 100120.

[111] IEC [2019], Photovoltaic devices - Part 3: Measurement principles for terrestrial photovoltaic (PV) solar devices with reference spectral irradiance data., Standard, International Electrotechnical Commission, Geneva, CH.

[112] Ivanov, I., Steparuk, A., Bolyachkina, M., Tsvetkov, D., Safronov, A. and Zuev, A. [2018], 'Thermodynamics of formation of hybrid perovskite-type methylammonium lead halides', *The Journal of Chemical Thermodynamics* **116**, 253–258.

[113] Jacobs, D. A., Wu, Y., Shen, H., Barugkin, C., Beck, F. J., White, T. P., Weber, K. and Catchpole, K. R. [2017], 'Hysteresis phenomena in perovskite solar cells: the many and varied effects of ionic accumulation', *Phys. Chem. Chem. Phys.* **19**, 3094–3103.

[114] Jacobsson, T. J., Correa-Baena, J.-P., Halvani Anaraki, E., Philippe, B., Stranks, S. D., Bouduban, M. E. F., Tress, W., Schenk, K., Teuscher, J., Moser, J.-E., Rensmo, H. and Hagfeldt, A. [2016], 'Unreacted PbI_2 as a Double-Edged Sword for Enhancing the Performance of Perovskite Solar Cells', *Journal of the American Chemical Society* **138**(32), 10331–10343.

[115] Jarzebski, Z. M. and Marton, J. P. [1976], 'Physical Properties of SnO_2 Materials: II. Electrical Properties', *Journal of The Electrochemical Society* **123**(9), 299C–310C.

[116] Jena, A. K., Kulkarni, A., Sanehira, Y., Ikegami, M. and Miyasaka, T. [2018], 'Stabilization of α-$CsPbI_3$ in Ambient Room Temperature Conditions by Incorporating Eu into $CsPbI_3$', *Chemistry of Materials* **30**(19), 6668–6674.

[117] Jena, A. K., Numata, Y., Ikegami, M. and Miyasaka, T. [2018], 'Role of spiro-OMeTAD in performance deterioration of perovskite solar cells at high temperature and reuse of the perovskite films to avoid Pb-waste', *J. Mater. Chem. A* **6**, 2219–2230.

[118] Jeng, J.-Y., Chiang, Y.-F., Lee, M.-H., Peng, S.-R., Guo, T.-F., Chen, P. and Wen, T.-C. [2013], '$CH_3NH_3PbI_3$ Perovskite/Fullerene Planar-Heterojunction Hybrid Solar Cells', *Advanced Materials* **25**(27), 3727–3732.

[119] Jeong, J., Kang, D., Chun, D. H., Shin, D., Park, J. H., Cho, S. W., Jeong, K., Lee, H. and Yi, Y. [2019], 'Unveiling the origin of performance reduction in perovskite solar cells with TiO_2 electron transport layer: Conduction band minimum mismatches and chemical interactions at buried interface', *Applied Surface Science* **495**, 143490.

[120] Jeong, J., Kim, M., Seo, J., Lu, H., Ahlawat, P., Mishra, A., Yang, Y., Hope, M. A., Eickemeyer, F. T., Kim, M., Yoon, Y. J., Choi, I. W., Darwich, B. P., Choi, S. J., Jo, Y., Lee, J. H., Walker, B., Zakeeruddin, S. M., Emsley, L., Rothlisberger, U., Hagfeldt, A., Kim, D. S., Grätzel, M. and Kim, J. Y. [2021], 'Pseudo-halide anion engineering for α-$FAPbI_3$ perovskite solar cells', *Nature* **592**(7854), 381–385.

[121] Jesper Jacobsson, T., Correa-Baena, J.-P., Pazoki, M., Saliba, M., Schenk, K., Grätzel, M. and Hagfeldt, A. [2016], 'Exploration of the compositional space for mixed lead halogen perovskites for high efficiency solar cells', *Energy Environ. Sci.* **9**, 1706–1724.

[122] Jodlowski, A. D., Roldán-Carmona, C., Grancini, G., Salado, M., Ralaiarisoa, M., Ahmad, S., Koch, N., Camacho, L., de Miguel, G. and Nazeeruddin, M. K. [2017], 'Large guanidinium cation mixed with methylammonium in lead iodide perovskites for 19% efficient solar cells', *Nature Energy* **2**(12), 972–979.

[123] Jones, T. W., Osherov, A., Alsari, M., Sponseller, M., Duck, B. C., Jung, Y.-K., Settens, C., Niroui, F., Brenes, R., Stan, C. V., Li, Y., Abdi-Jalebi, M., Tamura, N., Macdonald, J. E., Burghammer, M., Friend, R. H., Bulović, V., Walsh, A., Wilson, G. J., Lilliu, S. and Stranks, S. D. [2019], 'Lattice strain causes non-radiative losses in halide perovskites', *Energy Environ. Sci.* **12**, 596–606.

[124] Juarez-Perez, E. J., Hawash, Z., Raga, S. R., Ono, L. K. and Qi, Y. [2016], 'Thermal degradation of $CH_3NH_3PbI_3$ perovskite into NH_3 and CH_3I gases observed by coupled thermogravimetry–mass spectrometry analysis', *Energy Environ. Sci.* **9**, 3406–3410.

[125] Juarez-Perez, E. J., Ono, L. K., Maeda, M., Jiang, Y., Hawash, Z. and Qi, Y. [2018], 'Photodecomposition and thermal decomposition in methylammonium halide lead perovskites and inferred design principles to increase photovoltaic device stability', *J. Mater. Chem. A* **6**, 9604–9612.

[126] Juarez-Perez, E. J., Ono, L. K. and Qi, Y. [2019], 'Thermal degradation of formamidinium based lead halide perovskites into sym-triazine and hydrogen cyanide observed by coupled thermogravimetry-mass spectrometry analysis', *J. Mater. Chem. A* **7**, 16912–16919.

[127] Jung, K., Chae, W.-S., Lee, K.-H. and Lee, M.-J. [2021], 'Antisolvent-assisted one-step solution synthesis of defect-less 1D $MAPbI_3$ nanowire networks with improved charge transport dynamics', *Journal of Materials Research and Technology* **13**, 162–172.

[128] Kabir, E., Kumar, P., Kumar, S., Adelodun, A. A. and Kim, K.-H. [2018], 'Solar energy: Potential and future prospects', *Renewable and Sustainable Energy Reviews* **82**, 894–900.

[129] Kang, D.-H. and Park, N.-G. [2019], 'On the Current–Voltage Hysteresis in Perovskite Solar Cells: Dependence on Perovskite Composition and Methods to Remove Hysteresis', *Advanced Materials* **31**(34), 1805214.

[130] Kang, J. and Wang, L.-W. [2017], 'High Defect Tolerance in Lead Halide Perovskite $CsPbBr_3$', *The Journal of Physical Chemistry Letters* **8**(2), 489–493.

[131] Katz, E. A. [2020], 'Perovskite: Name Puzzle and German-Russian Odyssey of Discovery', *Helvetica Chimica Acta* **103**(6), e2000061.

[132] Ke, W., Fang, G., Liu, Q., Xiong, L., Qin, P., Tao, H., Wang, J., Lei, H., Li, B., Wan, J., Yang, G. and Yan, Y. [2015], 'Low-Temperature Solution-Processed Tin Oxide as an Alternative Electron Transporting Layer for Efficient Perovskite Solar Cells', *Journal of the American Chemical Society* **137**(21), 6730–6733.

[133] Khalid, S., Sultan, M., Ahmed, E. and Ahmed, W. [2021], Chapter 1 - Third-generation solar cells, *in* W. Ahmed, M. Booth and E. Nourafkan, eds, 'Emerging Nanotechnologies for Renewable Energy', Micro and Nano Technologies, Elsevier, pp. 3–35.

[134] Khenkin, M. V., Katz, E. A., Abate, A., Bardizza, G., Berry, J. J., Brabec, C., Brunetti, F., Bulović, V., Burlingame, Q., Di Carlo, A., Cheacharoen, R., Cheng, Y.-B., Colsmann, A., Cros, S., Domanski, K., Dusza, M., Fell, C. J., Forrest, S. R., Galagan, Y., Di Girolamo, D., Grätzel, M., Hagfeldt, A., von Hauff, E., Hoppe, H., Kettle, J., Köbler, H., Leite, M. S., Liu, S. F., Loo, Y.-L., Luther, J. M., Ma, C.-Q., Madsen, M., Manceau, M., Matheron, M., McGehee, M., Meitzner, R., Nazeeruddin, M. K., Nogueira, A. F., Odabaşı, C., Osherov, A., Park, N.-G., Reese, M. O., De Rossi, F., Saliba, M., Schubert, U. S., Snaith, H. J., Stranks, S. D., Tress, W., Troshin, P. A., Turkovic, V., Veenstra, S., Visoly-Fisher, I., Walsh, A., Watson, T.,

Xie, H., Yıldırım, R., Zakeeruddin, S. M., Zhu, K. and Lira-Cantu, M. [2020], 'Consensus statement for stability assessment and reporting for perovskite photovoltaics based on ISOS procedures', *Nature Energy* **5**(1), 35–49.

[135] Kieslich, G., Sun, S. and Cheetham, A. K. [2014], 'Solid-state principles applied to organic–inorganic perovskites: new tricks for an old dog', *Chem. Sci.* **5**, 4712–4715.

[136] Kim, G., Min, H., Lee, K. S., Lee, D. Y., Yoon, S. M. and Seok, S. I. [2020], 'Impact of strain relaxation on performance of α-formamidinium lead iodide perovskite solar cells', *Science* **370**(6512), 108–112.

[137] Kim, J., Yun, J. S., Wen, X., Soufiani, A. M., Lau, C. F. J., Wilkinson, B., Seidel, J., Green, M. A., Huang, S. and Ho-Baillie, A. W. Y. [2016], 'Nucleation and Growth Control of $HC(NH_2)_2PbI_3$ for Planar Perovskite Solar Cell', *The Journal of Physical Chemistry C* **120**(20), 11262–11267.

[138] Kim, N.-K., Min, Y. H., Noh, S., Cho, E., Jeong, G., Joo, M., Ahn, S.-W., Lee, J. S., Kim, S., Ihm, K., Ahn, H., Kang, Y., Lee, H.-S. and Kim, D. [2017], 'Investigation of Thermally Induced Degradation in $CH_3NH_3PbI_3$ Perovskite Solar Cells using In-situ Synchrotron Radiation Analysis', *Scientific Reports* **7**(1), 4645.

[139] Kim, S., Trinh, T. T., Park, J., Pham, D. P., Lee, S., Do, H. B., Dang, N. N., Dao, V.-A., Kim, J. and Yi, J. [2021], 'Over 30% efficiency bifacial 4-terminal perovskite-heterojunction silicon tandem solar cells with spectral albedo', *Scientific Reports* **11**(1), 15524.

[140] Klapetek, P., Ohlídal, I., Franta, D., Montaigne-Ramil, A., Bonanni, A., Stifter, D. and Sitter, H. [2003], 'Atomic force microscopy characterization of ZnTe epitaxial films', *Acta Physica Slovaca* **53**(3), 223–230.

[141] Klug, M. T., Milot, R. L., Patel, J. B., Green, T., Sansom, H. C., Farrar, M. D., Ramadan, A. J., Martani, S., Wang, Z., Wenger, B., Ball, J. M., Langshaw, L., Petrozza, A., Johnston, M. B., Herz, L. M. and Snaith, H. J. [2020], 'Metal composition influences optoelectronic quality in mixed-metal lead–tin triiodide perovskite solar absorbers', *Energy Environ. Sci.* **13**, 1776–1787.

[142] Kojima, A., Teshima, K., Shirai, Y. and Miyasaka, T. [2009], 'Organometal Halide Perovskites as Visible-Light Sensitizers for Photovoltaic Cells', *Journal of the American Chemical Society* **131**(17), 6050–6051.

[143] Kubicki, D. J., Prochowicz, D., Hofstetter, A., Saski, M., Yadav, P., Bi, D., Pellet, N., Lewiński, J., Zakeeruddin, S. M., Grätzel, M. and Emsley, L. [2018], 'Formation of Stable Mixed Guanidinium–Methylammonium Phases with Exceptionally Long Carrier Lifetimes for High-Efficiency Lead Iodide-Based Perovskite Photovoltaics', *Journal of the American Chemical Society* **140**(9), 3345–3351.

[144] Kubicki, D. J., Prochowicz, D., Hofstetter, A., Zakeeruddin, S. M., Grätzel, M. and Emsley, L. [2017], 'Phase Segregation in Cs-, Rb- and K-Doped Mixed-Cation $(MA)_x(FA)_{1-x}PbI_3$ Hybrid Perovskites from Solid-State NMR', *Journal of the American Chemical Society* **139**(40), 14173–14180.

[145] Kulkarni, S. A., Baikie, T., Boix, P. P., Yantara, N., Mathews, N. and Mhaisalkar, S. [2014], 'Band-gap tuning of lead halide perovskites using a sequential deposition process', *J. Mater. Chem. A* **2**, 9221–9225.

[146] Kumar, R. E., Quinn, X. L. and Fenning, D. P. [2021], 'Accounting for sample morphology in correlative X-ray microscopy via ray tracing', *MRS Advances* **6**, 547–553.

[147] Kung, P.-K., Li, M.-H., Lin, P.-Y., Chiang, Y.-H., Chan, C.-R., Guo, T.-F. and Chen, P. [2018], 'A Review of Inorganic Hole Transport Materials for Perovskite Solar Cells', *Advanced Materials Interfaces* **5**(22), 1800882.

[148] *Kyoto Protocol to the United Nations Framework Convention on Climate Change* [1997], UN Treaty, United Nations.

[149] Langford, J. I. and Louër, D. [1996], 'Powder diffraction', *Reports on Progress in Physics* **59**(2), 131–234.

[150] Lau, C. F. J., Deng, X., Zheng, J., Kim, J., Zhang, Z., Zhang, M., Bing, J., Wilkinson, B., Hu, L., Patterson, R., Huang, S. and Ho-Baillie, A. [2018], 'Enhanced performance via partial lead replacement with calcium for a $CsPbI_3$ perovskite solar cell exceeding 13% power conversion efficiency', *J. Mater. Chem. A* **6**, 5580–5586.

[151] Lau, C. F. J., Zhang, M., Deng, X., Zheng, J., Bing, J., Ma, Q., Kim, J., Hu, L., Green, M. A., Huang, S. and Ho-Baillie, A. [2017], 'Strontium-Doped Low-Temperature-Processed $CsPbI_2Br$ Perovskite Solar Cells', *ACS Energy Letters* **2**(10), 2319–2325.

[152] Lee, J.-W., Kim, S.-G., Bae, S.-H., Lee, D.-K., Lin, O., Yang, Y. and Park, N.-G. [2017], 'The Interplay between Trap Density and Hysteresis in Planar Heterojunction Perovskite Solar Cells', *Nano Letters* **17**(7), 4270–4276.

[153] Lee, Y. I., Jeon, N. J., Kim, B. J., Shim, H., Yang, T.-Y., Seok, S. I., Seo, J. and Im, S. G. [2018], 'A Low-Temperature Thin-Film Encapsulation for Enhanced Stability of a Highly Efficient Perovskite Solar Cell', *Advanced Energy Materials* **8**(9), 1701928.

[154] Leguy, A. M. A., Hu, Y., Campoy-Quiles, M., Alonso, M. I., Weber, O. J., Azarhoosh, P., van Schilfgaarde, M., Weller, M. T., Bein, T., Nelson, J., Docampo, P. and Barnes, P. R. F. [2015], 'Reversible Hydration of $CH_3NH_3PbI_3$ in Films, Single Crystals, and Solar Cells', *Chemistry of Materials* **27**(9), 3397–3407.

[155] Lehmann, F., Franz, A., Többens, D., Levcenco, S., Unold, T., Taubert, A. and Schorr, S. [2019], 'The phase diagram of a mixed halide (Br, I) hybrid perovskite obtained by synchrotron X-ray diffraction', *RSC Adv.* **9**, 11151–11159.

[156] Leineweber, A. and Krumeich, F. [2013], 'Broadening and shifting of Bragg reflections of nanoscale-microtwinned LT-Ni_3Sn_2', *Philosophical Magazine* **93**(35), 4440–4468.

[157] Leineweber, A. and Mittemeijer, E. J. [2010], 'Notes on the order-of-reflection dependence of microstrain broadening', *Journal of Applied Crystallography* **43**(5 Part 1), 981–989.

[158] Li, C., Guerrero, A., Zhong, Y. and Huettner, S. [2017], 'Origins and mechanisms of hysteresis in organometal halide perovskites', *Journal of Physics: Condensed Matter* **29**(19), 193001.

[159] Li, C., Lu, X., Ding, W., Feng, L., Gao, Y. and Guo, Z. [2008], 'Formability of ABX_3 (X = F, Cl, Br, I) halide perovskites', *Acta Crystallographica Section B* **64**(6), 702–707.

[160] Li, L., Zhou, P., Li, J., Mo, Y., Huang, W., Xiao, J., Li, W., Ku, Z., Zhong, J., Peng, Y., Cheng, Y.-B. and Huang, F. [2018], 'Suppressed hysteresis and enhanced performance of triple cation perovskite solar cell with chlorine incorporation', *J. Mater. Chem. C* **6**, 13157–13161.

[161] Li, N., Niu, X., Chen, Q. and Zhou, H. [2020], 'Towards commercialization: the operational stability of perovskite solar cells', *Chem. Soc. Rev.* **49**, 8235–8286.

[162] Li, Y., Liu, F. Z., Waqas, M., Leung, T. L., Tam, H. W., Lan, X. Q., Tu, B., Chen, W., Djurišić, A. B. and He, Z. B. [2018], 'Formamidinium-Based Lead Halide Perovskites: Structure, Properties, and Fabrication Methodologies', *Small Methods* **2**(7), 1700387.

[163] Li, Y., Lu, Y., Huo, X., Wei, D., Meng, J., Dong, J., Qiao, B., Zhao, S., Xu, Z. and Song, D. [2021], 'Bandgap tuning strategy by cations and halide ions of lead halide perovskites learned from machine learning', *RSC Adv.* **11**, 15688–15694.

[164] Li, Y., Xu, X., Wang, C., Ecker, B., Yang, J., Huang, J. and Gao, Y. [2017], 'Light-Induced Degradation of $CH_3NH_3PbI_3$ Hybrid Perovskite Thin Film', *The Journal of Physical Chemistry C* **121**(7), 3904–3910.

[165] Li, Z., Xu, J., Zhou, S., Zhang, B., Liu, X., Dai, S. and Yao, J. [2018], 'CsBr-Induced Stable $CsPbI_{3-x}Br_x$ (x<1) Perovskite Films at Low Temperature for Highly Efficient Planar Heterojunction Solar Cells', *ACS Applied Materials & Interfaces* **10**(44), 38183–38192.

[166] Liang, J., Wang, C., Wang, Y., Xu, Z., Lu, Z., Ma, Y., Zhu, H., Hu, Y., Xiao, C., Yi, X., Zhu, G., Lv, H., Ma, L., Chen, T., Tie, Z., Jin, Z. and Liu, J. [2016], 'All-Inorganic Perovskite Solar Cells', *Journal of the American Chemical Society* **138**(49), 15829–15832.

[167] Lide, D. R. [2003-2004], Atomic, Molecular, and Optical Physics. Ionization Potentials of Atoms and Atomic Ions, *in* 'Handbook of Chemistry and Physics (84th edition)', CRC Press, chapter 10, pp. 10–179.

[168] Lin, C.-T., De Rossi, F., Kim, J., Baker, J., Ngiam, J., Xu, B., Pont, S., Aristidou, N., Haque, S. A., Watson, T., McLachlan, M. A. and Durrant, J. R. [2019], 'Evidence for surface defect passivation as the origin of the remarkable photostability of unencapsulated perovskite solar cells employing aminovaleric acid as a processing additive', *J. Mater. Chem. A* **7**, 3006–3011.

[169] Lin, S., Yang, B., Qiu, X., Yan, J., Shi, J., Yuan, Y., Tan, W., Liu, X., Huang, H., Gao, Y. and Zhou, C. [2018], 'Efficient and stable planar hole-transport-material-free perovskite solar cells using low temperature processed SnO_2 as electron transport material', *Organic Electronics* **53**, 235–241.

[170] *Line position, MICA NIST SRM675, Sigma Aldrich* [n.d.]. Last accessed 12 April 2021.
URL: *https://www.sigmaaldrich.com/catalog/product/sial/nist675?lang=en&region=GB*

[171] Lira-Cantú, M. [2017], 'Perovskite solar cells: Stability lies at interfaces', *Nature Energy* **2**(7).

[172] Liu, C., Zhang, L., Zhou, X., Gao, J., Chen, W., Wang, X. and Xu, B. [2019], 'Hydrothermally Treated SnO_2 as the Electron Transport Layer in High-Efficiency Flexible Perovskite Solar Cells with a Certificated Efficiency of 17.3%', *Advanced Functional Materials* **29**(47), 1807604.

[173] Liu, D., Wang, Y., Xu, H., Zheng, H., Zhang, T., Zhang, P., Wang, F., Wu, J., Wang, Z., Chen, Z. and Li, S. [2019], 'SnO_2-Based Perovskite Solar Cells: Configuration Design and Performance Improvement', *Solar RRL* **3**(2), 1800292.

[174] Liu, F., Dong, Q., Wong, M. K., Djurišić, A. B., Ng, A., Ren, Z., Shen, Q., Surya, C., Chan, W. K., Wang, J., Ng, A. M. C., Liao, C., Li, H., Shih, K., Wei, C., Su, H. and Dai, J. [2016], 'Is Excess PbI_2 Beneficial for Perovskite Solar Cell Performance?', *Advanced Energy Materials* **6**(7), 1502206.

[175] Liu, P., Chen, Y., Xiang, H., Yang, X., Wang, W., Ran, R., Zhou, W. and Shao, Z. [2021], 'Benefitting from Synergistic Effect of Anion and Cation in Antimony Acetate

for Stable $CH_3NH_3PbI_3$-Based Perovskite Solar Cell with Efficiency Beyond 21%', *Small* **17**(46), 2102186.

[176] Liu, Y., Chen, P.-A. and Hu, Y. [2020], 'Recent developments in fabrication and performance of metal halide perovskite field-effect transistors', *J. Mater. Chem. C* **8**, 16691–16715.

[177] Liu, Y., Zheng, X., Fang, Y., Zhou, Y., Ni, Z., Xiao, X., Chen, S. and Huang, J. [2021], 'Ligand assisted growth of perovskite single crystals with low defect density', *Nature Communications* **12**(1), 1686.

[178] Long, M., Zhang, T., Liu, M., Chen, Z., Wang, C., Xie, W., Xie, F., Chen, J., Li, G. and Xu, J. [2018], 'Abnormal Synergetic Effect of Organic and Halide Ions on the Stability and Optoelectronic Properties of a Mixed Perovskite via In Situ Characterizations', *Advanced Materials* **30**(28), 1801562.

[179] Lou, Q., Han, Y., Liu, C., Zheng, K., Zhang, J., Chen, X., Du, Q., Chen, C. and Ge, Z. [2021], 'π-Conjugated Small Molecules Modified SnO_2 Layer for Perovskite Solar Cells with over 23% Efficiency', *Advanced Energy Materials* **11**, 2101416.

[180] Lu, M., Zhang, Y., Wang, S., Guo, J., Yu, W. W. and Rogach, A. L. [2019], 'Metal Halide Perovskite Light-Emitting Devices: Promising Technology for Next-Generation Displays', *Advanced Functional Materials* **29**(30), 1902008.

[181] Lu, W. and Fu, Y. [2018], Photoluminescence, *in* 'Spectroscopy of Semiconductors: Numerical Analysis Bridging Quantum Mechanics and Experiments', Springer International Publishing, chapter 4, pp. 107–158.

[182] Lv, Y., Zhang, H., Liu, R., Sun, Y. and Huang, W. [2020], 'Composite Encapsulation Enabled Superior Comprehensive Stability of Perovskite Solar Cells', *ACS Applied Materials & Interfaces* **12**(24), 27277–27285.

[183] Ma, J., Chang, J., Lin, Z., Guo, X., Zhou, L., Liu, Z., Xi, H., Chen, D., Zhang, C. and Hao, Y. [2018], 'Elucidating the Roles of $TiCl_4$ and PCBM Fullerene Treatment on TiO_2 Electron Transporting Layer for Highly Efficient Planar Perovskite Solar Cells', *The Journal of Physical Chemistry C* **122**(2), 1044–1053.

[184] Ma, S., Bai, Y., Wang, H., Zai, H., Wu, J., Li, L., Xiang, S., Liu, N., Liu, L., Zhu, C., Liu, G., Niu, X., Chen, H., Zhou, H., Li, Y. and Chen, Q. [2020], '1000 h Operational Lifetime Perovskite Solar Cells by Ambient Melting Encapsulation', *Advanced Energy Materials* **10**(9), 1902472.

[185] Mahmood, K., Sarwar, S. and Mehran, M. T. [2017], 'Current status of electron transport layers in perovskite solar cells: materials and properties', *RSC Adv.* **7**, 17044–17062.

[186] Mahmud, M. A., Elumalai, N. K., Upama, M. B., Wang, D., Soufiani, A. M., Wright, M., Xu, C., Haque, F. and Uddin, A. [2017], 'Solution-Processed Lithium-Doped ZnO Electron Transport Layer for Efficient Triple Cation (Rb, MA, FA) Perovskite Solar Cells', *ACS Applied Materials & Interfaces* **9**(39), 33841–33854.

[187] Maniammal, K., Madhu, G. and Biju, V. [2017], 'X-ray diffraction line profile analysis of nanostructured nickel oxide: Shape factor and convolution of crystallite size and microstrain contributions', *Physica E: Low-dimensional Systems and Nanostructures* **85**, 214–222.

[188] Marronnier, A., Roma, G., Boyer-Richard, S., Pedesseau, L., Jancu, J.-M., Bonnassieux, Y., Katan, C., Stoumpos, C. C., Kanatzidis, M. G. and Even, J. [2018], 'Anharmonicity and Disorder in the Black Phases of Cesium Lead Iodide Used for Stable Inorganic Perovskite Solar Cells', *ACS Nano* **12**(4), 3477–3486.

[189] Matsui, T., Yamamoto, T., Nishihara, T., Morisawa, R., Yokoyama, T., Sekiguchi, T. and Negami, T. [2019], 'Compositional Engineering for Thermally Stable, Highly Efficient Perovskite Solar Cells Exceeding 20% Power Conversion Efficiency with 85 °C/85 % 1000 h Stability', *Advanced Materials* **31**(10), 1806823.

[190] McGovern, L., Futscher, M. H., Muscarella, L. A. and Ehrler, B. [2020], 'Understanding the Stability of $MAPbBr_3$ versus $MAPbI_3$: Suppression of Methylammonium Migration and Reduction of Halide Migration', *The Journal of Physical Chemistry Letters* **11**(17), 7127–7132.

[191] McNaught, A. D. and Wilkinson, A. [1997], *in* 'IUPAC. Compendium of Chemical Terminology, 2nd ed.', Blackwell Scientific Publications.

[192] Meggiolaro, D., Motti, S. G., Mosconi, E., Barker, A. J., Ball, J., Andrea Riccardo Perini, C., Deschler, F., Petrozza, A. and De Angelis, F. [2018], 'Iodine chemistry determines the defect tolerance of lead-halide perovskites', *Energy Environ. Sci.* **11**, 702–713.

[193] Mendenhall, M. H., Mullen, K. and Cline, J. [2015], 'An Implementation of the Fundamental Parameters Approach for Analysis of X-ray Powder Diffraction Line Profiles', *Journal of research of the National Institute of Standards and Technology* **120**, 223–251.

[194] Merdasa, A., Kiligaridis, A., Rehermann, C., Abdi-Jalebi, M., Stöber, J., Louis, B., Gerhard, M., Stranks, S. D., Unger, E. L. and Scheblykin, I. G. [2019], 'Impact of Excess Lead Iodide on the Recombination Kinetics in Metal Halide Perovskites', *ACS Energy Letters* **4**(6), 1370–1378.

[195] Mesquita, I., Andrade, L. and Mendes, A. [2019], 'Temperature Impact on Perovskite Solar Cells Under Operation', *ChemSusChem* **12**(10), 2186–2194.

[196] Mi, Y., Zhong, Y., Zhang, Q. and Liu, X. [2019], 'Continuous-Wave Pumped Perovskite Lasers', *Advanced Optical Materials* **7**(17), 1900544.

[197] Momblona, C., Gil-Escrig, L., Bandiello, E., Hutter, E. M., Sessolo, M., Lederer, K., Blochwitz-Nimoth, J. and Bolink, H. J. [2016], 'Efficient vacuum deposited p-i-n and n-i-p perovskite solar cells employing doped charge transport layers', *Energy Environ. Sci.* **9**, 3456–3463.

[198] Nagabhushana, G. P., Shivaramaiah, R. and Navrotsky, A. [2016], 'Direct calorimetric verification of thermodynamic instability of lead halide hybrid perovskites', *Proceedings of the National Academy of Sciences* **113**(28), 7717–7721.

[199] Nakamura, M., Yamaguchi, K., Kimoto, Y., Yasaki, Y., Kato, T. and Sugimoto, H. [2019], 'Cd-Free Cu(In,Ga)(Se,S)$_2$ Thin-Film Solar Cell With Record Efficiency of 23.35%', *IEEE Journal of Photovoltaics* **9**(6), 1863–1867.

[200] Nath, D., Singh, F. and Das, R. [2020], 'X-ray diffraction analysis by Williamson-Hall, Halder-Wagner and size-strain plot methods of CdSe nanoparticles- a comparative study', *Materials Chemistry and Physics* **239**, 122021.

[201] National Institute of Standards and Technology [2021*a*], 'Table 3 - X-Ray Mass Attenuation Coefficients'. Last accessed 04 August 2021.
URL: *https://physics.nist.gov/PhysRefData/XrayMassCoef/tab3.html*

[202] National Institute of Standards and Technology [2021*b*], 'X-Ray Mass Attenuation Coefficients'. Last accessed 04 August 2021.
URL: *https://physics.nist.gov/PhysRefData/XrayMassCoef/chap2.html*

[203] Nayak, P. K., Sendner, M., Wenger, B., Wang, Z., Sharma, K., Ramadan, A. J., Lovrinčić, R., Pucci, A., Madhu, P. K. and Snaith, H. J. [2018], 'Impact of Bi^{3+} Heterovalent Doping in Organic–Inorganic Metal Halide Perovskite Crystals', *Journal of the American Chemical Society* **140**(2), 574–577.

[204] Ng, A., Ren, Z., Shen, Q., Cheung, S. H., Gokkaya, H. C., So, S. K., Djurišić, A. B., Wan, Y., Wu, X. and Surya, C. [2016], 'Crystal Engineering for Low Defect Density and High Efficiency Hybrid Chemical Vapor Deposition Grown Perovskite Solar Cells', *ACS Applied Materials & Interfaces* **8**(48), 32805–32814.

[205] Nguyen, J. and Larimer, G. [2019], '7.4: Standard enthalpy of formation'. Last accessed 19 September 2022.
URL: *https://chem.libretexts.org*

[206] Nishimura, K., Hirotani, D., Kamarudin, M. A., Shen, Q., Toyoda, T., Iikubo, S., Minemoto, T., Yoshino, K. and Hayase, S. [2019], 'Relationship between Lattice Strain and Efficiency for Sn-Perovskite Solar Cells', *ACS Applied Materials & Interfaces* **11**(34), 31105–31110.

[207] *NIST Chemistry WebBook, SRD 69* [n.d.]. Last accessed 19 September 2022.
URL: *https://webbook.nist.gov/*

[208] Niu, G., Li, W., Li, J., Liang, X. and Wang, L. [2017], 'Enhancement of thermal stability for perovskite solar cells through cesium doping', *RSC Adv.* **7**, 17473–17479.

[209] Noh, J. H., Im, S. H., Heo, J. H., Mandal, T. N. and Seok, S. I. [2013], 'Chemical Management for Colorful, Efficient, and Stable Inorganic–Organic Hybrid Nanostructured Solar Cells', *Nano Letters* **13**(4), 1764–1769.

[210] NREL [2021], 'Best Research-Cell Efficiency Chart - Photovoltaic Research'. Last accessed 31 May 2021.
URL: *https://www.nrel.gov/pv/cell-efficiency.html*

[211] Ochoa-Martinez, E., Ochoa, M., Ortuso, R. D., Ferdowsi, P., Carron, R., Tiwari, A. N., Steiner, U. and Saliba, M. [2021], 'Physical Passivation of Grain Boundaries and Defects in Perovskite Solar Cells by an Isolating Thin Polymer', *ACS Energy Letters* **6**(7), 2626–2634.

[212] Oga, H., Saeki, A., Ogomi, Y., Hayase, S. and Seki, S. [2014], 'Improved Understanding of the Electronic and Energetic Landscapes of Perovskite Solar Cells: High Local Charge Carrier Mobility, Reduced Recombination, and Extremely Shallow Traps', *Journal of the American Chemical Society* **136**(39), 13818–13825.

[213] Ohl, R. S. [1941], 'U.S. Patent US2402662A'.

[214] Okil, M., Salem, M. S., Abdolkader, T. M. and Shaker, A. [2021], 'From Crystalline to Low-cost Silicon-based Solar Cells: a Review', *Silicon* .

[215] Oku, T., Ohishi, Y. and Suzuki, A. [2016], 'Effects of Antimony Addition to Perovskite-type $CH_3NH_3PbI_3$ Photovoltaic Devices', *Chemistry Letters* **45**(2), 134–136.

[216] Oku, T., Ohishi, Y., Suzuki, A. and Miyazawa, Y. [2016], 'Effects of Cl Addition to Sb-Doped Perovskite-Type $CH_3NH_3PbI_3$ Photovoltaic Devices', *Metals* **6**(147).

[217] Onoda-Yamamuro, N., Matsuo, T. and Suga, H. [1990], 'Calorimetric and IR spectroscopic studies of phase transitions in methylammonium trihalogenoplumbates (II)†', *Journal of Physics and Chemistry of Solids* **51**(12), 1383–1395.

[218] *OSRAM Opto Semiconductors BPW 21 Photodiode* [n.d.]. Last accessed 1 September 2021.
URL: *https://www.mouser.co.uk/productdetail/osram-opto-semiconductors/bpw-21?qs=sGAEpiMZZMs0JOhy9PM0URes9W8cG8X5QoEk7eGMFF0=*

[219] Ostrouchov, C. [n.d.], 'Peak fitting XRD data with Python'. Last accessed 15 October 2020.
URL: *https://chrisostrouchov.com/post/peak_fit_xrd_python/*

[220] Paek, S., Schouwink, P., Athanasopoulou, E. N., Cho, K. T., Grancini, G., Lee, Y., Zhang, Y., Stellacci, F., Nazeeruddin, M. K. and Gao, P. [2017], 'From Nano- to Micrometer Scale: The Role of Antisolvent Treatment on High Performance Perovskite Solar Cells', *Chemistry of Materials* **29**(8), 3490–3498.

[221] *Paris Agreement* [2015], UN Treaty XXVII-7-d, United Nations.

[222] Park, B.-w., Kedem, N., Kulbak, M., Lee, D. Y., Yang, W. S., Jeon, N. J., Seo, J., Kim, G., Kim, K. J., Shin, T. J., Hodes, G., Cahen, D. and Seok, S. I. [2018], 'Understanding how excess lead iodide precursor improves halide perovskite solar cell performance', *Nature Communications* **9**(1), 3301.

[223] Park, H. H. [2021], 'Inorganic Materials by Atomic Layer Deposition for Perovskite Solar Cells', *Nanomaterials* **11**(1).

[224] Park, M., Kim, J.-Y., Son, H. J., Lee, C.-H., Jang, S. S. and Ko, M. J. [2016], 'Low-temperature solution-processed Li-doped SnO_2 as an effective electron transporting layer for high-performance flexible and wearable perovskite solar cells', *Nano Energy* **26**, 208–215.

[225] Park, Y. H., Jeong, I., Bae, S., Son, H. J., Lee, P., Lee, J., Lee, C.-H. and Ko, M. J. [2017], 'Inorganic Rubidium Cation as an Enhancer for Photovoltaic Performance and Moisture Stability of $HC(NH_2)_2PbI_3$ Perovskite Solar Cells', *Advanced Functional Materials* **27**(16), 1605988.

[226] Paterson, M. S. [1952], 'X-Ray Diffraction by Face-Centered Cubic Crystals with Deformation Faults', *Journal of Applied Physics* **23**(8), 805–811.

[227] *Perovskite* [n.d.]. Last accessed 01 April 2020.
URL: *https://chemicalstructure.net/portfolio/perovskite/*

[228] Petrucci, R. H., Harwood, W. S. and Herring, F. G. [2002], *in* 'General Chemistry (8th ed.)', Prentice Hall, pp. 237–238.

[229] Petrus, M. L., Schutt, K., Sirtl, M. T., Hutter, E. M., Closs, A. C., Ball, J. M., Bijleveld, J. C., Petrozza, A., Bein, T., Dingemans, T. J., Savenije, T. J., Snaith, H. and Docampo, P. [2018], 'New Generation Hole Transporting Materials for Perovskite Solar Cells: Amide-Based Small-Molecules with Nonconjugated Backbones', *Advanced Energy Materials* **8**(32), 1801605.

[230] Pham, N. D., Zhang, C., Tiong, V. T., Zhang, S., Will, G., Bou, A., Bisquert, J., Shaw, P. E., Du, A., Wilson, G. J. and Wang, H. [2019], 'Tailoring Crystal Structure of $FA_{0.83}Cs_{0.17}PbI_3$ Perovskite Through Guanidinium Doping for Enhanced Performance and Tunable Hysteresis of Planar Perovskite Solar Cells', *Advanced Functional Materials* **29**(1), 1806479.

[231] *Photovoltaics report* [2021], Online edition, Fraunhofer Institute for Solar Energy Systems (ISE) with support of PSE Projects GmbH, Freiburg.
URL: *https://www.ise.fraunhofer.de/content/dam/ise/de/documents/publications/studies/Photovoltaics-Report.pdf*

[232] Phung, N., Al-Ashouri, A., Meloni, S., Mattoni, A., Albrecht, S., Unger, E. L., Merdasa, A. and Abate, A. [2020], 'The Role of Grain Boundaries on Ionic Defect Migration in Metal Halide Perovskites', *Advanced Energy Materials* **10**(20), 1903735.

[233] Phung, N., Félix, R., Meggiolaro, D., Al-Ashouri, A., Sousa e Silva, G., Hartmann, C., Hidalgo, J., Köbler, H., Mosconi, E., Lai, B., Gunder, R., Li, M., Wang, K.-L., Wang, Z.-K., Nie, K., Handick, E., Wilks, R. G., Marquez, J. A., Rech, B., Unold, T., Correa-Baena, J.-P., Albrecht, S., De Angelis, F., Bär, M. and Abate, A. [2020], 'The Doping Mechanism of Halide Perovskite Unveiled by Alkaline Earth Metals', *Journal of the American Chemical Society* **142**(5), 2364–2374.

[234] Pistor, P., Burwig, T., Brzuska, C., Weber, B. and Fränzel, W. [2018], 'Thermal stability and miscibility of co-evaporated methyl ammonium lead halide (MAPbX3, x = i, br, cl) thin films analysed by in situ X-ray diffraction', *J. Mater. Chem. A* **6**, 11496–11506.

[235] Pockett, A., Eperon, G. E., Sakai, N., Snaith, H. J., Peter, L. M. and Cameron, P. J. [2017], 'Microseconds, milliseconds and seconds: deconvoluting the dynamic behaviour of planar perovskite solar cells', *Phys. Chem. Chem. Phys.* **19**, 5959–5970.

[236] Post, E., Alley, R. B., Christensen, T. R., Macias-Fauria, M., Forbes, B. C., Gooseff, M. N., Iler, A., Kerby, J. T., Laidre, K. L., Mann, M. E., Olofsson, J., Stroeve, J. C., Ulmer, F., Virginia, R. A. and Wang, M. [2019], 'The polar regions in a 2 °C warmer world', *Science Advances* **5**(12), eaaw9883.

[237] Protesescu, L., Yakunin, S., Bodnarchuk, M. I., Krieg, F., Caputo, R., Hendon, C. H., Yang, R. X., Walsh, A. and Kovalenko, M. V. [2015], 'Nanocrystals of Cesium Lead Halide Perovskites ($CsPbX_3$, X = Cl, Br, and I): Novel Optoelectronic Materials Showing Bright Emission with Wide Color Gamut', *Nano Letters* **15**(6), 3692–3696.

[238] Qiao, H. W., Yang, S., Wang, Y., Chen, X., Wen, T. Y., Tang, L. J., Cheng, Q., Hou, Y., Zhao, H. and Yang, H. G. [2019], 'A Gradient Heterostructure Based on Tolerance Factor in High-Performance Perovskite Solar Cells with 0.84 Fill Factor', *Advanced Materials* **31**(5), 1804217.

[239] Qiao, W.-C., Yang, J., Dong, W., Yang, G., Bao, Q., Huang, R., Wang, X. L. and Yao, Y.-F. [2020], 'Metastable alloying structures in $MAPbI_{3-x}Cl_x$ crystals', *NPG Asia Materials* **12**(1), 68.

[240] Quinn, X. L., Kumar, R. E., Kodur, M., Cakan, D. N., Cai, Z., Zhou, T., Holt, M. V. and Fenning, D. P. [2021], 'Europium Addition Reduces Local Structural Disorder and Enhances Photoluminescent Yield in Perovskite $CsPbBr_3$', *Advanced Optical Materials* **9**, 2002221.

[241] Rahman, S. I., Lamsal, B. S., Gurung, A., Chowdhury, A. H., Reza, K. M., Ghimire, N., Bahrami, B., Luo, W., Bobba, R. S., Pokharel, J., Baniya, A., Laskar, A. R., Emshadi, K., Rahman, M. T. and Qiao, Q. [2020], 'Grain Boundary Defect Passivation of Triple Cation Mixed Halide Perovskite with Hydrazine-Based Aromatic Iodide for Efficiency Improvement', *ACS Applied Materials & Interfaces* **12**(37), 41312–41322.

[242] Ramos, F. J., Maindron, T., Béchu, S., Rebai, A., Frégnaux, M., Bouttemy, M., Rousset, J., Schulz, P. and Schneider, N. [2018], 'Versatile perovskite solar cell encapsulation by low-temperature ALD-Al_2O_3 with long-term stability improvement', *Sustainable Energy Fuels* **2**, 2468–2479.

[243] Ricciarelli, D., Meggiolaro, D., Ambrosio, F. and De Angelis, F. [2020], 'Instability of Tin Iodide Perovskites: Bulk p-Doping versus Surface Tin Oxidation', *ACS Energy Letters* **5**(9), 2787–2795.

[244] Richardson, G., O'Kane, S. E. J., Niemann, R. G., Peltola, T. A., Foster, J. M., Cameron, P. J. and Walker, A. B. [2016], 'Can slow-moving ions explain hysteresis in the current–voltage curves of perovskite solar cells?', *Energy Environ. Sci.* **9**, 1476–1485.

[245] RokerHRO [2009], 'White corner of an RGB color cube in isometric projection'. Last accessed 18 October 2021.
URL: *https://upload.wikimedia.org/wikipedia/commons/0/03/RGB_Colorcube_Corner_White.png*

[246] Rong, Y., Hu, Y., Mei, A., Tan, H., Saidaminov, M. I., Seok, S. I., McGehee, M. D., Sargent, E. H. and Han, H. [2018], 'Challenges for commercializing perovskite solar cells', *Science* **361**(6408), eaat8235.

[247] Roose, B., Dey, K., Chiang, Y.-H., Friend, R. H. and Stranks, S. D. [2020], 'Critical Assessment of the Use of Excess Lead Iodide in Lead Halide Perovskite Solar Cells', *The Journal of Physical Chemistry Letters* **11**(16), 6505–6512.

[248] Rumble, J. [2022], *in* 'CRC Handbook of Chemistry and Physics', Taylor & Francis Ltd.

[249] Rühle, S. [2016], 'Tabulated values of the Shockley–Queisser limit for single junction solar cells', *Solar Energy* **130**, 139–147.

[250] Sai, H., Matsui, T. and Matsubara, K. [2016], 'Stabilized 14.0%-efficient triple-junction thin-film silicon solar cell', *Applied Physics Letters* **109**(18), 183506.

[251] Saidaminov, M. I., Abdelhady, A. L., Murali, B., Alarousu, E., Burlakov, V. M., Peng, W., Dursun, I., Wang, L., He, Y., Maculan, G., Goriely, A., Wu, T., Mohammed, O. F. and Bakr, O. M. [2015], 'High-quality bulk hybrid perovskite single crystals within minutes by inverse temperature crystallization', *Nature Communications* **6**(1), 7586.

[252] Saidaminov, M. I., Kim, J., Jain, A., Quintero-Bermudez, R., Tan, H., Long, G., Tan, F., Johnston, A., Zhao, Y., Voznyy, O. and Sargent, E. H. [2018], 'Suppression of atomic vacancies via incorporation of isovalent small ions to increase the stability of halide perovskite solar cells in ambient air', *Nature Energy* **3**(8), 648–654.

[253] Sakai, N., Wang, Z., Burlakov, V. M., Lim, J., McMeekin, D., Pathak, S. and Snaith, H. J. [2017], 'Controlling Nucleation and Growth of Metal Halide Perovskite Thin Films for High-Efficiency Perovskite Solar Cells', *Small* **13**(14), 1602808.

[254] Saliba, M., Matsui, T., Domanski, K., Seo, J.-Y., Ummadisingu, A., Zakeeruddin, S. M., Correa-Baena, J.-P., Tress, W. R., Abate, A., Hagfeldt, A. and Grätzel, M. [2016], 'Incorporation of rubidium cations into perovskite solar cells improves photovoltaic performance', *Science* **354**(6309), 206–209.

[255] Saliba, M., Matsui, T., Seo, J.-Y., Domanski, K., Correa-Baena, J.-P., Nazeeruddin, M. K., Zakeeruddin, S. M., Tress, W., Abate, A., Hagfeldt, A. and Grätzel, M. [2016], 'Cesium-containing triple cation perovskite solar cells: improved stability, reproducibility and high efficiency', *Energy Environ. Sci.* **9**, 1989–1997.

[256] Scardi, P. [2008], Microstructural properties: Lattice defects and domain size effects, *in* 'Powder Diffraction. Theory and practice', RSC Publishing, chapter 13, pp. 376–413.

[257] Schultes, M., Helder, T., Ahlswede, E., Aygüler, M. F., Jackson, P., Paetel, S., Schwenzer, J. A., Hossain, I. M., Paetzold, U. W. and Powalla, M. [2019], 'Sputtered transparent electrodes (io:h and izo) with low parasitic near-infrared absorption for perovskite–cu(in,ga)se2 tandem solar cells', *ACS Applied Energy Materials* **2**(11), 7823–7831.

[258] Seitz, M., Gant, P., Castellanos-Gomez, A. and Prins, F. a. [2019], 'Long-Term Stabilization of Two-Dimensional Perovskites by Encapsulation with Hexagonal Boron Nitride.', *Nanomaterials (Basel)* **9**(8), 1120.

[259] Senocrate, A., Acartürk, T., Kim, G. Y., Merkle, R., Starke, U., Grätzel, M. and Maier, J. [2018], 'Interaction of oxygen with halide perovskites', *J. Mater. Chem. A* **6**, 10847–10855.

[260] Senocrate, A., Kim, G. Y., Grätzel, M. and Maier, J. [2019], 'Thermochemical Stability of Hybrid Halide Perovskites', *ACS Energy Letters* **4**(12), 2859–2870.

[261] Shai, X., Wang, J., Sun, P., Huang, W., Liao, P., Cheng, F., Zhu, B., Chang, S.-Y., Yao, E.-P., Shen, Y., Miao, L., Yang, Y. and Wang, M. [2018], 'Achieving ordered and stable binary metal perovskite via strain engineering', *Nano Energy* **48**, 117–127.

[262] Shai, X., Zuo, L., Sun, P., Liao, P., Huang, W., Yao, E.-P., Li, H., Liu, S., Shen, Y., Yang, Y. and Wang, M. [2017], 'Efficient planar perovskite solar cells using halide Sr-substituted Pb perovskite', *Nano Energy* **36**, 213–222.

[263] Shannon, R. D. [1976], 'Revised effective ionic radii and systematic studies of interatomic distances in halides and chalcogenides', *Acta Crystallographica Section A* **32**(5), 751–767.
URL: *https://onlinelibrary.wiley.com/doi/abs/10.1107/S0567739476001551*

[264] Shao, F., Qin, P., Wang, D., Zhang, G., Wu, B., He, J., Peng, W., Sum, T. C., Wang, D. and Huang, F. [2019], 'Enhanced Photovoltaic Performance and Thermal Stability of $CH_3NH_3PbI_3$ Perovskite through Lattice Symmetrization', *ACS Applied Materials & Interfaces* **11**(1), 740–746.

[265] Sherkar, T. S., Momblona, C., Gil-Escrig, L., Ávila, J., Sessolo, M., Bolink, H. J. and Koster, L. J. A. [2017], 'Recombination in Perovskite Solar Cells: Significance of Grain Boundaries, Interface Traps, and Defect Ions', *ACS Energy Letters* **2**(5), 1214–1222.

[266] Shi, B., Yao, X., Hou, F., Guo, S., Li, Y., Wei, C., Ding, Y., Li, Y., Zhao, Y. and Zhang, X. [2018], 'Unraveling the Passivation Process of PbI_2 to Enhance the Efficiency of Planar Perovskite Solar Cells', *The Journal of Physical Chemistry C* **122**(37), 21269–21276.

[267] Shi, L., Bucknall, M. P., Young, T. L., Zhang, M., Hu, L., Bing, J., Lee, D. S., Kim, J., Wu, T., Takamure, N., McKenzie, D. R., Huang, S., Green, M. A. and Ho-Baillie, A. W. Y. [2020], 'Gas chromatography-mass spectrometry analyses of encapsulated stable perovskite solar cells', *Science* **368**(6497).

[268] Shockley, W. and Queisser, H. J. [1961], 'Detailed Balance Limit of Efficiency of p-n Junction Solar Cells', *Journal of Applied Physics* **32**(3), 510–519.

[269] Shukla, S., Koh, T. M., Patidar, R., Lew, J. H., Kajal, P., Mhaisalkar, S. G. and Mathews, N. [2021], 'Suppressing the δ-Phase and Photoinstability through a Hypophosphorous Acid Additive in Carbon-Based Mixed-Cation Perovskite Solar Cells', *The Journal of Physical Chemistry C* **125**(12), 6585–6592.

[270] Shukla, S., Shukla, S., Haur, L. J., Dintakurti, S. S. H., Han, G., Priyadarshi, A., Baikie, T., Mhaisalkar, S. G. and Mathews, N. [2017], 'Effect of Formamidinium/Cesium Substitution and PbI_2 on the Long-Term Stability of Triple-Cation Perovskites', *ChemSusChem* **10**(19), 3804–3809.

[271] *Silver behenate, Alfa Aesar* [n.d.]. Last accessed 12 April 2021.
URL: *https://www.alfa.com/en/catalog/045494/*

[272] *SINGLE CRYSTAL X-RAY DIFFRACTION (SC-XRD) D8 VENTURE* [n.d.]. Last accessed 28 August 2022.
URL: *https://www.bruker.com/en/products-and-solutions/diffractometers-and-scattering-systems/single-crystal-x-ray-diffractometers/d8-venture.html*

[273] Sirbu, D., Balogun, F. H., Milot, R. L. and Docampo, P. [2021], 'Layered Perovskites in Solar Cells: Structure, Optoelectronic Properties, and Device Design', *Advanced Energy Materials* **11**(24), 2003877.

[274] Snaith, H. J., Abate, A., Ball, J. M., Eperon, G. E., Leijtens, T., Noel, N. K., Stranks, S. D., Wang, J. T.-W., Wojciechowski, K. and Zhang, W. [2014], 'Anomalous Hysteresis in Perovskite Solar Cells', *The Journal of Physical Chemistry Letters* **5**(9), 1511–1515.

[275] *Solar Cell I-V Test System* [n.d.]. Last accessed 20 October 2021.
URL: *https://www.ossila.com/products/solar-cell-iv-test-system?variant=18259985924192*

[276] Sopian, K., Cheow, S. L. and Zaidi, S. H. [2017], 'An overview of crystalline silicon solar cell technology: Past, present, and future', *AIP Conference Proceedings* **1877**(1), 020004.

[277] Speakman, S. A. [n.d.], 'Estimating Crystallite Size Using XRD'. Last accessed 08 February 2021.
URL: *http://prism.mit.edu/XRAY/oldsite/CrystalSizeAnalysis.pdf*

[278] Steirer, K. X., Schulz, P., Teeter, G., Stevanovic, V., Yang, M., Zhu, K. and Berry, J. J. [2016], 'Defect Tolerance in Methylammonium Lead Triiodide Perovskite', *ACS Energy Letters* **1**(2), 360–366.

[279] Stoddard, R. J., Rajagopal, A., Palmer, R. L., Braly, I. L., Jen, A. K.-Y. and Hillhouse, H. W. [2018], 'Enhancing Defect Tolerance and Phase Stability of High-Bandgap Perovskites via Guanidinium Alloying', *ACS Energy Letters* **3**(6), 1261–1268.

[280] Stolterfoht, M., Caprioglio, P., Wolff, C. M., Márquez, J. A., Nordmann, J., Zhang, S., Rothhardt, D., Hörmann, U., Amir, Y., Redinger, A., Kegelmann, L., Zu, F., Albrecht, S., Koch, N., Kirchartz, T., Saliba, M., Unold, T. and Neher, D. [2019], 'The impact of energy alignment and interfacial recombination on the internal and external open-circuit voltage of perovskite solar cells', *Energy Environ. Sci.* **12**, 2778–2788.

[281] *Stop free icon* [n.d.]. Last accessed 28 November 2021.
URL: *https://www.flaticon.com/free-icon/stop_1670204*

[282] Straus, D. B., Guo, S., Abeykoon, A. M. and Cava, R. J. [2020], 'Understanding the Instability of the Halide Perovskite $CsPbI_3$ through Temperature-Dependent Structural Analysis', *Advanced Materials* **32**(32), 2001069.

[283] Subhani, W. S., Wang, K., Du, M. and Liu, S. F. [2019], 'Goldschmidt-rule-deviated perovskite $CsPbIBr_2$ by barium substitution for efficient solar cells', *Nano Energy* **61**, 165–172.

[284] Sutton, R. J., Eperon, G. E., Miranda, L., Parrott, E. S., Kamino, B. A., Patel, J. B., Hörantner, M. T., Johnston, M. B., Haghighirad, A. A., Moore, D. T. and Snaith, H. J. [2016], 'Bandgap-Tunable Cesium Lead Halide Perovskites with High Thermal Stability for Efficient Solar Cells', *Advanced Energy Materials* **6**(8), 1502458.

[285] Svanström, S., García Fernández, A., Sloboda, T., Jacobsson, T. J., Rensmo, H. and Cappel, U. B. [2021], 'X-ray stability and degradation mechanism of lead halide perovskites and lead halides', *Phys. Chem. Chem. Phys.* **23**, 12479–12489.

[286] Takaki, S., Jiang, F., Masumura, T. and Tsuchiyama, T. [2018], 'Correction of Elastic Anisotropy in Williamson-Hall Plots by Diffraction Young's Modulus and Direct Fitting Method', *ISIJ International* **58**(4), 769–775.

[287] Tan, W., Bowring, A. R., Meng, A. C., McGehee, M. D. and McIntyre, P. C. [2018], 'Thermal Stability of Mixed Cation Metal Halide Perovskites in Air', *ACS Applied Materials & Interfaces* **10**(6), 5485–5491.

[288] Tan, W. L., Cheng, Y.-B. and McNeill, C. R. [2020], 'Direct assessment of structural order and evidence for stacking faults in layered hybrid perovskite films from X-ray scattering measurements', *J. Mater. Chem. A* **8**, 12790–12798.

[289] Tavakoli, M. M., Saliba, M., Yadav, P., Holzhey, P., Hagfeldt, A., Zakeeruddin, S. M. and Grätzel, M. [2019], 'Synergistic Crystal and Interface Engineering for Efficient and Stable Perovskite Photovoltaics', *Advanced Energy Materials* **9**(1), 1802646.

[290] The-Materials-Project [2020*a*], 'Materials Data on PbI_2 by Materials Project'.

[291] The-Materials-Project [2020*b*], 'Materials Data on SbI_3 by Materials Project'.

[292] Travis, W., Glover, E. N. K., Bronstein, H., Scanlon, D. O. and Palgrave, R. G. [2016], 'On the application of the tolerance factor to inorganic and hybrid halide perovskites: a revised system', *Chem. Sci.* **7**, 4548–4556.

[293] Tumen-Ulzii, G., Qin, C., Klotz, D., Leyden, M. R., Wang, P., Auffray, M., Fujihara, T., Matsushima, T., Lee, J.-W., Lee, S.-J., Yang, Y. and Adachi, C. [2020], 'Detrimental Effect of Unreacted PbI_2 on the Long-Term Stability of Perovskite Solar Cells', *Advanced Materials* **32**(16), 1905035.

[294] Tumen-Ulzii, G., Qin, C., Matsushima, T., Leyden, M. R., Balijipalli, U., Klotz, D. and Adachi, C. [2020], 'Understanding the Degradation of Spiro-OMeTAD-Based Perovskite Solar Cells at High Temperature', *Solar RRL* **4**(10), 2000305.

[295] Turren-Cruz, S.-H., Hagfeldt, A. and Saliba, M. [2018], 'Methylammonium-free, high-performance, and stable perovskite solar cells on a planar architecture', *Science* **362**(6413), 449–453.

[296] Ulatowski, A. M., Wright, A. D., Wenger, B., Buizza, L. R. V., Motti, S. G., Eggimann, H. J., Savill, K. J., Borchert, J., Snaith, H. J., Johnston, M. B. and Herz, L. M. [2020], 'Charge-Carrier Trapping Dynamics in Bismuth-Doped Thin Films of $MAPbBr_3$ Perovskite', *The Journal of Physical Chemistry Letters* **11**(9), 3681–3688.

[297] UNIST [2021], 'UNIST, EPFL claim 25.6% efficiency world record for perovskite solar cell'. Last accessed 18 October 2021.
URL: *https://www.pv-magazine.com/2021/04/06/unist-epfl-claim-25-6-efficiency-world-record-for-perovskite-solar-cell/*

[298] Utama, M. I. B., Zhang, J., Chen, R., Xu, X., Li, D., Sun, H. and Xiong, Q. [2012], 'Synthesis and optical properties of II–VI 1D nanostructures', *Nanoscale* **4**, 1422–1435.

[299] Van Reenen, S., Kemerink, M. and Snaith, H. J. [2015], 'Modeling Anomalous Hysteresis in Perovskite Solar Cells', *The Journal of Physical Chemistry Letters* **6**(19), 3808–3814.

[300] Vigil-Galán, O., Courel, M., Andrade-Arvizu, J. A., Sánchez, Y., Espíndola-Rodríguez, M., Saucedo, E., Seuret-Jiménez, D. and Titsworth, M. [2015], 'Route

towards low cost-high efficiency second generation solar cells: current status and perspectives', *Journal of Materials Science: Materials in Electronics* **26**(8), 5562–5573.

[301] Vitz, E., Moore, J. W., Shorb, J., Prat-Resina, X., Wendorff, T. and Hahn, A. [2022], '16.7: Standard molar entropies'. Last accessed 19 September 2022.
URL: *https://chem.libretexts.org*

[302] Wang, J. T.-W., Wang, Z., Pathak, S., Zhang, W., deQuilettes, D. W., Wisnivesky-Rocca-Rivarola, F., Huang, J., Nayak, P. K., Patel, J. B., Mohd Yusof, H. A., Vaynzof, Y., Zhu, R., Ramirez, I., Zhang, J., Ducati, C., Grovenor, C., Johnston, M. B., Ginger, D. S., Nicholas, R. J. and Snaith, H. J. [2016], 'Efficient perovskite solar cells by metal ion doping', *Energy Environ. Sci.* **9**, 2892–2901.

[303] Wang, P., Wu, Y., Cai, B., Ma, Q., Zheng, X. and Zhang, W.-H. [2019], 'Solution-Processable Perovskite Solar Cells toward Commercialization: Progress and Challenges', *Advanced Functional Materials* **29**(47), 1807661.

[304] Wang, S., Huang, Z., Wang, X., Li, Y., Günther, M., Valenzuela, S., Parikh, P., Cabreros, A., Xiong, W. and Meng, Y. S. [2018], 'Unveiling the role of tbp–litfsi complexes in perovskite solar cells', *Journal of the American Chemical Society* **140**(48), 16720–16730.

[305] Wang, S., Sina, M., Parikh, P., Uekert, T., Shahbazian, B., Devaraj, A. and Meng, Y. S. [2016], 'Role of 4-tert-Butylpyridine as a Hole Transport Layer Morphological Controller in Perovskite Solar Cells', *Nano Letters* **16**(9), 5594–5600.

[306] Wang, Y., Guan, X., Chen, W., Yang, J., Hu, L., Yang, J., Li, S., Kalantar-Zadeh, K., Wen, X. and Wu, T. [2020], 'Illumination-Induced Phase Segregation and Suppressed Solubility Limit in Br-Rich Mixed-Halide Inorganic Perovskites', *ACS Applied Materials & Interfaces* **12**(34), 38376–38385.

[307] Wang, Y., Liu, Y., Cao, S. and Wang, J. [2021], 'A review on solution-processed perovskite/organic hybrid photodetectors', *J. Mater. Chem. C* **9**, 5302–5322.

[308] Wang, Z.-K., Li, M., Yang, Y.-G., Hu, Y., Ma, H., Gao, X.-Y. and Liao, L.-S. [2016], 'High Efficiency Pb–In Binary Metal Perovskite Solar Cells', *Advanced Materials* **28**(31), 6695–6703.

[309] Wang, Z., Zeng, L., Zhang, C., Lu, Y., Qiu, S., Wang, C., Liu, C., Pan, L., Wu, S., Hu, J., Liang, G., Fan, P., Egelhaaf, H.-J., Brabec, C. J., Guo, F. and Mai, Y. [2020], 'Rational Interface Design and Morphology Control for Blade-Coating Efficient Flexible Perovskite Solar Cells with a Record Fill Factor of 81%', *Advanced Functional Materials* **30**(32), 2001240.

[310] Wei, H. and Huang, J. [2019], 'Halide lead perovskites for ionizing radiation detection', *Nature Communications* **10**, 1066.

[311] Wei, J., Zhao, Y., Li, H., Li, G., Pan, J., Xu, D., Zhao, Q. and Yu, D. [2014], 'Hysteresis Analysis Based on the Ferroelectric Effect in Hybrid Perovskite Solar Cells', *The Journal of Physical Chemistry Letters* **5**(21), 3937–3945.

[312] Wetzelaer, G.-J. A. H., Scheepers, M., Sempere, A. M., Momblona, C., Ávila, J. and Bolink, H. J. [2015], 'Trap-Assisted Non-Radiative Recombination in Organic–Inorganic Perovskite Solar Cells', *Advanced Materials* **27**(11), 1837–1841.

[313] *World population prospects 2019* [2019], Online edition, United Nations, Department of Economic and Social Affairs, Population Division.

[314] Wu, S., Li, Z., Zhang, J., Liu, T., Zhu, Z. and Jen, A. K.-Y. [2019], 'Efficient large guanidinium mixed perovskite solar cells with enhanced photovoltage and low energy losses', *Chem. Commun.* **55**, 4315–4318.

[315] Wu, W.-Q., Liao, J.-F., Zhong, J.-X., Xu, Y.-F., Wang, L. and Huang, J. [2020], 'Suppressing Interfacial Charge Recombination in Electron-Transport-Layer-Free Perovskite Solar Cells to Give an Efficiency Exceeding 21%', *Angewandte Chemie International Edition* **59**(47), 20980–20987.

[316] Wu, Y., Wan, L., Fu, S., Zhang, W., Li, X. and Fang, J. [2019], 'Liquid metal acetate assisted preparation of high-efficiency and stable inverted perovskite solar cells', *J. Mater. Chem. A* **7**, 14136–14144.

[317] Xiang, S., Li, W., Wei, Y., Liu, J., Liu, H., Zhu, L. and Chen, H. [2018], 'The synergistic effect of non-stoichiometry and Sb-doping on air-stable α-$CsPbI_3$ for efficient carbon-based perovskite solar cells', *Nanoscale* **10**, 9996–10004.

[318] Xiang, W., Wang, Z., Kubicki, D. J., Tress, W., Luo, J., Prochowicz, D., Akin, S., Emsley, L., Zhou, J., Dietler, G., Grätzel, M. and Hagfeldt, A. [2019], 'Europium-Doped $CsPbI_2Br$ for Stable and Highly Efficient Inorganic Perovskite Solar Cells', *Joule* **3**(1), 205–214.

[319] Xiao, M., Huang, F., Huang, W., Dkhissi, Y., Zhu, Y., Etheridge, J., Gray-Weale, A., Bach, U., Cheng, Y.-B. and Spiccia, L. [2014], 'A Fast Deposition-Crystallization Procedure for Highly Efficient Lead Iodide Perovskite Thin-Film Solar Cells', *Angewandte Chemie International Edition* **53**(37), 9898–9903.

[320] Xiao, S., Zhang, K., Zheng, S. and Yang, S. [2020], 'Good or evil: what is the role of water in crystallization of organometal halide perovskites?', *Nanoscale Horiz.* **5**, 1147–1154.

[321] Xiao, X., Hu, J., Tang, S., Yan, K., Gao, B., Chen, H. and Zou, D. [2020], 'Recent Advances in Halide Perovskite Memristors: Materials, Structures, Mechanisms, and Applications', *Advanced Materials Technologies* **5**(6), 1900914.

[322] Xing, G., Wu, B., Chen, S., Chua, J., Yantara, N., Mhaisalkar, S., Mathews, N. and Sum, T. C. [2015], 'Interfacial Electron Transfer Barrier at Compact TiO_2/$CH_3NH_3PbI_3$ Heterojunction', *Small* **11**(29), 3606–3613.

[323] Xiong, L., Guo, Y., Wen, J., Liu, H., Yang, G., Qin, P. and Fang, G. [2018], 'Review on the Application of SnO_2 in Perovskite Solar Cells', *Advanced Functional Materials* **28**(35), 1802757.

[324] Xu, S., Liu, G., Zheng, H., Xu, X., Zhang, L., Xu, H., Zhu, L., Kong, F., Li, Y. and Pan, X. [2020], 'Boosting Photovoltaic Performance and Stability of Super-Halogen-Substituted Perovskite Solar Cells by Simultaneous Methylammonium Immobilization and Vacancy Compensation', *ACS Applied Materials & Interfaces* **12**(7), 8249–8259.

[325] Xu, Z., Liu, Z., Li, N., Tang, G., Zheng, G., Zhu, C., Chen, Y., Wang, L., Huang, Y., Li, L., Zhou, N., Hong, J., Chen, Q. and Zhou, H. [2019], 'A Thermodynamically Favored Crystal Orientation in Mixed Formamidinium/Methylammonium Perovskite for Efficient Solar Cells', *Advanced Materials* **31**(24), 1900390.

[326] Yagi, E., Hasiguti, R. R. and Aono, M. [1996], 'Electronic conduction above 4 K of slightly reduced oxygen-deficient rutile TiO_{2-x}', *Phys. Rev. B* **54**, 7945–7956.

[327] Yang, D., Zhang, X., Hou, Y., Wang, K., Ye, T., Yoon, J., Wu, C., Sanghadasa, M., Liu, S. F. and Priya, S. [2021], '28.3%-efficiency perovskite/silicon tandem solar cell by optimal transparent electrode for high efficient semitransparent top cell', *Nano Energy* **84**, 105934.

[328] Yang, F., Kamarudin, M. A., Kapil, G., Hirotani, D., Zhang, P., Ng, C. H., Ma, T. and Hayase, S. [2018], 'Magnesium-Doped $MAPbI_3$ Perovskite Layers for Enhanced Photovoltaic Performance in Humid Air Atmosphere', *ACS Applied Materials & Interfaces* **10**(29), 24543–24548.

[329] Yang, S., Chen, S., Mosconi, E., Fang, Y., Xiao, X., Wang, C., Zhou, Y., Yu, Z., Zhao, J., Gao, Y., Angelis, F. D. and Huang, J. [2019], 'Stabilizing halide perovskite surfaces for solar cell operation with wide-bandgap lead oxysalts', *Science* **365**(6452), 473–478.

[330] Yang, S., Niu, W., Wang, A.-L., Fan, Z., Chen, B., Tan, C., Lu, Q. and Zhang, H. [2017], 'Ultrathin Two-Dimensional Organic–Inorganic Hybrid Perovskite Nanosheets with Bright, Tunable Photoluminescence and High Stability', *Angewandte Chemie International Edition* **56**(15), 4252–4255.

[331] Yang, X., Wang, W., Ran, R., Zhou, W. and Shao, Z. [2020], 'Recent Advances in $Cs_2AgBiBr_6$-Based Halide Double Perovskites as Lead-Free and Inorganic Light Absorbers for Perovskite Solar Cells', *Energy & Fuels* **34**(9), 10513–10528.

[332] Yang, Y., Yang, M., Moore, D., Yan, Y., Miller, E., Zhu, K. and Beard, M. [2017], 'Top and bottom surfaces limit carrier lifetime in lead iodide perovskite films', *Nature Energy* **2**(2), 16207.

[333] Yi, H., Duan, L., Haque, F., Bing, J., Zheng, J., Yang, Y., him Mo, A. C., Zhang, Y., Xu, C., Conibeer, G. and Uddin, A. [2020], 'Thiocyanate assisted nucleation for high performance mix-cation perovskite solar cells with improved stability', *Journal of Power Sources* **466**, 228320.

[334] Yin, Y., Fu, S., Zhou, S., Song, Y., Li, L., Zhang, M., Wang, J., Mariyappan, P., Alshehri, S. M., Ahamad, T. and Yamauchi, Y. [2020], 'Efficient and Stable Ideal Bandgap Perovskite Solar Cell Achieved by a Small Amount of Tin Substituted Methylammonium Lead Iodide', *Electronic Materials Letters* **16**(3), 224–230.

[335] Yun, J. S., Ho-Baillie, A., Huang, S., Woo, S. H., Heo, Y., Seidel, J., Huang, F., Cheng, Y.-B. and Green, M. A. [2015], 'Benefit of Grain Boundaries in Organic–Inorganic Halide Planar Perovskite Solar Cells', *The Journal of Physical Chemistry Letters* **6**(5), 875–880.

[336] Zaleski, J., Jakubas, R., Sobczyk, L. and Mróz, J. [1990], 'Properties and structural phase transitions of $(CH_3NH_3)_3$ Sb_2I_9', *Ferroelectrics* **103**(1), 83–90.

[337] Zhang, H., Li, R., Zhang, M. and Guo, M. [2020], 'Effect of Sr substitution on the air-stability of perovskite solar cells', *Ceramics International* **46**(9), 14038–14047.

[338] Zhang, J., Shang, M.-h., Wang, P., Huang, X., Xu, J., Hu, Z., Zhu, Y. and Han, L. [2016], 'n-Type Doping and Energy States Tuning in $CH_3NH_3Pb_{1-x}Sb_{2x/3}I_3$ Perovskite Solar Cells', *ACS Energy Letters* **1**(3), 535–541.

[339] Zhang, M., Xin, D., Zheng, X., Chen, Q. and Zhang, W.-H. [2020], 'Toward Greener Solution Processing of Perovskite Solar Cells', *ACS Sustainable Chemistry & Engineering* **8**(35), 13126–13138.

[340] Zhang, M., Zheng, Z., Fu, Q., Chen, Z., He, J., Zhang, S., Yan, L., Hu, Y. and Luo, W. [2017], 'Growth and characterization of all-inorganic lead halide perovskite semiconductor $CsPbBr_3$ single crystals', *CrystEngComm* **19**, 6797–6803.

[341] Zhang, S., Shaw, P. E., Zhang, G., Jin, H., Tai, M., Lin, H., Meredith, P., Burn, P. L., Neher, D. and Stolterfoht, M. [2020], 'Defect/Interface Recombination Limited Quasi-Fermi Level Splitting and Open-Circuit Voltage in Mono- and Triple-Cation Perovskite Solar Cells', *ACS Applied Materials & Interfaces* **12**(33), 37647–37656.

[342] Zhang, S., Wu, S., Chen, R., Chen, W., Huang, Y., Yang, Z. and Chen, W. [2020], 'Formamidine-assisted fast crystallization to fabricate formamidinium-based perovskite films for high-efficiency and stable solar cells', *J. Mater. Chem. C* **8**, 1642–1648.

[343] Zhang, S., Wu, S., Chen, R., Chen, W., Huang, Y., Zhu, H., Yang, Z. and Chen, W. [2019], 'Controlling Orientation Diversity of Mixed Ion Perovskites: Reduced Crystal Microstrain and Improved Structural Stability', *The Journal of Physical Chemistry Letters* **10**(11), 2898–2903.

[344] Zhang, W., Furtado, K., Wu, P., Zhou, T., Chadwick, R., Marzin, C., Rostron, J. and Sexton, D. [2021], 'Increasing precipitation variability on daily-to-multiyear time scales in a warmer world', *Science Advances* **7**(31), eabf8021.

[345] Zhang, W., Xiong, J., Li, J. and Daoud, W. A. [2019], 'Guanidinium induced phase separated perovskite layer for efficient and highly stable solar cells', *J. Mater. Chem. A* **7**, 9486–9496.

[346] Zhang, X., Xu, B., Zhang, J., Gao, Y., Zheng, Y., Wang, K. and Sun, X. W. [2016], 'All-Inorganic Perovskite Nanocrystals for High-Efficiency Light Emitting Diodes: Dual-Phase $CsPbBr_3$-$CsPb_2Br_5$ Composites', *Advanced Functional Materials* **26**(25), 4595–4600.

[347] Zhao, Y.-C., Zhou, W.-K., Zhou, X., Liu, K.-H., Yu, D.-P. and Zhao, Q. [2017], 'Quantification of light-enhanced ionic transport in lead iodide perovskite thin films and its solar cell applications', *Light: Science & Applications* **6**, e16243.

[348] Zhao, Y., Dai, Y., Wang, Q., Dong, Y., Song, T., Mudryi, A., Chen, Q. and Li, Y. [2021], 'Anions-Exchange-Induced Efficient Carrier Transport at $CsPbBr_xCl_{3-x}/TiO_2$ Interface for Photocatalytic Activation of C(sp^3)-H bond in Toluene Oxidation', *ChemCatChem* **13**(11), 2592–2598.

[349] Zhao, Y., Zhang, H., Ren, X., Zhu, H. L., Huang, Z., Ye, F., Ouyang, D., Cheah, K. W., Jen, A. K.-Y. and Choy, W. C. H. [2018], 'Thick TiO_2-Based Top Electron Transport Layer on Perovskite for Highly Efficient and Stable Solar Cells', *ACS Energy Letters* **3**(12), 2891–2898.

[350] Zheng, C. and Rubel, O. [2017], 'Ionization Energy as a Stability Criterion for Halide Perovskites', *The Journal of Physical Chemistry C* **121**, 11977–11984.

[351] Zheng, G., Zhu, C., Ma, J., Zhang, X., Tang, G., Li, R., Chen, Y., Li, L., Hu, J., Hong, J., Chen, Q., Gao, X. and Zhou, H. [2018], 'Manipulation of facet orientation in hybrid perovskite polycrystalline films by cation cascade', *Nature Communications* **9**(1), 2793.

[352] Zheng, X., Wu, C., Jha, S. K., Li, Z., Zhu, K. and Priya, S. [2016], 'Improved Phase Stability of Formamidinium Lead Triiodide Perovskite by Strain Relaxation', *ACS Energy Letters* **1**(5), 1014–1020.

[353] Zhong, Y., Hufnagel, M., Thelakkat, M., Li, C. and Huettner, S. [2020], 'Role of PCBM in the Suppression of Hysteresis in Perovskite Solar Cells', *Advanced Functional Materials* **30**(23), 1908920.

[354] Zhumekenov, A. A., Saidaminov, M. I., Haque, M. A., Alarousu, E., Sarmah, S. P., Murali, B., Dursun, I., Miao, X.-H., Abdelhady, A. L., Wu, T., Mohammed, O. F. and Bakr, O. M. [2016], 'Formamidinium Lead Halide Perovskite Crystals with Unprecedented Long Carrier Dynamics and Diffusion Length', *ACS Energy Letters* **1**(1), 32–37.

[355] Zou, S., Liu, Y., Li, J., Liu, C., Feng, R., Jiang, F., Li, Y., Song, J., Zeng, H., Hong, M. and Chen, X. [2017], 'Stabilizing Cesium Lead Halide Perovskite Lattice through Mn(II) Substitution for Air-Stable Light-Emitting Diodes', *Journal of the American Chemical Society* **139**(33), 11443–11450.

[356] Zuo, C., Bolink, H. J., Han, H., Huang, J., Cahen, D. and Ding, L. [2016], 'Advances in Perovskite Solar Cells', *Advanced Science* **3**(7), 1500324.

Appendix A. Instrumental aberrations

ERROR	DIAGRAM	CONTRIBUTION
Finite X-ray source	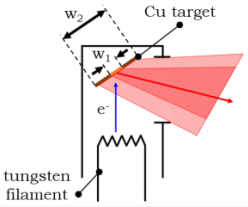	**FWHM + tails** This error is particularly relevant in broad focus tubes, as the beam is dependent on the size of the target. Additionally, most of the target's surface produces X-rays at a lower intensity than the focal point, modifying the peak tails. The effect is significant when analysing intense lines.
Flat sample	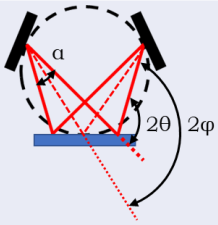	**FWHM + asymmetry** Samples are not curved to the diffraction focus circle which generates defocussing of the beam (2φ – 2θ). Operating in fixed divergence angle (α), the function is maximum at low 2θ and decreases with increasing diffraction angle. The opposite occurs when operating in fixed illumination length, where the maximum is set at 2θ = 90° .
Sample transparency	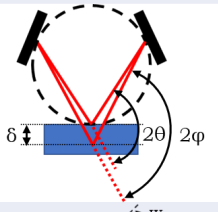	**FWHM + asymmetry** Defocussing occurs as the beam penetrates deep in the sample. This error is particularly relevant in samples with linear absorption coefficients (μ) below 50 cm^{-1}. The function increases with 2θ, reaching its maximum at 90°.
Finite width of receiving slit	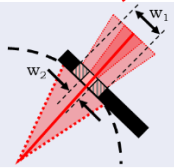	**FHWM** The size of the receiving slit directly affects the width of the diffracted rays detected. For slits wider than 0.15 mm, this instrumental contribution is often the dominant aberration between 15°<2θ<60° in a diffractometer.
Axial divergence	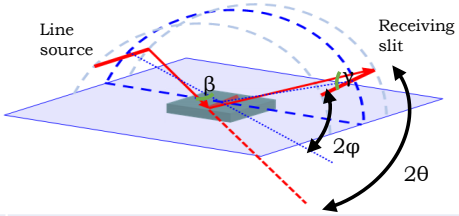	**FWHM + asymmetry** When X-rays both in the source and diffracting beam are angled to the equatorial plane (β,γ), the diffractometer will detect them at an angle 2φ, which differs from the parallel beam recorded at 2θ, causing the axial divergence aberration. The function is maximum at low angles and decreases with 2θ up until 90°.
Si-PSD detector	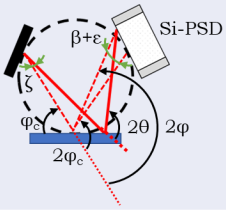	**FWHM** The presence of a flat detector produces a similar effect on the beam to the defocussing occurring in a flat sample (ζ). With both effects, now the defocussing (ε = 2φ-2θ) is no longer symmetric about the centre of the Si-PSD and so the beam is detected at an additional angle (β) than the one expected at the centre of the detector ($2\varphi_c$)

Figure A.1: Summary of the main instrumental contributions present in a standard laboratory XRD diffractometer. Diagrams adapted with permission from [39].

Appendix B. Chapter 4 supplementary figures

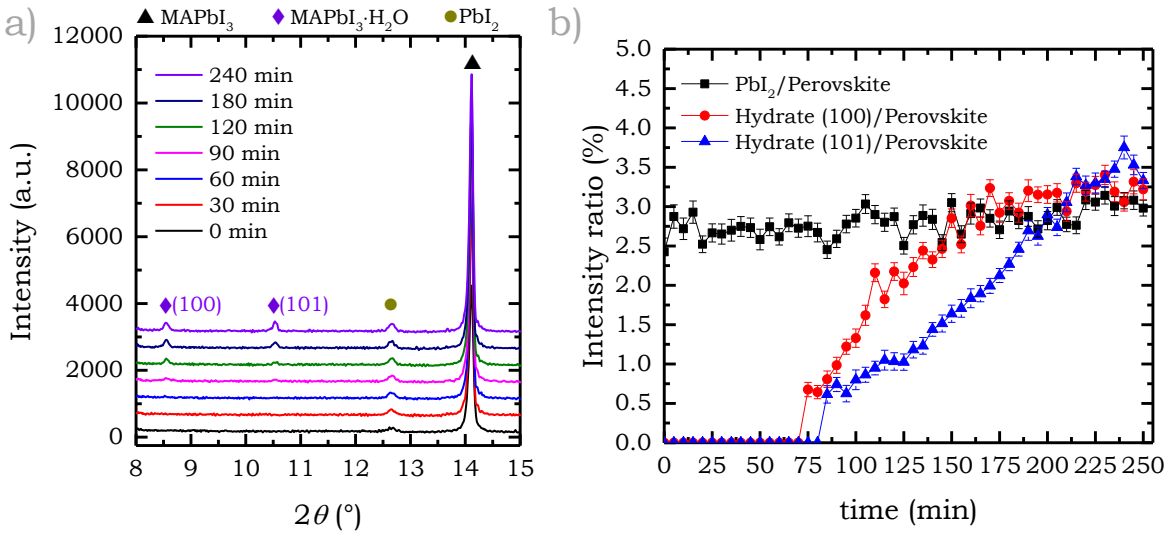

Figure B.1: *In-situ* evolution of a $MAPbI_3$ film over time upon >90 % RH exposure. a) XRD patterns. b) XRD peak height ratio of degradation products vs perovskite.

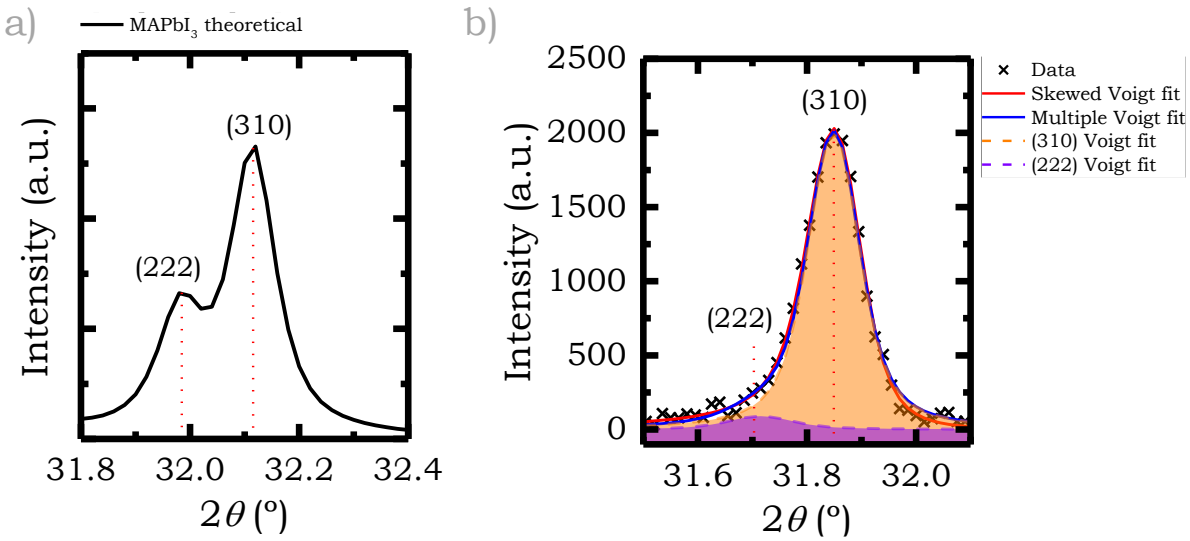

Figure B.2: a) Theoretical diffraction peaks for tetragonal $MAPbI_3$ powder between 31.8° and 32.2°. b) Comparison between a skewed Voigt fit and a multiple Voigt fit for the diffraction peaks of a $MAPbI_3$ film between 31.5° and 32.1°. The scan was taken in Bragg-Brentano configuration at a 0.5 s/step rate.

MEASUREMENT						
Name	**Knife**	**step (°)**	**T (s/step)**	**PS (mm)**	**SS (mm)**	**PSD (°)**
No-Knife	No				5.4	
Knife	Yes	0.015	0.16	1	5.4	2.93
Low SS	Yes				2.0	

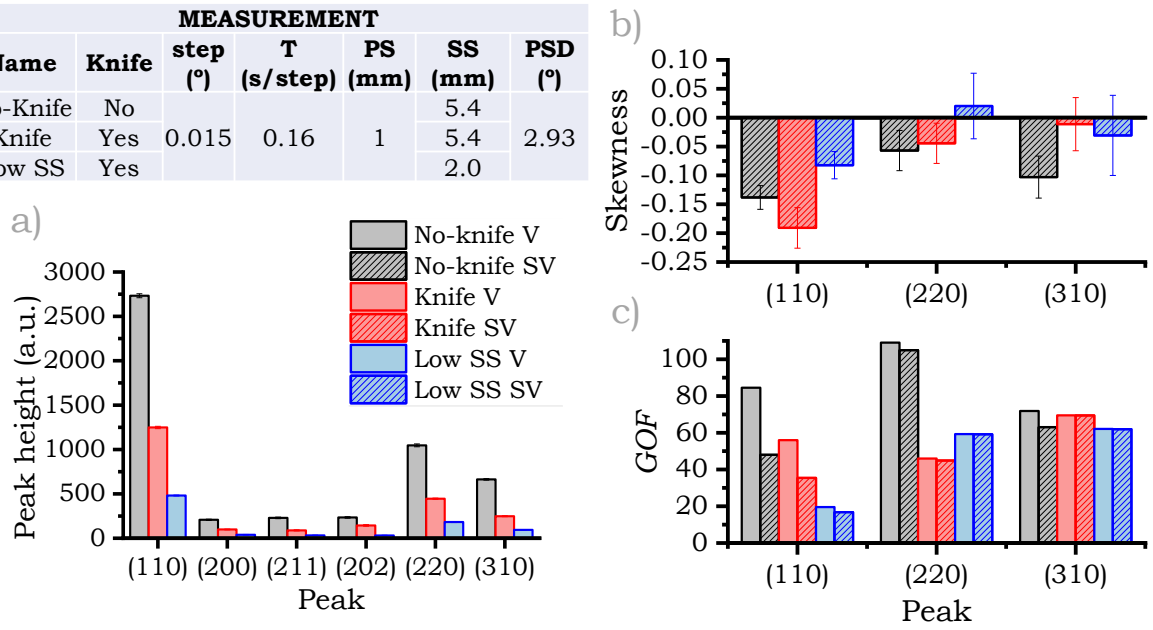

Figure B.3: Peak height, plotted per indexed crystallographic plane, extracted from a Voigt fit of the perovskite diffracting peaks of a $MAPbI_3$ film in three Bragg-Brentano scans. Details on the differences between scans are included on top of the graph, with PS and SS standing for the opening length of the primary and secondary slit, respectively, and PSD for the opening degree of the position-sensitive device detector. b) Skew value obtained from the skewed Voigt fit of the most intense peaks from the diffraction patterns processed in figure a. c) Plot of the goodness of fit (GOF) of the most intense peaks from the diffraction patterns processed in figure a.

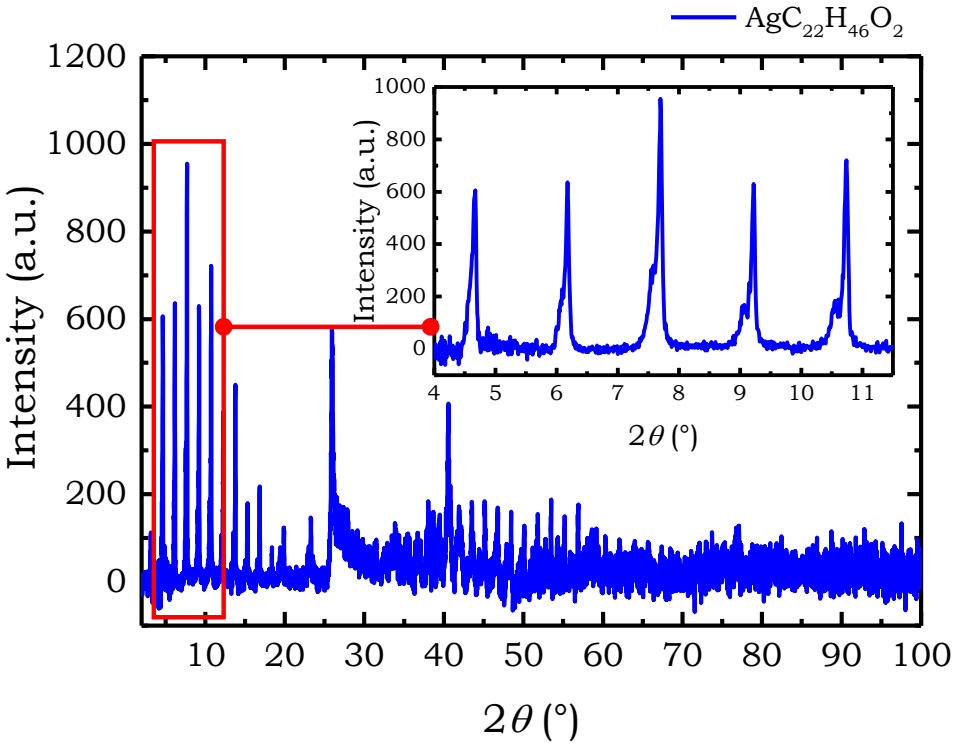

Figure B.4: XRD of a silver behenate ($AgC_{22}H_{46}O_2$) powder sample. The inset in the figure highlights the presence of a doublet in the diffraction peaks with increasing 2θ.

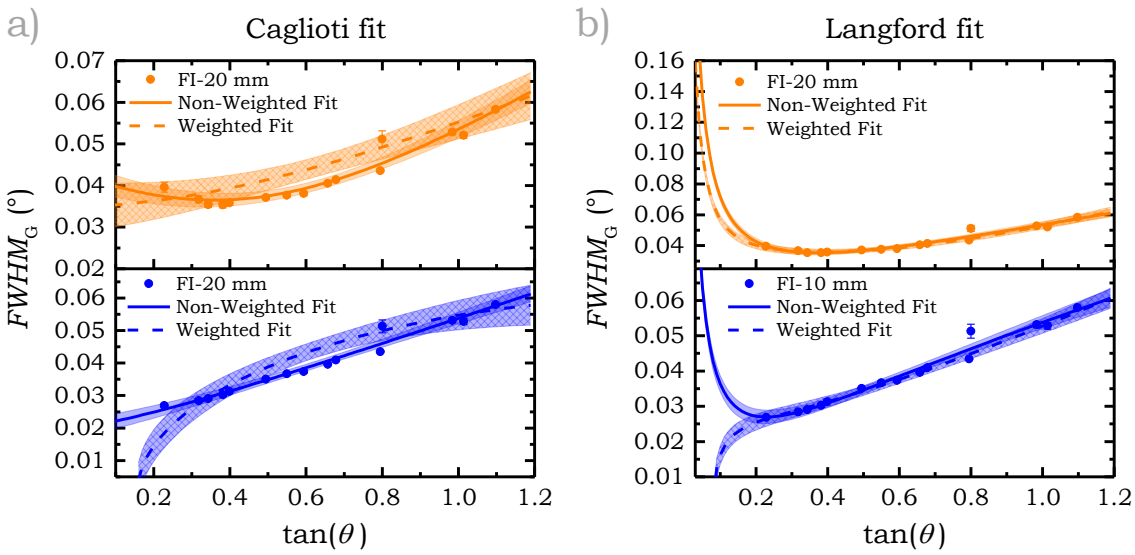

Figure B.5: Instrumental Caglioti (a) and Langford (b) curve fits of the Gaussian widths ($FWHM_G$) of the diffraction peaks of the NIST SRM-1976 corundum plate with and without considering error weights. Coloured areas represent the 95 % confidence interval of the fits. The XRD scans were acquired in a fixed illumination configuration (FI) with primary and secondary openings of 20 mm (top plots) and 10 mm (bottom plots).

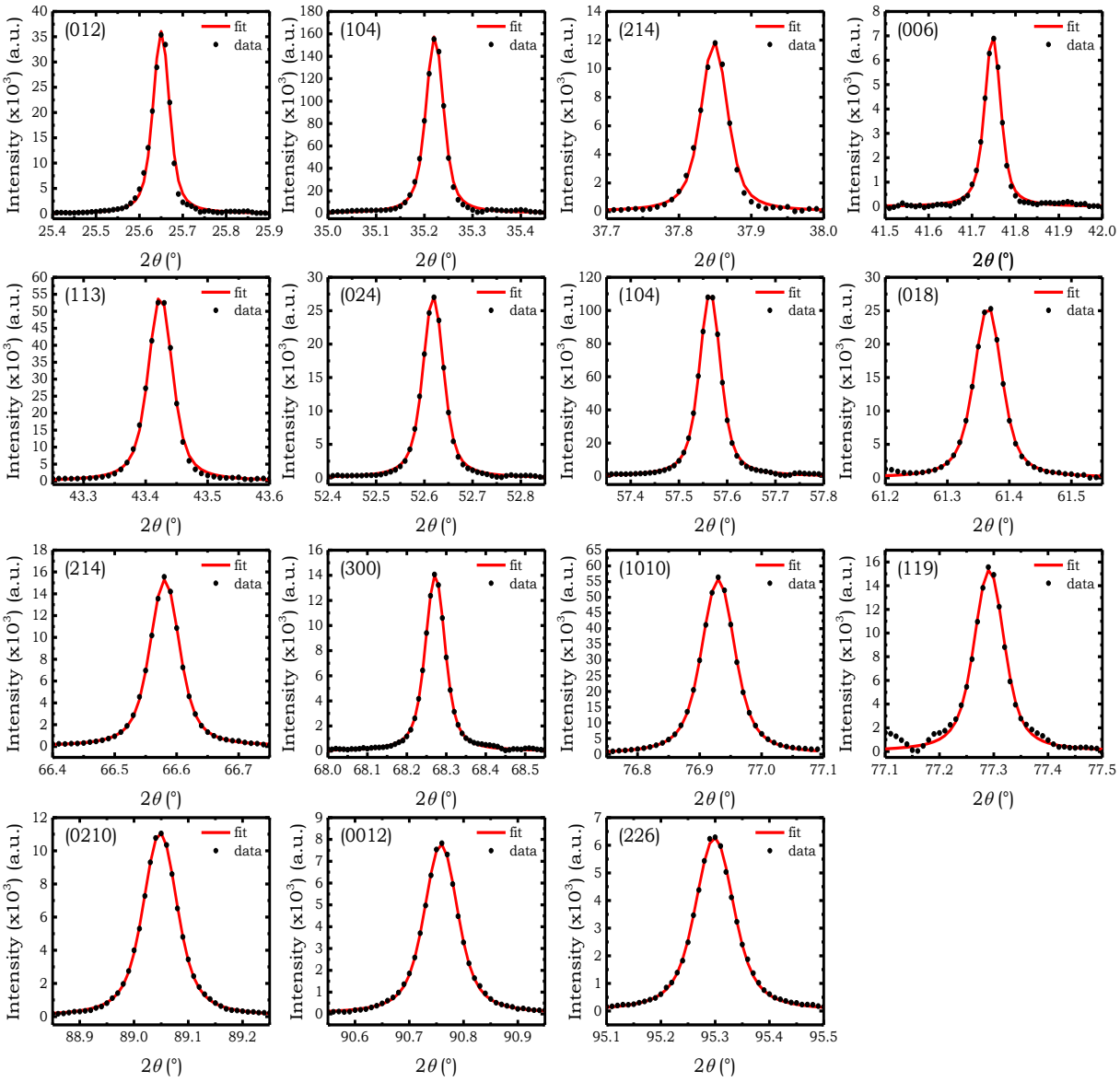

Figure B.6: Voigt fits of the Corundum NIST SRM-1976b diffraction peaks in a fixed slit setup with maximum aperture (primary slit 1.0 mm, secondary slit 5.4 mm)

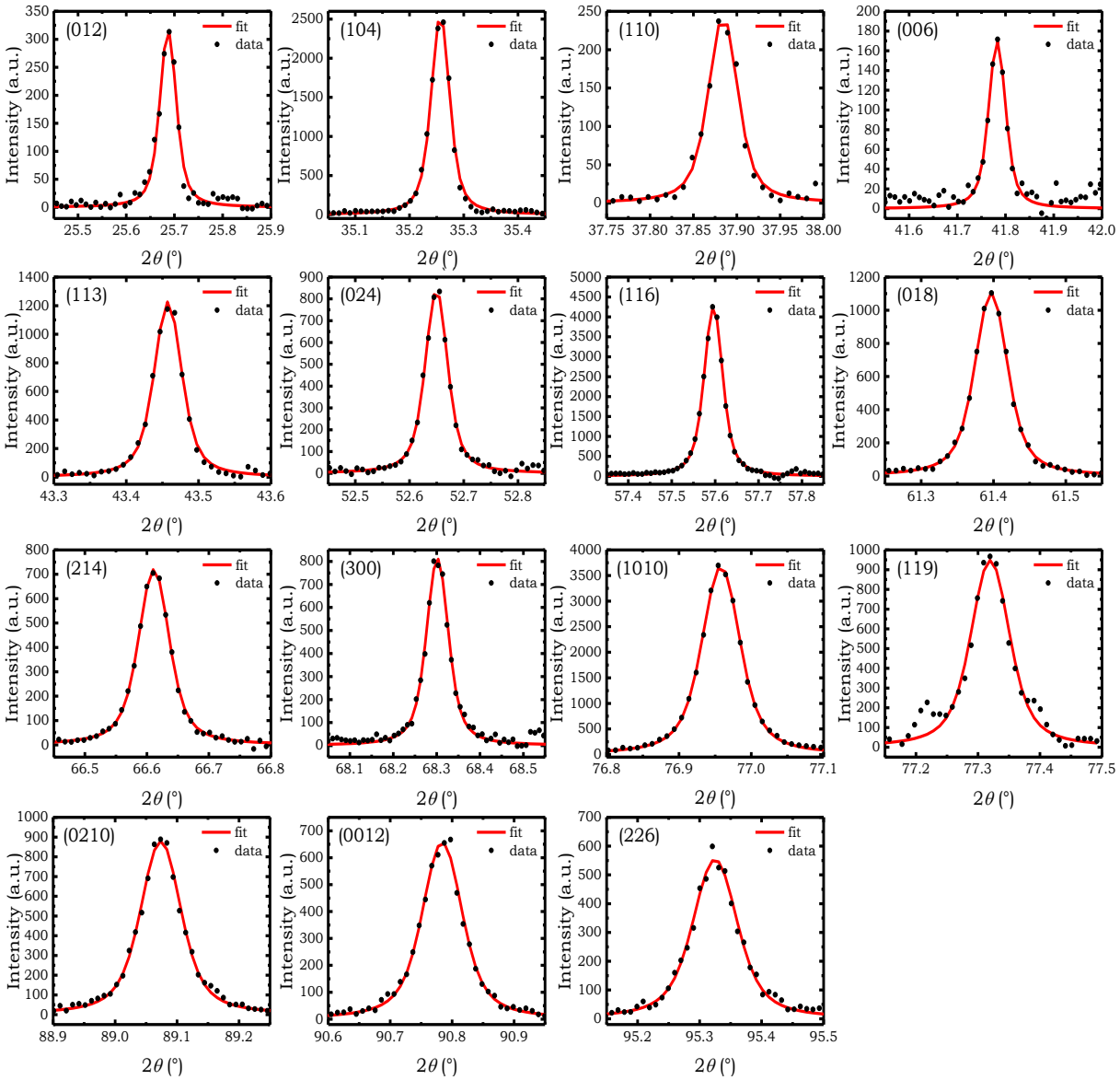

Figure B.7: Voigt fits of the Corundum NIST SRM-1976b diffraction peaks in a fixed illumination setup with a 2 mm illumination length of both the primary and secondary optics.

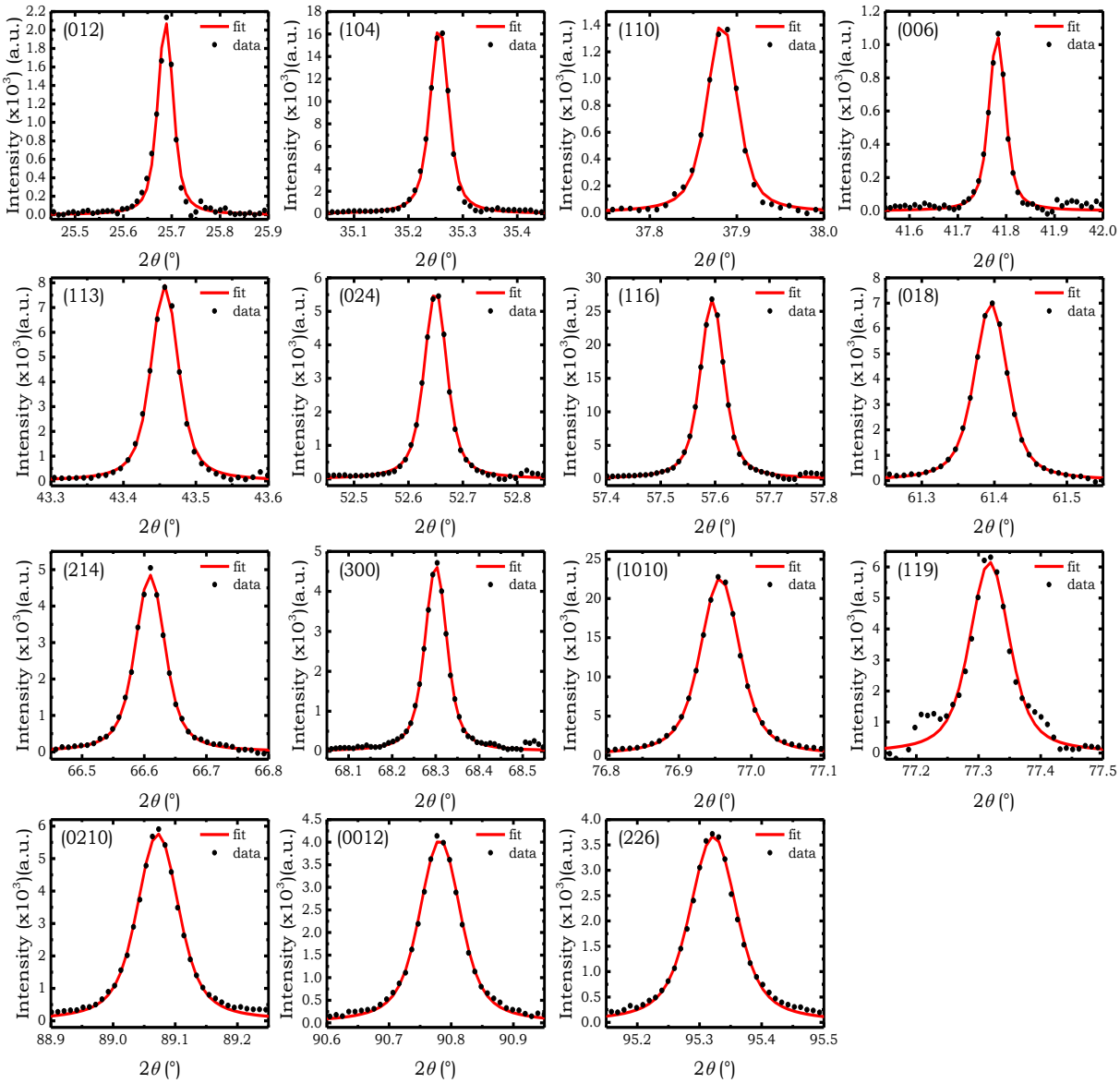

Figure B.8: Voigt fits of the Corundum NIST SRM-1976b diffraction peaks in a fixed illumination setup with a 5 mm illumination length of both the primary and secondary optics.

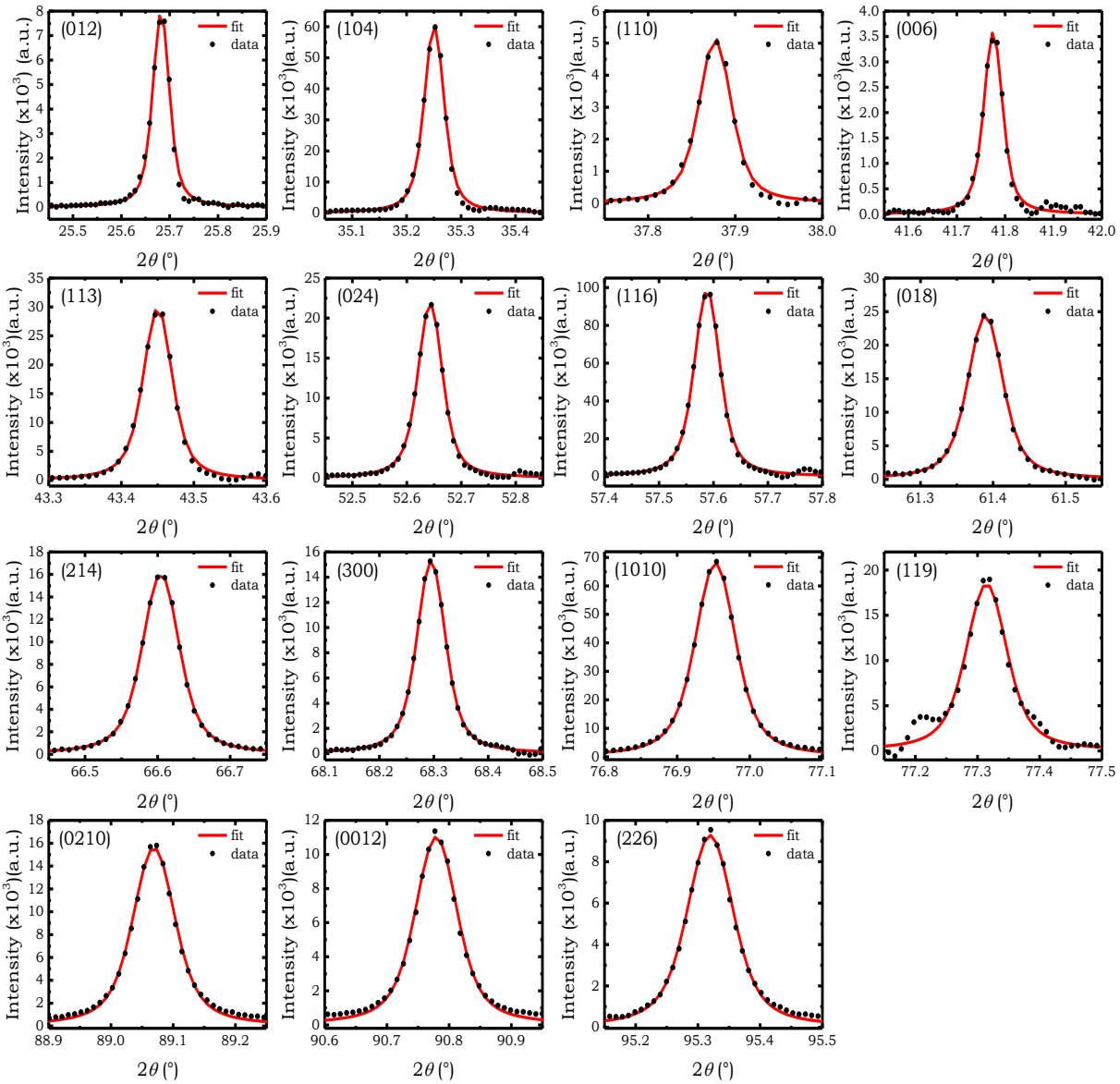

Figure B.9: Voigt fits of the Corundum NIST SRM-1976b diffraction peaks in a fixed illumination setup with a 10 mm illumination length of both the primary and secondary optics.

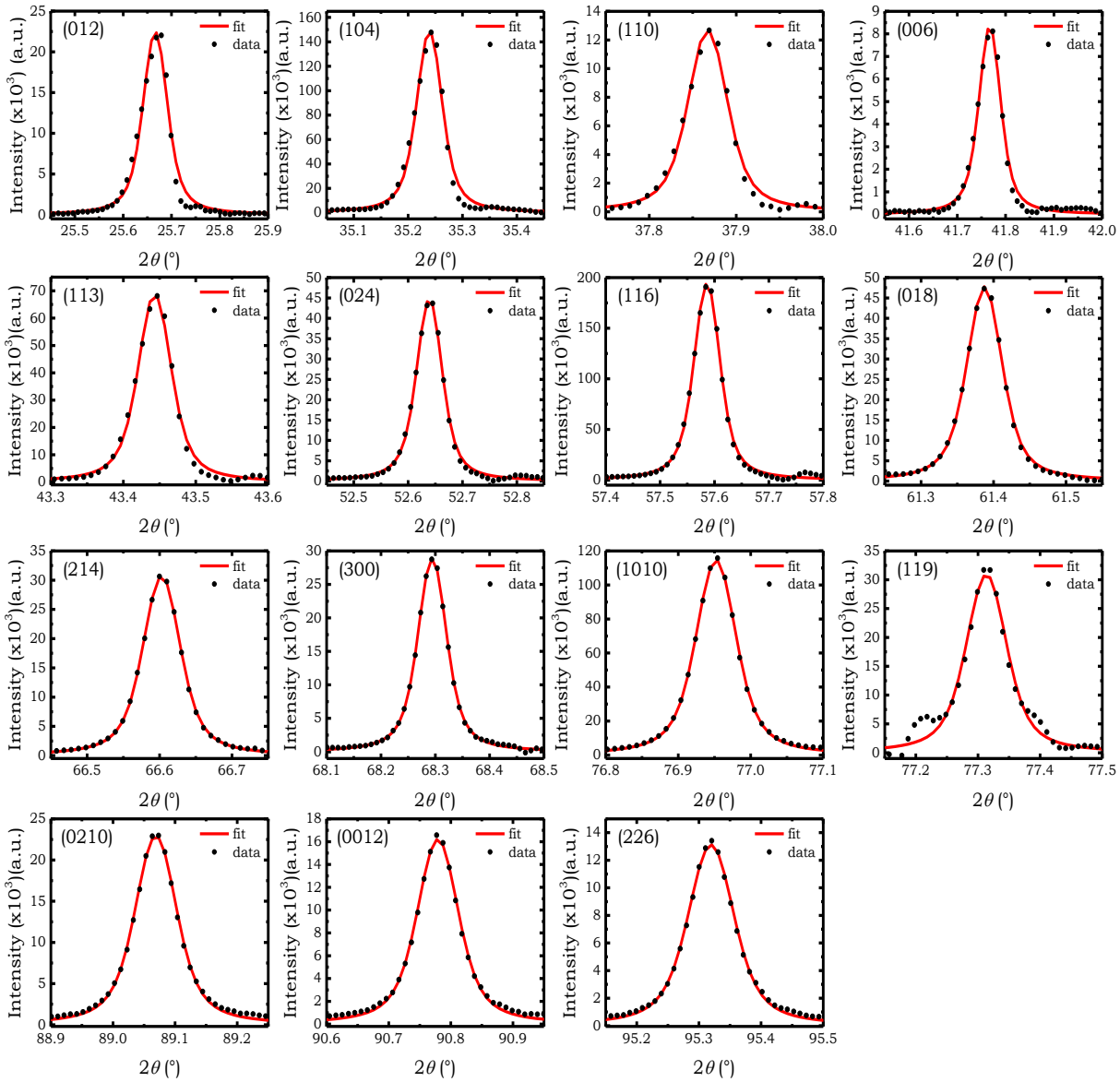

Figure B.10: Voigt fits of the Corundum NIST SRM-1976b diffraction peaks in a fixed illumination setup with a 20 mm illumination length of both the primary and secondary optics.

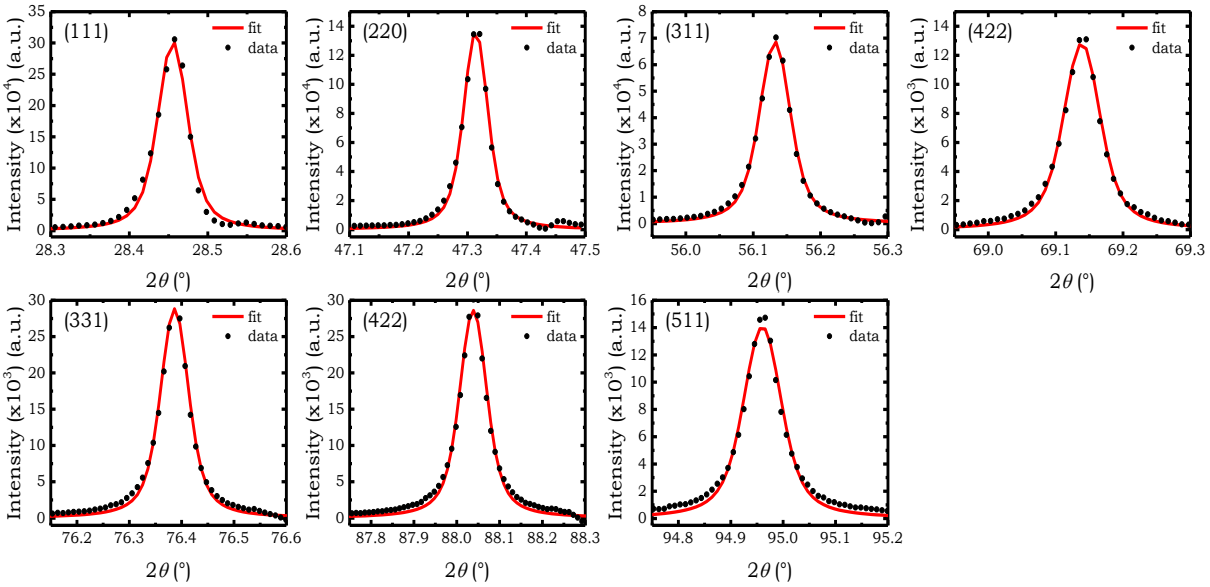

Figure B.11: Voigt fits of the Si powder sample diffraction peaks in a fixed slit setup with maximum aperture (primary slit 1.0 mm, secondary slit 5.4 mm).

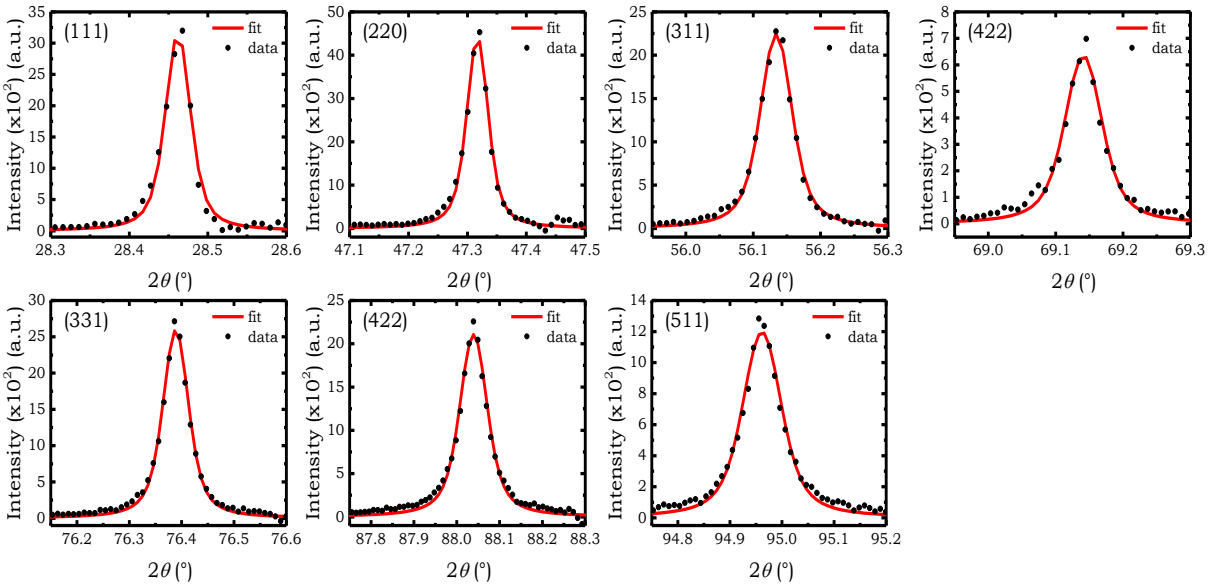

Figure B.12: Voigt fits of the Si powder sample diffraction peaks in a fixed illumination setup with a 2 mm illumination length of both the primary and secondary optics.

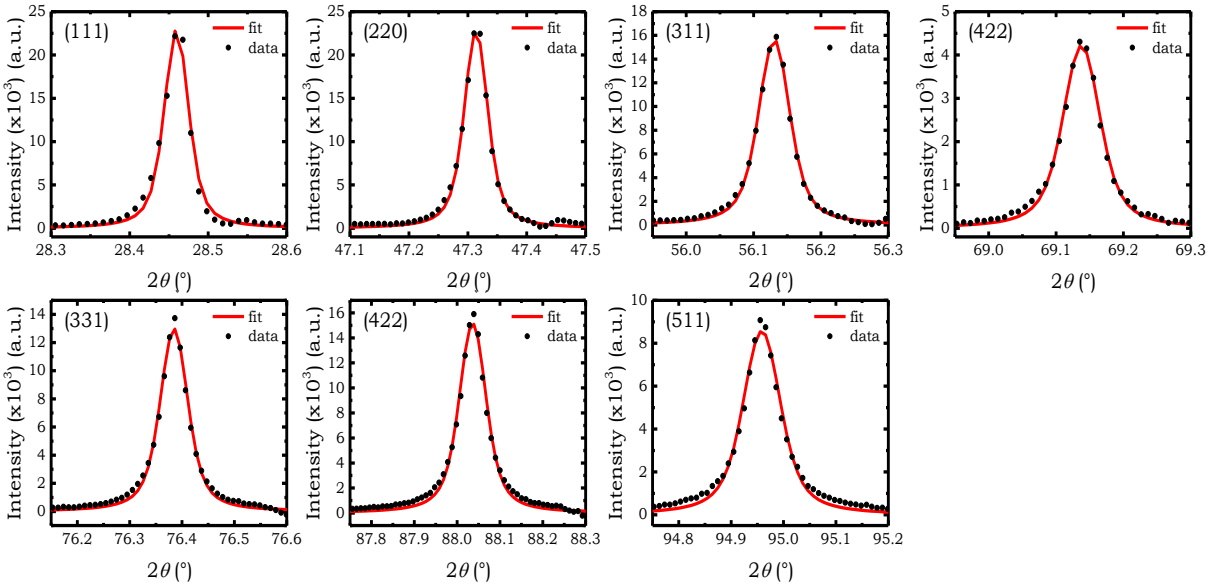

Figure B.13: Voigt fits of the Si powder sample diffraction peaks in a fixed illumination setup with a 5 mm illumination length of both the primary and secondary optics.

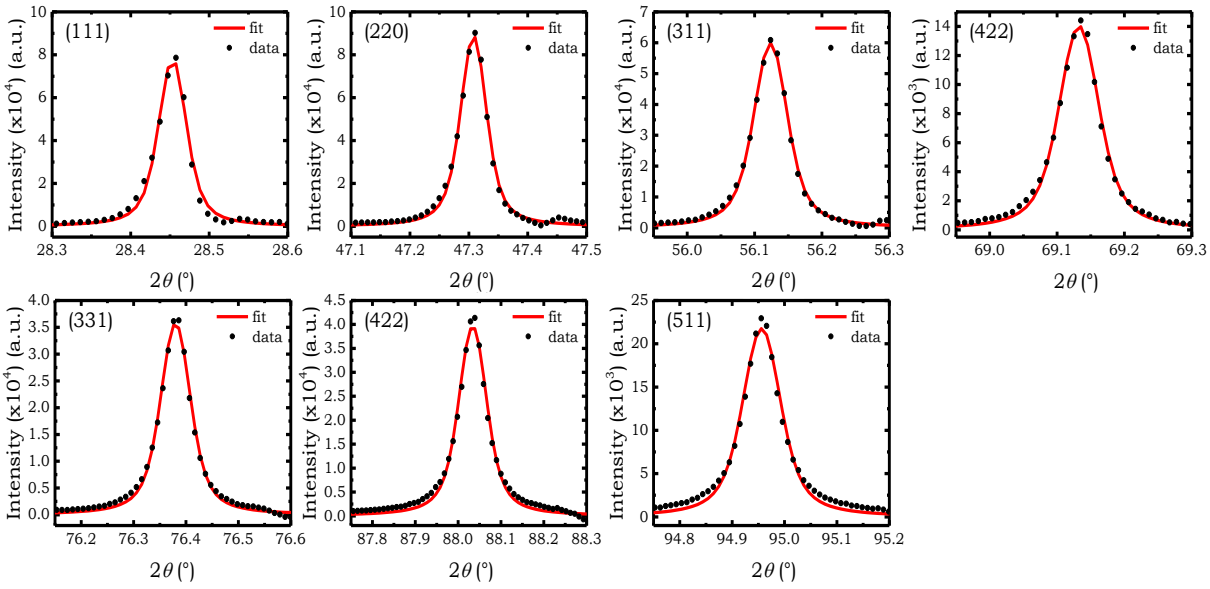

Figure B.14: Voigt fits of the Si powder sample diffraction peaks in a fixed illumination setup with a 10 mm illumination length of both the primary and secondary optics.

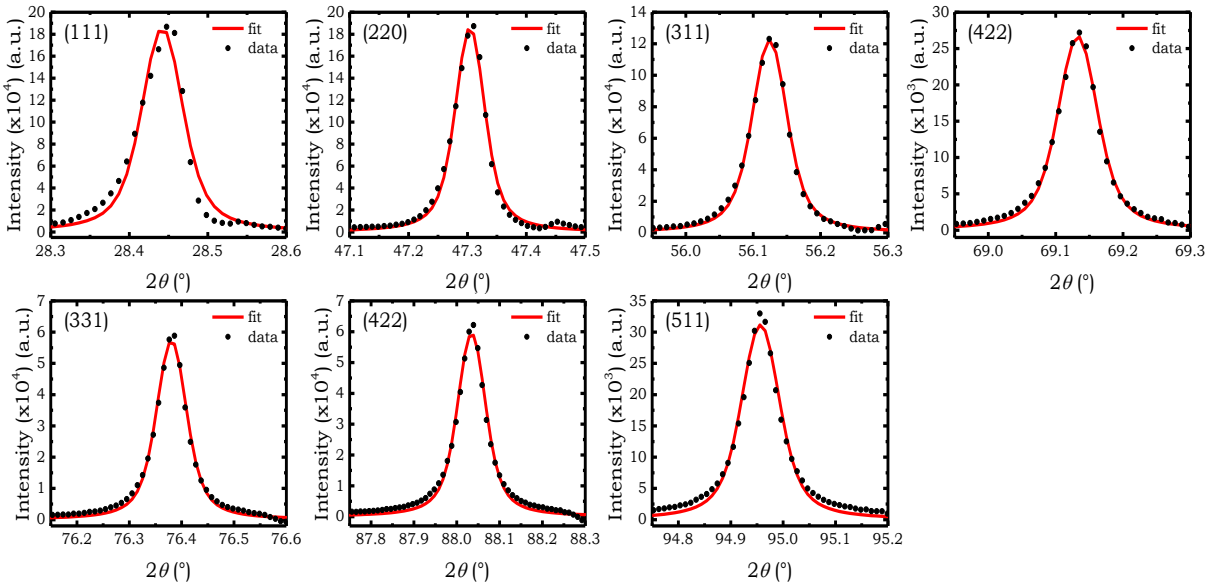

Figure B.15: Voigt fits of the Si powder sample diffraction peaks in a fixed illumination setup with a 20 mm illumination length of both the primary and secondary optics.

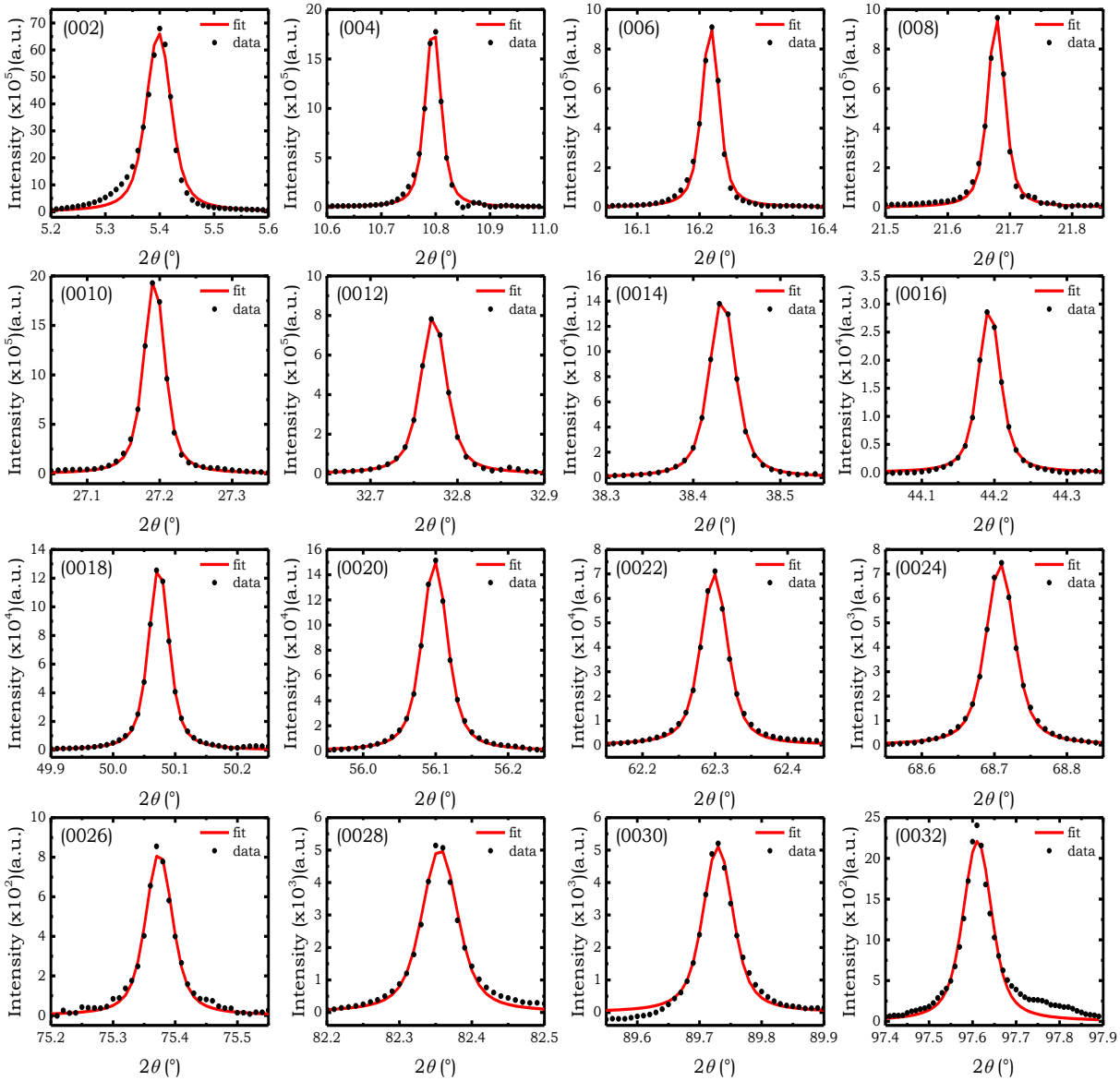

Figure B.16: Voigt fits of the $(PEA)_2PbI_4$ single crystal diffraction peaks in a fixed slit setup with maximum aperture (primary slit 1.0 mm, secondary slit 5.4 mm).

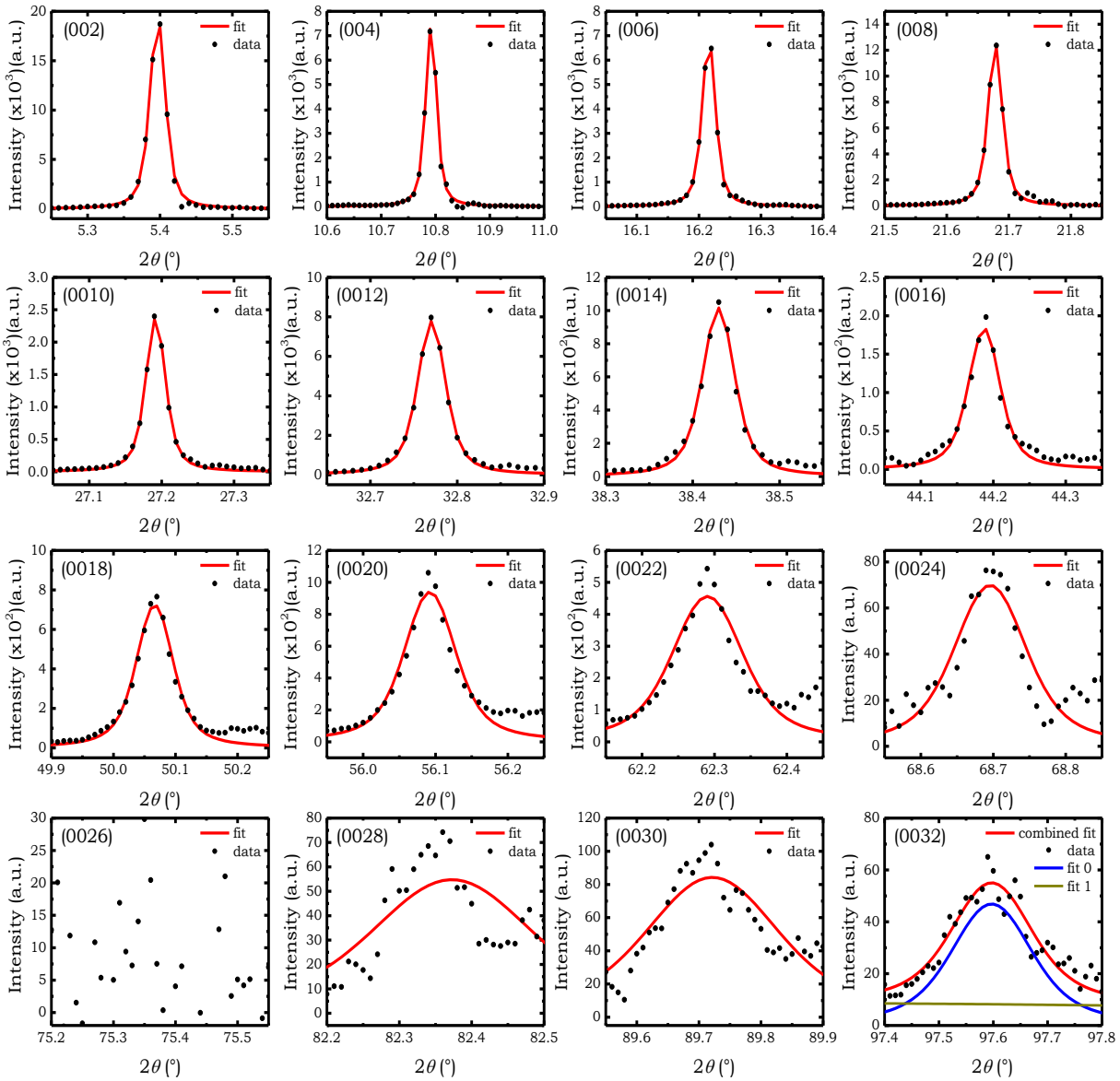

Figure B.17: Voigt fits of the $(PEA)_2PbI_4$ single crystal diffraction peaks in a fixed illumination setup with a 2 mm illumination length of both the primary and secondary optics.

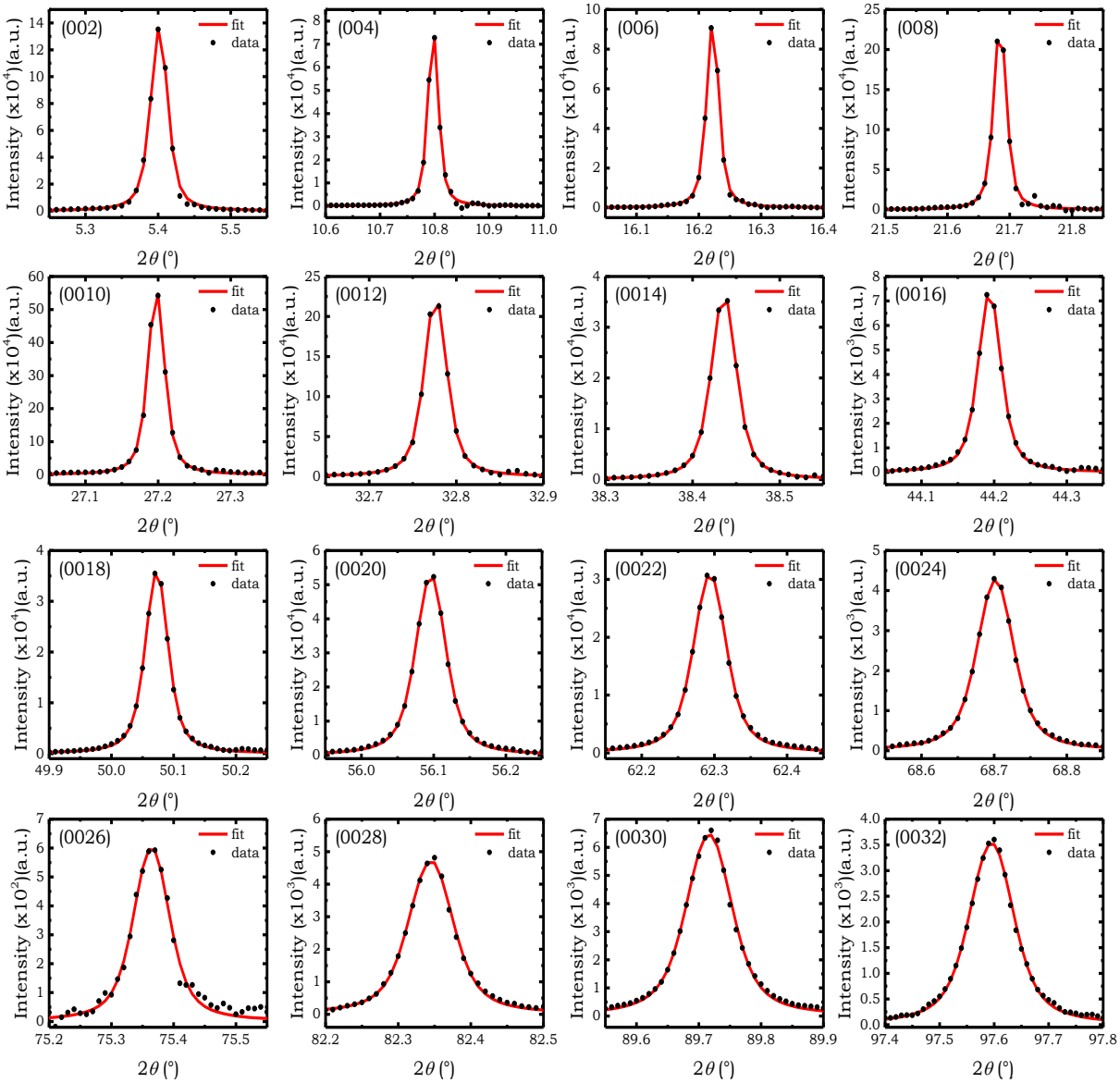

Figure B.18: Voigt fits of the $(PEA)_2PbI_4$ single crystal diffraction peaks in a fixed illumination setup with a 5 mm illumination length of both the primary and secondary optics.

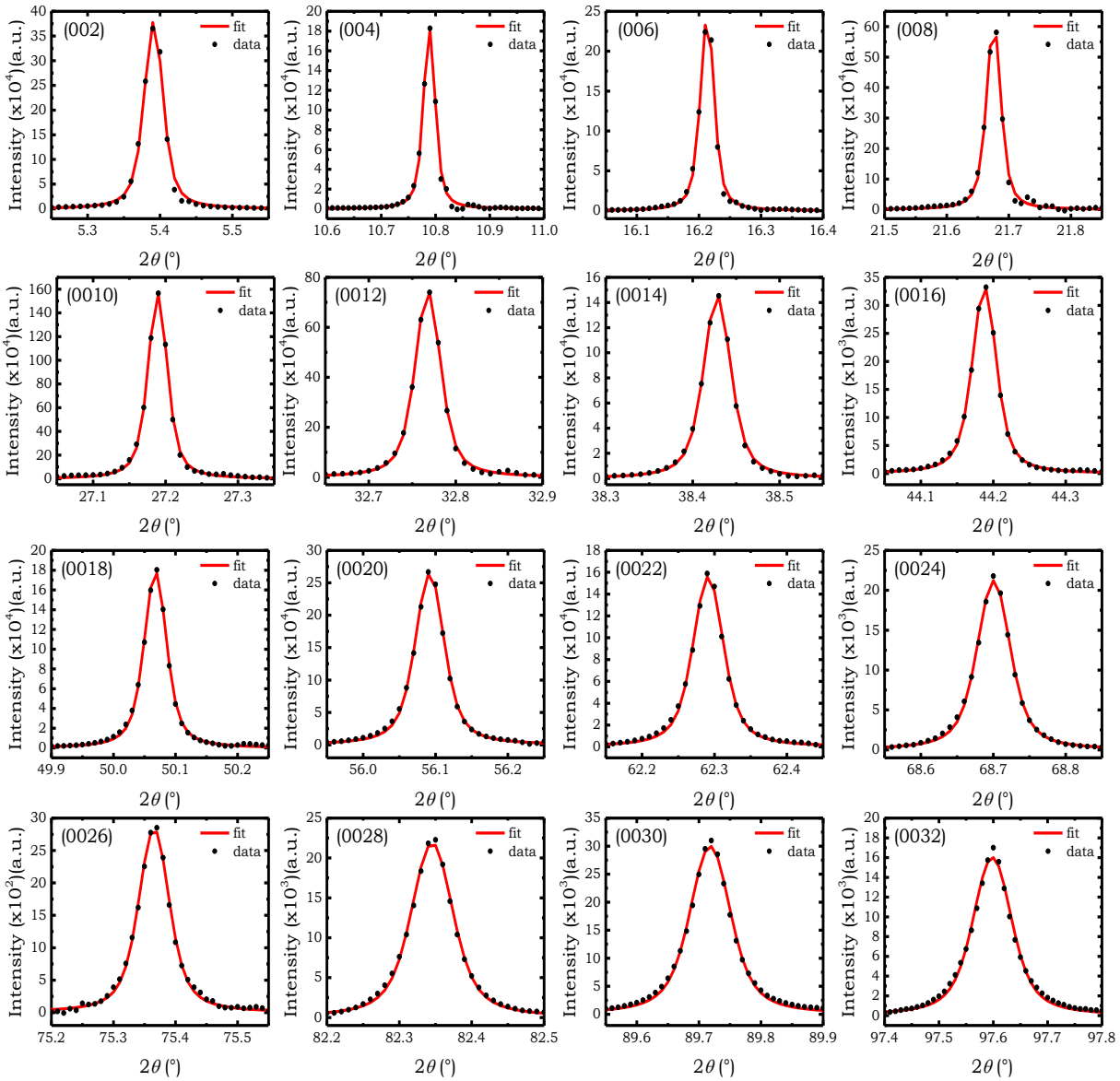

Figure B.19: Voigt fits of the $(PEA)_2PbI_4$ single crystal diffraction peaks in a fixed illumination setup with a 10 mm illumination length of both the primary and secondary optics.

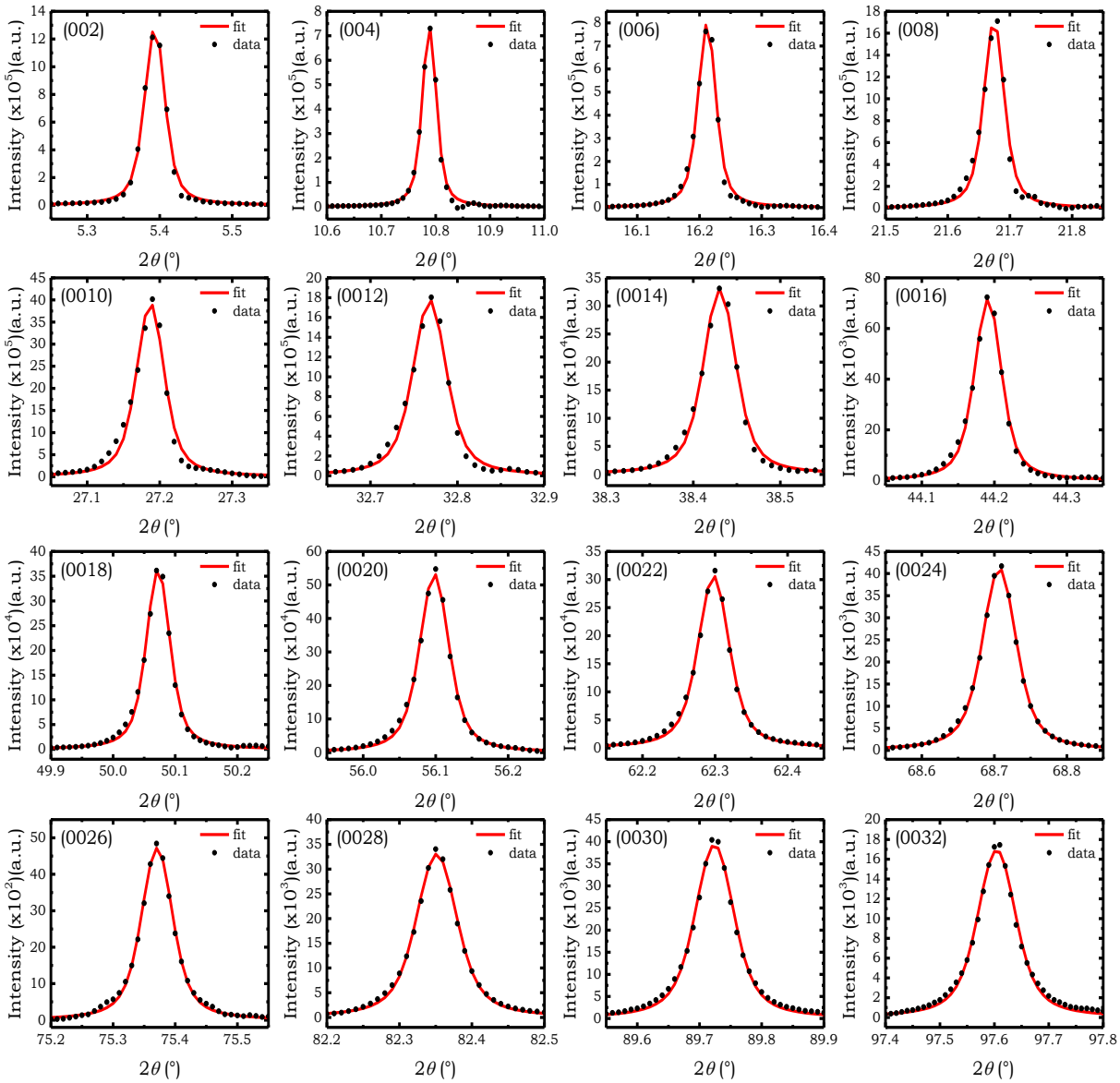

Figure B.20: Voigt fits of the $(PEA)_2PbI_4$ single crystal diffraction peaks in a fixed illumination setup with a 20 mm illumination length of both the primary and secondary optics.

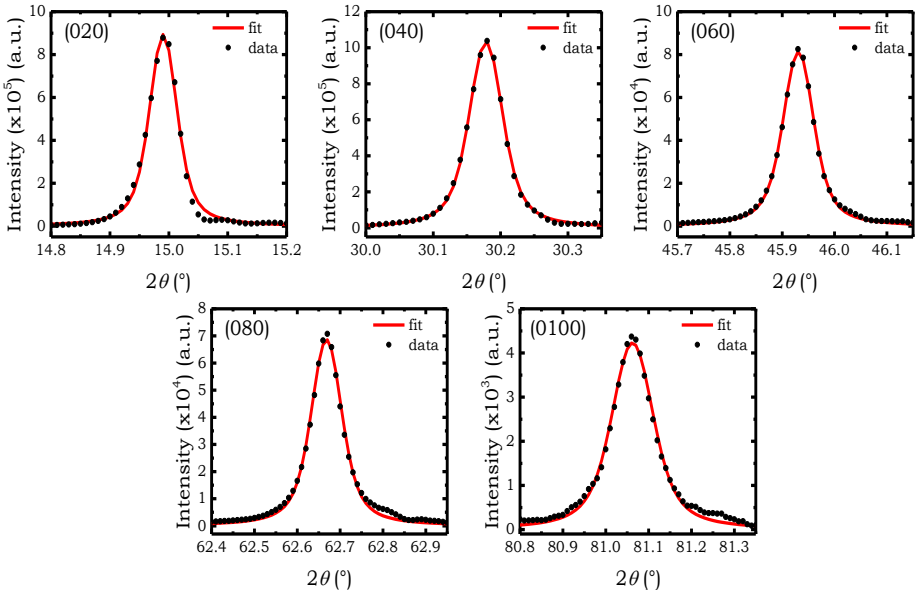

Figure B.21: Voigt fits of the $MAPbBr_3$ single crystal $(0k0)$ diffraction peaks in a fixed slit setup with maximum aperture (primary slit 1.0 mm, secondary slit 5.4 mm).

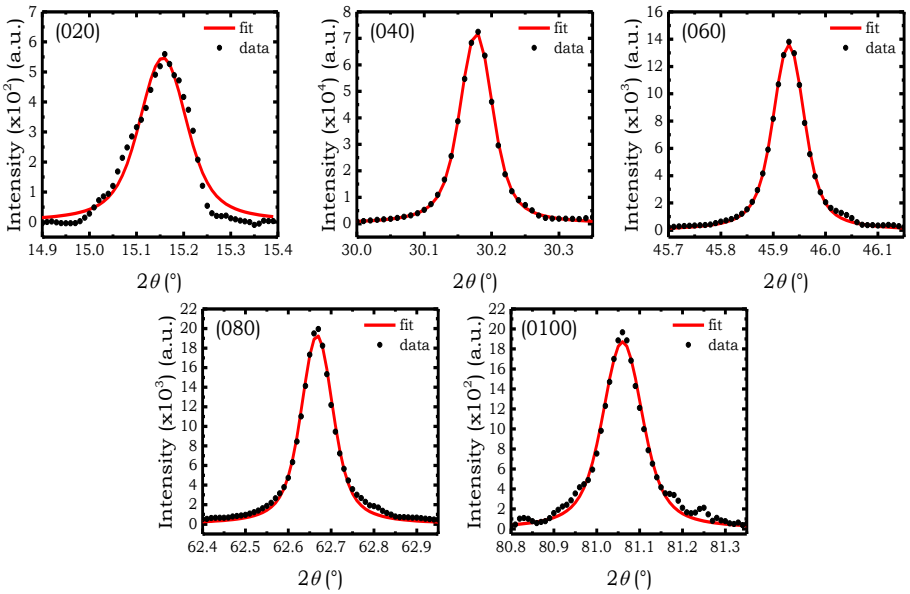

Figure B.22: Voigt fits of the $MAPbBr_3$ single crystal $(0k0)$ diffraction peaks in a fixed illumination setup with a 5 mm illumination length of both the primary and secondary optics.

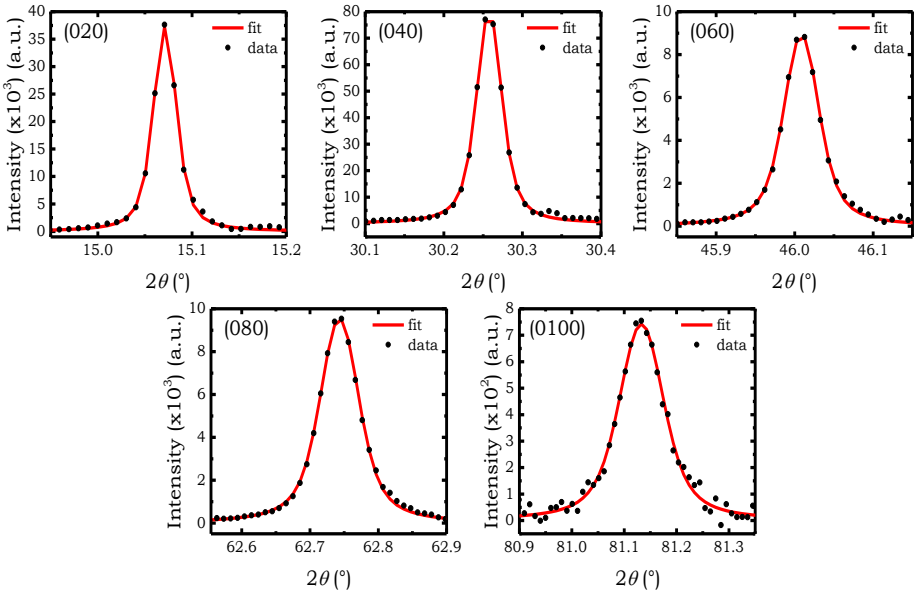

Figure B.23: Voigt fits of the $MAPbBr_3$ film $(0k0)$ diffraction peaks in a fixed illumination setup with a 5 mm illumination length of both the primary and secondary optics.

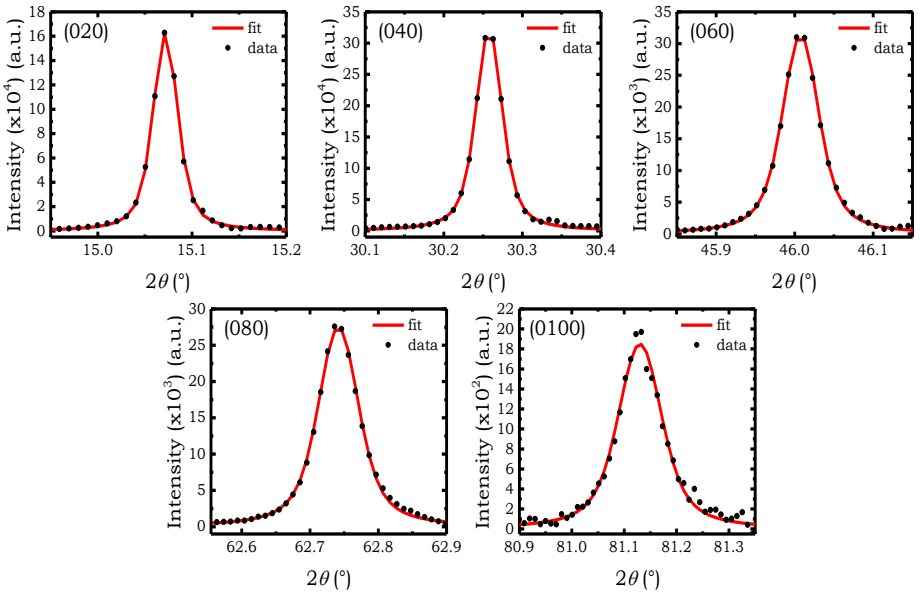

Figure B.24: Voigt fits of the $MAPbBr_3$ film $(0k0)$ diffraction peaks in a fixed illumination setup with a 10 mm illumination length of both the primary and secondary optics.

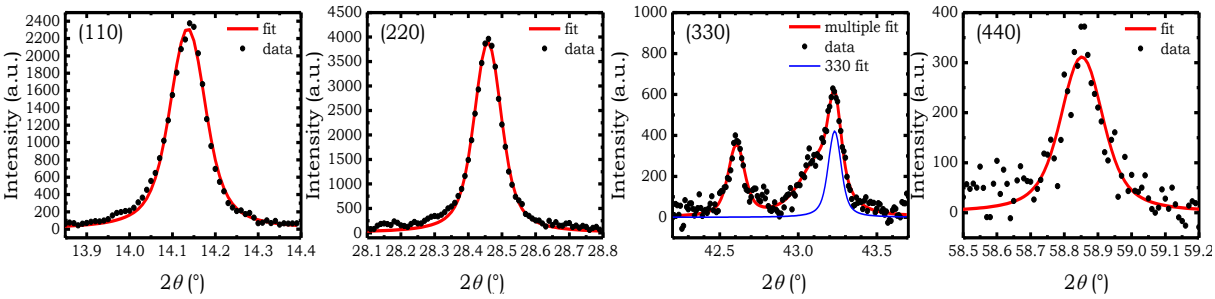

Figure B.25: Voigt fits of the $MAPbI_3$ film ($hk0$) diffraction peaks in a fixed illumination setup with a 10 mm illumination length of both the primary and secondary optics.

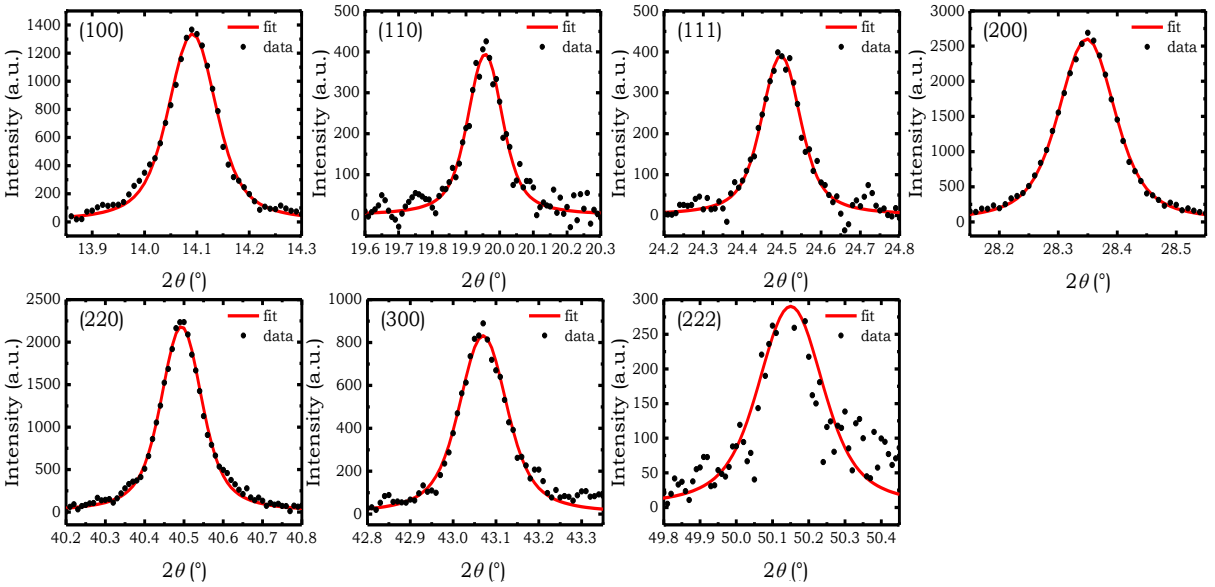

Figure B.26: Voigt fits of the $CsFAMAPb(IBr)_3$ film diffraction peaks in a fixed illumination setup with a 10 mm illumination length of both the primary and secondary optics.

Appendix C. Mass attenuation coefficient curves

Mass attenuation coefficients were obtained according to simple additivity, following the methodology reported by NIST:[202]

$$\mu/\rho = \sum_i w_i(\mu/\rho)_i \tag{C.1}$$

where w_i is the fraction by weight of the i^{th} atomic constituent, and the elemental $(\mu/\rho)_i$ values are extracted from the NIST reference.[201]

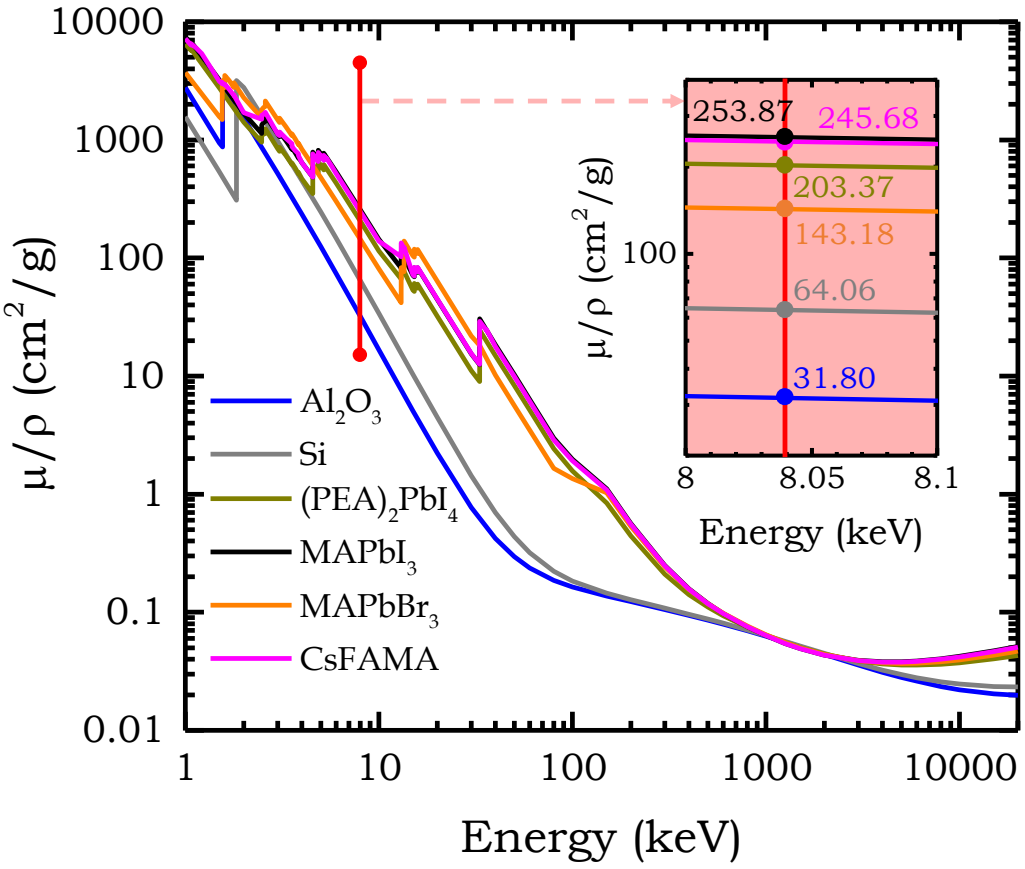

Figure C.1: Mass attenuation coefficients (μ/ρ) as a function of photon energy for different halide perovskites and XRD reference materials.

Appendix D. Chapter 5 supplementary figures

Calculations performed on the AFM images to quantify the variation in roughness and grain size were evaluated through the RMS parameter, defined as the standard deviation from the average height, and the mean grain size, represented by the equivalent radius parameter (r_{eq}).

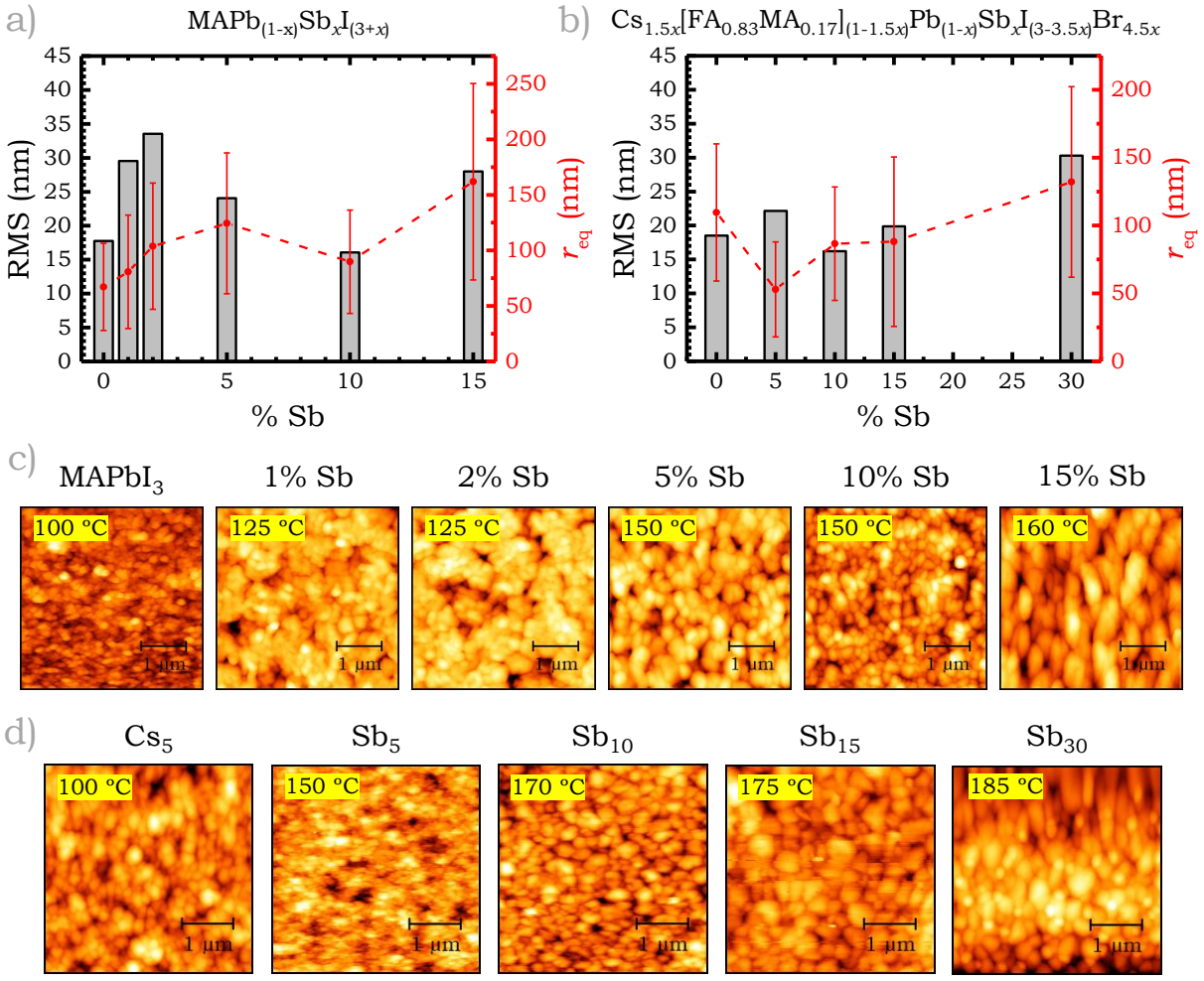

Figure D.1: RMS and r_{eq} parameters of XRD patterns of $MAPb_{(1-x)}Sb_xI_{(3+x)}$ and $Cs_{1.5x}FA_{0.83(1-1.5x)}MA_{0.17(1-1.5x)}Pb_{(1-x)}Sb_xI_{(3-3.5x)}Br_{4.5x}$) (b) perovskite films extracted from the AFM images in c and d, respectively.

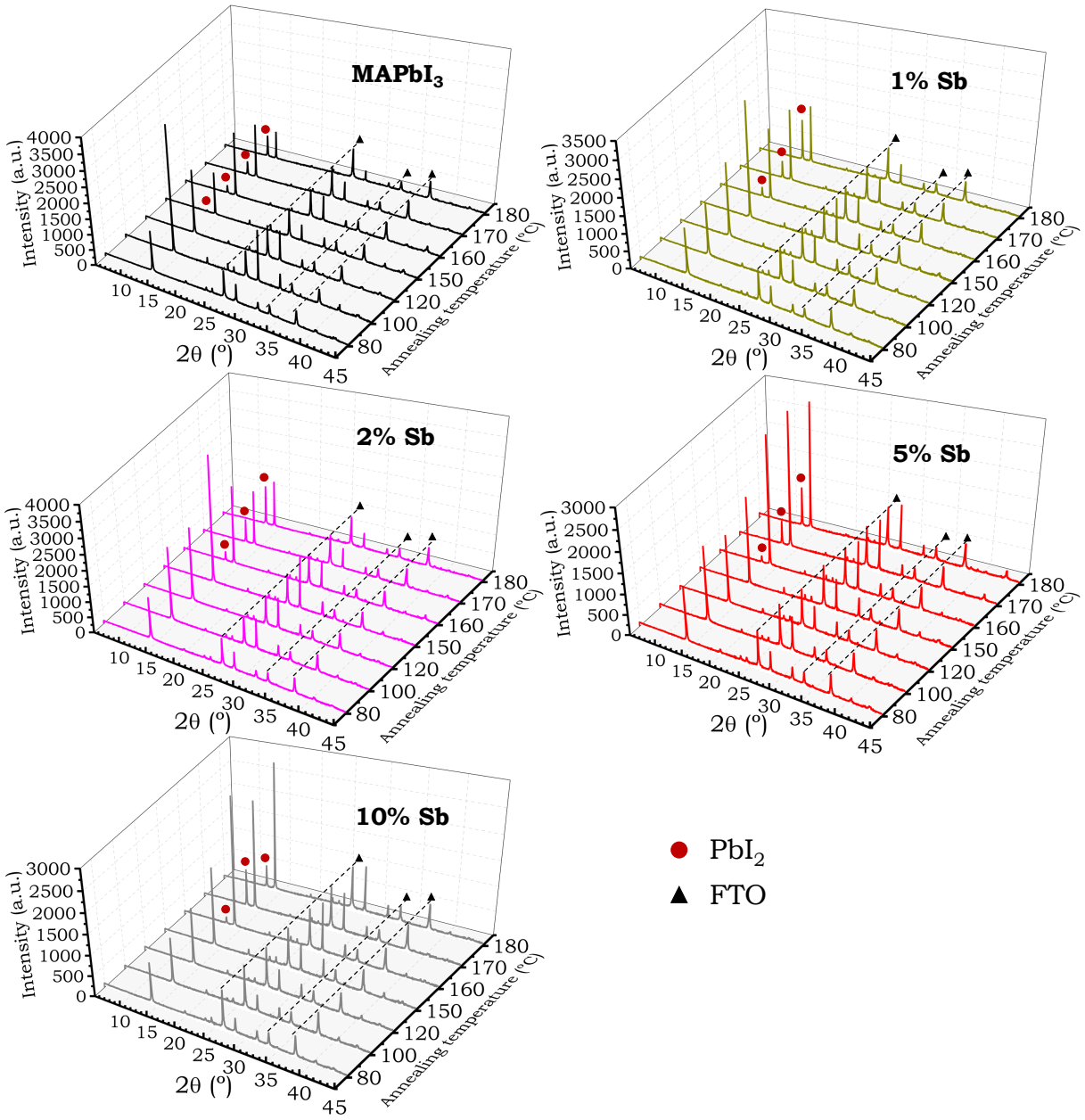

Figure D.2: XRD patterns of $MAPb_{(1-x)}Sb_xI_{(3+x)}$ films (x=0-10 %) annealed between 80 °C and 180 °C.

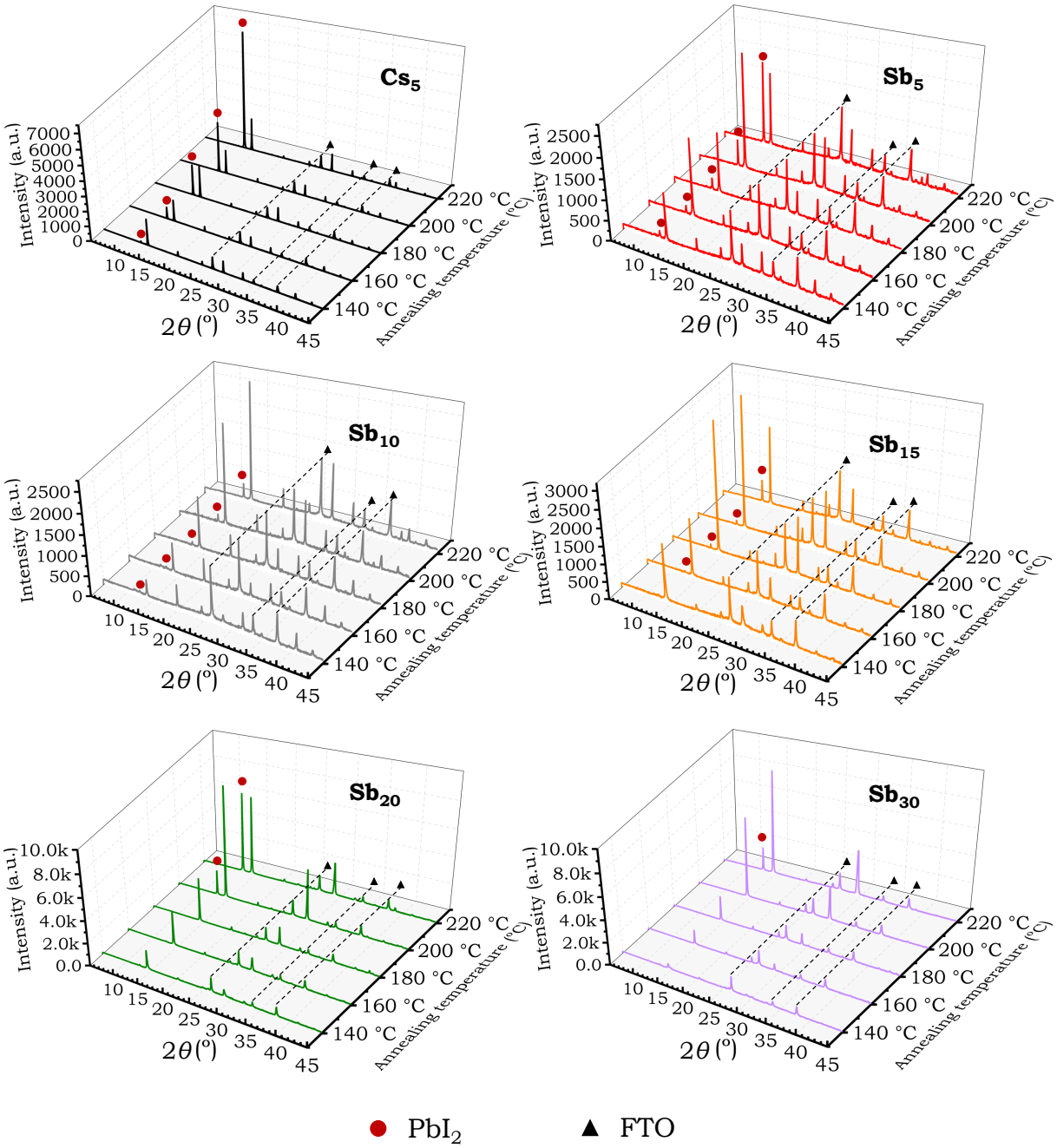

Figure D.3: XRD patterns of $Cs_{1.5x}FA_{0.83(1-1.5x)}MA_{0.17(1-1.5x)}Pb_{(1-x)}Sb_xI_{(3-3.5x)}Br_{4.5x}$ films (x=0-30 %) annealed between 140 °C and 220 °C.

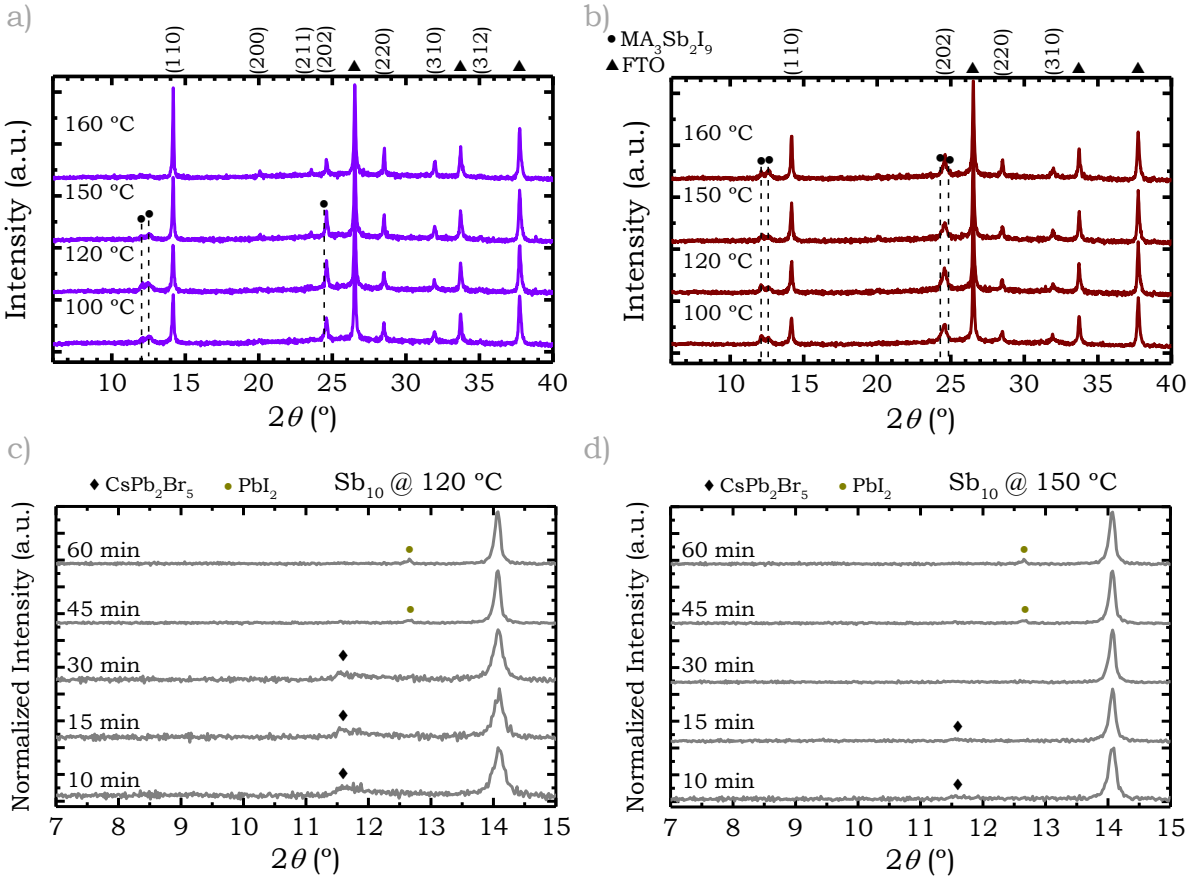

Figure D.4: Indexed XRD patterns of $MAPb_{(1-x)}Sb_xI_{(3+x)}$ films on FTO, annealed between 100 °C and 160 °C, for $x = 0.3$ (a) and $x = 0.5$ (b). Indexed XRD patterns of $Cs_{0.15}FA_{0.71}MA_{0.14}Pb_{0.9}Sb_{0.1}I_{2.65}Br_{0.45}$ samples annealed between 10 and 60 min at 120 °C (c) and 150 °C (d).

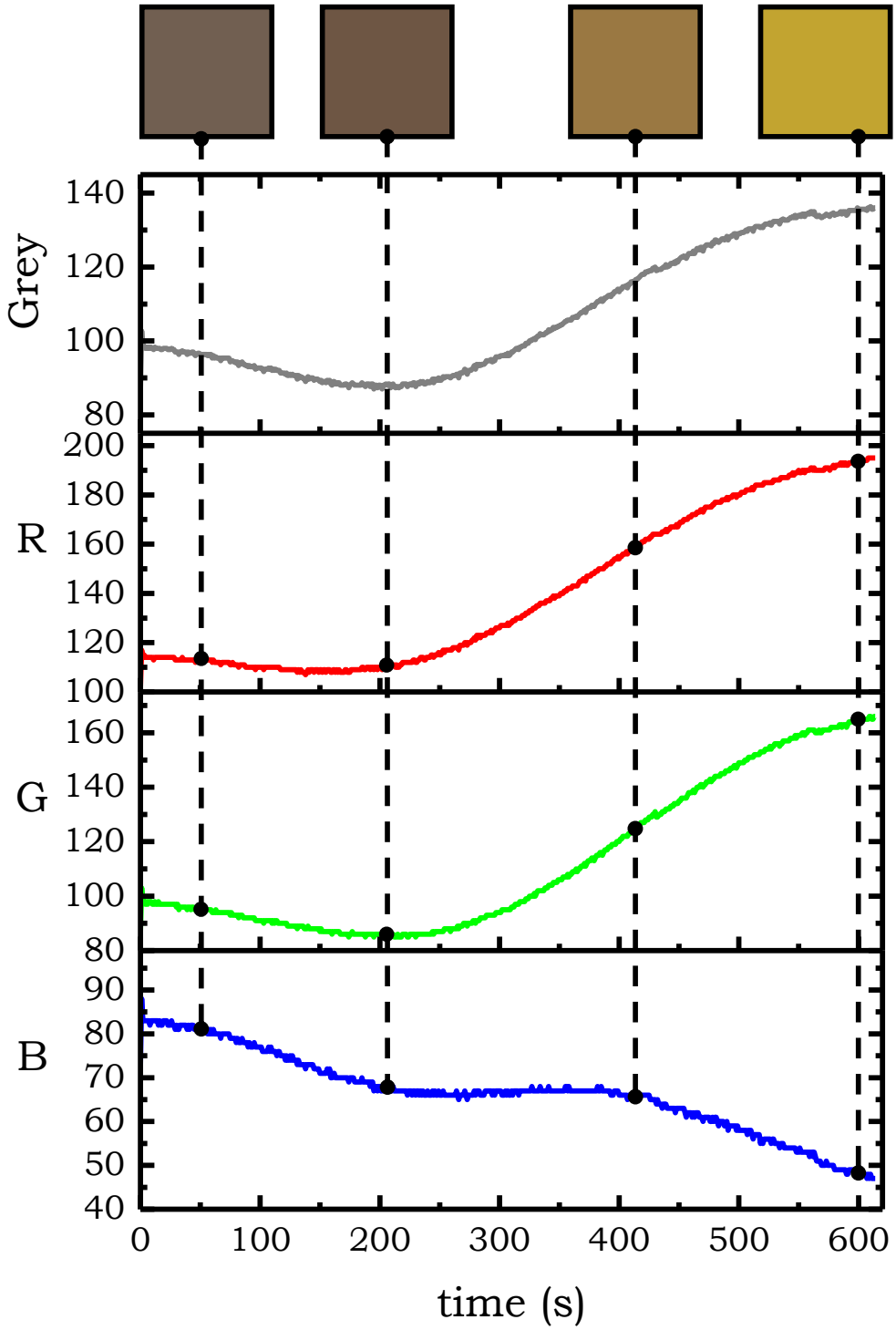

Figure D.5: Evolution of the RGB channels and grey-scale average of a $MAPb_{0.7}Sb_{0.3}I_{3.3}$ film upon exposure to 180 °C in room conditions of humidity. Transformation into PbI_2 requires the increase of the R and G channels and the decrease of the B channel to reach the yellow coordinates (RGB, (255,255,0)). The initial decrease in the red and green channels corresponds to a darkening of the film due to perovskite grain recrystallization.

Appendix E. Chapter 6 supplementary figures

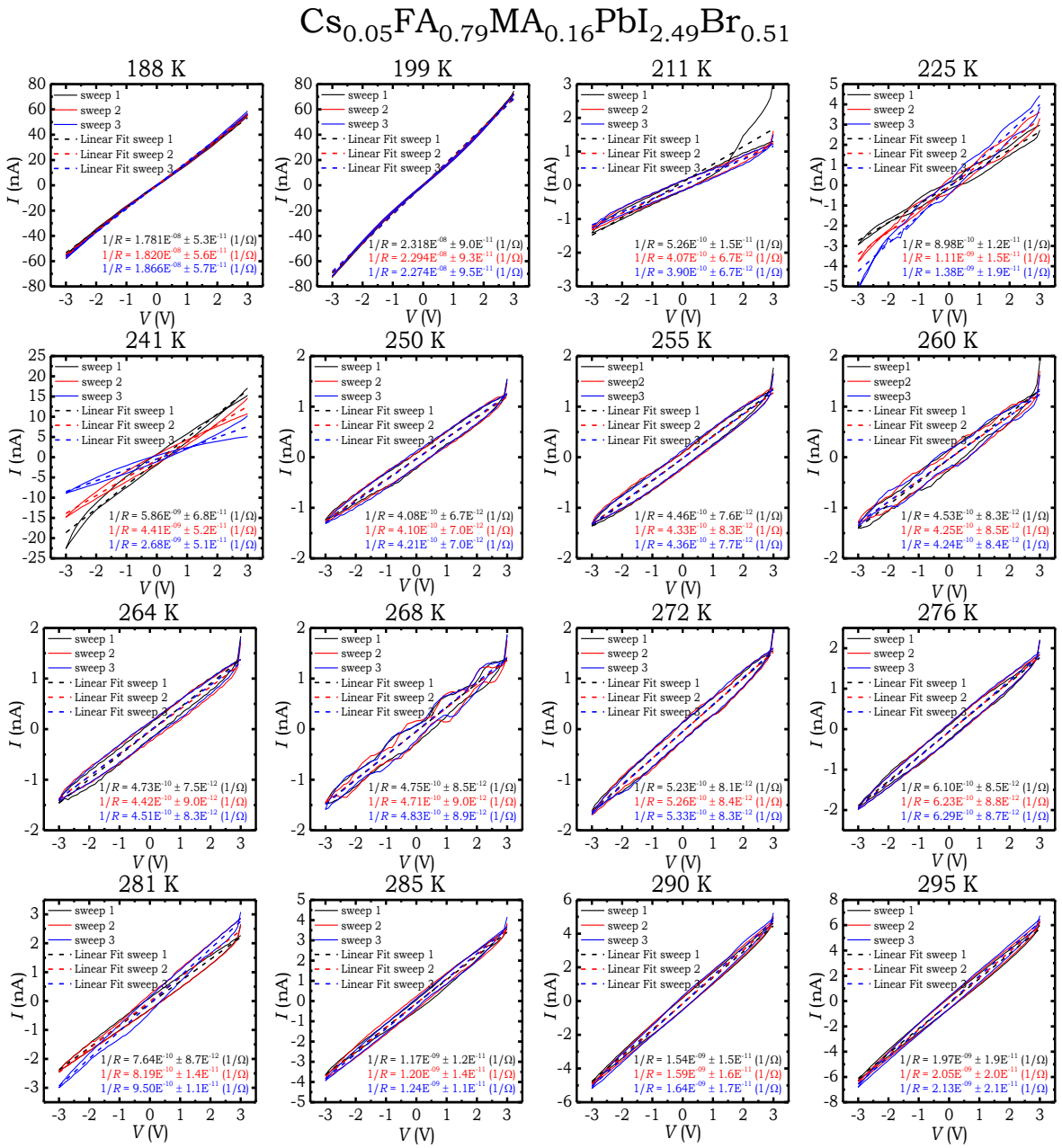

Figure E.1: Cs_5 IV curves taken at different temperatures with their correspondent linear fits and slopes ($1/R$).

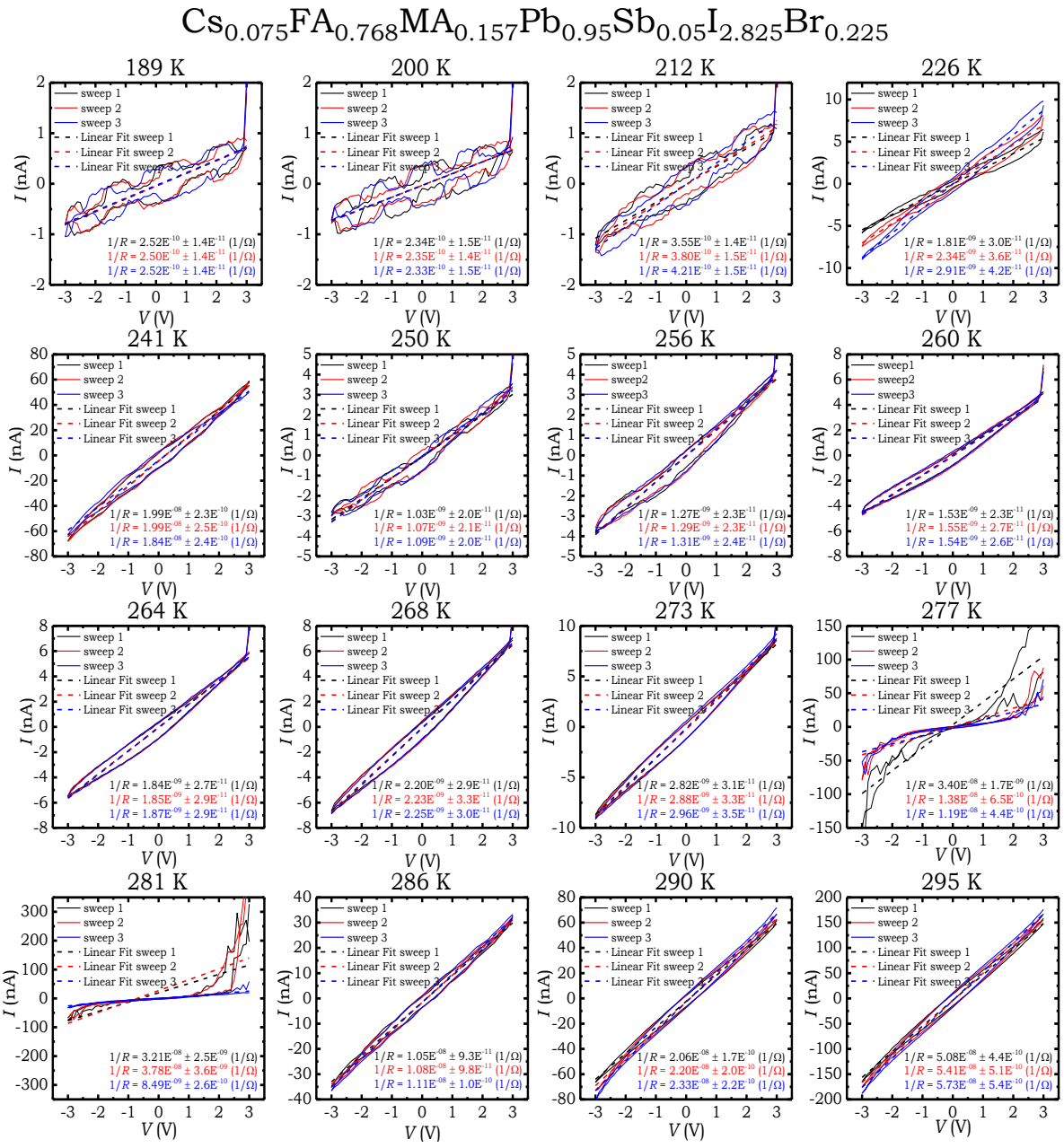

Figure E.2: Sb_5 IV curves taken at different temperatures with their correspondent linear fits and slopes ($1/R$).

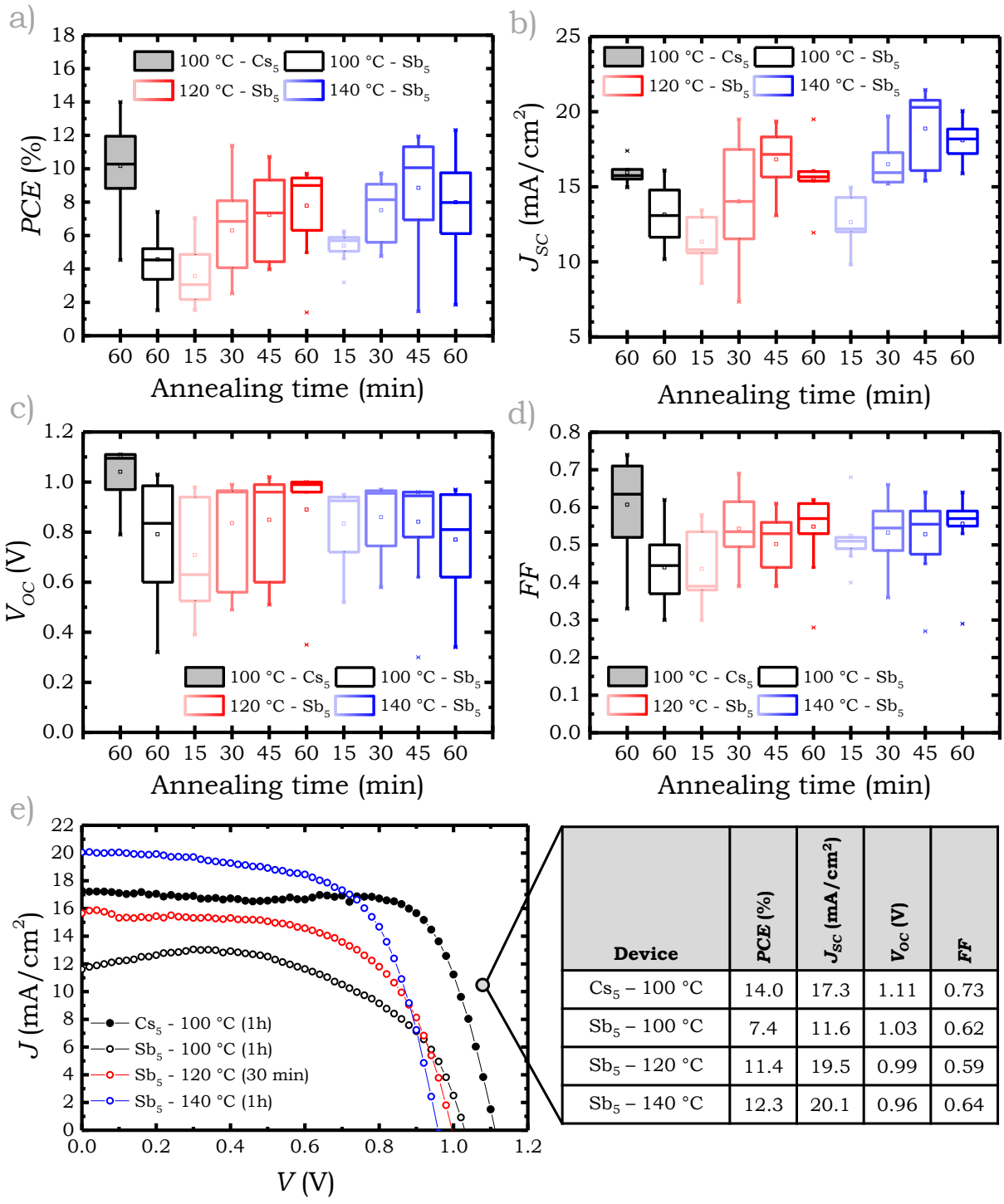

Device	PCE (%)	J_{SC} (mA/cm²)	V_{OC} (V)	FF
Cs_5 – 100 °C	14.0	17.3	1.11	0.73
Sb_5 – 100 °C	7.4	11.6	1.03	0.62
Sb_5 – 120 °C	11.4	19.5	0.99	0.59
Sb_5 – 140 °C	12.3	20.1	0.96	0.64

Figure E.3: Box plot statistics of *PCE* (a), J_{SC} (b), V_{OC} (c) and *FF* (d) from the reverse *JV* scan of Cs_5 and Sb_5 perovskite solar cells annealed at 100 °C, 120 °C and 140 °C; plotted as a function of annealing time. e) *JV* scans of the record devices.

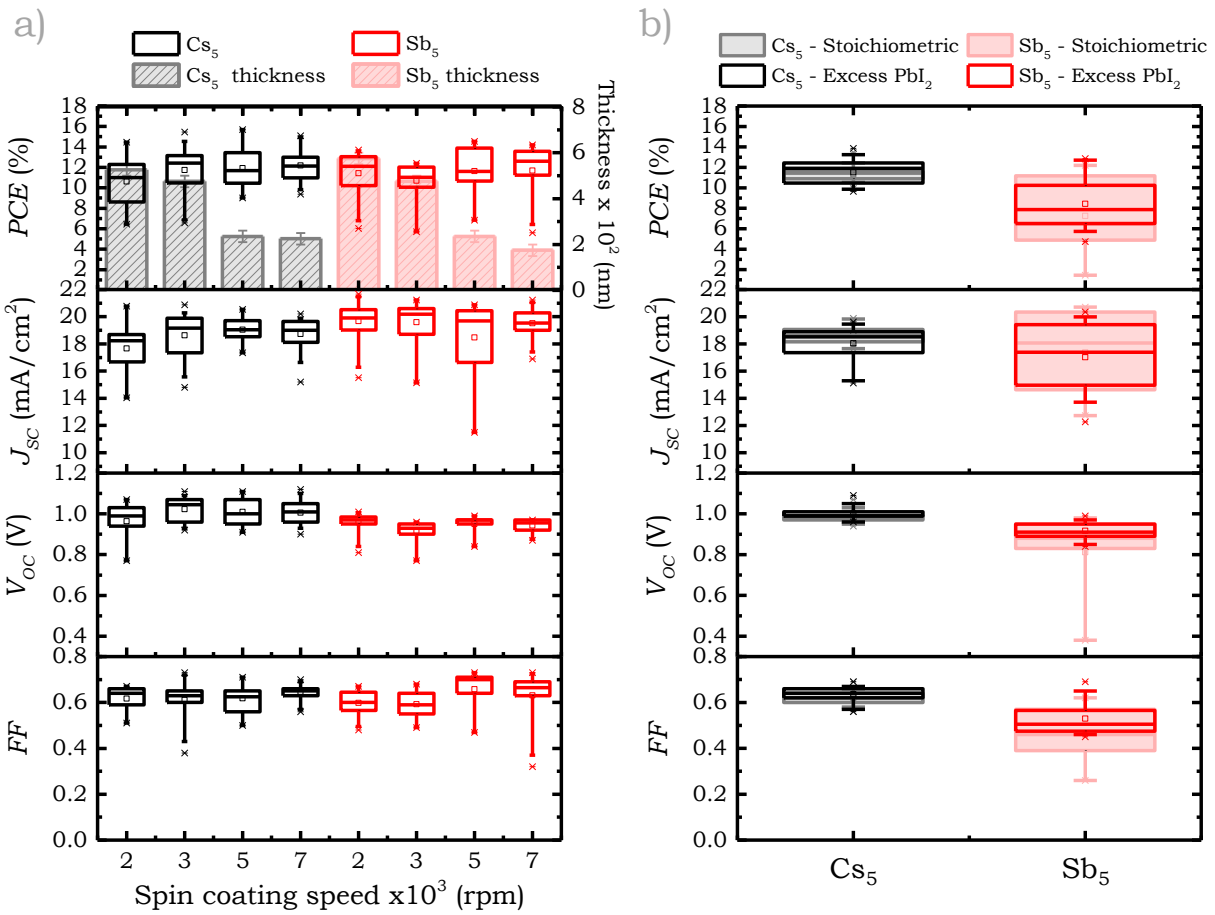

Figure E.4: a) Box plot statistics of the photovoltaic parameters from the reverse *JV* scans of Cs_5 and Sb_5 perovskite solar cells, plotted as a function of spin-coating speed. The thickness of the perovskite layer (measured with a profilometer) is included in the *PCE* plot. b) Box plot statistics of the device parameters from the reverse *JV* scans of Cs_5 and Sb_5 perovskite solar cells fabricated in stoichiometric conditions and with excess PbI_2.

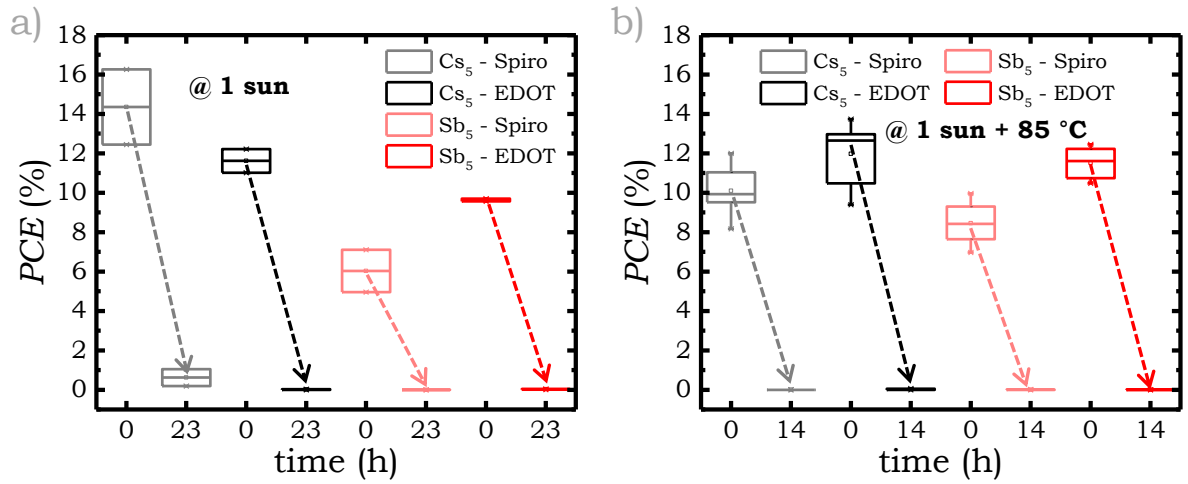

Figure E.5: *PCE* box plot statistics of Cs_5 and Sb_5 perovskite solar cells fabricated with Spiro-OMeTAD and EDOT-Amide-TPA as the HTL over time, exposed to 1 sun illumination without (a) and with heat (b).

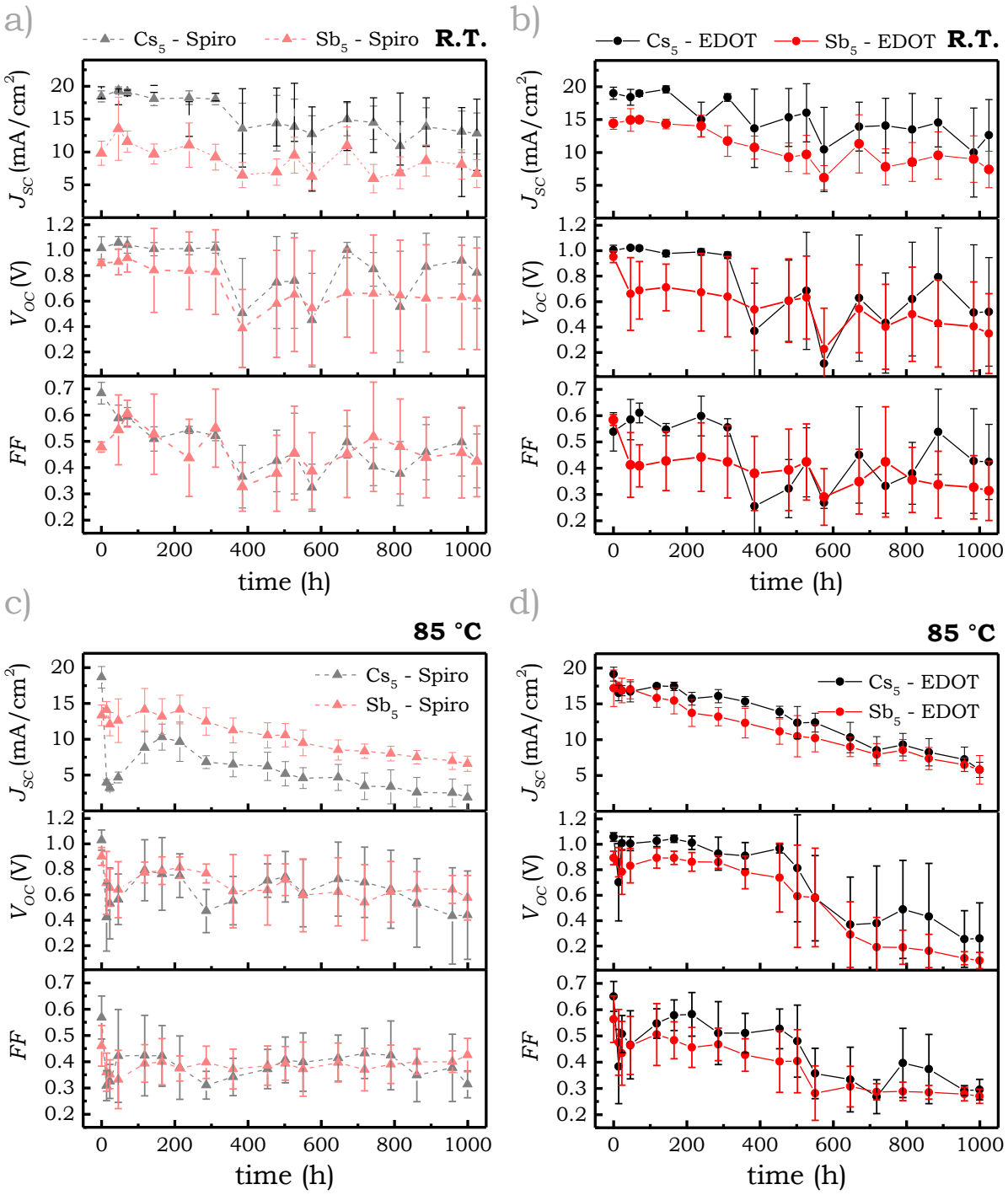

Figure E.6: Device statistical values from the reverse JV scans of Cs_5 and Sb_5 perovskite solar cells over time during dark ageing (a-Spiro, b-EDOT) and thermal ageing (c-Spiro, d-EDOT).